

Experimental Search for Signatures of Zonal Flow Physics in a Large Spherical Tokamak using Beam Emission Spectroscopy

A. P. Malcolm-Neale

Doctor of Philosophy

University of York

Physics

September, 2021

Abstract

Cross-field turbulent transport in magnetically confined plasmas is a highly effective loss mechanism of the heat and mass of fusion fuels and principally responsible for degrading the quality of confinement. Recently, an inter-dependence of turbulence and flows has been demonstrated in conventional tokamaks, including zonal flows that take energy directly out of turbulence. Data, in particular an experiment in a spherical tokamak, is scarce. This project uses a Beam Emission Spectroscopy (BES) diagnostic on the MAST spherical tokamak to measure local fluctuation of plasma density. We develop correlation and spectral analysis techniques to facilitate investigation of flow structure across the plasma profile.

I first developed a velocimetry routine using cross-correlation time delay estimation (CCTDE) optimising the length of correlation functions of fluctuating MAST BES data to achieve high time resolution for zonal flow detection. Tests using surrogate data were included to improve the accuracy and reliability of the code, achieving up to a 98% successful measurement rate in broadband data. The new code's performance was benchmarked using three realistic examples of spherical tokamak physics that previously had made velocimetry unusable. Each had an imposed mode mimicking zonal flow shown to be observable and measurable in my velocity spectra.

Results from this spectroscopy identify four classes of spectra observed in real BES data. Spectra with the clearest coherent peaks are shown to exist concurrently with a long-lasting magnetic mode. A systematic test of zonal flow physics at shot times that produce velocity spectra with coherent peaks was developed. Automating and weighting scores for those tests created a framework for GAM detection; adaptable as expectations of GAM physics change.

In this project it enabled the first search of a substantial MAST data set of 63 shots in which BES observed the plasma edge. No examples matched all expected physics. The observed spectrum patterns match GAM theory that accounts for safety factor and plasma rotation, but not elongation; the modal average extent of matches covers four columns (about 8 cm plasma radius) of the detector. A scan of 209 shots at L-H transition times found 5 cases with good matches to expected zonal flow physics but relatively weak velocity modes.

Declaration

This thesis has not previously been accepted for any degree and is not being concurrently submitted in candidature for any degree other than Doctor of Philosophy of the University of York. This thesis is the result of my own investigations, except where otherwise stated. All other sources are acknowledged by explicit references.

I declare that this thesis is a presentation of original work and I am the sole author.

The work presented herein was funded by the Engineering and Physical Sciences Research Council (EPSRC), grant reference number: EP/K504178/1 .

Publications & Presentations From This Work

Papers

A. Malcolm-Neale, Using the wider science curriculum to investigate fusion energy, 2019, Phys. Educ., 54, 044001

Talks

A. Malcolm-Neale, Peak Significance: Hunting for evidence of zonal flows in spectra of velocity measurements of plasma in a spherical tokamak, Post-Graduate Conference, York, 2019 [*Conference talk 1st Prize*]

Posters

I. Cziegler, L. Howlett, **A. Malcolm-Neale** et al., Coordinated Experimental and Computational Search for Zonal Flow Characteristics, 25th Joint EU-US Transport Task Force Meeting, York, 2021 **A. Malcolm-Neale**, Velocimetry on MAST with Beam Emission Spectroscopy (BES), LGBT STEMinar 2018, York, 2018

Acknowledgments

The support and input of many generous people is gratefully acknowledged.

Roddy Vann for his focus and timely interventions to see that this project's targets would be met.

Anthony Field for astute insights into the shortcuts (or 'sensitivity') of experimental physics and a great deal of technical support - especially now our diagnostic handbook entry for BES encouragingly reads "Data is very labour intensive to analyse... ask the RO to provide required data."

Istvan Cziegler for a wealth of meetings, conversation, optimism and patience; my principal source of advice throughout and a phenomenal eye for detail that has improved everything. For the RAPtors journal club that taught us to consider graphs with the question 'what would we expect to see if...' and allowed what is now a BES/ zonal flow group to share wisdom. We at least started out with a plan to do it smarter not harder!

Thanks also go to the department for opportunities to work on science communication, outreach, teaching and equality & diversity work that have kept me motivated. Out of these came newfound understanding, the fantastic 'Glass of Seawater' fusion energy podcast project and a wonderful opportunity to teach high school physics using fusion energy that I wrote up in Physics Education [2019 Phys. Educ. 54 044001 doi.org/10.1088/1361-6552/ab129a]¹

To Twitter, for solidarity in our ongoing effort to correctly spell fleu...floure...fluorescence?

Thanks to those who got me here. To Grandpa whose example reminded me science can be a career, the teacher who insisted I was too creative to be an accountant and to mum and dad - who each taught my sister and I to be curious and see beyond our front door. To our close-knit cohort for their friendship and especially to Will, my flatmate for the first 12 months of my final PhD year, for keeping the passion for cool physics alive and for easing off the jokes about MAST-U being ready for me. Finally, to the York RI Templars inclusive rugby team. Playing with you didn't get me the serious injury I needed to get out of writing this up but it has been a source of amazing support and perspective.

Contents

Abstract	2
Declaration	3
Acknowledgements	5
Contents	6
List of Tables	9
List of Figures	10
1 Introduction	14
1.1 Tokamak Geometry	15
1.2 Turbulence	16
1.2.1 Sources and Stabilisers	18
1.2.2 Shapes and Sizes	19
1.3 The Problem: Cross-Field Transport	20
1.4 A Solution: Zonal Flow	20
1.4.1 Mean Flow versus Zonal Flow	22
1.4.2 Summary of Experimental Base	24
1.4.3 Confinement Transition Effect	28
1.5 Mega Ampere Spherical Tokamak (MAST)	28
1.5.1 Zonal Flow Experiments on MAST	29
1.6 Summary and Structure	30
2 Methods	32
2.1 Beam Emission Spectroscopy (BES)	32
2.2 Cross-Correlation Time Delay Estimation (CCTDE)	35
2.2.1 Limitations of CCTDE on MAST	39

3	Code Development	41
3.1.1	Filtering	42
3.1.2	Noise Elimination	43
3.1.3	Surrogate Data	44
3.2	Cross-Correlation Time Delay Estimation Technique Design	47
3.2.1	Measurement Limits	47
3.2.2	Correlation Function Size	49
3.3	Velocity Measurement Failure Modes	52
3.3.1	Preemptive Tests Introduced To The Code	54
3.4	Introducing the Null Hypothesis	63
3.4.1	Spectrum Metrics	64
3.5	Summary	66
4	Benchmarking Code Performance	69
4.1	Introducing Noise	69
4.2	Mode in the Velocimetry Input Signal	71
4.3	High Frequency Burst Modes	78
4.4	Time Varying Imposed Velocity	85
5	Velocity Spectra of MAST BES Data	92
5.1	Velocity Spectra Classification	92
5.2	On Zero-Frequency Peaks in Velocimetry Spectra	94
5.3	On Medium-Frequency Peaks in Velocimetry Spectra	95
5.3.1	Mirnov Coil Signals	97
5.3.2	Theory in Support of Magnetic Mode and GAM Co-existence	99
5.3.3	Study of high contrast velocity spectrum peaks	102
5.4	Summary	105
6	A Systematic Search for Signatures of GAMs	107
6.1	Study of Cases with a Magnetic Mode: Developing Systematic Tests of MAST Data	107
6.1.1	Literature Sources for Zonal Flow Characteristics	107
6.1.2	Tests	109
6.1.3	Weighting the Scores Assigned to Tests	116
6.2	Overall Test Results From Study of BES Turbulence Shots	119
6.2.1	Distribution of Results	119
6.2.2	GAM Theory Representation	121
6.2.3	Tests That Predict High Scores	126
6.3	Cases From the Study of BES Turbulence Shots	131

6.3.1	Highest Scoring Cases	131
6.3.2	Low Confinement Mode Cases	140
6.3.3	Cases Without Magnetic Mode	142
6.3.4	Lowest Scoring Cases	145
6.4	Fully Automated Study of Confinement Transition Times	145
6.5	Summary	150
7	Discussion and Conclusions	154
7.1	Discussion	154
7.1.1	Part 1: Adapted Cross Correlation Time Delay Velocity Estimation	154
7.1.2	Part 2: Studies of BES data from MAST experiments	156
7.1.3	Tension: Expected Identification versus Incomplete Evidence	158
7.1.4	Future Routes to Verification	163
7.2	Conclusions	163
8	Appendices	180
8.1	Appendix A: Copy of the Code	180
8.2	Appendix B: List of Shot Numbers Targeted	187
8.2.1	Classification Survey [80 Shots Total, 22 Edge Shots]	187
8.2.2	12 Shot Study	187
8.2.3	63 Shot Study	187
8.2.4	209 Shot Study	187

List of Tables

3.1	Shot numbers and start times used to generate surrogate BES data. All signals are 0.01 s long.	46
3.2	Velocimetry performance measured by quality of gradient fit compared to imposed velocity	60
4.1	Measurements of real velocity spectra peaks resulting from cases with powerful input modes.	75
4.2	Measurements of real bursting modes from spectrograms of BES data - times	78
4.3	Measurements of real bursting modes from spectrograms of BES data - frequencies	79
5.1	Reported values of magnetic fluctuation amplitude	101
6.1	The locations of Mirnov coils on MAST used to measure mode axisymmetry and poloidal mode number.	112
6.2	Count of accurately marked L-H transition times with D_α filter cutoff frequency	115
6.3	Success rate of each test metric	121
6.4	Statistics of the frequency difference between predicted and measured peaks .	123
6.5	A sample of cases from the high scoring category.	132
6.6	The coherence of columns for each high scoring sample case	134
6.7	Duration of the velocity peaks	140
6.8	Sample of highest scoring L mode cases	140
6.9	Coherence across radial positions for cases in the L mode sample set.	141
6.10	A sample of cases in which no magnetic mode was identified.	142
6.11	A sample of lowest scoring cases.	145
6.12	The highest scoring cases from L-H transition shots.	148
6.13	The highest scoring cases from L-H transition shots without a magnetic mode identified.	150
6.14	Coherence across radial positions for highest scoring transition time cases. . .	150

List of Figures

1.1	Interdependence of turbulence and flow in tokamak plasmas.	23
1.2	Magnetic field line geometry in MAST	29
2.1	BES optical pathways in MAST	34
2.2	BES field of view in MAST and MAST-U	34
2.3	Still density map from a gif using the fluctuation amplitudes of each of 4×8 channels of BES data at a single timestep.	35
2.4	Plasma data from shot 29378	36
2.5	A cartoon showing the principle of CCTDE operation.	37
2.6	An exemplar cross-correlation function	38
2.7	Turbulence mapping using undelayed cross-correlation information	39
2.8	Apparent poloidal velocity with advected turbulence	40
3.1	Velocity time series of all columns	42
3.2	Mesh plots showing the velocity calculated in each channel of the BES detector	42
3.3	NBI and BES coherence	43
3.4	Butterworth filter response	44
3.5	High energy particle noise elimination from BES data	45
3.6	Random phase method for surrogate data	46
3.7	Spectrograms of BES data used to make surrogate data for code testing	47
3.8	Example velocity time series	49
3.9	Imposing a physical limit on acceleration in measured velocity	50
3.10	Correlation significance defined by the t-test	51
3.11	Scan of correlation function correlation window sizes	52
3.12	Correlation function tests of velocity measurement quality	55
3.13	Three examples of a negative velocity measurements	56
3.14	Effect of bandpass filtering BES data on velocimetry	58
3.15	Filter order effects on velocimetry	59
3.16	Correlation function correlation window size effects on velocimetry	59
3.17	The linear fit of inaccurate velocity measurements	60

3.18	Corrected velocimetry error rate and performance	61
3.19	Replacing ‘NaN’ velocity measurements to regularise the velocity time series	62
3.20	Effect of imposed velocity on velocimetry spectrum	63
3.21	A robust spectrum pattern of velocimetry	64
3.22	Velocimetry spectra metrics	65
3.23	Variation of velocity spectra with code design	67
4.1	Adding Gaussian noise to surrogate input data.	70
4.2	Realistic cross-correlation values across BES columns	71
4.3	Spectrum of an imposed mode in filtered BES data	72
4.4	The impact of mode amplitude on spectrum metrics	73
4.5	Spectra for the signals produced with an imposed mode	76
4.6	Comparing real detected peaks to the surrogate data	77
4.7	Spectra and spectrograms of real intermittent bursting patterns	79
4.8	Synthetic bursting signals imposed to test the code	80
4.9	Effect of bursting signals on velocimetry metrics	81
4.10	The effect on velocity measurements of increasing bursting mode amplitudes.	82
4.11	Comparing broadband and bursting spectra and metrics	83
4.12	Velocimetry with stepwise variation of imposed velocity with time	85
4.13	Velocimetry with smoothly varying imposed velocity	87
4.14	Table showing the average overestimation of the velocimetry	88
4.15	Time varying imposed velocity effect on velocimetry metrics	88
4.16	Average overestimation versus correlation correlation window size	89
4.17	Linear fit of velocimetry overestimation over full measurable velocity range	91
5.1	An illustration of the four types of spectra	93
5.2	Real examples of type one and two velocity spectra.	93
5.3	A comparison of typical spectra from surrogate and real cases.	94
5.4	Comparison of spectra and a spectrogram for an example of type three spectra	96
5.5	Examples of sharp spectral features at extremely low frequencies	96
5.6	Spectrograms of continuous magnetic modes	98
5.7	Spectrogram of Mirnov coil signal containing continuous magnetic mode with H factor	98
5.8	Spectrograms of Mirnov signals with continuous magnetic modes with plasma parameters that determine GAM frequency	100
5.9	Comparison of BES and Mirnov spectrograms with continuous magnetic mode	103
5.10	Changing bandpass filter lower cutoff on BES data	104
5.11	Comparison of type four velocity spectra before and after the BES bandpass cutoff frequency is raised	105

6.1	The D_α signal transition time methods	115
6.2	Spectrogram of the Mirnov signal for shot number 30169 with D-alpha plotted	116
6.3	A full list of tests, success criteria, scores and saved data. Highlighted cells mark tests that can be scored without a magnetic mode.	118
6.4	Histograms of the distribution of scores	120
6.5	The distribution of scores per test for all cases	122
6.6	The number of cases with a magnetic mode matching each GAM frequency prediction model	123
6.7	Histogram of the differences between measured and predicted frequencies of velocity spectrum peaks.	124
6.8	The number of velocity peaks in all spectra for all cases matching any model of GAM frequency.	125
6.9	Radius and frequency of velocity spectrum peaks that match GAM models .	125
6.10	The radius and frequency results for each matching peak plotted as a function on the total score in each case.	126
6.11	Measured parameters of the peaks for model-matching cases plotted as a func- tion of score.	127
6.12	The number of columns per case containing velocity spectrum peaks that match GAM models or the fundamental long magnetic mode	128
6.13	Density and magnetic signal and spectrum parameters are plotted against total score	129
6.14	Magnetic spectrum peak height compared to total signal RMS.	130
6.15	Velocity time series total RMS amplitude versus total score	130
6.16	The models of GAM theory matched by peaks of the velocity spectra of cases in the high scoring category.	132
6.17	The GAM models matched by the frequency of the fundamental magnetic mode in high scoring cases with a continuous magnetic band in their spectro- gram.	133
6.18	Distribution of radius and frequency of model-matching velocity peaks	133
6.19	Spectrograms of Mirnov signals for cases in the high scoring sample set . . .	135
6.20	The data from a case in each of three high-scoring types found	137
6.21	Spectrograms of velocity series for high scoring cases	138
6.22	Spectrograms of velocity in consecutive time series for one high scoring case .	139
6.23	Velocity spectra peak frequencies against the predictions of 4 GAM models .	141
6.24	Data from two high scoring L mode cases	143
6.25	Data from cases with no magnetic mode	144
6.26	Data from the lowest scoring cases	146
6.27	Automatic L-H transition survey method data	147

<i>LIST OF FIGURES</i>	13
6.28 Magnetic signal data for the L-H transition survey	148
6.29 Distribution of L-H survey case scores with magnetic mode and poloidal mode number	149
6.30 GAM models and velocity spectra peaks for best cases in L-H transition times survey	151
7.1 Key Results	168

Chapter 1

Introduction

This thesis aims to provide direct evidence of zonal flows in large spherical tokamaks in order to support reduction of the cross-field loss of fusion energy fuel and heat by turbulent transport. We seek to provide a reference experiment for their detection on MAST. A rigorous understanding of zonal flow physics provides a route to controlling the oldest challenge in confining plasma - turbulence. Spherical tokamaks are prized as a new design for high fusion energy performance because of their inherent relative plasma stability. A comprehensive characterisation of zonal flow in high performance spherical tokamaks has yet to be carried out by anyone. This project will report on a study of data from previous experimental campaigns on the MAST tokamak using Beam Emission Spectroscopy (BES), a density diagnostic, to discover direct evidence of zonal flow. Zonal flows in tokamaks are turbulence driven, $E \times B$ oriented plasma flows that can dominate turbulence suppression. Direct experimental evidence for them using velocity measurements requires measuring changing poloidal flow velocity across plasma radius and with time.

The argument presented in this introduction proceeds by first introducing the germane features of tokamak physics and then discussing turbulence in tokamaks - summarising the problem of turbulent transport and then showing evidence from other works that BES can study the problem at relevant scales. Zonal flows will then be introduced as a means to diminish edge turbulence. The theory of these flows will be summarised and then we will interrogate the existing experimental evidence for them found primarily, so far, in conventional aspect ratio tokamaks. These results highlight the importance of confirmation with direct evidence; the robust reproduction in indirect and direct experiments of basic zonal flow physics and a number of phenomena that require more experimentation before a generic theory of zonal flows is complete. Finally, we evaluate the current state of research in spherical tokamaks and show the evidence gap that motivates this work.

1.1 Tokamak Geometry

This research uses data from the Mega-Ampere Spherical Tokamak (MAST) spherical tokamak pending its upgrade. MAST is an example of the tokamak approach to producing fusion energy that confines fuel in a toroidal geometry using magnetic fields. It is one of few machines with metre-scale minor radius built to a spherical design characterised by a much reduced aspect ratio between the radius of confined plasma and of the axis of the torus.

The co-ordinates of toroidal geometry (which will be referred to extensively) are described by orthogonal radial r , toroidal φ , and poloidal θ directions – spherical-like coordinates. Since a torus is the product of two circles, these directions are the distance outwards from the centre of the small circle, angle around the large circle and angle around the small circle respectively. The geometric description is simplified for tokamaks with cylindrical machine coordinates R , φ , Z . These are radius measured outwards from the centre of the large circle, angle around the large circle and height relative to the ‘midplane’ of the toroidal axis. These ‘fixed’ coordinates are used to describe the machine and position of diagnostic instrumentation. From these we get the ‘major radius’ from the centre of the machine to the toroidal axis and ‘minor radius’ measured from the toroidal axis to the edge of the confinement vessel. The ratio of these is the reported aspect ratio.

By layering orthogonal magnetic fields, particles can be effectively constrained in axisymmetric, divergence free magnetic fields with field lines organised on surfaces of constant flux ($\psi(R, Z)$) to travel around the torus. The Lorentz force causes Larmor orbits of charged particles bound to follow field lines. In the absence of external forces, their guiding centres are fixed to field lines and they move along them. Field lines thus restrict motion perpendicular to the field oriented around the torus. The trajectory may be perturbed radially by Coulomb collisions (causing Larmor radius length steps down the pressure gradient) of particles with trapped and passing orbits and by turbulence (eddy wavenumber step size.) Many steps create diffusion processes. The non-uniform environment makes the classically random walk directional in magnetised tori (i.e. a kind of drift). There is a gradient in magnetic field from centre to edge and a centrifugal effect of confining particles in a torus. The particles’ response is dependent on their charge so ions and electrons drift differently upwards and downwards, establishing an electric field. Then the electric and magnetic fields interact to drive particles outward, perpendicular to both.

The drift necessitates a rotational transform in tokamaks –field lines are spun helically to neutralise the drift of charged particles. The tokamak safety factor is the inverse of the transform (describing the pitch angle of field lines.) Since not all field lines have the same rotational transform, there is a magnetic shear across the plasmas. The twist, induced by a current around the plasma’s magnetic axis, connects top and bottom plasma (ions and electrons,) substantially diminishing the electric field.

These current loops swept out around the torus have a magnetic moment acting to oppose

the imposed field since plasmas are diamagnetic. This limits the kinetic energy that a given field may confine. Confinement then can be understood as the balance of magnetic and plasma pressures in a device, the performance of which is commonly described by a figure of merit given by their ratio as in equation 1.1 known as the ‘plasma beta.’ In this expression n is density, T is temperature, k_b is the Boltzmann constant, B is magnetic field strength, and μ is the permeability of free space.

$$\beta = \frac{nk_bT}{B^2/2\mu_0} \quad (1.1)$$

However, it has long been clear that this is insufficient for ‘good confinement’ of fuel heat and mass. Instability, collisionality and turbulence all act to further reduce performance. Cross-field (outward) transport of fuel was shown to be determined by collective plasma physics processes and not collisional or even neoclassical transport models that combine Coulomb collisions with the twisted magnetic geometry. Rather, so-called ‘anomalous’ transport, a consequence of the turbulent behaviour of plasma, was the dominant loss mechanism by at least an order of magnitude gap measured between neoclassical models and thermal diffusivity. The confinement time of a tokamak plasma is defined as the ratio of energy stored in the plasma to rate of loss and we seek to maximise it to preserve high pressure in the core for fusion power.

Since the turn of the millennium more detailed study of this issue has revealed the generation of turbulence from the free energy of steepened profiles is itself insufficient to describe transport physics. A model has emerged of interdependent sources and sinks of turbulent energy. Beam Emission Spectroscopy (BES) has the capability to study plasma physics in two dimensions across the radius of confined plasma and with high temporal resolution. These mean a unique potential to measure the interactions of all parts of the turbulence model; key aspects of which will be explored in the remainder of this chapter.

1.2 Turbulence

This thesis is concerned with measuring the effects of plasma turbulence. In common with other fluid turbulence, ours is a problem without analytic solution. Turbulence is therefore characterised and understood in terms of statistical properties. We can define turbulence as a stochastic fluid flow regime populated by eddying vortices with diffusivity, viscosity and rotationality characteristic to the fluid system. Familiar features of such a system include a driving eddy size scale at which turbulent energy is injected and a smaller dissipation scale at which turbulence ceases to be recognisable and energy is lost. Between is an ‘inertial range’, a continuum of eddy wavenumbers across which turbulent energy transfers. In this range the rate at which turbulent energy is transferred to smaller scales as large eddies decohere depends only on the dissipation rate of turbulent energy and not viscosity etc. The

elongation of eddies in magnetised plasma along field lines in tokamaks creates an effectively 2D model of turbulence. In such a system the spectral transfer of energy follows a dual cascade pattern.² Energy is transferred to both larger and smaller scales.

A neutral, incompressible fluid is described by the Navier-Stokes equation containing a non-linear third term on the right-hand side of 1.2 that encompasses turbulence. In this description the statistical properties that describe the turbulence are a characteristic velocity, viscosity and length. Non-linear stress is a combination of the fluid pressure P and the final viscous stress term. These were combined into a single dimensionless parameter to describe fluids in the work of Reynolds shown in equation 1.3.

$$\rho \left(\frac{\partial \mathbf{U}}{\partial t} + \mathbf{U} \cdot \nabla \mathbf{U} \right) = -\nabla P + \rho g + \mu \nabla^2 \mathbf{U} \quad (1.2)$$

$$Re = \frac{\rho \mathbf{U} L}{\mu} \quad (1.3)$$

Here ρ is the density, U the velocity and L a characteristic length scale of the fluid system. μ is the dynamic viscosity of the fluid. A larger Reynolds number is more likely a turbulent flow. Studies of turbulence driven flows will usually consider either smooth (laminar) flow or a densely packed turbulent field. The latter involves coherent features (eddies) that are self-similar across different wavenumber scales in the inertial range. That the fluctuations of this field are stochastic means they are sensitive to variations across the range of length and time scales of the system.

Plasma turbulence deviates from the generic turbulence model described above in a few important regards. Most obviously, as a fluid of charged particles, it produces and is influenced by electric and magnetic fields. These allow plasma to couple energy to waves as linear solutions in incompressible turbulent systems. In tokamaks, the isotropy of fluid turbulence is broken by the direction of the magnetic field. Tokamak plasma turbulence is elongated parallel to field lines because of relatively rapid transport in that direction. The correlation length of turbulent structures along a field line can reach metres compared to a typical length of a few centimetres parallel to field lines. This allows turbulence to be studied accurately in two dimensional radial-poloidal models; correcting for pitch angle effects.

In magnetised plasma, turbulence is driven at scales determined by free energy sources that are linear instabilities of the plasma. They transfer energy from gradients in the equilibrium field or perturbations of the plasma to turbulence. The growth of linear mode energy is then saturated by non-linear energy transfer.

Familiar fluid instabilities are common to magnetised plasmas. A seed perturbation may result in the Rayleigh-Taylor instability where the radial density gradient establishes regions of 'heavier' and 'lighter' fluid. Plasma follows curved magnetic field lines and therefore experiences the centrifugal inertial effect. When this opposes the density gradient, that is

when the low density 'lighter' region is supporting the 'heavier' pushing out, a perturbation is liable to result in a Rayleigh-Taylor instability.³⁴ A similar conception of there being an interface between regions of the radial tokamak plasma profile motivates the presence of the Kelvin-Helmholtz instability. Rather than one fluid penetrating another, the 'fluids' shearing past one another may result in Kelvin-Helmholtz vortices.

In addition to fluid instabilities, magnetised plasma in a torus is subject to a 'zoo' of instabilities. Some, like the ion temperature gradient (ITG) mode, electron temperature gradient (ETG), micro-tearing modes and, in shaped plasmas especially, trapped electron modes contribute especially to edge turbulence.⁵⁶ We describe two mechanisms linked to the ion scale turbulence that will be studied in this work. First, in the edge plasma, considering the magnetic field itself as a fluid introduces an instability that is Rayleigh-Taylor-like, known as the interchange instability.⁷⁸ Here the plasma is supported by the (curved) magnetic field. At the interface, any perturbation results in a small diamagnetic current. This allows charge separation and so drift as the electric field exponentially grows. The mode is unstable in curvature where the drift exaggerates the perturbation (ie outboard) resulting in flutes of hot plasma lost to cold. The electric field resulting from the perturbation and neutral plasma surrounding it acts in the reverse direction to push a region of cold plasma either side back towards the hot - high and low density plasma is therefore interchanged. Second, the steep edge temperature gradient itself can promote instability by a similar mechanism and is commonly related to anomalous transport. The temperature gradient and magnetic field strength gradient are aligned on the outboard side of tokamak plasmas. The ∇B drift due to the latter is faster in hotter regions. If the temperature gradient is perturbed then particles will drift at different speeds resulting, again, in charge separation. The electric field again results in a drift that tends to exaggerate the initial perturbation on the outboard side. This is the Ion Temperature Gradient instability.⁹

Descriptions of spectral energy transfer in turbulence assume a 'fully developed' turbulent field. Beyond the stability threshold this strong or 'critical' turbulence is unstable to small perturbations. Assuming homogenous, isotropic plasma this is characterised by scale invariance – a statistically stationary turbulent pattern across all length scales present. Colloquially this is described by densely packed, overlapping (volume filling) turbulent eddies at a range of scales. In that state, energy transfer is a throughput of the turbulent system; described by a spectrally local energy cascade i.e. energy passes through intermediate turbulent scales before dissipation or transfer via the interaction of similar scales.¹⁰

1.2.1 Sources and Stabilisers

Tokamak plasmas are force-balanced and so support steep gradients, notably in plasma density and temperature as well as in the imposed magnetic field. Their presence can provide the energy to drive linear instabilities in the plasma. Plasma turbulence arises from the non-

linear self-interactions of these. This means the system is unstable to small perturbations and then free energy is available to grow the amplitude of turbulence. Understanding these sources of turbulence and the localised position of steep gradients implies regions of strong fluctuation near the edge of the plasma. The linear instabilities that source the turbulence can be stabilised by field line bending and strong flow shear which motivates the spherical design concept.

1.2.2 Shapes and Sizes

Plasma turbulence manifests as populations of eddies characterised by a range of wavenumbers associated with the eddy diameter (in two dimensional representations). In tokamaks, the gradients' free energy is the macro-scale source that defines the injection size scale of turbulent eddies. The gradient is much steeper at edge and pedestal radii. Viscosity, i.e. a diffusive limit, sets the upper bound on wavenumber, excepting that eddies may not be smaller than the Larmor orbit of particles driving them. The result is that turbulent eddies in plasma have a limit on the width they can achieve of a few electron/ion Larmor radii. Turbulent energy cascades by spectral transfer from the injection to dissipation scales in accordance with a free-decay model. For large Reynolds number (typical of fusion grade plasmas) the intermediate range is inertial i.e. unaffected by the energetic drivers and sinks which are at widely separated scales. Analogously to fluid turbulence, these scales dictate the dynamic range across which turbulence affects mass, momentum and heat transport.

The relevant scale in a tokamak depends on the particle type – it is different for ions and electrons. The general pattern of turbulence is broadband with the dominant scale by amplitude usually recognised as $k_{\perp}\rho_i < 1$ or ion-scale. As such this is an important length scale for turbulent transport. We also define a turnover time. Conceptually this corresponds to the time for an eddy to rotate fully and indicates how long an eddy can remain a coherent dense structure. It is defined in relation to the eddy's size and speed so that the eddy loses most of its energy in a single turnover time and turbulence dies out after several turnover times without injected energy.

Howard et al. reported¹¹ significant differences when they simulated turbulent transport in the presence of zonal flow across both electron and ion turbulent scales. Including both scales allowed them to match heat flux (in particular electron heat loss from the core) and profile stiffness to experiments performed at Alcator C-MOD. We have access to ion scale turbulence measurements but their results indicate that not only do both scales contribute but that an interaction between the two scales can be the only way to closely match experiment to theory. BES is only able to resolve the ion scale; higher wavenumber fluctuations are lost below the noise level and exceed our spatial resolution. There is still a need to quantify transport and transfer in turbulence at a purely ion-scale, however, this work alone will likely be insufficient to fully validate turbulence modelling.

1.3 The Problem: Cross-Field Transport

With this understanding of the presentation of turbulence in tokamak plasmas, the problem this thesis is designed to address can be stated. Described in terms of a diffusion coefficient, turbulent transport is at least an order of magnitude more than any other mechanism.^{12 13 14} Neoclassical transport, the losses resulting from Coulomb collisions in a magnetic torus down a density gradient, are calculated to account for at least an order of magnitude less loss than is observed in tokamaks.¹⁵ Note, though, that the transport is qualitatively different from diffusive thermal ‘walk’ transport in many ways. The vorticity of eddies, plasma density and range of turbulent size scales (dictated by the injection scale associated with the edge plasma gradient) determine this highly effective cross-field transport in developed turbulence. While transport characteristics are a macroscale property of tokamaks of interest, and despite it being the principal loss mechanism of their ordinary operation as well as a major constraint on their design, turbulence and transport is currently accepted as an immutable feature of tokamak plasmas.

1.4 A Solution: Zonal Flow

Stable sheared plasma flow has been comprehensively reviewed as a key mechanism that suppresses turbulent transport.⁵ This pattern of flow has the ability to strain coherent vortices in excess of their decorrelation rate and so, by enhancing decorrelation, present a transport barrier to heat and mass loss. Shear flow can also stabilise plasma modes and avalanches that drive turbulences. While some such flows can be driven – especially toroidal flow by momentum deposition from heating in the core – others are spontaneous modes of the plasma. Here we introduce one of the latter type – zonal flow. In tokamaks this is poloidal flow, sheared in the radial direction, that emerges from developed turbulent plasma. As such it is of particular interest for controlling turbulence because in addition to the suppression mechanisms of shear flow generally, it takes its energy out of the turbulent field.

After the onset of turbulence, a further parameter is found using Reynolds Decomposition method¹⁶ to describe turbulent impacts on flows. This involves taking a statistical approach to fluid velocity by considering turbulence as a perturbation to an average flow as in equation 1.4. Substituting this into the Navier – Stokes equation and time averaging the result reveals a new term in the tensor bracket of the right-hand side of equation 1.5.

$$\tilde{\mathbf{U}} = \mathbf{U} + \mathbf{u}' \quad (1.4)$$

$$\rho \left(\frac{\partial U_i}{\partial t} + \frac{\partial}{\partial x_j} (U_j U_i) \right) = - \frac{\partial P}{\partial x_i} + \rho g + \frac{\partial}{\partial x_j} \left(\mu \frac{\partial U_i}{\partial x_j} - \overline{u'_i u'_j} \right) \quad (1.5)$$

Since it acts against the stress tensor in that equation, we can say that turbulent patterns

affect flows as an apparent “viscous stress.” This term – called the Reynolds stress^{6 17 18 19} – is not dissipative but rather mediates momentum transfer between the laminar and turbulent flows in the system. Its value is that of the rate of momentum transfer across a surface in a fluid system due to turbulence. In a sheared flow, this is the transfer of momentum down the gradient in kinetic energy from fast to slow flowing sides. This makes turbulence the driver of zonal flows, with a characteristic Lotka-Volterra relationship of growth and decay of one then the other. Equation 1.6 defines this in real space for the radial-poloidal tensor component which is of particular interest as the plane in which zonal flow moves.²⁰

$$\tau_{Re} \cong \rho \langle v_r v_\theta \rangle \quad (1.6)$$

Here ρ is the density of a homogenous fluid and v is the fluctuating component of flow velocity. Velocities are time averaged to get each component of the Navier-Stokes tensor using pairs of the radial, poloidal and toroidal dimensions. Therefore, only 2D imaging allows experimental study of the stress parameter.

It is our expectation that a tokamak with critical turbulence is the most likely driver of zonal flow and so the stress described above the most useful picture as the whole spectrum contributes. Zonal flow growth may also be described by parametric instability - a non-linear resonance between the frequencies of a spectrum of drift waves reinforcing deviations from their periodicity. In magnetised plasma the potential gradient is purely radial but coupling via the magnetic field curvature (a ballooning drift wave) allows waves to interact to grow perturbations. Primary drift waves couple to modulating zonal flow inducing two secondary drift waves. Allowing frequency and wavenumber matching, these are unstable at long wavelengths where the growth rate exceeds collisional damping. This is the analogy of zonal flow to the vorticity of a convective cell described in Diamond’s review⁶ where he also emphasises the physical picture is more properly of coupling to a spectrum of drift waves rather than a single wave frequency. The consequence of that is a separation of timescales between faster drift waves and slower zonal flow frequency. By amplifying the modulation this non-linear instability can tend to drive a Reynolds stress with only a narrow spectrum of drift wave frequencies i.e. in weak, sub-critical turbulence.

By these means zonal flow is generated from turbulence by energy exchange between very different wavenumber scales (i.e. not by spectral transfer of fluid turbulence.) Zonal flow in tokamaks may be distinguished from that of atmospheric turbulence by several key characteristics. Bands are axisymmetric with a pattern that evolves radially defined by the changing plasma potential. The flow has a characteristic oscillation frequency with direction given by equation 1.7 for the $E \times B$ drift.

$$\mathbf{V}_{E \times B} = \frac{(\mathbf{b} \times \nabla \phi)}{B} \quad (1.7)$$

Since this drift direction is typically poloidal where the pressure profile of tokamak plasmas is radial, the flow cannot exchange energy along those gradients and so cannot contribute to increase the transport problem. The flow is locally non-linearly driven only. Without transport or adiabatic coupling to a slower perturbation, the flow can exist once excited by turbulence independently of the dissipation of turbulence until damped.

Zonal flow physics is reviewed by Fujisawa²¹ and Diamond⁶.

1.4.1 Mean Flow versus Zonal Flow

The theory of zonal flow is well understood. The present paradigm of a complex interdependence of turbulence, linear instability and flows emerged from the ubiquity of zonal flow growth in work simulating turbulent plasmas.^{6,22} The turbulence-flow system has self-regulating dynamics, with energy conserved between turbulence as a drift wave and zonal flow. Diamond identifies the saturation of the flow mode in collisionless plasma as a poorly understood subject, however, the growth by a ational instability and collisional damping (at the ion-ion collision timescale) mechanisms are well understood.²³ These are responsible for the zonal flow pattern of turbulent timescales temporal evolution and sharp radial evolution described in figure 1.1.

Further understanding of zonal flow is best gained by comparison to the mean field $E \times B$ flow in the same direction and at the same mesoscale. The latter is smoothly varying over radius of a tokamak. This kind of shear flow promotes ballistic shearing and decorrelation of turbulent eddies i.e. moving eddies to the dissipation size scale. Zonal flow can be described as transferring the vortex size to the largest available in the system. Crucially, while mean shear flow can be driven by the global equilibrium or external torque, zonal flow is uniquely turbulence driven. It is commonly stated, as in the review papers cited above, that these processes occur at ion scales, in particular collisional damping at the ion gyro scale. Very recently it has been proposed that a synergy exists between ion and electron scales affecting zonal flow growth.¹¹ It is a recognised limitation of this and other experimental work on turbulence that the electron spatial scales are inaccessible to most instrumentation.

Zonal flow is understood to have two readily discoverable branches (others have been proposed) – a basic zero-frequency zonal flow (ZFZF) described above and the Geodesic Acoustic Mode (GAM). Their frequency refers to the changing flow velocity measured at any location in the flow. GAMs are immediately distinguished from ZFZF by a ‘bounce’ property in which the flow reverses near upper and lower nulls of shaped, diverted plasmas (the top and bottom of the reactor.) It follows that GAMs are a product of (uncompensated) compressibility of $E \times B$ flow.²⁴ Both kinds of zonal flow are axisymmetric but coupling to the edge geodesic in the presence of a magnetic field gradient creates a density accumulation. The result is an $m = 1$ pressure (density) perturbation unique to GAMs, though all zonal flow modes share $m = n = 0$ potential perturbation. The current density that results

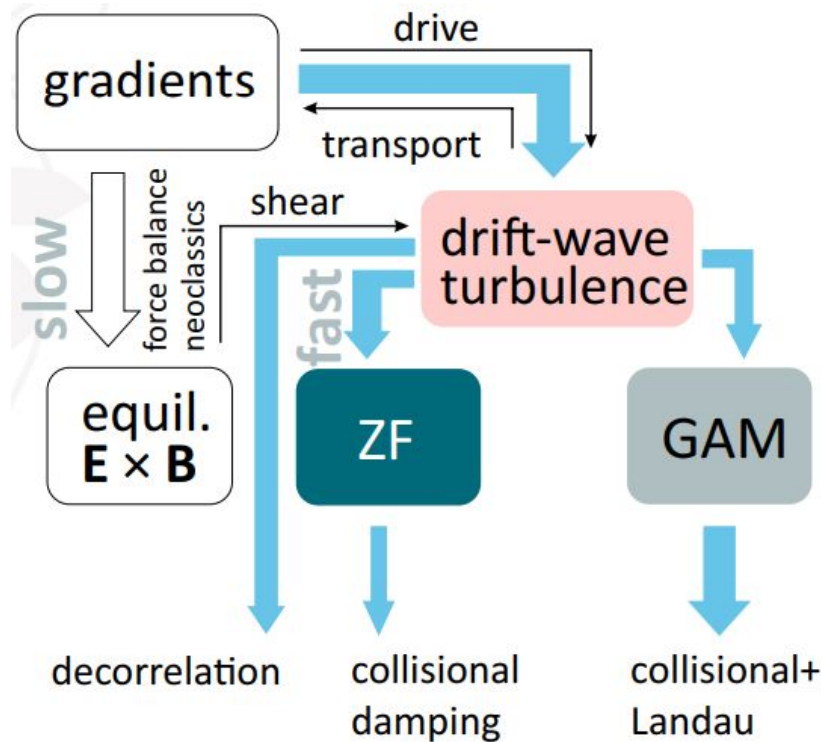


Figure 1.1: Interdependence of turbulence and flow in tokamak plasmas. Graphic by Istvan Cziegler²⁷

from the perturbation is able to modify the electric field allowing both the reversal of flow and the presence of bands of different velocity flow within a sheared region. Proposing this mechanism, Winsor noted that one-in-a-thousand fluctuation of density would be sufficient to produce detectable electric field variation independent of the rotational transform and radial electric field profile.²⁵ Through an analysis of vorticity, this model was fully described as an oscillatory solution of linearised magnetohydrodynamics (MHD) in a toroidal geometry.²⁶

The effects of GAMs on turbulence are similar to other sheared flows. The turbulence correlation length decreases and wavenumber increases with shear velocity, the correlation length increases with collisionality as expected for collisionally damped flow.²⁸ Additional consideration of the interaction between the flow phase velocity, turbulent drift wave group velocity and propagation of the mode is given by Miki and Diamond²⁹. With finite frequency, GAMs also differ from other zonal flows in being susceptible to Landau resonance (at the ion scale) as a damping mechanism. There is therefore an inverse-square dependence on the safety factor of the growth rate of GAMs. The radial propagation of GAMs' position (and extent) observed in modelling work allows for non-local effects of GAMs on turbulence – in particular, increasing decorrelation time. The spectrum shape, heating power, temperature gradient and safety factor can all affect turbulence suppression.

The dominance of the energy exchange mechanism means the effect on turbulent transport is principally perturbative – the amplitudes of turbulence are reduced rather than direct interference with the turbulent mode structure. Since the rate of shear and Reynolds stress

is directly proportional to the depth of the radial electric field well at the edge³⁰ – the edge transport barrier – there is some interest in zonal flows for active control of turbulent transport. The radial electric field is determined by the radial pressure gradient, poloidal and toroidal rotation as shown in equation 1.8. In this equation n is density, Z atomic number, P is the plasma pressure, B the magnetic field strength and v is flow velocity. In principle then any of either species' density or heat gradients, angular momentum or the current profile could be used to control $E \times B$ flow and so turbulent transport.³¹

$$E_r = \frac{1}{n_i Z_i e} \nabla P_i - v_\theta B_\phi + v_\phi B_\theta \quad (1.8)$$

This general theory of zonal flow physics is well developed. In summary, two modes have been emphasised with a focus on GAMs. These have a characteristic finite frequency of the flow velocity making them easier to detect and distinguish from other plasma flows. The growth rate of these modes can be affected by collisionality, elongation, safety factor profile and external drive. Interaction and especially competition between the branches of zonal flow is poorly understood in theory, though Miki and Diamond find that inverse aspect ratio is a determinant of their relative production rates.²⁹ They later show that a reduction in one branch is necessary to allow the other to grow.³² Further gaps in the theory of zonal flows include a collisionless saturation mechanism, control parameters and quantitative prediction of the extent and strength of the mode.

1.4.2 Summary of Experimental Base

We proceed by recapitulating experiments that verified the theory of zonal flow in order to elucidate the detection methods used and quality of evidence in other investigations. Zonal flow in turbulent plasma has a substantial evidence base in conventional tokamaks. A predictive theory in machines with fusion energy relevant conditions, including plant size, is still missing. Basics of zonal flow theory are corroborated in measurements; several phenomena that have been associated with zonal flows are not yet reliably reproduced. These are discussed here through experimental results and some simulations where those used real shot parameters to inform initial conditions.

The earliest reports of zonal flow physics in tokamaks used data from small tori and linear plasma devices. These relatively cool, short radius plasmas meant direct measurement of potential with probes was possible. What is now recognised as a fundamental characteristic of zonal flow in fusion devices was quickly established in such experiments with axisymmetric poloidal flow reported and connected to transport.^{33 34 35} Many experiments would confirm these results in Langmuir probe studies of plasmas, identifying a stationary flow with finite radial wavelength.³⁶ Soon thereafter, experiments focused on the turbulent driver and non-linear effects, with initial evaluations of the Reynolds Stress using shear velocity measurements demonstrating momentum conservation.^{6 37 38 39 40 41} Evidently, these studies

of the plasma potential with probes were very effective at measuring the basic patterns of zonal flow. Achieving the same resolution in larger and hotter devices is a significant challenge, necessary for detecting either the electric field or plasma flow in sufficient detail. Very recently a similar approach was taken at JET⁴² in which a pattern of perturbations of the radial field profile calculated using a multi-diagnostic approach including Doppler Back-Scattering and Charge Exchange Recombination Spectroscopy achieved this for a large device; revealing a pattern consistent with the presence of zonal flow.

In contrast to ZFZF, large devices detected the distinct behaviour of GAMs early into zonal flow research. Reported as the first indirect evidence of zonal flow, experiments on DIII-D using phase contrast imaging of density were used to imply the radial extent of potential fluctuations.⁴³ This was followed by analysis of the density fluctuations that showed a 15 kHz GAM with narrow radial extent.⁴⁴ Again, this was tied to turbulence regulation as the flow shearing rate matched the decorrelation rate of turbulence in that region. A full analysis of the GAM was enabled by the use of BES and time-delay velocimetry on the same machine, once again revealing a 15 kHz feature,⁴⁵ and potentially a zero-frequency feature at the same time.⁴⁶ In these experiments Reynolds stress was evaluated using phase coherence to show the radial shearing rate of velocity – the evidence from BES data allowing for investigation of zonal flow as an energy sink. Finally, the comparator GAM result with BES built on all of these analyses to show a high contrast 15 kHz velocity spectrum peak from BES with 7 vertical edge channels.⁴⁷ With that information the DIII-D study could show evidence of Landau damping, an amplitude scaling with safety factor (a proposed limit of detection of $q = 4$) and with plasma elongation.

Though GAM was measured first with BES on DIII-D, many smaller devices found similar results using reflectometry, probes and Heavy Ion Beam Probe (HIBP) diagnostics. HIBP studies on small tokamak JFT-2M found GAM with strength varying over a narrow edge region that propagated radially and caused radial electric field fluctuation.⁴⁸ Particle flux was shown to be reduced by the flow. HIBP on T-10 identified fluctuations that cause high contrast spectral peaks near 20 kHz over a wide region from $\rho = 0.6$ to the edge.⁴⁹ Subsequent work would identify these with low safety factor surfaces in the plasma and a temperature (external drive energy) scaling of the frequency.⁵⁰ At the same time Langmuir probe studies of H-1 demonstrate an axisymmetric GAM preceded by coherent oscillations in the plasma potential that is Landau damped.⁵¹ Probe experiments on JFT-2M find fluctuations of the potential at GAM frequencies not otherwise associated with magnetic signals.⁵² Bicoherence analysis of the modes and background density fluctuations robustly indicates a non-linear interaction. The $E \times B$ convection of turbulent vortices is shown to be a part of the energy transfer mechanism. The same bispectral analysis of probe data from TEXTOR shows transfer between GAM frequency modes and background turbulence – strong evidence of zonal flow.⁵³ The same approach taken on JET could find only weak evidence of interaction,

given the distance from the closed plasma.⁵⁴ One last approach used Doppler Back-Scattering and a proprietary signal classification algorithm on Tore Supra to measure velocity and found a spectral peak at 10 kHz and near the plasma edge at $\rho = 0.9$.⁵⁵ The frequency was found to scale with temperature (heating power) and radius.

These and other findings of the initial evidence base for zonal flows are summarised in reviews by Fujisawa⁵⁶ and Van Oost.⁵⁷

More recent experiments have accepted the framework set out above and looked to understand ‘higher order’ behaviour of zonal flows, focussing on GAMs. Studying the spectral characteristics of GAMs with probes on HT-7 and looking at wavenumber-frequency spectra showed modes in the range 20 - 50 kHz that were seen to propagate outwards (ZFZF was observed propagating in both directions.)⁵⁸ Further evidence of GAM propagation was found in GAM characterisation on TCV⁵⁹ and eikonal optical methods in simulation.⁶⁰

One hypothesis that has received considerable attention is the radial pattern of GAM frequency. The naively understood picture is of a ‘continuum’ solution in which the theoretical scaling of GAM frequency with temperature and major radius (as well as safety factor, shaping etc) applies at every position the GAM is measured so that its frequency changes across the plasma. Recent experiments have found evidence instead of an ‘eigenfrequency’ solution i.e. that the GAM oscillations take a fixed frequency across their whole radial extent. This was hypothesised in relation to low safety factor GAM locations in propagation work.⁶¹ Experimental work identified such a pattern on DIII-D along with fluctuations in multiple plasma parameters (suggesting not just a density perturbation determined the pressure mode number.)⁶² Experiments on C-Mod with Gas Puff Imaging⁶³ and modelling with TCV data⁶⁴ identified the eigenmode structure too. The TCV studies indicate that either frequency pattern may be adopted by a plasma. Experiments on T-10 with first probes⁶⁵ then reflectometry (i.e. studying potential and density)^{66 67} found a 22 – 27 kHz eigenmode, exaggerated in the presence of Electron Cyclotron Resonance Heating. Similar work recently has sought to investigate the radial profile of sheared flow to determine whether a ‘staircase’ or avalanche type behaviour is typical.⁶⁴

Quantifying the non-linear energy transfer has been attempted in a number of experiments. The collisionless saturation mechanism remains unproven but the parametric dependences of damping have been studied as part of intrinsic rotation studies.^{68 69} One key result to come out of quantifying Reynolds Stress as a zonal flow driver⁷⁰ is a mismatch in the energy reduction in turbulence and the energy in zonal flow. Several studies have sought to account for or reduce the gap and identify the sink for turbulent energy. The smallest gap is a factor of three found by Cziegler.^{71 72 73} These results demonstrate the need for fine spatial scale experiments to determine turbulent physics in tokamak plasmas.

Another area of growing interest is the impact of electron scale effects. The suppression of the electron scale by zonal flow was reported first.⁷⁴ As simulations included the full range of

plasma scales simultaneously it was noted that ion scale turbulent transport increases. It was determined that this is an electron (streamer) scale effect that acts to damp zonal flows.⁷⁵ This damping effect was tied to safety factor,⁷⁶ in turn connected to critical turbulence stability.⁷⁷ The impact on zonal flow magnitude, velocity shearing rate in particular, has been confirmed in further simulation work.⁷⁸ The radial electric field is still governed at the ion scale and electron scale drive has only weak evidence.¹⁹

As the evidence base for each branch of zonal flow is developing, some evidence has been presented of interaction - both coexistence and competition - between the branches. Early evidence supported a coexistence of the zero and finite frequency branches with GAM near the edge and ZFZF in the core.⁷⁹ Their interaction was linked to macroscale changes of plasma confinement.⁸⁰ Continuous coexistence was verified by Gas Puff Imaging and velocimetry on Alcator C-Mod in an intermediate global confinement mode.⁶³ Subsequent study with the same techniques revealed evidence of competition between them for turbulent energy.⁸¹

Finally, one of the most interesting recent developments in the field has been experimental investigation of the electromagnetic fluctuations from the motion of charged particles caused by GAMs' density perturbation. The pattern of these was predicted to be $m = 2$ in early theoretical work.⁸² Since then multiple experiments in small devices have examined the pattern and found with Langmuir probes, reflectometry and Mirnov coils GAMs that exhibit a fluctuating $m = 2$ electromagnetic pattern.^{83 84 85 86 87 62} Though an approximation has been made⁸⁸, no compelling experimental study of the amplitude (and its cause) of these fluctuations has been undertaken. However, a study by Seidl et al. in limited plasmas identified scaling of amplitude with safety factor again and suppression of the magnetic signal in co-current NBI heating shots.⁸⁹ Other magnetic effects found include simulation of small scale (low shear) collisional models with zonal flow in which the action of Resonant Magnetic Perturbation coils reduced the growth of zonal flow modes.⁹⁰

Many of these more recent results are summarised in the IAEA contribution of joint experiments of small tokamaks review article⁹¹.

Taken together they offer a picture of a mature theory of turbulent drift wave – zonal flow interaction. The fragmented picture from multiple classes of device supports the basic pattern of zonal flow branches – of location, extent, propagation and drivers. Experimental work is lacking a consistent base of measurements for observed higher order physics, only some of which have been reproduced. It remains easier to detect GAMs and difficult to disaggregate diamagnetic flow and ZFZF. Without direct access to the electric field, velocity data or spectral interaction, much of the evidence found so far is indirect and merely 'consistent with' zonal flows. Our understanding of zonal flow branch interactions, persistence and parametric dependences is still not settled. Characterisation of each of these is essential to a predictive framework for zonal flow physics in tokamaks.

1.4.3 Confinement Transition Effect

A major finding of recent work has been the driving role zonal flows play in the low to high (L-H) confinement mode transition usually taken as necessary for high performance plasmas. Zonal flow has been linked to other global plasma effects – the Dimits shift in stability threshold for critical turbulence and the density stability limit for example. The confinement bifurcation is an especially important phenomenon to understand, though, because this passive effect of plasma behaviour relies on especially powerful zonal flow modes. It is therefore of interest for their detection – motivating shot number and time selection.

Though a link between these phenomena was suggested in some early literature,^{92 80} only recent advances in time resolution have enabled a rigorous understanding of the relationships between turbulence and flows involved. It has been shown that the non-linear interaction acts first, with the rate of energy transfer from turbulence to zonal flow growing.^{93 94} This Lotka-Volterra type relationship continues to exchange energy until the net transfer of energy into zonal flow (Reynolds Power) exceeds the turbulence growth rate. In the absence of strong turbulence, the edge pressure gradient can increase, altering the radial electric field, which then promotes diamagnetic flows that preserve the suppression of turbulence. Note that without strong turbulence there is then no zonal flow energy source. Ion collision rates and safety factor both affect flow damping and the non-linear interaction.⁷³ Given the multiple flow – turbulence interaction the model is extended to a ‘two-predator-prey’ picture in which the confinement transition is facilitated by a lasting suppression of turbulence in the presence of a sufficiently strong pressure gradient.⁹⁵ The transition to other confinement modes has been shown to rely on the same process.⁸¹

1.5 Mega Ampere Spherical Tokamak (MAST)

The research into zonal flow in this project is done on a new class of fusion machine. Spherical tokamaks, as opposed to the conventional design, keep their plasma confined in a vessel much closer to the central column and taller to preserve the plasma volume. In this way they substantially reduce the aspect ratio of major to minor radius as compared to conventional designs (a typical value of 1.5 compared to 3.) They also have more strongly shaped radial-poloidal plasma cross sections than conventional circular plasmas, as can be seen in figure 1.2, especially as measured by the elongation metric. Our BES diagnostic studies the Mega Ampere Spherical Tokamak (MAST, now MAST-U) itself unique as a medium sized, spherical tokamak and one of only two with Mega Ampere plasma currents necessary for high beta performance – MAST-U and NSTX-U.

Spherical tokamaks have been built for their inherent stability, in particular to kink instability modes. Owing to their shape, particles following field lines spend more time on the inboard side of the plasma cross-section than the outboard where these times would

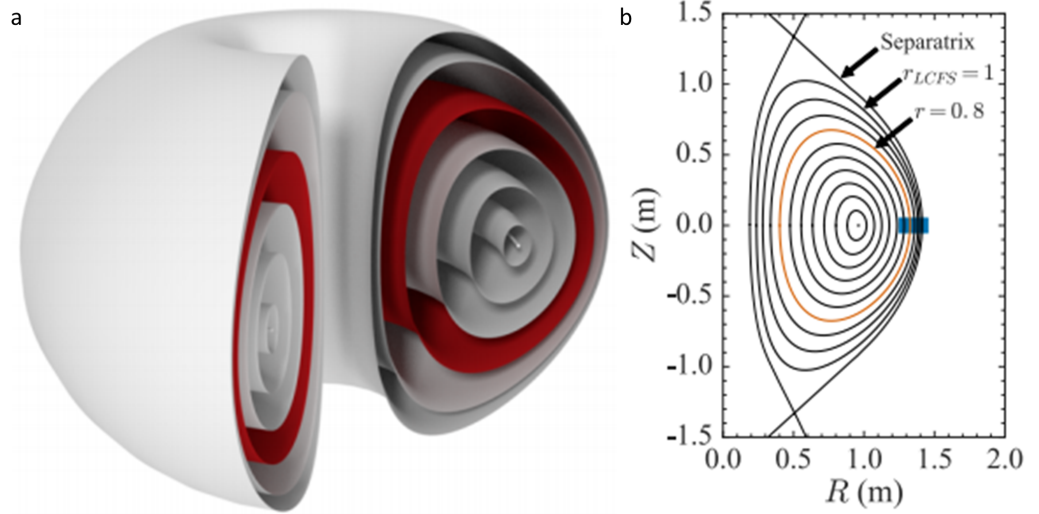


Figure 1.2: (a) Nested flux surfaces of the magnetic field line geometry in MAST, and (b) the radial-poloidal cross section including an indicative BES field of view. Reproduced from F Van Wyk.⁹⁶

be roughly equal in a conventional design. These designs are also explored for their efficiency; potentially confining plasmas at higher pressure for lower magnetic field strength than conventionally required.

Our interest in spherical tokamaks is in their improved quenching of turbulence. A well in the plasma current profile at the core and much higher current than conventional tokamaks towards the edge means these machines have a distinctive magnetic pitch angle profile. This stays relatively constant and low for much of the radius and then steepens markedly at the edge, promoting shearing of the plasma. Pursuing smaller radius machines is contrary to the typical scaling used in tokamak design that motivates larger devices to prolong confinement time. However, since shear parallel to edge field lines drives turbulence and perpendicular shear suppresses it, the turbulence in a spherical tokamak manifests as the ratio of the two. That is as a function of the ratio of safety factor to aspect ratio.²⁸ The increased intrinsic rotation in spherical designs has also been shown to be essential to suppression of both turbulent and MHD instabilities.^{97 98 99 100 101} Continued research into the behaviour of turbulence in the highly shaped plasma environment of spherical tokamaks is essential to compare these designs to the conventional benchmark. The steep safety factor profiles near the edge may have important consequences for zonal flows too given the evidence of their damping and frequency dependence of safety factor set out above.

1.5.1 Zonal Flow Experiments on MAST

Finally we can summarise the existing evidence base of zonal flow in spherical tokamaks. In the small device Globus-M very good evidence has been found of GAMs in line with the experimental approach taken in conventional devices. Velocity measurements identify ax-

isymmetric, edge, GAM theoretic frequency modes. A spectrogram indicates an intermittent mode.¹⁰² Additional characterisation of the magnetics pattern and bicoherence analysis of the background turbulence supports the identification of zonal flow.⁸⁵

On the larger machines there is a marked lack of detailed evidence. NSTX has used BES to study turbulence^{28 103} but without presenting evidence of zonal flows. Gas Puff Imaging studies of very low frequency fluctuations in the L-H transition on NSTX found long range correlations and Reynolds Stress patterns consistent with zonal flow.¹⁰⁴

On MAST, BES has been used extensively to characterise turbulence typically using long windows (2 ms) of data to study correlation.^{105 106} It has also been used to provide evidence of equilibrium flow shear suppression of turbulence. Some of these data have been used to simulate zonal flow. In a study of the transition to turbulence, zonal flow is described as the dominant regulator of that regime with strong shear due to zonal flow in scenarios far from the critical turbulence onset threshold.⁹⁶ Probe data from shot 29150 were used to study the radial structure of GAM by matching simulated and experimental results.¹⁰⁷ These showed frequency agreement with conventional devices when aspect ratio was enlarged. A potential self-interaction producing harmonics at the midplane was suggested. The effect of zonal flows on heat flux in MAST has also been simulated, suggesting a linear scaling with collisionality consistent with slow decay of zonal flow modes as a result of collisional viscosity.¹⁰⁸

The best experimental evidence of zonal flows in MAST shots was found by Robinson using Langmuir probe data on shot numbers 21856 to 21858.¹⁰⁹ GAM frequencies were found in L mode plasmas without other MHD activity measured in Mirnov coil signals and with evidence of interaction with turbulence scales in bispectral analysis of potential fluctuations. The experiment does not otherwise directly measure the radial electric field or velocity. The GAMs were reported 2 – 4 cm inside the plasma edge where safety factor was roughly 6 at frequencies between 5 and 20 kHz. A coupling to Resonant Magnetic Perturbation coils was proposed since these shots do not otherwise contain strong turbulence or a confinement transition typical of zonal flow growth.

1.6 Summary and Structure

Plasma turbulence has been long established as the dominant loss mechanism for fusion heat and fuel from the plasma core. In recent years an understanding of zonal flow in tokamaks has grown up that demonstrates a potent energy sink for suppressing turbulence. The basic presentation of zonal flow branches – predominantly as a zero-frequency zonal flow ZFZF and finite frequency GAM – has been established in many devices along with the mechanisms for their growth and damping. A substantial evidence base on the location, extent and action of zonal flows has been established. Record confinement has been shown in the presence of strong flow shear in many of these experiments.

More recent progress in conventional aspect ratio tokamaks has included evidence of zonal flows in global plasma effects like the confinement transition and increasingly for stability limits too; of zonal flow acting in multiple confinement regimes; of an eigenmode radial structure and of an electromagnetic pattern associated with the density perturbation of finite frequency GAMs. Whether these are generic behaviours is now the focus of many experimental campaigns.

Spherical tokamaks are a relatively new design and as such lack the same experimental basis. There is a need for a reference experiment on MAST as one of the most powerful of these devices to identify a clear signature of zonal flow in spherical tokamaks and a benchmark characterisation. With direct access to flow velocity measurements, BES is one of few diagnostics able to provide this. If the task of achieving fusion burn is one of ‘stabilising instabilities’, robust zonal flow detection provides a route to stabilising turbulence, the most ubiquitous of all. With good detection a predictive theory of parametric dependence can be used to promote zonal flow growth. We seek to identify and characterise zonal flow on MAST to further a generic theory of its effects and parametric dependences.

To address this question this thesis will proceed by first reviewing the BES diagnostic and the time delay estimation method used for calculating flow velocity. Then we ask what the optimal implementation of that technique with BES on MAST is and show that we can adapt it to maximise temporal resolution of velocimetry for zonal flow detection and, using synthetic data, introduce a number of tests and limits to improve the accuracy of the velocity output. Next we ask whether the code’s performance is reliable and predictable. We show that across three tests - a powerful continuous modes in the input signal mimicking magnetic activity; high frequency bursting modes mimicking MHD instability and a time-varying imposed velocity on the input signal mimicking time-evolving plasma flow - the null turbulent spectrum is robust and velocimetry produces predictable outputs. From these results we move to use this tool in real data and ask whether high contrast peaks in velocity spectra – critical evidence of zonal flow – can be found in MAST data. The answer turns out to be yes, infrequently and often associated with persistent magnetic activity in the H mode when those peaks have wide radial extent. This question is then adapted to ask whether this is consistent with zonal flow physics expectations or a basis to discard these spectra from further consideration. Finally we sample those high contrast peaks and/or peaks at common frequency across the BES radius that we observe and compare their shots and times to measurements of expected zonal flow physics; asking whether any appears to be a candidate zonal flow case. To maximise the data surveyed we devise a systematic approach with weighted tests which is lastly automated to study L-H confinement transitions. Accepting that the highest contrast velocity spectrum peaks are associated with medium frequency magnetic signals, none of these ‘best’ cases reproduces expected GAM physics fully.

Chapter 2

Methods

2.1 Beam Emission Spectroscopy (BES)

The MAST tokamak is attached to an extremely fast Beam Emission Spectroscopy (BES) diagnostic system at 2 MHz with 2D heating beam coverage in the radial-poloidal plane that is being upgraded alongside the machine, my contribution to which is in figure 2.1. The diagnostic works on the principle of detecting light emitted from the interaction of neutral beam particles and charged particles in the plasma bulk. In hydrogenic fusion plasmas this means measuring the D-alpha (Deuterium Balmer α line) emission from relaxation. The basis of BES is that plasma density can be inferred from the measured light intensity as a result. Light emission is directly proportional to the electron density of the quasi-neutral fusion plasma and so the plasma density. The measurement is dependent on plasma temperature and beam energy. We can infer density directly from the intensity of detected light with appropriate adjustments. This is supported by evidence from coherence studies of the amplitudes of light fluctuation and ion saturation current in Langmuir probes, video images and spectral analysis of the gas puff imaging and Langmuir probe signals detailed in Zweben, 2002.¹¹⁰ These concur that the D-alpha light signal fluctuation corresponds to that of plasma density. Since fluid turbulence introduces eddies and other dense structures in the plasma, it introduces such fluctuations in BES data allowing it to be measured. The fullest expression of this relationship is shown in equation 2.1.¹⁰⁵

$$\delta I_i = \int P_i(r - r_i, Z - Z_i) \cdot \beta \cdot \delta n(r, Z) dr dZ \quad (2.1)$$

The fluctuating light intensity δI is proportional to the fluctuating density field inside the plasma at the focal plane of the BES optics $\delta n(r, Z)$. That density fluctuation is caused by the turbulence in a tokamak plasma. r and Z are again the radial and poloidal coordinates, respectively, $P_i(r - r_i, Z - Z_i)$ is a function for channel i with focal point at (r_i, Z_i) describing the region of captured light and β is a coefficient of the atomic physics of the line emission

($\beta = 0.7$ in experiments¹⁰⁵ and is approximated elsewhere¹¹¹). The fluctuating density signal and NBI signal that produces it are compared to other key plasma parameters for a representative MAST shot in figure 2.4.

The neutral beam used in our experiments is the ‘south’ neutral beam injection system beam (SSNBI) - one of two such systems on MAST used to heat the plasma. This has a wider diameter and is more powerful than dedicated alkali diagnostic beams elsewhere.¹¹² However, its usual operating energy at 60-70 keV means injected particles’ light emission is Doppler-shifted relative to the background plasma. At full power this shift is around 3 nm above the line radiation expected at $\lambda = 656.3$ nm. The shift is sufficient for the use of an optical filter to isolate light radiated from the beam and so to localise BES measurements on MAST along the beam. Identifying density fluctuations with plasma radius allows for significant additional investigations of patterns. However, the localisation (spatial resolution) is limited in two ways. Firstly, misalignment of magnetic field line (along which the excitement-causing plasma particles are guided) and captured emission ray path causes a depth of view across the heating beam. If the line of sight of the optics is misaligned with the magnetic field at the beam along which the turbulence is oriented, the region of captured light is widened. The second limit comes from the relaxation time of neutrals that once excited by charged particles continue to travel inward along the neutral beam axis before relaxing (and only then radiating). The location of the light intensity measurement is, therefore, not precisely that of the density fluctuation that caused it. High energy particle noise affects the measurements too but not the resolution. There is no automatic deconvolution of the noise. The net effect is an average radial uncertainty of around 1 cm. We note that magnetohydrodynamic instabilities can perturb the plasma, altering the mean plasma density at a given machine radius without necessarily changing the fluctuation amplitude.

The BES detector on MAST captures light from the axis of the SSNBI beam using a 32 pixel avalanche photodiode detector (APD) array. The choice of an APD is justified in the signal to noise ratio and sensitivity it affords at high sampling rate¹¹³: on MAST, fluctuations down to 0.1 % limited by etendue should be detectable¹¹⁴, digitised at 2 MHz. Pixels are arranged in a two-dimensional grid of 4 rows by 8 columns that, magnified through the optics of the detector, captures signals from locations approximately 2 cm apart. These are projected in the radial-poloidal plane of the machine. A 2D map of the fluctuations can be used as a visual guide to turbulence patterns as in figure 2.3. This gives coverage of the central portion the SSNBI beam (diameter 16 cm.) This BES resolution matches the ion turbulence length scales of a tokamak. The 2 cm pixel separation compares with an outer machine ion turbulence scale of $k_r \rho_i \sim 0.3$ ¹¹⁵ and ion Larmor radius $\rho_i \sim 1$ cm. That resolution makes BES a diagnostic capable of studying changes in plasma turbulence. That the scales are similar has to be taken into account in turbulence analyses.¹¹⁶

The range of ion scales varies from, $1 < k_{\perp} \rho_i < 100$ for fluctuations caused by microtur-

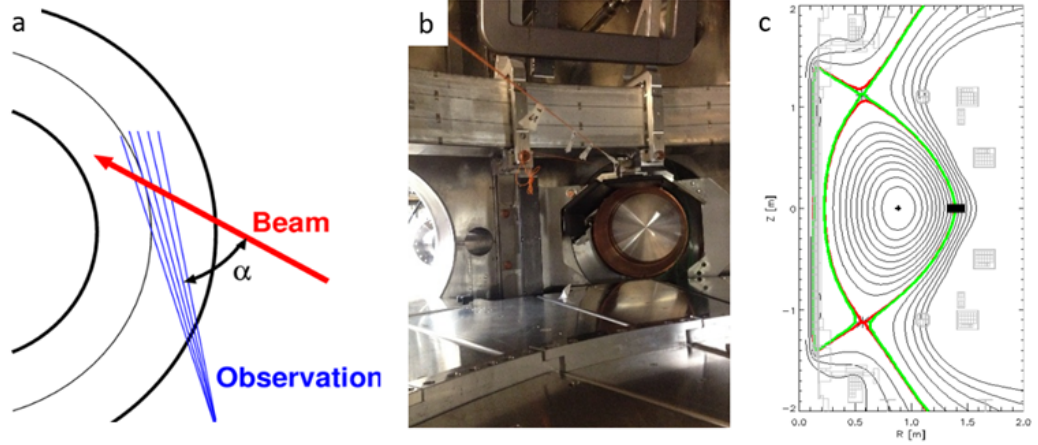


Figure 2.1: (a) Plan view sketch of the in-vessel optical paths intersecting the heating beam. (b) photograph of the variation of major radius marked off in 10 cm intervals along the heating beam axis measured in-vessel during commissioning. (c) cross-section view of the overlap of the BES field of view (black box) and flux surfaces (including separatrix in green) varying with major radius R and height Z for shot 29378.¹¹³

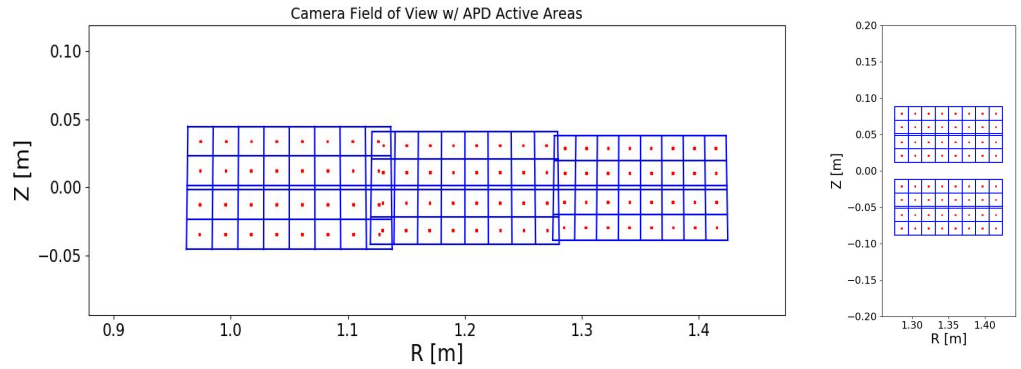


Figure 2.2: Variation of resolution of the APD with different viewing radii of the detector. Red dots mark pixel centres and blue magnified edges of active detection areas. Shown right is the expected spatial resolution of the upgraded detector with two adjacent APD arrays at the nominal viewing location.

bulence.¹¹⁷ Ion scales are characteristic of larger turbulent structures and so transport. The optics include a periscope and stepper motor that allows the position along the beam axis of the centre of the detector to vary. This allows beam coverage from the inboard side of the core to the plasma scrape-off layer. The beam axis and optical path are not perpendicular so that, while the viewing radius may be uniquely identified by a major radius value, the exact spatial coverage of the detector alters with the viewing radius as shown in figure 2.2. The MAST BES system is optimised for expected alignment in the plasma core at $R = 1.35$ m where resolution is 2 cm, and can scan (by moving between shots) a range of major radii from $R = 0.7$ to 1.6 m.

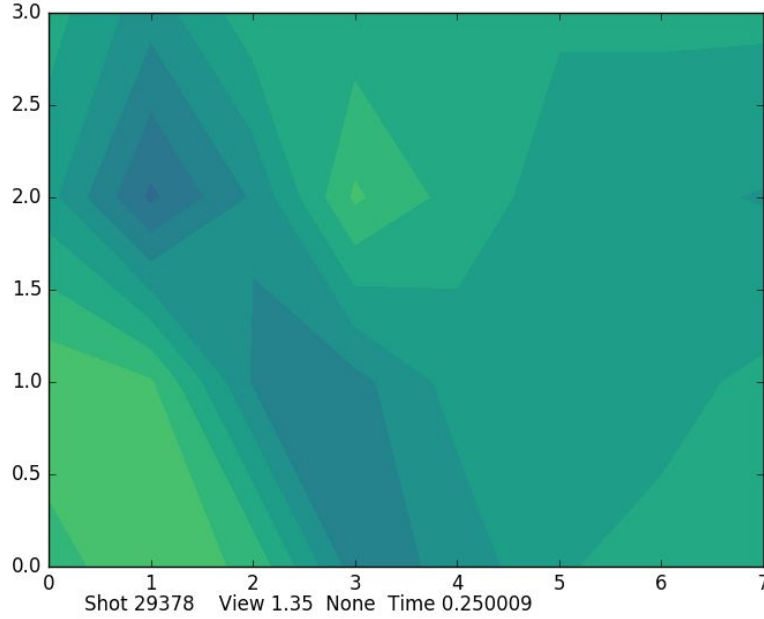


Figure 2.3: Still density map from a gif using the fluctuation amplitudes of each of 4×8 channels of BES data at a single timestep.

2.2 Cross-Correlation Time Delay Estimation (CCTDE)

Zonal flows are revealed in the spatial and temporal variation of plasma flow velocity. This feature of turbulent plasma physics is the focus of this project. Our approach to investigating this phenomenon will use the Cross-Correlation Time Delay Estimation (CCTDE) method for determining velocity. In this chapter it is described in general terms and hereafter will refer to the specific implementation developed here for use with BES data. A cross-correlation function is used to compare time series and quantify how much they vary together. It is the convolution of the two signals as a function of delayed copies of one, calculated as in equation 2.2. Cross-correlation measures the similarity between the reference signal f and delayed copies of test signal g as a function of the delay between them.

$$K_{XY}(\tau) = (X * Y)(\tau) = \int_{-\infty}^{\infty} \overline{X(t)} Y(t + \tau) dt \quad (2.2)$$

$$\rho_{XY}(\tau) = \frac{K_{XY}(\tau)}{\sigma_X \sigma_Y} \quad (2.3)$$

This velocimetry is done by quantifying the similarity of signals using correlation functions for signal analysis. This definition of cross-correlation uses a combination of Fourier transforms and the convolution theorem to evaluate the cross power spectral density between two input signals per equation 2.2. Here f and g are two signals of the same length, σ is the square-root of power of each signal and τ is the delay between them. A reverse Fourier

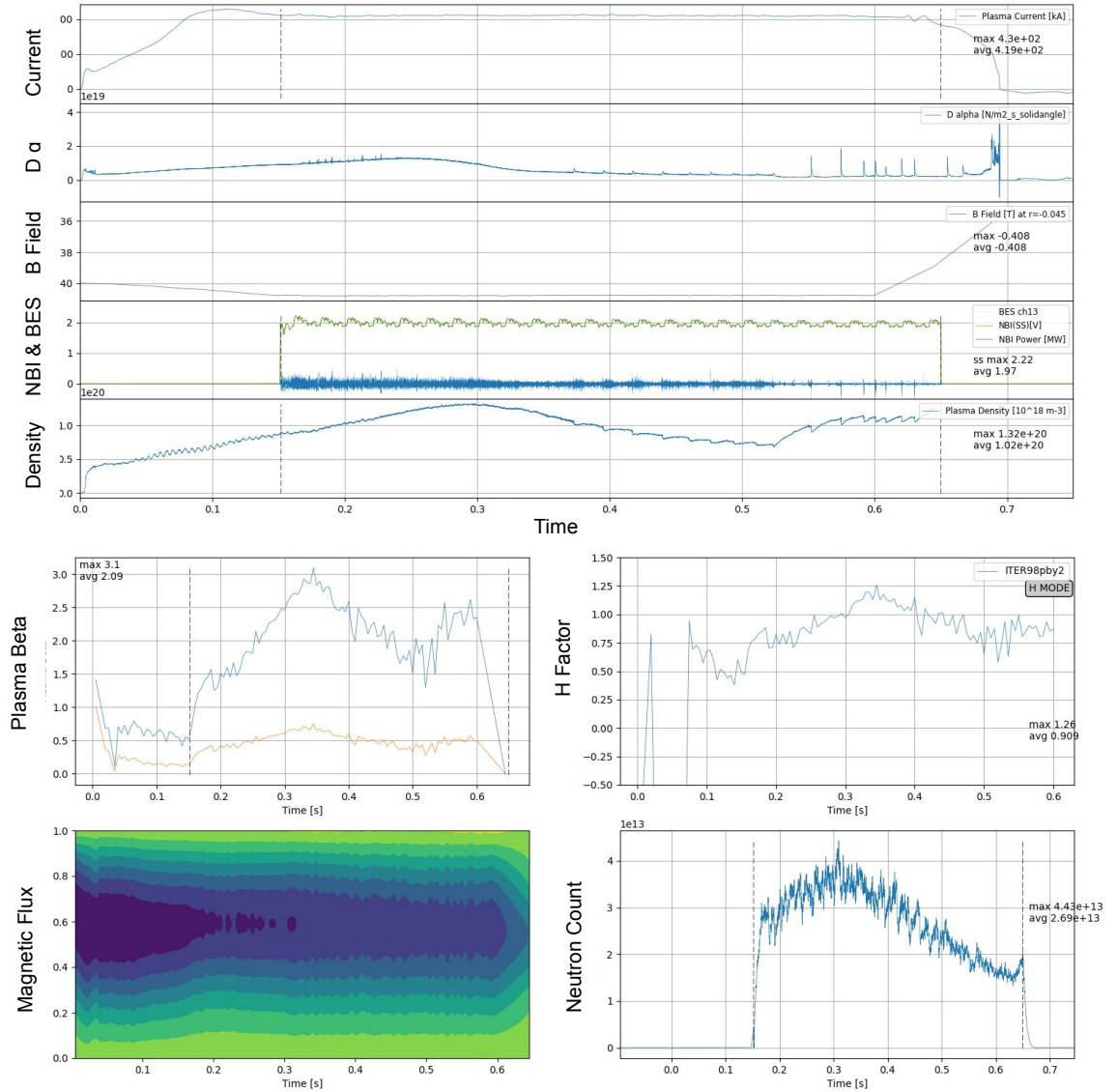


Figure 2.4: Example data from MAST shot 29378 showing the NBI and BES signals varying with key plasma parameters plasma current, density and magnetic field inputs. Also shown is the D α emission from the whole plasma. Below are the variation of some plasma performance metrics for the same shot including plasma beta, H factor, flux surfaces and neutron counts.

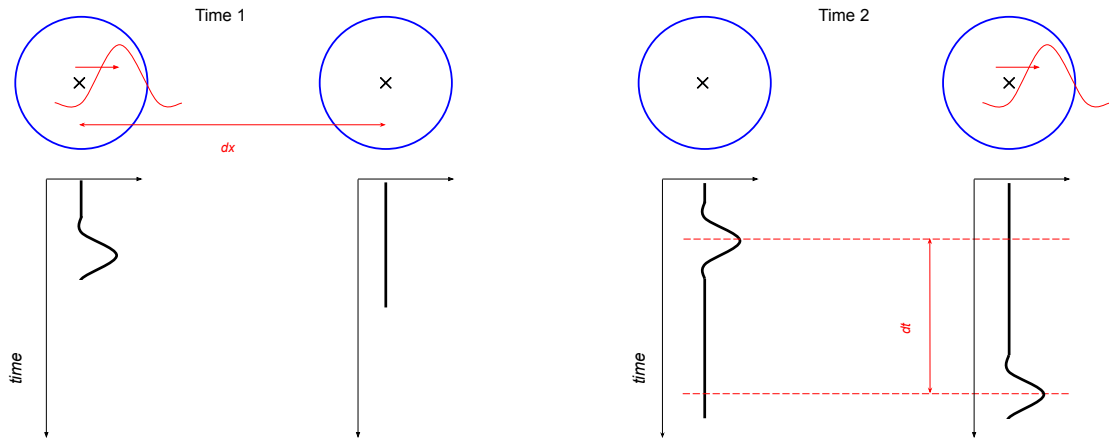


Figure 2.5: A cartoon showing the principle of CCTDE operation. What is shown is how a propagating feature of some plasma parameter that we might measure in one location may occur at another measuring location at some later time. If we have continuous measurement at both locations, we can compare the known distance separation of locations to the measured time separation of a feature common to both signals to estimate the velocity of physics that caused the feature.

transform gives the cross-covariance of the signals – their covariance as a function of the delay of one signal relative to the other. By normalising this result to the power of both signals as in equation 2.3 we return the cross-correlation – the same pattern assigning values on a -1 to +1 scale.

Each value in the cross-correlation function is the equivalent of plotting one signal against the other and measuring the correlation coefficient. The function is then built up by repeating the measurement keeping one signal the same and shifting all the data points of the other by one timestep (computationally achieved by wrapping the data.) The resolution of the correlation is therefore the same as that of the input signal (and the time domain goes from plus to minus half the length of the signal.) The correlation function peaks at the delay equivalent to the number of timesteps the signal has to be shifted for both signals to have a maximally co-varying pattern. In a simple example, such as in figure 2.5, this can be conceived of as two time series increasing and decreasing at the same times.

Real signals, especially in plasma physics, are a convolution of many complicated patterns. This results in pattern matching and correlation functions with more features as in figure 2.6. They are also affected on multiple timescales, some much slower than the detector resolution and non-linear interactions that are instantaneous. The propagation of those signals will not capture the same physics across all channels of the detector. The correlation function is the same length as the signals being compared – each delayed up to half of its length in each time direction. More data points then can reveal complex patterns. Previous turbulence analyses have used signals of lengths 0.5 – 40 ms. ¹¹⁸

TDE techniques often, and the velocimetry designed in this project always, use the Fast Fourier Transform (FFT) technique. FFT is a computational method for speeding up the

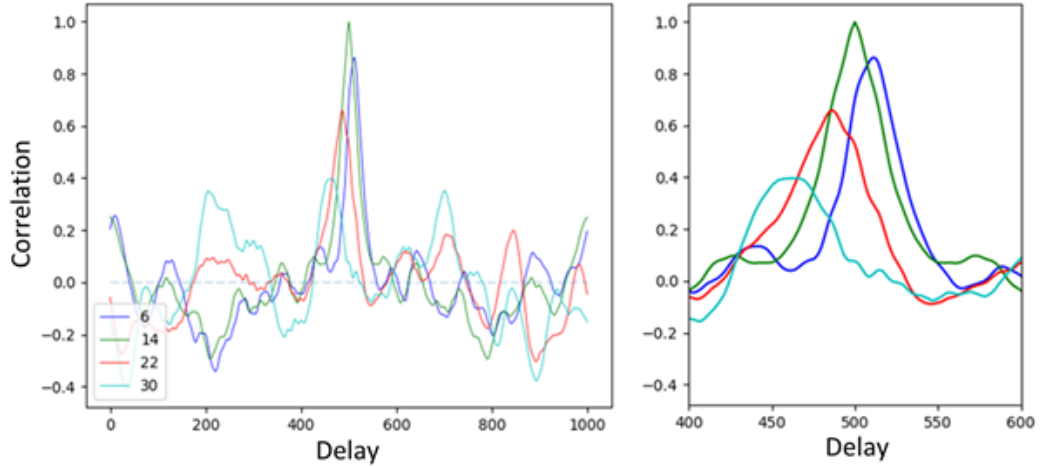


Figure 2.6: An exemplar cross-correlation function plotted for adjacent channels in one column of the BES detector for shot 29378 for the interval from 0.23 to 0.2305 s of the shot. Channel 14 is the reference channel (i.e. its auto-correlation is found) to which the others are in turn compared. Note there is information from the centre of the function, which we have zoomed in on on the right, of propagation across each channel in turn as well as periodicity in the wings of the functions implying a common mode.

production of discrete Fourier transforms on regular time series by optimising for powers of two signal lengths. This will also inform the size of our correlation functions.

CCTDE is easily applied to measuring speed in scenarios where a distance between the measurement locations of the two signals being compared can be fixed. In this regard it is not unlike other means of estimating velocity based on tracers. In this case, rather than adding any tangible object to a flow, it is the pattern of fluctuation itself that is the tracer. Plotting the cross-correlation function between two channels of the BES diagnostic allows us to compare the changes in signals from spatially separated locations of the plasma. Where the result is a high (near unity) correlation we may infer that the similarity of signal features implies the same dense pattern (for example, of turbulent eddies) passes both channels.

Its application in the BES/MAST context requires care. First, The BES diagnostic on MAST has a uniquely good time resolution and so has potential to measure velocity with high resolution. Second, the combination of short shot length (about half a second) on MAST and high frequency plasma modes confounds measurements with the CCTDE technique. With good data, BES can measure correlation length, decorrelation time, eddy velocity, dominant wavenumber (poloidal) and fluctuation amplitude.

We can do these because we have the fluctuating time series and capture the correlation information. By switching from measuring the delay at the correlation function peak to measuring the correlation at undelayed times we can map the extent of eddies as in figure 2.7. From there other turbulence data can be characterised by fitting an ellipse to the data (an 'eddy') and recording its parameters. Fourier transforming data along the real space axis of our grid allows us to produce wavenumber spectra.

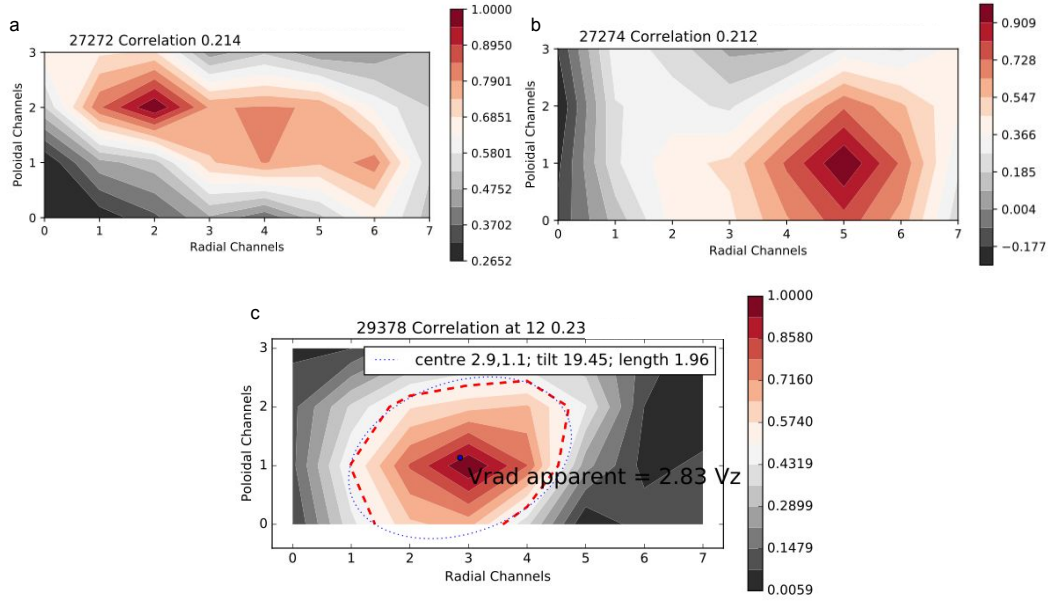


Figure 2.7: A turbulence map using the undelayed cross-correlation information from (a) shot 27272 0.2140 to 0.2141 seconds, (b) shot 27274 from 0.21200 to 0.21225 seconds. The reference signal always has undelayed autocorrelation of unity. (c) is an example from shot 29378 time 0.230 to 0.231 seconds in which an ellipse has been fitted to the interpolated 0.5 correlation locations and its parameters characterised including centre, tilt angle and major diameter. As superimposed, these data can be used to suggest the apparent radial velocity of such a shape travelling purely vertically.

2.2.1 Limitations of CCTDE on MAST

In addition to the generic problems of spatial resolution outlined here, there are two principal limits to the ability of CCTDE to reliably measure velocity in the radial-poloidal plane as in the BES arrangement on MAST. These are first the effect of timescales of turbulence coherence and second the effect of orthogonal flows. Note these are for the measurement of vertical velocity and the radial variation of plasma (including field line bending) would also affect horizontal coherence.

There are two potentially limiting time scales. The first is the degradation of delayed-similarity across widely separated channels of the detector as the dense structures change while transported across the detector. A comparison of typical eddy turnover times and reported flow speeds suggests that only a slight change (roughly 1 / 15 of the eddy lifetime) is expected, a far smaller problem for velocity measurement than other fluctuation of the density signal. The second time scale concerns non-linear energy exchange. The loss of energy from turbulence that we expect to drive zonal flow may similarly result in a diminution of eddies as they cross our field of view. While the non-linear exchange itself is near instantaneous, the effect on turbulent amplitude is longer. The effect is described by the Reynolds work done as discussed experimentally with Gas-Puff Imaging approaches⁹³. The timescales of the limit cycle of energy exchange between turbulence and zonal flow is show to be far longer (0.002 s) than that of our detector resolution (0.0000005 s) as well as the

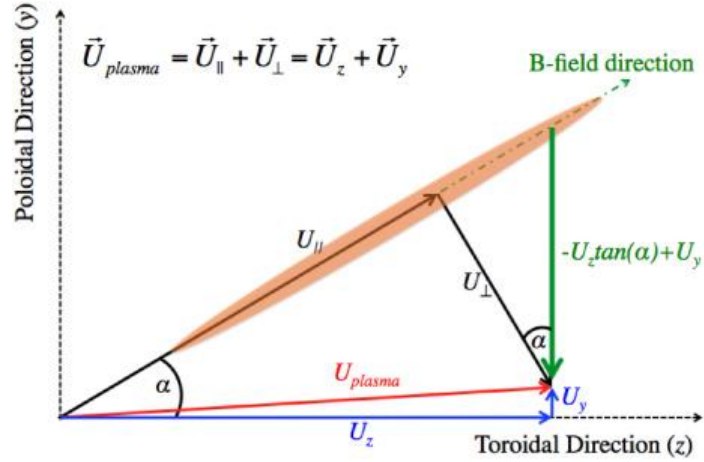


Figure 2.8: Illustration from Ghim 2012¹¹¹ showing how toroidal plasma flow (U_z) of tilted eddies creates the appearance of poloidal motion. An eddy elongated along the B field (coloured oval) is advected by toroidal flow (blue arrow). The apparent velocity is $U_z \cdot \tan(\alpha)$, where α is magnetic pitch angle; the measured velocity is $U_y U_z \cdot \tan(\alpha)$.

delay between farthest separated signals even for slow flow (0.00003 s for 2 km/s). Neither limit affects our ability to find correlation across the detector.

It was noted by Sierchio¹¹⁹ that attempting to use CCTDE alone to measure in two orthogonal dimensions of a detector is prone to error when both directions involve fast flows. Our measurement dimension is the vertical (poloidal) direction of the detector and, while we can, we do not measure a horizontal (radial) velocity. Nonetheless we do not expect a uniform fast flow velocity in that direction, despite radial transport. We do expect a fast toroidal rotation of the plasma. This direction is not directly measured by our field of view but the flow can affect our measurements by introducing a 'barber-pole effect'. As illustrated in figure 2.8, the anisotropy of eddies in magnetised plasma combined with the tilt of field lines relative to both field of view and advection direction means creates an illusory velocity measurement. They are detected in different channels of the detector at different times because of their tilt and not because of a true vertical advection of the eddy. The magnitude of this 'apparent velocity' can be readily calculated given the toroidal flow velocity and pitch angle of field lines where velocity is being measured. Charge Exchange Recombination Spectroscopy and fitting of the plasma equilibrium can provide these (albeit with reduced spatial and temporal resolution compared to BES.) A correction can therefore be applied to measurements to subtract the apparent velocity and be left with the true vertical flow speed.

Chapter 3

Code Development

Our implementation of the cross-correlation time delay estimation (CCTDE) velocimetry technique has had to be adapted from the widely known basic version¹²⁰ in a number of ways. This was necessary to manage accuracy in the context of studying spherical tokamak data and to achieve the time resolution necessary for studying the evolution of plasma flows. Our approach goes beyond two-point correlation methods using only a pair of signals from distinct times to fitting multiple adjacent measurement positions. This was done in order to sharply reduce error in the absolute velocity measurement. The approach used in this work makes continuous velocity measurements by reducing the time between velocity measurements to that of the Beam Emission Spectroscopy (BES) data. We assume, based on the advection velocity across the detector, that turbulence and flow will be sufficiently well correlated across the detector that the average measurements of multiple adjacent channels can be used to produce a well-fitted velocity in each column, reducing error compared to only two data points. Example patterns of flow velocity measured in each channel of the detector are shown in figure 3.2. The assumption of coherent turbulence (and reliable velocity fitting) was investigated for velocimetry in both dimensions of the detector. Since we are primarily concerned with the discovery of $E \times B$ flows only the ‘poloidal’ (vertical) dimension will be discussed in what follows i.e. four adjacent channels are used for velocity measurements.

The CCTDE velocimetry code’s implementation is as follows (a copy is included as Appendix A.) BES data are imported and at each timestep the correlation function of a window of each channel cross-correlated with the other three in its column is determined. The delay to peak cross-correlation is plotted against channel separation and the gradient of the line of best fit is recorded as the velocity at that timestep. When the velocity time series for each channel has been measured at every timestep, the results are averaged to give a single velocity for each column (i.e. radial position of the detector.) Some post-measurement adjustments set out below are then done to ensure a regular time series from which spectra can be made. There are many possible ‘forks’ in this path where data could be used for other analyses besides velocimetry e.g. the zero-delay correlation information for eddy mapping.

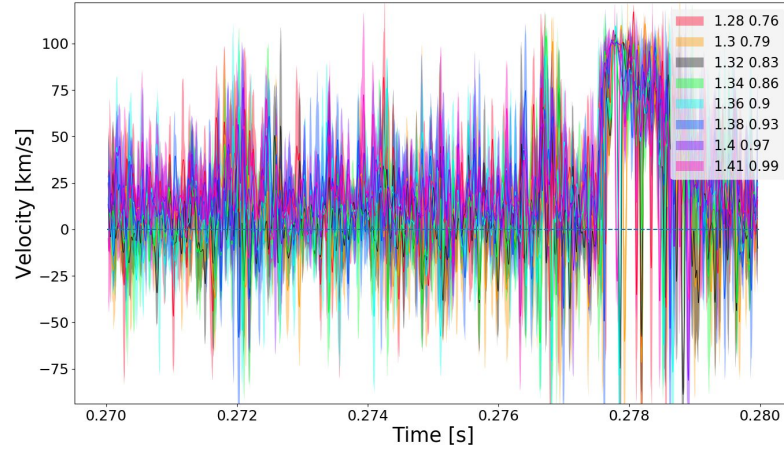


Figure 3.1: Smoothed and full fluctuating velocity time series found in each column for shot 26885 at 0.27 seconds. Column radii (major [m] and normalised) are listed.

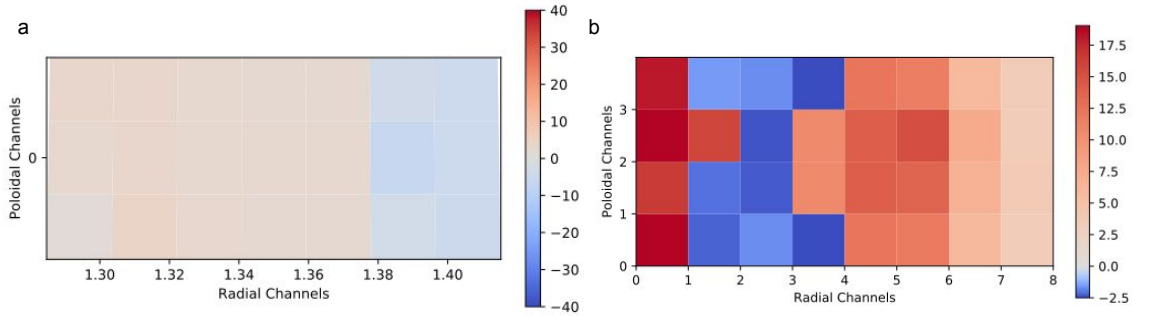


Figure 3.2: Mesh plots showing the velocity in km/s calculated at each channel of the BES detector. (a) shot 29378 at 0.23 seconds showing clearly the change in direction of flow velocity associated with the edge plasma then scrape-off layer. Axes are R,Z coordinates. (b) shot 26977 at 0.217575 seconds showing alternating bands of flow inside the edge. Axes are row and column numbers.

Although the spectrum of poloidal velocity is expected to be the principal identifier of candidate data for zonal flow study, rigorous analysis requires an accurate absolute measure of velocity. We hope to see evolution of the flow across space as well as time. The velocity in all columns is shown plotted on top of each other in figure 3.1. Moreover we expect evaluations of shear $S = \partial_r$

3.1.1 Filtering

We begin with a discussion on the treatment of BES data for use in turbulence analysis. As indicated in 2.1 all our study is performed on just the fluctuating part of each channel's signal. Clearly this implies removing the average value of the signal. In our case this is done by first removing sharp noisy features (detail in the next section) and then subtracting the mean of the BES signal. Then we divide throughout by the slow-varying component of the signal, found by filtering, and subtract unity (to fluctuate around 0 not 1). Because the plasma is constantly evolving we use a filter (rather than a simple time average) to describe

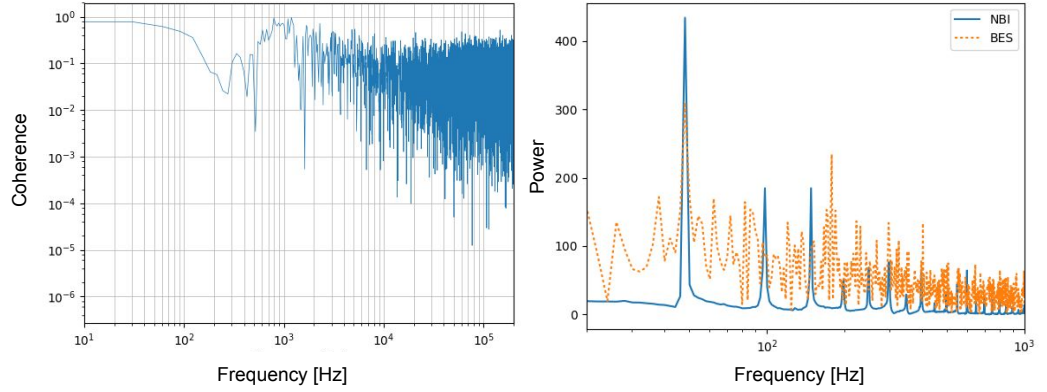


Figure 3.3: The coherence of the SS NBI heating beam signal and BES signal for channel 20 from shot 26889 for the period 0.152 to 0.409 s is plotted. The spectra of NBI and BES signals from shot 29378 channel 10 for the period 0.152 to 0.65 s (overlaid by scaling down the BES spectrum) illustrate common powerful peaks below 1 kHz.

this component. Many things can affect the intensity measured by BES besides density fluctuations like temperatures and the relative location of flux surfaces and detector field of view. However, the principal driver of slow time variation at relevant shot times is the Neutral Beam Injection (NBI) heating power changing. We therefore define slow variation as the extent of coherency between NBI and BES signals. As indicated in figure 3.3 when tested in a range of channel and shot numbers the highest matching frequency is around 1 kHz. A standardised cutoff frequency is used for speed of computation and to limit calls on the MAST data archive.

All filtering is done using an infinite impulse response Butterworth filter. This type preserves the pass-band as much as possible. Note that we observe when using the SciPy package filter function the spectrum amplitude is diminished as expected but does not tend to zero as illustrated in figure 3.4. Investigating this revealed it to be a feature of the function kernel preserving its size by wrapping the ends of time series. As such all spectra filtered in this way are raised by a constant amplitude of white noise at every frequency. When quantifying spectral information we will only be concerned with the relative heights of spectral features or peaks on top of the noise floor so having identified the issue no further correction was made. The same effect appears using finite response filter functions so the Butterworth method was preferred for the flat response below the cutoff frequency.

3.1.2 Noise Elimination

One other well known feature of BES using avalanche photodiode detectors is the extremely sharp peaks in the time series recorded with incident gamma or x-ray and neutrons, introducing noise to the signal and measurements. A look at the spectrum of a BES channel as in figure 3.4 shows this as photon noise at higher frequencies. The noise starts at around 200 kHz so this is taken as the upper cutoff frequency when filtering the raw data. Looking at the

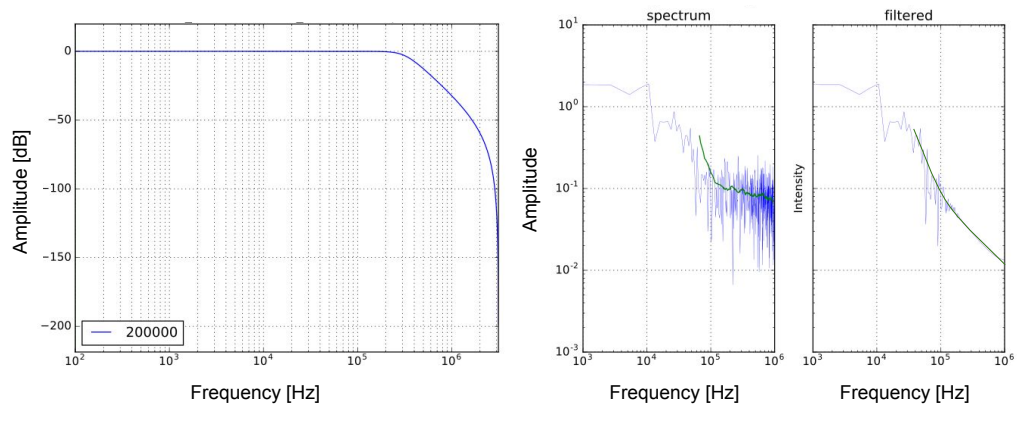


Figure 3.4: The filter response of a lowpass IIR Butterworth (digital) filter to data is shown with a cutoff frequency of 200 kHz. The effect of the filter on the spectrum of BES data (Nyquist frequency 1 MHz) from shot number 29378, channel 15, is shown next to it. Smoothed data is overlaid in both.

signal after filtering, though, shows that the noise spikes are not completely eliminated by filtering per figure 3.5 and so a specific method for deleting those data had to be designed. Without removal, these peaks dominate the spectrograms we need to plot to interrogate BES data, as well as being artefacts of the plasma environment rather than signal properly captured by light emission in the beam path. We eliminate high-energy particle noise by differentiating the signal and setting a threshold for the rate of change to exclude the sharp peaks (those with only one or two data points in the peak.) Thresholds were set as multiples of the standard deviation of the differentiated time series. Signals with data points replaced at each threshold level were compared to establish that extremely sharp noise data had been removed and that broad peaks were not. Satisfactory noise deletion was achieved at a threshold of 1.5 times the standard deviation.

The fluctuating data used in all following analysis is found by adjusting the raw BES signal for slow varying physics with a high-pass Butterworth filter, cutting off at 1 kHz, eliminating noisy data points and then low-pass filtering the remaining noise in the signal with a Butterworth filter using cutoff frequency 200 kHz.

3.1.3 Surrogate Data

Trials of the code were also performed using synthetic data. We seek to test the ability of the velocimetry algorithm we have developed to measure velocity in turbulent data accurately and to understand the spectrum of velocity time series that result from the CCTDE measurement and additional processing unique to our method.

Various approaches to producing synthetic data are used in fusion diagnostics. A number of sophisticated tools for replicating tokamak conditions exist¹²¹ as well as reduced models of the turbulent plasma field which are then measured as if by the diagnostic being tested. To test the CCTDE velocimetry implementation as described it is sufficient to reproduce

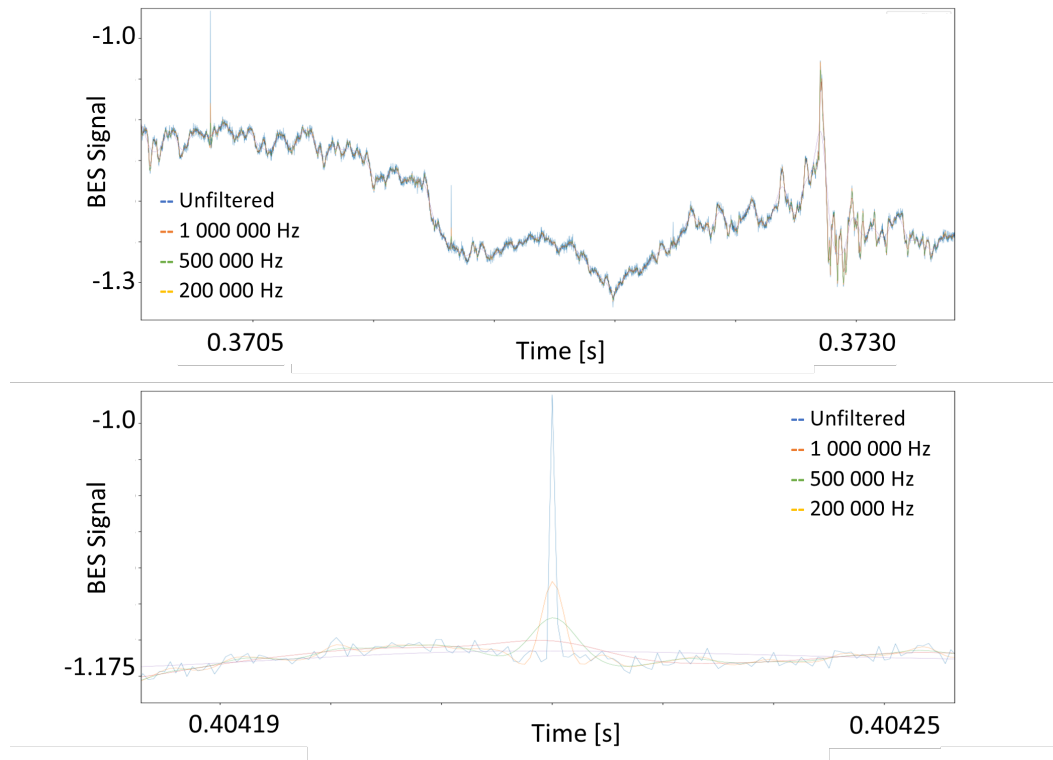


Figure 3.5: The raw BES signal [V] from shot 29378 showing the presence of high energy particle noise as extremely sharp spikes earlier in the data is plotted. Later in the shot a broad peak can be seen attributable to density change. The raw signal of just a noise spike is then plotted with increasing filter cutoff frequencies showing that the spike is still present in the signal even with strong filtering.

the data of four channels i.e. one column of the detector only. Since a measured velocity is equivalent to a delay between data for channels of known, fixed separation, evaluating the velocity measurement requires only one original data series. Recall that branches of the same code may be used to test other turbulence properties for which the 2D pattern across the detector becomes relevant and this is no longer true.

The relevant comparator data for testing the velocimetry is a purely turbulent field. Fast and slow ‘flow’ velocities can later be imposed on these time series. We therefore want to reproduce the signal of broadband turbulence. This can be achieved using real measured data as seen by the BES system and reproducing its statistical properties according to the standard practices of producing surrogate data.¹²² The process to generate surrogate data by randomising the phases in a data series is described in The Journal of The Textile Institute.¹²³ The random phase method of surrogate data preserves the correlation of the signals while removing particular amplitude distributions of the data. First we identify a segment of broadband BES data. Then measure its autocorrelation function and check this has finite width in the middle (not resembling a delta function.) The Fourier Transform of the autocorrelation function gives the power spectral density of the (broadband) signal the

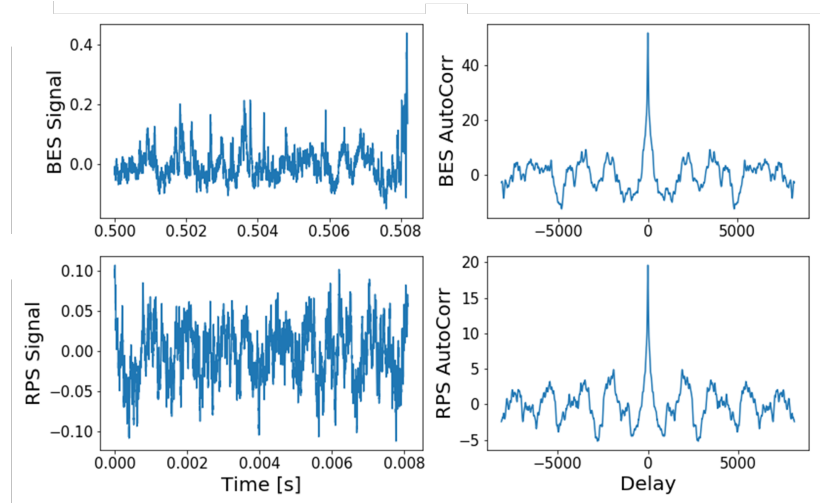


Figure 3.6: A short section of BES data from shot 29380 channel 11 and its autocorrelation function are plotted. Then the same for a stochastic signal generated using these data and the random phase method which (as shown) preserves the correlation statistics of the signal while removing artefacts of plasma physics.

phases of which are then randomly reassigned. Inverse Fourier Transforming the spectrum with random phase produces a broadband, stochastic time series on which we can test the velocimetry. This data series is unaffected by artefacts of BES measurement or tokamak physics that affect the density fluctuations of BES data as evident in figure 3.6 in which a time series without sharp excursions can be seen. That means the velocity signals produced by surrogate testing data can be compared with those from ‘real’ data and deviations might indicate physical activity. This would be revealed without having to characterise turbulence itself.

The reproduced signals should be of broadband turbulence with as monotonic a spectrum as possible. BES data was studied by producing spectrograms to identify continuous regions of broadband signal such as those in 3.7. Those regions used in the tests that follow are included in table 3.1.

Shot	30449	30449	30449	29380	29380	29380
Channel	11	15	22	10	11	18
Time [s]	0.34	0.34	0.34	0.5	0.5	0.5
Radius [m]	1.30	1.49	1.44	0.95	0.99	0.95

Table 3.1: Shot numbers and start times used to generate surrogate BES data. All signals are 0.01 s long.

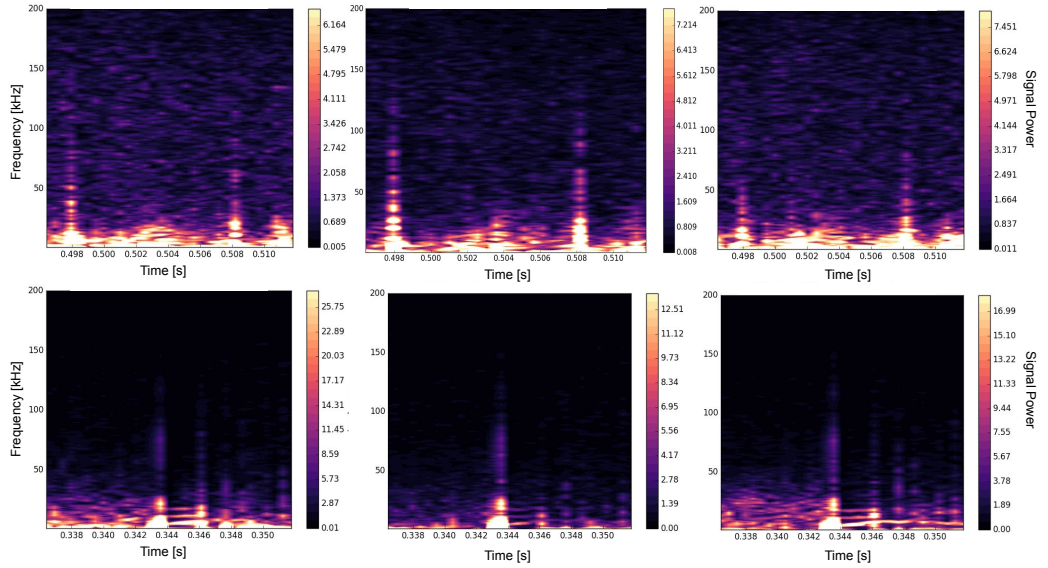


Figure 3.7: Plots of the spectrograms of the data listed in table 3.1 showing regions of largely broadband signal that are the input data to our code testing. These signals will be the basis of the stochastic signals used as inputs to the velocimetry routine. Top 29380 ch 18 then 11 then 10. Bottom 30449 ch 22 then 15 then 11.

3.2 Cross-Correlation Time Delay Estimation Technique Design

The generic model of Cross-Correlation Time-Delay Estimation (CCTDE) for velocity measurement has been described in section 2.2. In the remainder of this chapter we describe the tests and code breaks introduced in the development of that technique for application to spherical tokamaks. To describe the version of CCTDE that works in the physical environment of a spherical tokamak we start with hard-coded limits to the algorithm's output to discard unphysical results. Because this implementation of the CCTDE technique will make a large number of measurements, their output must be controlled in the code rather than verified afterward. *We then consider how to develop the technique in response to features of input data taken from a spherical tokamak.*

3.2.1 Measurement Limits

The first limit is on the measured velocity. Our method considers only the resolution of the detector as a limit on possible measured velocity - a feature crossing the full width in one time step. Fitting to multiple channels allows for velocities faster than that to be measured. The BES system on MAST has a sampling time of half a microsecond and spatial resolution that varies across plasma radius but is optimised near the edge at approximately 2 cm. 4 vertical channels gives pixels at most 6 cm apart. Taken together these imply the fastest velocity detectable (seen to cross the detector in one time step) is moving at 120 km/s.

This is an order of magnitude above expected mean flow velocities¹¹¹ and allows for speed up due to strong flow. Velocities measured above this cutoff we say can only be erroneous measurements and will be cast to ‘NaN’ and not recorded.

The velocity limit is applied as each measurement is made. Once a full time series has been recorded we can make similar consideration of the physicality of the accelerations in that data set. Little data is reported on the evolution of poloidal flow (part of the motivation of this work.) However, a reported example of the onset of a poloidal flow gives a good estimate of a likely change in velocity in the presence of strong flow. Schmitz reports 100 000 km/s/s though corroborating numbers are hard to find.¹²⁴ Allowing a wide margin for higher torque in NBI driven spherical tokamak geometry we choose a threshold of 1 000 000 km/s/s. This is implemented by adapting the noise removal routine used to treat the raw BES data as described above. This time the threshold for an ‘unphysical’ data point in the differentiated time series dv/dt is found using the reference value for acceleration as previously stated. Introducing these limits marks erroneous measurements and avoids artificial high frequency changes being carried to the spectrum. That threshold is introduced as a multiplier of the standard deviation as in 3.1

$$multiplier = \frac{1000000 \times dt - \overline{\delta_t v}}{\sigma_{\delta_t v}} \quad (3.1)$$

in which the mean and standard deviation are those of the signal dv/dt . Figure 3.9 shows the change of this threshold in different test data. It was decided that rather than smoothing the data series, when an unphysical plasma acceleration is found the measurement is ‘corrected’ to the running, weighted median average value. This is to fully remove the effect of such extreme changes in velocity evident in figure 3.8 while (as will be shown) not affecting the spectral output. The velocity time series is only swept once for extreme changes after a comparison with two runs (ie finding a second threshold) found a high time cost with no better removal of extremes.

The last threshold included in the code is a statistical t-test. This is an important part of evaluating the accuracy of the code given the dependence on statistical correlation. On the assumption that the velocity time series generated by a purely turbulent field is likely normally distributed we use the cut-off prescribed by a two-tail t-test at a 95% confidence interval. The formula in equation 3.2 tells us what value of correlation ‘r’ is the cutoff for a sample size ‘n’ (equal to the number of data points in the correlated signals) with corresponding t value for a statistical probability of 0.05 that the events are correlated by chance.

$$r^2 = \frac{\alpha}{1 + \alpha} \quad (3.2)$$

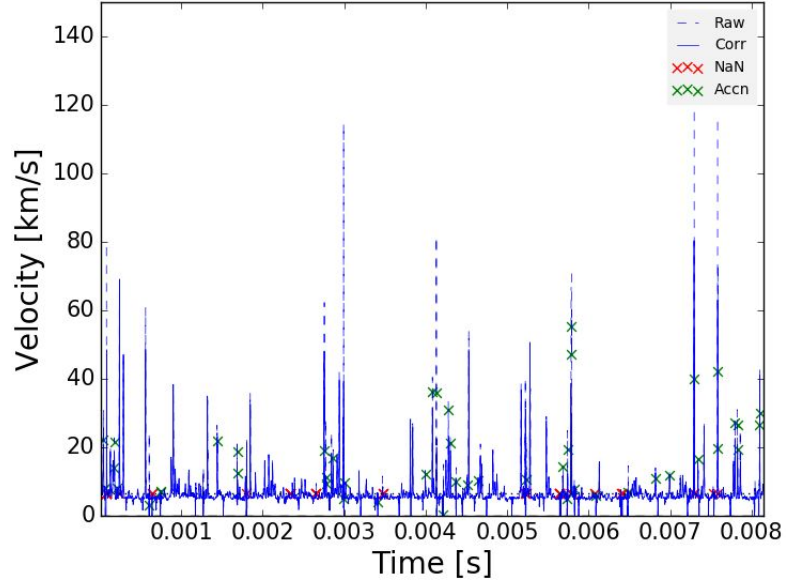


Figure 3.8: Example velocity time series generated from the data for shot 30449 channel 22. An imposed velocity of 5 km/s is applied (mean measurement is 6.16 km/s.) 2.6% of data points are in some way corrected by the velocimetry – the corrected velocity time series is shown as a solid line, the raw measurements as a dashed line. Crosses mark positions no valid measurement was made i.e. NaN data (red) or the limit on acceleration removed a spike in the series (green.)

$$\alpha = \frac{t^2}{n - 2} \quad (3.3)$$

The value of ‘t’ is found from the t distribution shown in figure 3.10. The test provides a threshold for statistical significance of a correlation measurement. The value depends on the most important parameter of this code’s design – ‘correlation window size’ - the size of the data array used to calculate the cross-correlation.

Each of these thresholds – velocity, acceleration and statistical significance - can be varied as inputs to the velocimetry algorithm but will remain with the values stated here for the work of this project.

3.2.2 Correlation Function Size

The one input parameter of our CCTDE routine before all others in importance for flow physics is the length of data from each channel compared to produce correlation functions. This will be referred to as ‘correlation window size’ throughout our work. Flow physics revealed by the temporal and spatial changes of velocity in the plasma is subject to the resolution of the velocity measurement, whereas regular density fluctuation study depends only on the detector sampling rate. Along with the time between velocity measurements, the correlation window size determines the time resolution of the algorithm. The interval is hard-coded in our design as the same as that of the BES sampling rate leaving the correlation

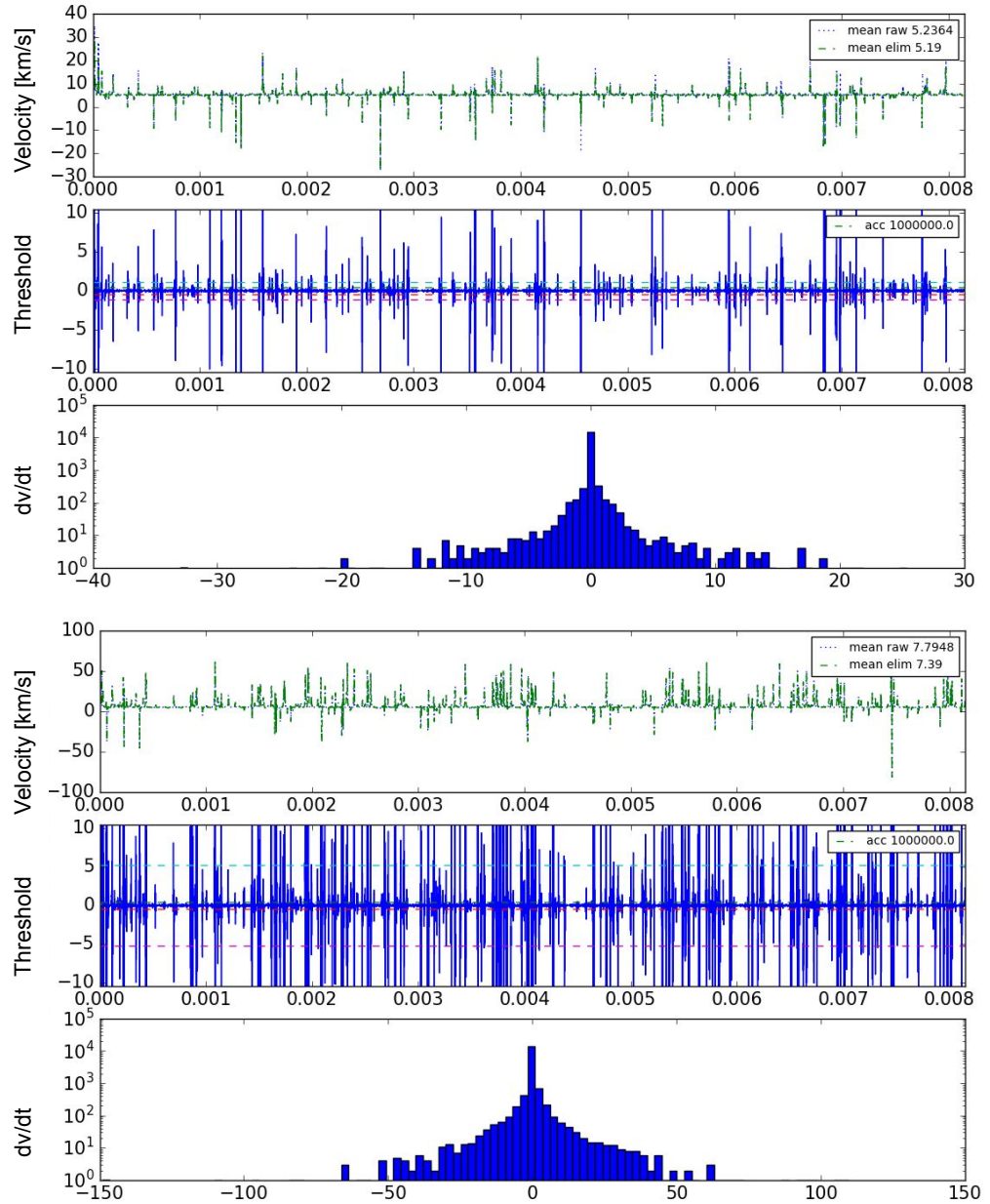


Figure 3.9: Two velocity time series generated from the data from shot 29380 channel 18 and channel 11 respectively show the operation of the acceleration limit in the code. The first band details the time series and average velocity measure before and after the acceleration filter is applied (showing only modest changes get made.) The middle band shows the signal dv/dt and dashed lines mark the threshold for too rapid acceleration. The last band of each case is a logarithmic histogram showing the dv/dt signal distribution.

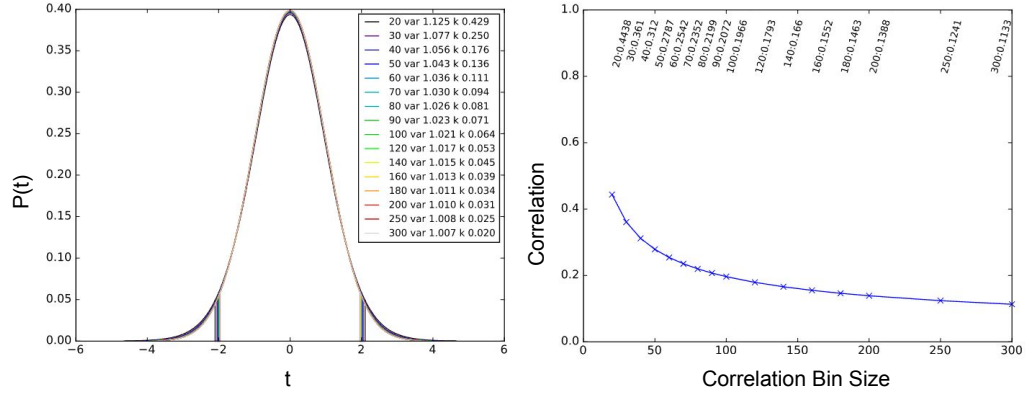


Figure 3.10: The t-distribution for different sample sizes with variance and kurtosis marked. Also shown by vertical lines are the values of t corresponding to $p=0.025$ on either side. The variation of the critical correlation threshold with sample size (including our powers of two) is plotted right.

window size as a variable input. Note that, since the velocity measurement uses correlation window sizes of data from multiple adjacent time steps but a measure is made at every timestep, the data in each measurement overlap. Thus, they are locally (in time) non-independent measurements and this is reflected in interpreting the uncertainty of measured data.

The resolution we are concerned with is that of the spectral analysis of BES data. The characteristic frequency of GAMs being a key marker of their presence, it is essential that we can reliably measure and characterise changes of velocity in the appropriate spectral range. Here we look to two metrics – the frequency resolution of velocimetry as the frequency gap between data points in a spectrum and a nominal Nyquist frequency of the velocimetry routine. The former is ideally as small as possible and reduced by minimising the interval between velocity measurements made over maximised amounts of time. The latter is ideally as large as possible and increased by minimising the correlation window size N for velocity measurements as well as the interval between them dt .

$$f_{v,nyq} = \frac{1}{2 \cdot dt \cdot N} \quad (3.4)$$

These criteria imply the use of short correlation window sizes for correlation for velocimetry. There is a trade-off in going to shorter correlation functions in the reduced accuracy of shorter data. Small sections of fluctuating data are more likely to produce correlation patterns strongly affected by fast changes in the signal that longer data would neglect. The key question in developing the velocimetry code is how short a correlation window size can be used without materially compromising the accuracy of the output (measured velocities) and therefore what frequency-space resolution is achievable.

Previous studies with BES on MAST data^{111 106} answered this question by using hundreds of data points to produce a correlation function. We know that the ‘Fast Fourier

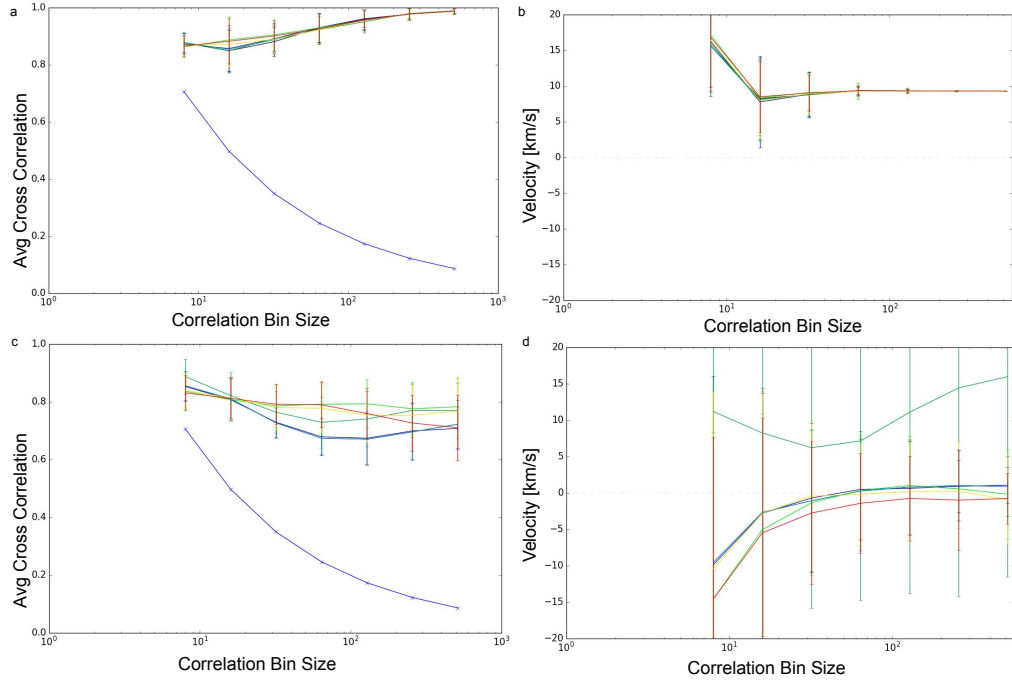


Figure 3.11: The variation of measured peak correlation values (a,c) and velocities (b,d) for surrogate data (a,b) and real BES data (c,d) inputs as correlation correlation window size (width) is varied in powers of two. Each line is one of the exemplar data series or surrogate data reproducing it. The significance threshold correlation with sample size is also marked in blue.

Transform' (FFT) routine is going to be used to produce data in our study and so an initial sweep of correlation window size increasing by powers of two was performed in line with optimised FFT speed. This was to identify the viable correlation window size range for the new velocimetry design we are using. Real and surrogate data were compared for their convergence on a velocity measurement and the statistical significance of the measurements as shown in figure 3.11. Longer sample sizes may pick up true slow variation of velocity and so some change in measured velocity there is viable. The narrowing of error bars recording the variation with each set of input data happens in the mid-tens of data points. It is clear from that test of convergence that tens rather than hundreds of data points could be used – significantly increasing the analytic potential of this approach to velocimetry by enhancing the time resolution of velocity measurements. In particular it seems that well correlated data that converge can be found using correlation window sizes above 32 data points. The remainder of the chapter takes this result forward in further tests of the smallest correlation window size options that converged – 32, 64 and 128 data points.

3.3 Velocity Measurement Failure Modes

Having constructed a basic version of our CCTDE design and done a coarse scan of its performance with correlation correlation window size, we now seek to refine the tool. To

improve its overall accuracy means to maximise the number of accurate measurements of velocity in the output time series. Since we have made sure the input is a non-noisy signal without missing data, errors of velocity measurement will principally be due to the calculation of velocity. Various physics and geometric effects may alter the density signals or their delay relative to one another so as to add information to the signals beyond turbulence and flow alone. In these cases the code-measured velocity is still properly that seen by the detector (lab frame) but may not be the flow phase velocity of the plasma. This is not what is intended by ‘accuracy’ as it relates to developing the code. The purpose of this testing is to understand in which circumstances the routine will fail to make a sensible velocity measurement and where possible pre-empting that in the code. The effects will be compared for each of the correlation window sizes suggested above for comparison.

There are three identifiers of erroneous velocity measurements used in this analysis. First, examining the velocity time series produced by the code shows substantial, sharp excursions in the measured velocity for short durations inconsistent with the time scales of turbulent physics. Second, it is one thing to measure the wrong gradient, to measure one with opposite sign to that expected is quite another. While we cannot presuppose a ‘correct’ velocity in the measurement routine – no a priori knowledge will be available for real data - we review the measurements that return a negative velocity (where a positive one – imitating flow advected vertically upwards across the detector – was imposed.) Lastly, the average goodness of fit for each time step is saved with the velocities and, since smooth velocity is imposed, scattered data with poor fit are also a clue to failure of the routine.

Figure 3.12 shows the attempt to find a correspondence between these ‘poor measurement’ indicators and properties of the CCTDE measurement. It can be seen that those data these indicators mark out always have worse fit (correlation coefficients) than other velocity measurements. The two other best performing metrics were an evaluation of the standard deviation (of correlation values) of the correlation functions and the number of un-delayed peaks in cross-correlation measurements (NB the autocorrelation function will always peak at zero delay.) Recall that at each time step the recorded velocity is an average of that seen by each of four channels in a column. We count (out of 16) where the ratio of standard deviation of a correlation function to its maximum amplitude is greater than 0.5 marked by blue triangles. We also count (out of 4) how many of the channels’ velocity measurements return three or more undelayed peaks shown with green squares. We know from the plots that the average fit coefficient of a velocity measurement at each timestep is a good proxy for the accuracy of the measurement (note bad measurements always have low average fit) so each metric is plotted against that. The undelayed peaks test has a modest correlation to poor velocity measurement markers (r^2 of 0.26 and 0.49 in the two plotted cases respectively) and so will be mitigated against as set out below. The peak to function amplitude ratio is informative about the shape of the correlation functions (as explained below also) but insuf-

ficiently predictive of poor measurements (r^2 of 0.01 and 0.02) to be used as a preemptive test in the code.

It is in the examples of negative (reversed) velocity measurements that hidden sources of error are best seen. Strictly, any underestimation of velocity is unexpected since the CCTDE technique is known to overestimate measurements. It happens because the approach fixes the distance between measuring locations and so we are strictly fitting the reciprocal of velocity. Error in the measured lag time is therefore expected to cause faster velocity measurements. For positive imposed velocities, this makes a change of sign an especially stark problem. The examples shown in figure 3.13 indicate patterns associated with error. The impact of multiple correlation function peaks at zero delay on the weighted fit approach. They also reveal occurrences when the correct pattern is found in all but one channel. Finally, there are cases where the input BES signals change amplitude from the start of the correlation window size to the end. These each inform mitigating steps introduced to our CCTDE code.

3.3.1 Preemptive Tests Introduced To The Code

Given the small size of the correlation bin we use, no restriction is made on the delay at which to find the correlation function peak. As such it is possible that signals with rapid periodicity might feature multiple cycles (correlation peaks) within the span of each bin. The first test then was to identify all the peaks in every correlation function and evaluate their amplitude relative to the peak closest to zero time delay. If a taller peak exists at longer delay then this would be used to calculate velocity and have the effect of sharply increasing the recorded delay and so reducing the measured velocity. When this was investigated it was found that not only was the occurrence of a second tall peak rare (seen once on velocimetry run with each of four surrogate signals) but also that at maximum delay the signals are typically strongly anti-correlated (rather than dissimilar i.e. no correlation.) This is evident when a quantitative comparison of the ratio of maximum cross-correlation to standard deviation of the correlation function was produced for a whole velocity time series with ratio values consistently at or above unity. Therefore no adaptation of the code for second peaks was made.

The significant anti-correlation at the edges of the correlation functions alerts us to another source of error. It implies a substantial difference between edges and centre such that even at small delays the positive and negative delay directions are distinct. This creates a discontinuity in the gradient of the correlation function as it crosses the zero delay axis. This effect is introduced by the FFT routine - used to calculate the correlation function - that wraps data series on themselves as delay increases in order to preserve kernel size and calculation speed. The effect on velocity measurement is to make the correlation function resemble one with a sharp peak at zero time delay. The velocimetry records this peak and

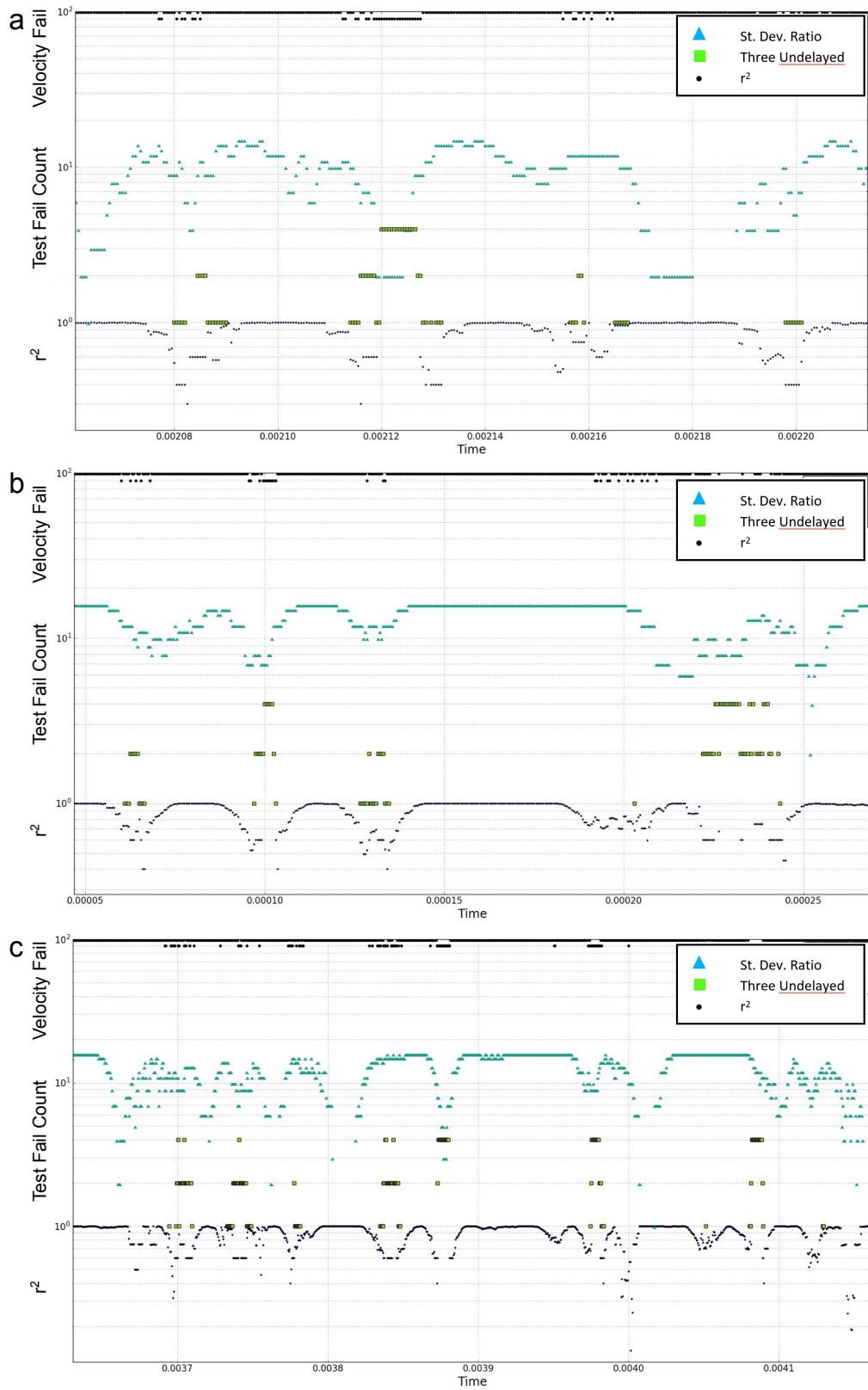


Figure 3.12: Three examples of the pattern of failed velocity measurements from input data using shots 29380 channel 18 (a) and then two times from 30449 channel 15 (b,c). The imposed velocity is 5 km/s. First, data in the time series are marked valid measurements or not by assigning a score of 100 or 95 respectively. The average correlation coefficient of each velocity measurement is shown at the bottom (range 0-1). In between, we plot the results of tests of the ratio of deviation to maximum of the correlation function and number of cases with three undelayed peaks.

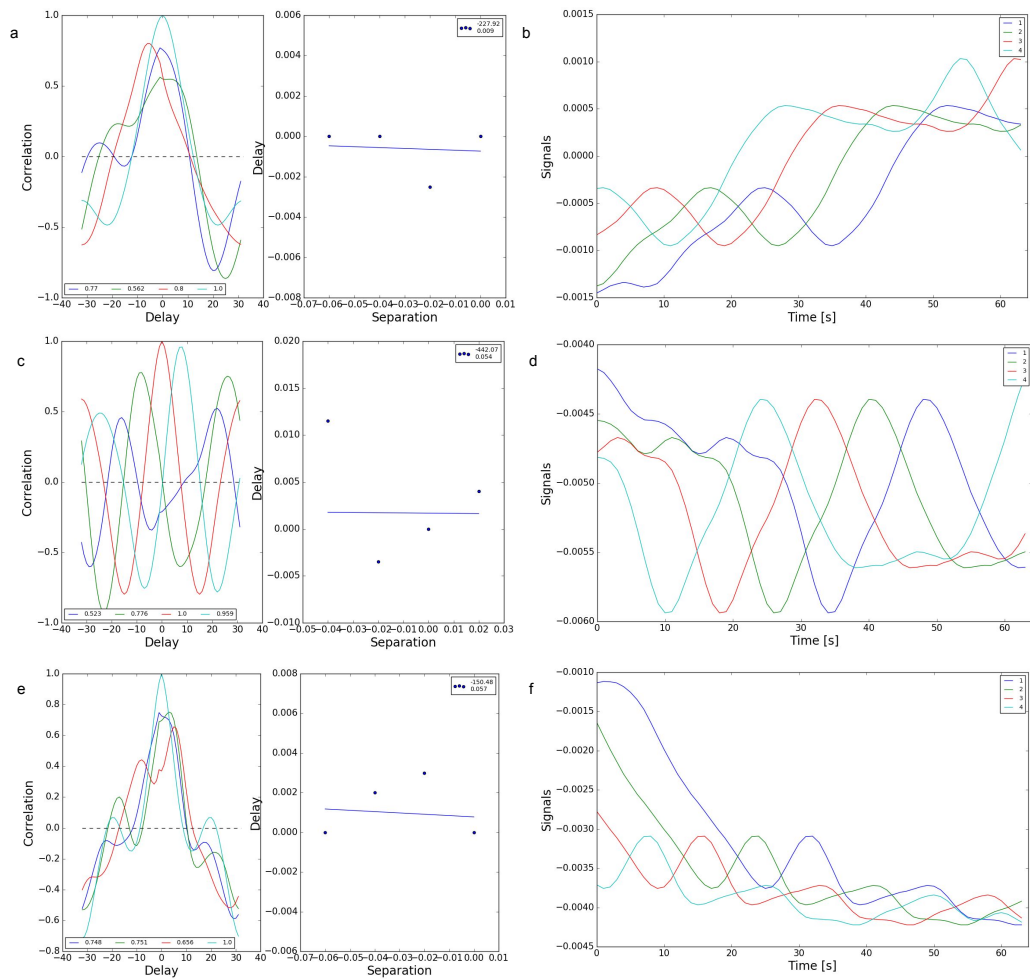


Figure 3.13: Three examples of a negative velocity measured using input data from shot 30449 channel 15 and imposing a velocity of 5 km/s are shown. a,c,e are the correlation functions that produce the negative measure next to the surrogate BES signals b,d,f being correlated.

the overall velocity calculated is extremely fast. In these cases, and in order to preserve measurements on smooth correlation functions only, the code tests for three or more undelayed peaks in each velocity measurement, as suggested by figure 3.14. Where we would naively have assumed a rapid motion across the detector before, we now recognise this as the marker of a distorted series of correlation functions and discard the measurement. This test will also discard truly rapid measurements (i.e. physics that causes density fluctuations fast enough to cross the detector in one time step and only register in a single channel's signal.) As stated, we do not anticipate plasma flow physics at that velocity, however.

It is also true that turbulent physics is not expected to affect the lowest frequencies measurable by the velocimetry. It is therefore possible to mitigate the FFT kernel effect by increasing the lower cut-off frequency of the band-pass filtering of density data. Recall that initially the input data is filtered to include only the range 1 – 200 kHz. The intended effect is to reduce the slowly varying component of the signal in each time slice (i.e. correlation bin) leaving only fluctuations of the physics we wish to study. This should eliminate substantial differences of amplitude between the start and end of the signal slice that distort the correlation when wrapped.

The benefit of doing this was tested for a range of cut-off frequencies in figure 3.14. It was expected that the advantage of this would be seen up to a frequency equivalent to one-quarter of a sine wave in the time slice. In fact raising the bandpass filter cut-off continues to improve the accuracy of measurements (by reducing the incidence of erroneous measures) up to one-half wavelength. The effect of which is to eliminate the full range of the wave caused by slow variation (minimum to maximum) rather than only its amplitude. This is, of course, the same as the nominal Nyquist frequency of the velocimetry. The order of the filter used has no effect per figure 3.15.

The same effect of introducing a bandpass filter was compared in 3.16 using different sizes of correlation function to produce velocity measurements on data from shot 30449 channel 15. A reduced set of performance and error metrics was tested. For shorter correlations a similar though more modest improvement with higher cutoff frequency is seen (again up to the new nominal Nyquist at 32 kHz.) The longer correlation function produces velocity measurements that fail too rarely to measure the bandpass effect.

The tests so far implemented have accounted for circumstances where a velocity would likely not be measured. We now turn to testing accuracy in terms of proximity to a correct value. First by considering high positive values for velocity. The code is tested by producing time series with the surrogate data and a fixed delay between the signals as seen by channels in a single 'column' (though the velocimetry is naïve to the orientation of channels only measuring their order.) Consequently, we can input a low velocity and assess the output time series measurements that exceed it by a significant fraction. Though some of these are well-fitted measurements, many show low determinant values 'r'. This is a useful statistical

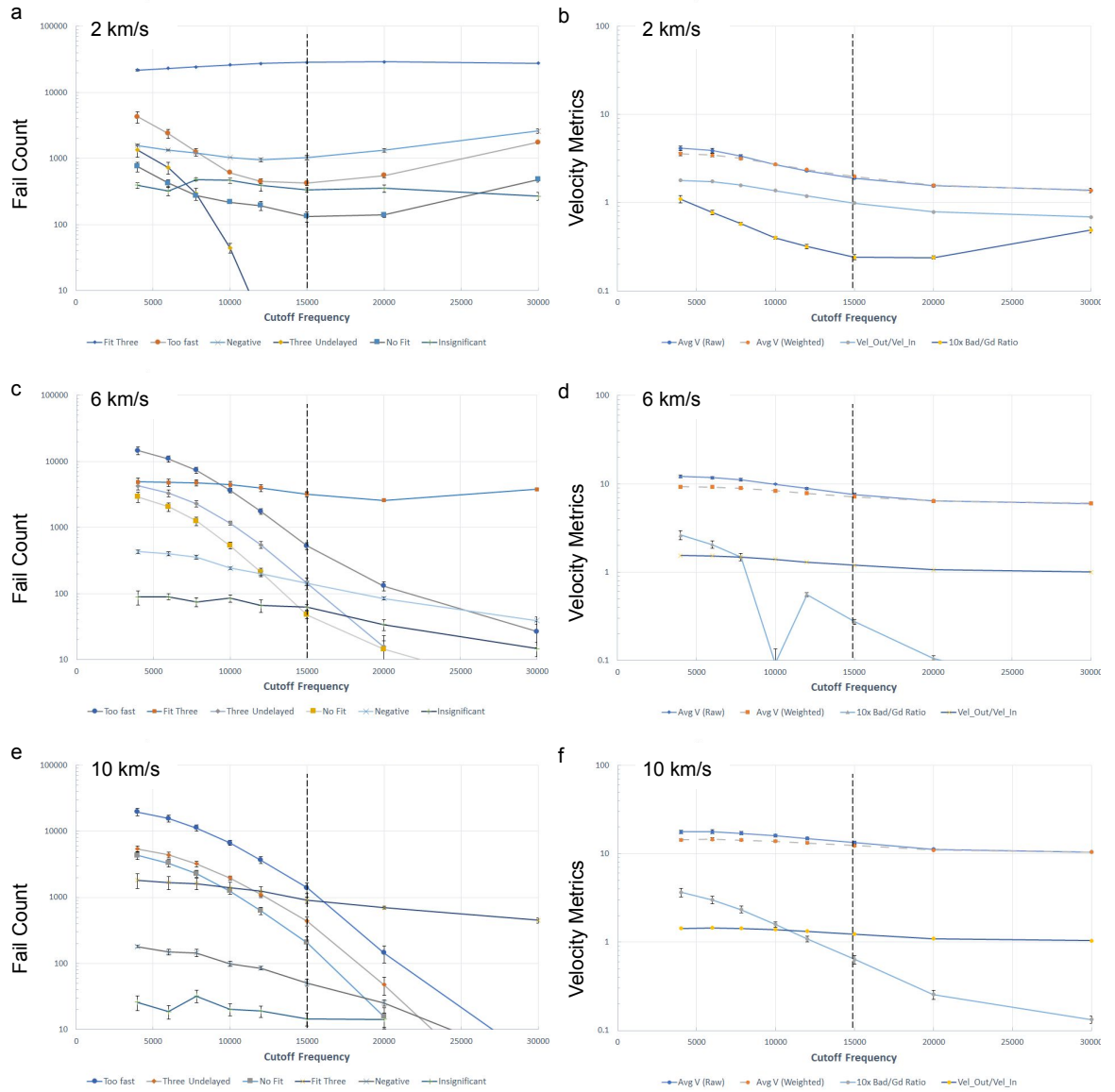


Figure 3.14: The effect of introducing a bandpass filter on the input signal to the velocimetry on the count of each of the metrics for poor measurement varying with the lower cutoff frequency of the filter for three different carrier velocities (a,c,e). The data are averaged over two runs of input data from shots 29380 channel 11, 30449 channel 11 and 30449 channel 22. Error bars show the standard error of the mean. Plots b,d and f are the results for the velocimetry performance metrics. Marked improvements are reproduced across a range of carrier velocities up to a cutoff equivalent to the nominal Nyquist frequency, dashed.

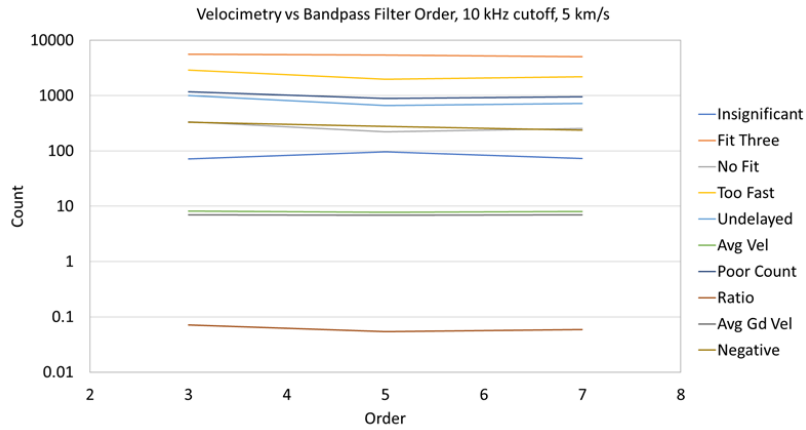


Figure 3.15: The effect of varying the order of the bandpass filter was also investigated using data from shot 30449 channel 15 but no significant effect was evident. Shown are the data using a 10 kHz cutoff frequency and 5 km/s velocity.

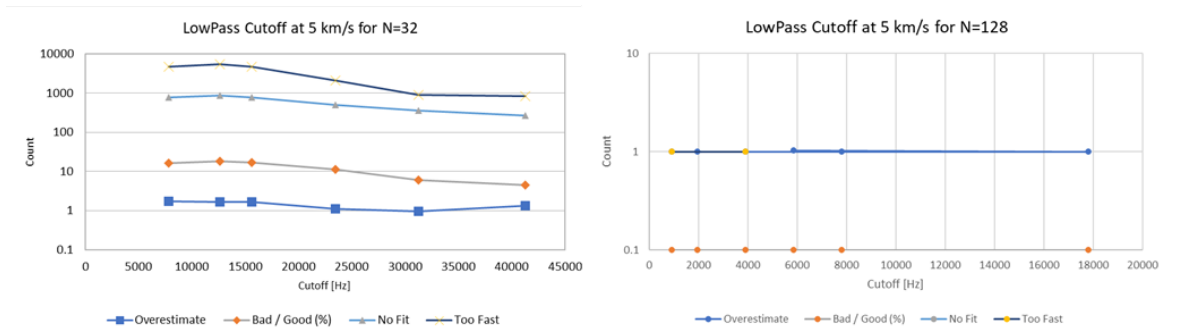


Figure 3.16: Velocimetry performance and error metrics compared using different sizes of correlation function bin.

test to weight the ‘goodness’ of a measurement in the same way that correlation was used to weight the fitted gradient. The cases with large measured velocity show increased scatter in the delay data fitted to measure velocity or else high weighting given to the measurements in channels farthest apart. The fit line therefore lies away from the actual data points. However, when, as in figure 3.17, we plot the known input velocity from the reference channel we see that in a large number of cases a more accurate fit could be found if one data point were excluded at the edge of the array of channels. Both in the sense of finding the gradient of the true velocity and of improved goodness of fit coefficient (even allowing for reducing the number of data points.) Two examples of an inaccurate velocity measurement are shown in figure 3.17 from velocimetry using shot 30258 channel 18 – again the correlation function and fitting (left) and signal data (right). Included as a dashed line is the imposed velocity extending from the reference channel data point. It is evident that two channels out of four often pick up the correct velocity and using fewer than all four would produce a more accurate measurement, though this is a challenge to mitigate without knowing the velocity a priori. We therefore amended the velocity calculation to compare the ‘goodness of fit’ statistic for a velocity measured using all four channels and that measured with only three

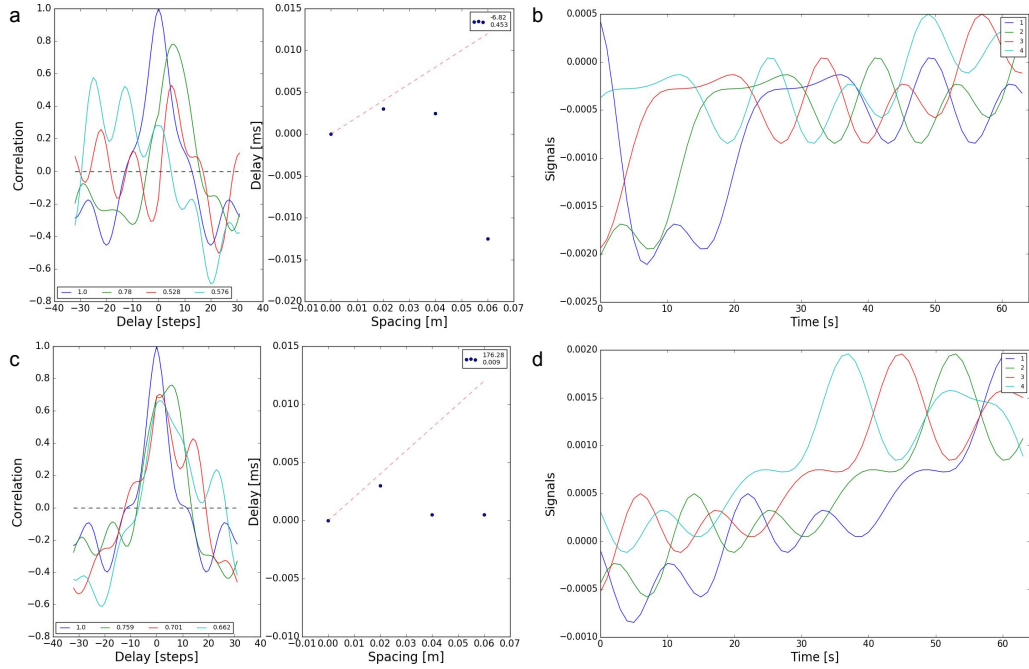


Figure 3.17: Two examples of an inaccurate velocity measurement comparing the gradient fitting (a,c) and the surrogate BES data that produce them (b,d). The imposed velocity through the reference channel is plotted as a dashed red line.

(including the reference channel.) The routine selects the velocity associated with the better fit. This is only done for ‘scattered’ data defined as those that include a first or last data point below the second or third respectively i.e. non-monotonic arrangement of the four points. The effect of the test is to exclude the position that ‘changed direction’ if it results in a better weighted fit.

In principle, a more sophisticated version of this test could assess the magnitude of the change of direction before deciding to exclude data. However, setting a threshold for that would beg the question by presupposing the ‘correct’ velocity was known which is precisely what this tool is intended to measure (and indeed its importance comes from the lack of corroborating measurements in other diagnostics.) For our purposes we note that default selecting a three-point fit either changes the gradient (ie velocity) by a lot, in which case the initial measure likely had scattered data, or it changes the gradient a little, in which case the velocity will be approximately the same. In either case the better fit gradient is preferable.

Velocity [km/s]	Poor Fit [%]
2	2.5
10	6.5

Table 3.2: Velocimetry performance measured by quality of gradient fit compared to imposed velocity

The effect of introducing all of these additional steps in our CCTDE technique is graphed in figure 3.18. The relative occurrence of each error is shown to be typically higher at faster

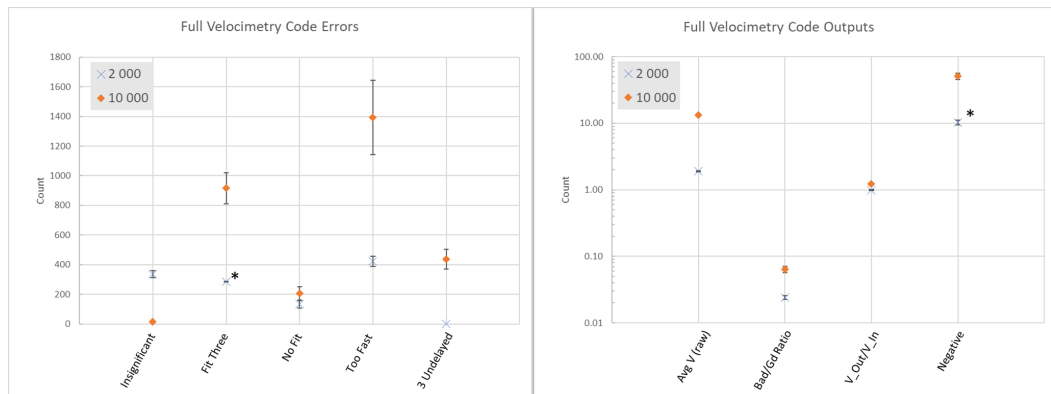


Figure 3.18: The average results of velocimetry errors (left) and performance (right) for analysis using all the test data signals and all the corrections described in this chapter are shown for a slow (2 km/s) and fast (10 km/s) imposed velocity. Error bars show the standard error of the mean. Asterisked data points have been reduced by a factor of 100.

flow velocities though still low compared to the total number of timesteps (16 384.) The strong reliability of this implementation of the code is demonstrated in the narrow deviation across test cases of measured velocity only slightly above the imposed – a ratio of 1.0 for slow and 1.2 for fast speeds. The introduction of a number of pre-emptive tests has brought the number of data points measured with poor fit down to an average 2.5% for slow and 6.5% for fast velocities as indicated in 3.2. The best data tested (which should be the most truly broadband inputs) had 1% failure rate of measurements and returned velocities within 5% of the input. Slower velocities were found to be more likely to include negative velocities (partly because they are fluctuating closer to the zero axis) and as such can underestimate the flow velocity.

The final test of the code’s construction is to identify the appropriate treatment of those errors identified above. Typically the discovery of an error ends the velocity calculation by casting it as a ‘NaN’ floating point value. These cannot be left in the time history because we are interested in spectral analysis of our velocimetry data using an FFT routine and that requires a perfectly regular data set. Three options were compared – replacing the missing data with a mean average value of the time series, a median average and using the protocol developed for photon noise in the raw data to bridge the gap with neighbouring data values. The middle, median option was preferred because it avoids skewing the data set toward the higher velocity values that have been identified with poor velocimetry. Removing these velocity excursions will slightly shift power in the spectrum to lower frequencies. The effect on velocimetry can be seen in figure 3.19 where a smoothing approach preserves spikes and defaulting to the local median produces some modified domains of constant velocity.

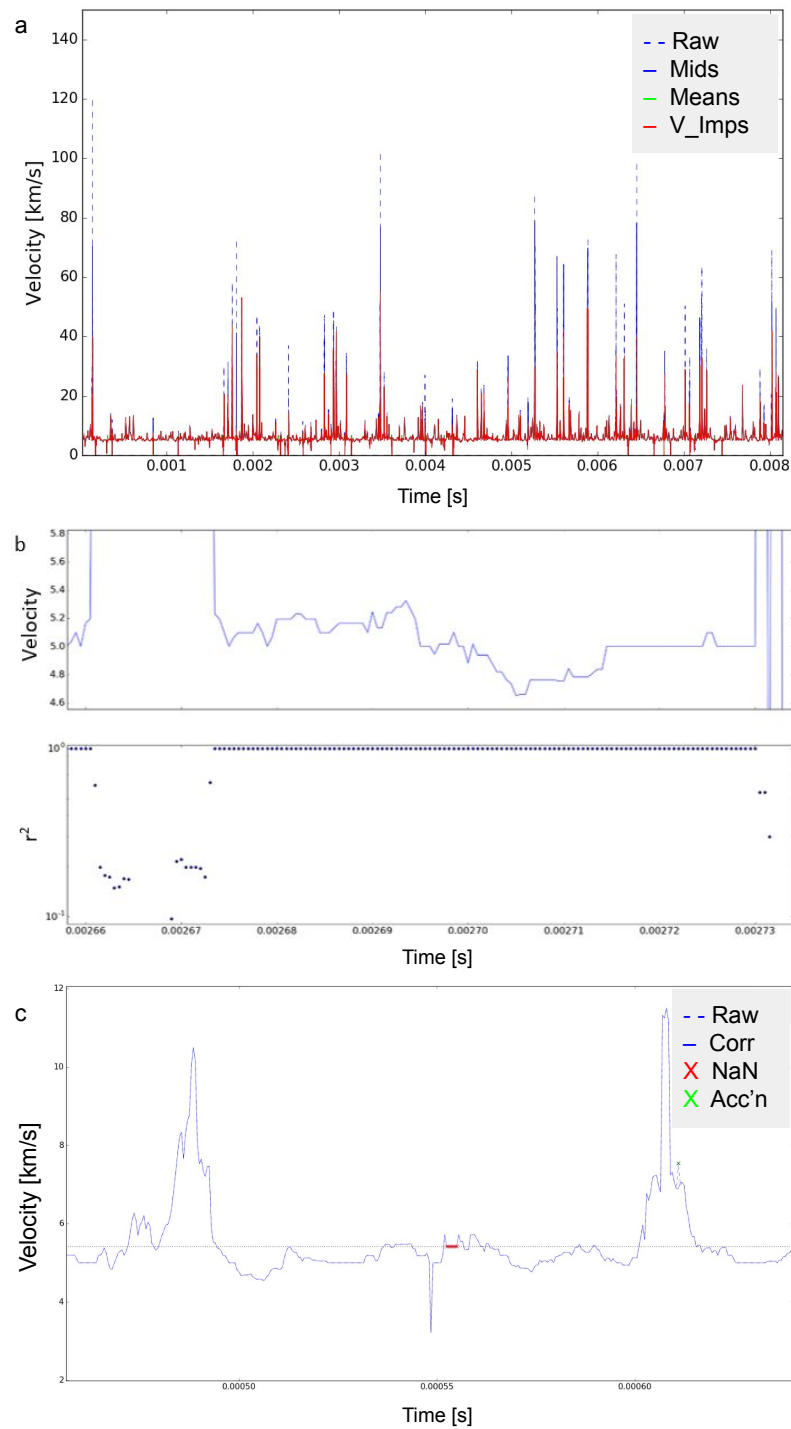


Figure 3.19: (a) is a plot of an example velocity time series showing the traces using different methods of NaN replacement for data from shot 30449 channel 22. The uncorrected signal is the dashed line, the solid blue line is the result of smoothing the signal, a green line shows the result of replacing with averages. The red line shows replacement with the imposed velocity of 5 km/s. (b) is a short section of the data showing the low correlation coefficients for velocity excursions, in (c) the variation of good data and a flat series where data has been replaced can be seen.

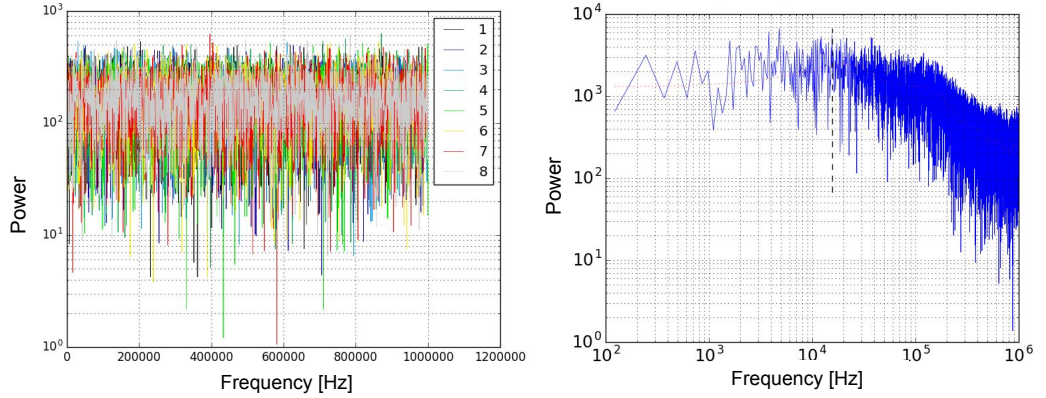


Figure 3.20: (a) and (b) compare the spectra from two runs using purely Gaussian input signals in all 8 columns without and then with an imposed velocity (at 5 km/s.) With an imposed velocity, the pattern of flat 'white' then falling 'red' spectrum is established.

3.4 Introducing the Null Hypothesis

Having developed a reliable CCTDE velocimetry tool for MAST BES data with improved accuracy, we close by reviewing the impact of design parameters on the velocity spectrum. We can use our surrogate density data to understand the spectrum of a stochastic field with constant flow as the null case against which we compare candidate zonal flow spectra. The spectra are produced by plotting the power spectral density of signals against frequency, calculated using the FFT routine as

$$PSD(g) = dt \cdot \left(\frac{|FFT(g)|}{t} \right)^2 \quad (3.5)$$

where dt is the sampling interval and t is the total time in seconds of the signal g studied.

There are two key features of the null spectrum pattern. The first, the result of a randomly distributed signal, is a region of flat power. It can be established by running the velocimetry using both a purely Gaussian signal and the realistic stochastic signals without any imposed velocity that a flat region leads the spectrum from low frequencies. The velocity time series produced in these cases is also randomly distributed around a zero value; its transform is equally powerful across the entire frequency range. When a constant delay between common signals is added, at higher frequencies the pattern becomes one of a diminishing power relation to frequency as shown in figure 3.20. The second feature is a consequence of imposition of a velocity, not detectable above the nominal Nyquist frequency. The transition between these regions occurs at approximately the nominal Nyquist frequency associated with the velocimetry routine marked in figure 3.20 b. Our method cannot accurately resolve frequencies of the velocity above this frequency and so they are lose amplitude in the spectrum. The null spectrum for turbulent flow we take to be a flat, white noise-like region followed by a steep, red noise-like region above the measurement Nyquist frequency of the type exemplified in figure 3.20.

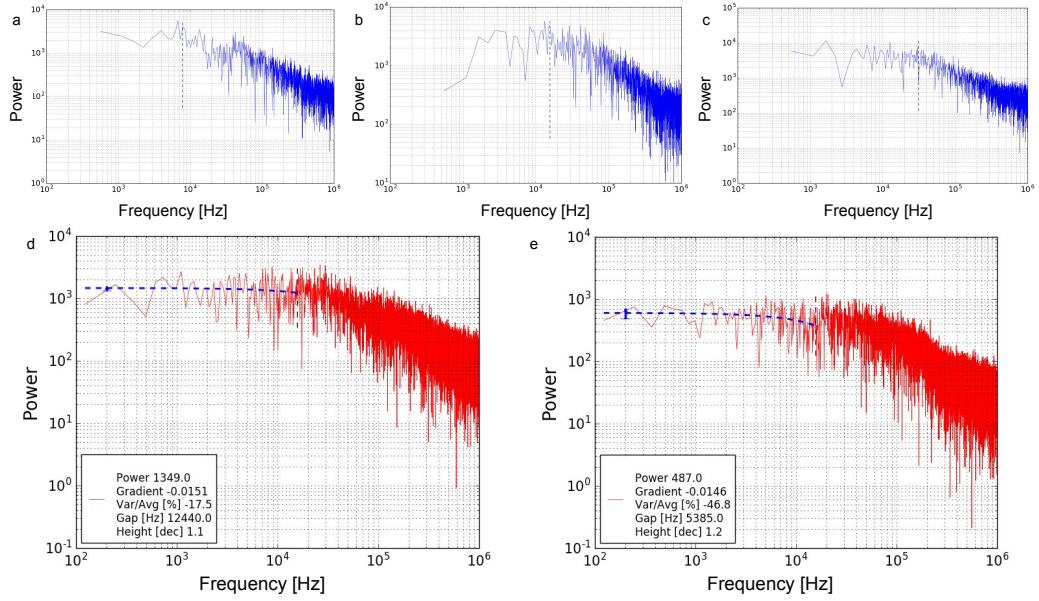


Figure 3.21: (a-c) show in data from shot 29380 channel 10 for the same imposed velocity of 5 km/s for each candidate correlation function correlation window size of 32, 64 and 128 timesteps that the spectrum pattern is robustly repeated. (d) and (e) are the spectra for data from input signals 30449 channel 11 and 29380 channel 18 for a slow (3 km/s) and fast (12 km/s) imposed velocity signals respectively, demonstrating the same and giving indicative values for the metrics used to measure spectra in the legend.

3.4.1 Spectrum Metrics

To test the robustness of this base case we investigated the parameter dependence of its distinct pattern. Varying the inputs of correlation function size and imposed velocity we measure changes in the spectrum. These are marked for the examples of velocity spectra shown in 3.21 and those metrics with clear trends against flow velocity are shown in figure 3.22. We are particularly interested in the robustness of the flat then falling 'white-to-red-noise-like' pattern to carrier flow velocity, the frequency of the transition between these regions and the flatness of the lower frequency noise region. These should characterise a purely turbulent flow and deviations from the patterns found in testing here will guide the identification of different flow physics.

The plots of key metrics measuring the spectra are shown in figure 3.22, averaged over the cases shot 30449 channel 11, 29380 channels 10, 11 and 18 to investigate the parameter dependence of the spectrum pattern. The metrics shown are the gradient of the 'flat' region, the height of the flat region, the standard deviation of the flat region and the gap between the nominal Nyquist frequency and transition between flat and falling regions is. The correlation function size is varied with imposed velocity. We also show the error bars (standard error of mean) as a percentage of the data in each case.

Not shown in figure 3.22 are the plots for the decadal span of the falling power for each case. This is because they stay similar across cases with roughly two decades of power

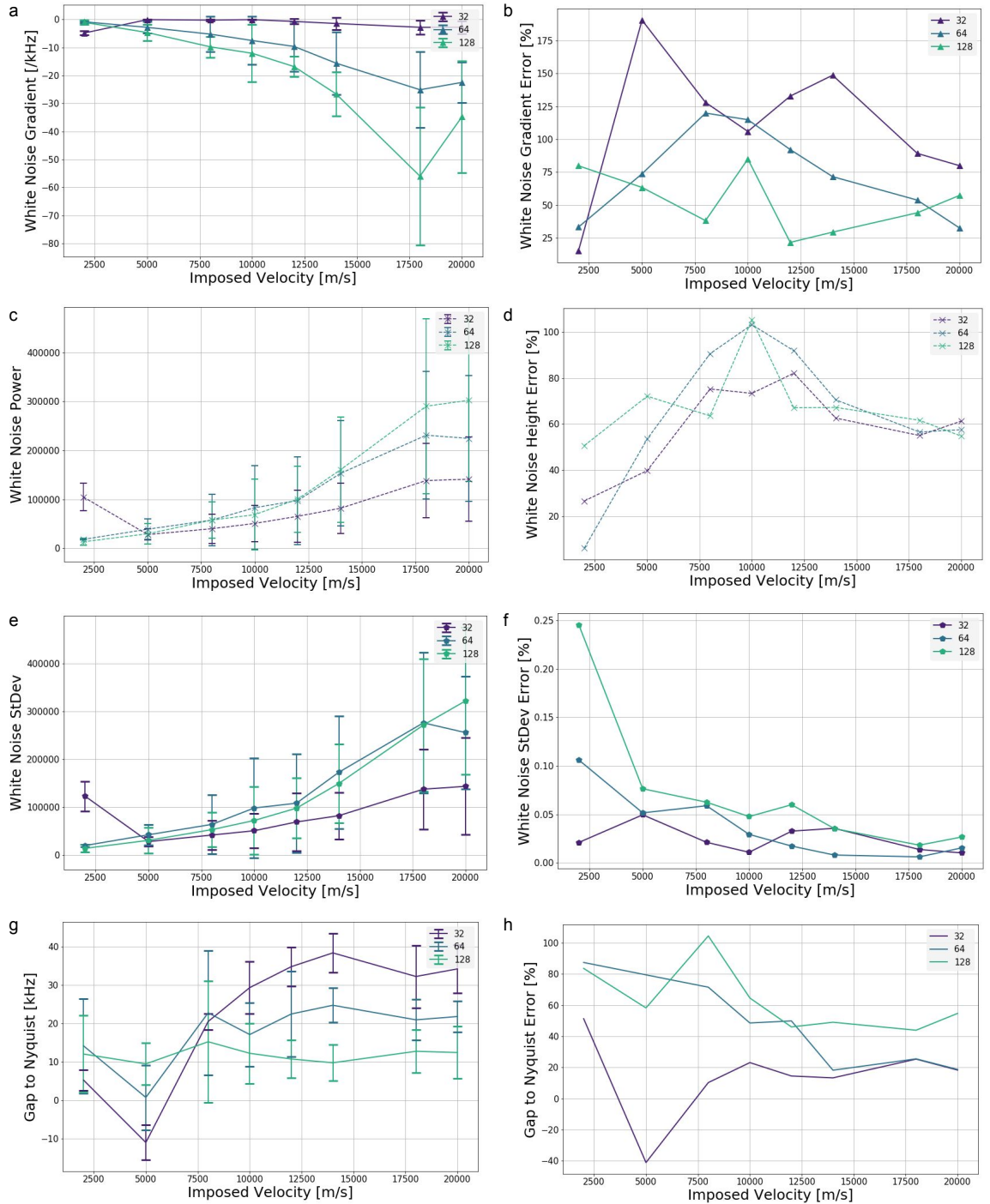


Figure 3.22: Metrics measuring the velocity spectra are shown in (a,c,e,g) as a function of the correlation function size and imposed velocity. Error bars show the standard error of the mean and plotted in (b,d,f,h) are the error bars as a percentage of the data on the left.

(slightly more for longer correlation functions.) The height of the flat region reflects the increased power in a signal with more information – both as correlation function size and imposed velocity increase, the noise height increases. Similarly, the range spanned by that noise increases as reflected in the variance of values recorded in this part of the spectrum. Whereas the deviation is similar across cases, we can see that the middle range of velocities involves large inconsistency in the power of the velocity spectra depending on the input fluctuating data.

A clear trend can be seen in the change of gradient with velocity. The gradient (of a linear fit through low and medium frequency data) clearly steepens with velocity in all cases. This effect would appear to be exaggerated by the choice of correlation function size, though. A larger correlation captures more power at lower frequencies, especially at faster velocities. We should expect a fast purely turbulent flow to appear to have a shallow gradient across the lower frequency region. The other interesting plot is the turnover frequency, found by measuring the intercept of a flat line at the flat region and a line fitted to the established falling frequency region. What is shown is the difference between this frequency and the nominal Nyquist frequency. Nearly everywhere in parameter space, the turnover is found to happen above the nominal Nyquist frequency. Only a slow velocity and short correlation function has power falling below the nominal Nyquist frequency. The short correlation function produces the biggest difference in average turnover and nominal Nyquist frequency with velocity. The longest correlation function produces a consistent spectrum that turns over 10 kHz above the nominal Nyquist at all velocities. This extension of the flat region implies a wider range of parameter space in which we can measure changes to the spectrum than first thought.

We close this exploration of the spectrum by commenting that the code design decisions discussed above, including the bandpass filtering of data and ‘NaN’ replacement choices, were also assessed for their impact on the null spectrum as shown in figure 3.23. While band-pass filtering affects the overall height of the spectrum, it does not affect its pattern. The number of ‘NaN’ data points that need to be replaced is now so few that no difference was found in the spectrum using either mean or median method (though inserting the known value reduced the overall power in the signal.)

3.5 Summary

We have written a cross-correlation time delay estimation (CCTDE) code for velocimetry using beam emission spectroscopy (BES) data. The primary motivation of its design was to reduce the size and separation of data used for each velocity measurement in order to maximise the time resolution of the resulting velocity time series. Our approach can take either real or surrogate BES data as input. The former is treated to remove high energy

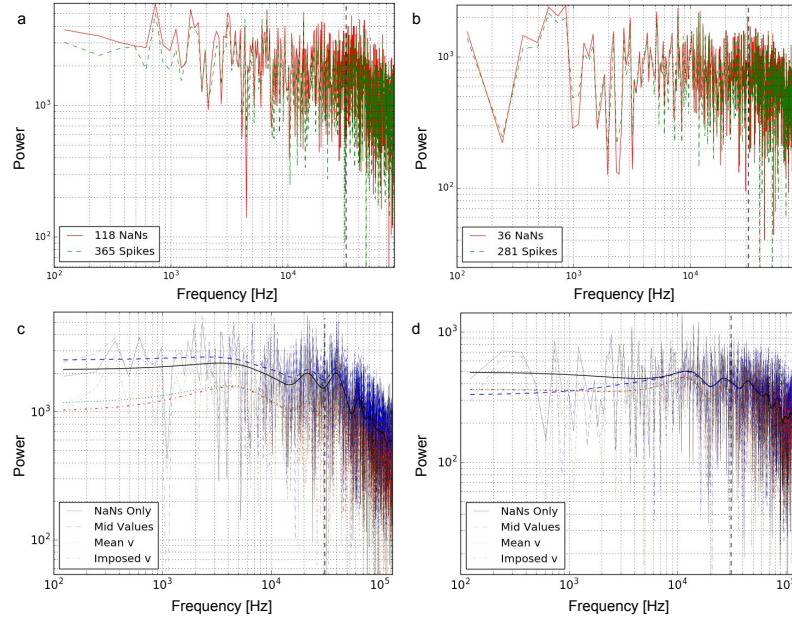


Figure 3.23: Velocity spectra comparing different design choices for the velocimetry using input data from shot 30449 channel 22 (a,c) and for 29380 channel 18 (b,d). (a,b) show the effect of eliminating the spikes in velocity time series based on the acceleration limit (the number of data points changed is shown in the legend.) (c,d) are the spectra for different options replacing the ‘NaN’s.

particle noise and then bandpass filtered to a range associated with ion scale plasma turbulence. The latter is reproduced from BES data by mimicking the statistical properties of a BES signal. This purely stochastic input reproduces a turbulent field absent other physics. Testing the response of the code to parameter changes with these data means we are secure in our understanding that changes are not the result of convolution with changing physical phenomena.

We seek to balance frequency resolution of a velocity spectrum with accuracy of velocimetry. The first test compares both input data types to identify the convergence of velocity measurements. This finds the minimum possible correlation function size in our design to be of order tens of time steps, significantly shorter than the hundreds used in previous turbulence studies with BES. We studied powers of two to maximise the potential of using fast Fourier transforms (FFTs) to find velocity. By comparing a nominal Nyquist frequency associated with correlation function sizes in this range we identified a correlation window size of 64 timesteps as a balance of useful frequency resolution for zonal flow (GAM) studies and accuracy of results.

Having fixed an overall accuracy of the measurements in this basic sense we turned to improving the closeness of individual measurements in the velocity time series to a fixed input velocity. By examining cases that produced poor measurements, multiple limits and tests to the measurements in our CCTDE design could be introduced to improve the reliability of the output at each time step. These included increasing the lower cut-off of the bandpass filtering

of data from a low frequency associated with the raw measured signal to the nominal Nyquist frequency of the velocimetry. We then return to accuracy by introducing refinements of the time series output to remove unphysical accelerations and regularise invalid measurements. The net effect of these changes was a code that across multiple examples of input data could return measurements (not a NaN) 98% of the time, reducing to 94% for fast imposed velocities, that on a weighted average are within 5% of the input velocity (error increases with imposed velocity.)

A spectrum of the time series produced according to our velocimetry design using surrogate input data provides a null hypothesis for velocity spectra in the tokamak. We find it has the generic pattern of flat then falling signal power regions with increasing frequency. As the imposed velocity increases, the lower frequencies (initially flat) acquire a steepening gradient. The transition between regions is seen to be approximately constant but above the nominal Nyquist frequency. This is potentially advantageous for detecting finite frequency zonal flows. Observations in real data of the generic presentation of this plot will account for the technique and broadband turbulence. Deviations from it will reveal the action of plasma physics.

Chapter 4

Benchmarking Code Performance

In the previous chapter we developed a velocimetry technique with high temporal resolution and accuracy to study tokamaks. We will use it with Beam Emission Spectroscopy (BES) data. In the work that follows we will investigate how known features of spherical tokamak plasmas affect the code's inputs and outputs. We have already established that in addition to a regular time history of velocity the analysis of plasma flows that we are aiming to achieve centres on the study of spectra of those time series. Both outputs will be considered in the investigations that follow.

An intelligent interpretation of absolute velocity measures or changes in velocity each requires an understanding of the response of the velocimetry algorithm to interruptive physics scenarios i.e. where more than an unperturbed turbulent field is being measured. This is true of any physical interpretation, for example, comparing our results to other diagnostics needs a clear understanding of the uncertainty of measurements. Three scenarios will be studied in anticipation of spherical tokamak plasma behaviour to evaluate their effect on measuring accurate velocities and observing GAM-like modes that we will introduce into the surrogate data in the velocity time series. First, a powerful, persistent single frequency mode in the BES data will be studied as a common feature of velocity spectra with high contrast peaks. Next, a repeated, short burst at high and low frequencies that imitates MHD activity in MAST plasmas. Finally we reproduce the surrogate turbulent field but impose a time-evolving flow velocity in the delay between channels to evaluate the impact of slow changes in the plasma to our spectrum pattern and measure the code's ability to track the changing flow velocity.

4.1 Introducing Noise

As we move to understanding the code's performance and away from testing individual measurements, we add realistic effects to the test data. Tests of particular phenomena will be described in turn below, however, as a general addition, we introduce noise to the

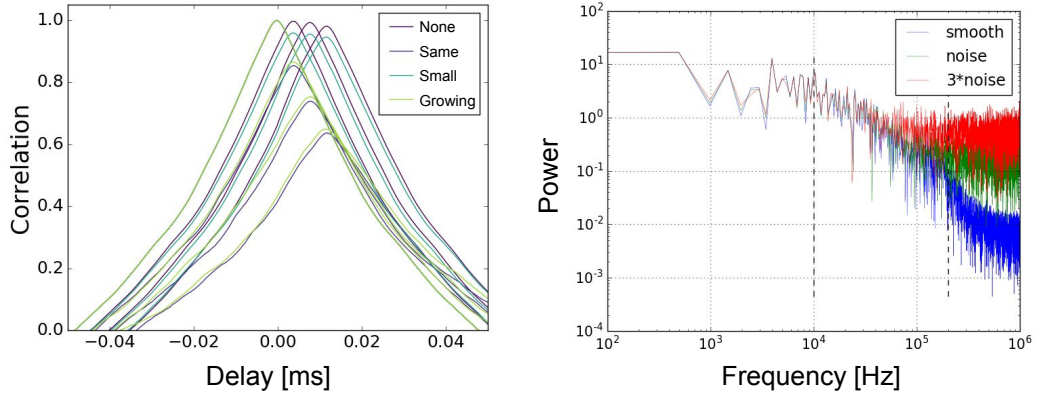


Figure 4.1: Adding Gaussian noise to surrogate input data with common and varying amplitudes. The effect on the cross-correlation of channels in a column of different methods to introduce noise is shown next to the spectra of signals with different amplitudes of noise added.

stochastic signals. The signal recreated from BES data is already fluctuating in a noisy way but the purpose of the additional noise is to make the delayed copies of the signal dissimilar. Doing this recreates the reducing correlation of spatially farther separated measurements of the BES detector due to the decorrelation of an eddy advected across them.

The noise is generated using a normal distribution of values centred at zero and with standard deviation unity. Figure 4.1 shows the effect of adding noise in different ways. The ‘grow’ method in which noise is multiplied by channel separation gets closest to realistic reduction in the correlation across the detector. The full spectrum of noise includes high frequency components, of course, and so the noise is added after the signal is bandpass filtered in the velocimetry. The signals are changed within the bandpass cut-off frequencies but most of the change is at very high frequencies. This means adding noise to the short signal used for each cross-correlation calculation rather than the full surrogate time series. Recalling that each channel in a column is treated in turn, this makes it possible to add noise only to those channels not being used as the reference signal. The noise added to channels is therefore multiplied by an integer equal to how many channels the signal is away from the reference channel. In effect, channels farther apart on the detector are less similar. We therefore add realism to the velocity measurement that considers all four channels in a column.

A common noise signal is being added to the channels, its amplitude is designed to mimic the correlation functions of a representative sample of BES data shown in figure 4.2. These are chosen from a column in the middle of the detector of shot 29378. In order to achieve a reduction in correlation that matches these correlation values the noise (generated between plus/minus one) is scaled to the signal it is added to by multiplying by a factor of $1/5$ the standard deviation of the signal.

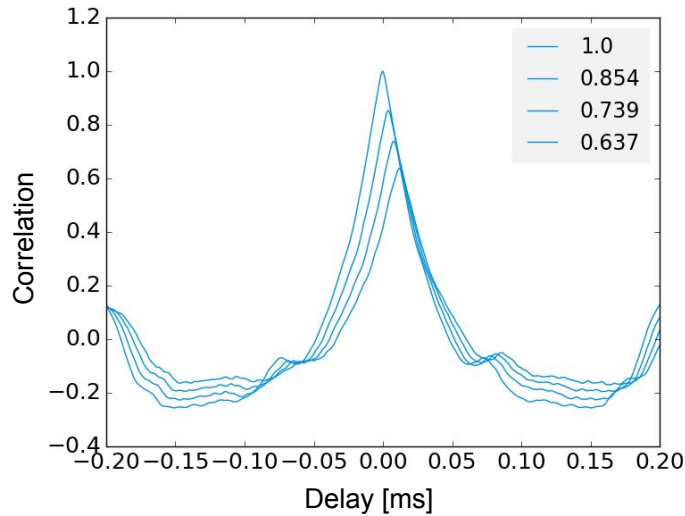


Figure 4.2: Measured correlation of peaks recorded in the legend for exemplar BES data across the detector to record realistic cross-correlation values.

4.2 Mode in the Velocimetry Input Signal

The first question is what the effect of a powerful coherent mode on the outputs of the velocimetry algorithm is. It will be shown in the chapters that follow that a magnetic mode is a recurring feature of spectra with prominent peaks. Understanding these effects therefore contributes to an active research question. This motivates splitting the investigation to follow two routes – the effect of a mode in the input (BES) data and then in the output (velocity) data. With both options we are concerned with first ascertaining the magnitude of mode required for a clearly visible peak in the velocity spectrum with test data and, second, with changes to the null spectrum pattern. An associated question arises – how much of an input mode is transferred to the output?

In order to test this we construct a version of the test code that starts with a common stochastic signal recreated from real data as in previous work. This version then runs velocimetry on a stochastic signal and a stochastic signal with a medium frequency mode (of order 10 kHz.) The velocity output of each then has a medium frequency mode added and is turned into a spectrum. The end result is a comparison of velocity time series and spectra for each of an input mode, an output mode and a mode in both.

Mode amplitude is defined in relation to the variance of the input signal. For a given stochastic input signal and constant delay across channels in a single column, the amplitude is defined as the product of a multiplier and the signal’s standard deviation. The effect of this is shown in figure 4.3. This is true for the modes in both density and velocity signals (the same multiplier is applied to each when studying modes in both signals.) The mode is imposed simultaneously (without velocity and in phase) in all input signals.

Sinusoidal modes with amplitude multiplied by between 0.2 and 2.5 times the standard

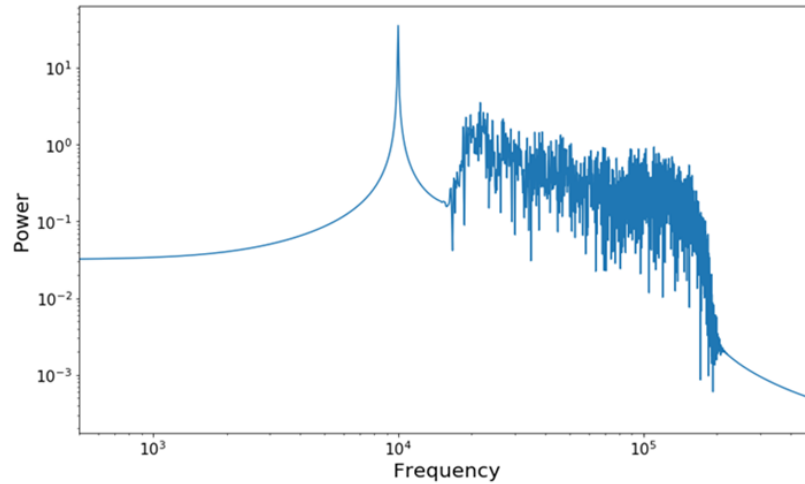


Figure 4.3: The spectrum of an input signal with an imposed mode at 10 kHz (below the nominal Nyquist frequency of the velocimetry.) The mode amplitude is equivalent to the standard deviation of the time series at 10 kHz. The mode is added to the signal from shot 29380 channel 11 after filtering.

deviation of BES or velocity time series as appropriate were added to the velocimetry input (BES), output (velocity) signals and to both. The imposed mode was always at 10 kHz to be well below the nominal Nyquist frequency of the routine. The spectra were studied for an imposed velocity of 3 km/s and 10 km/s over three test signals. The averaged outputs are shown in figure 4.4. These velocities correspond to previous measurements of flow in MAST while being slow enough to limit the effect of fast flow on the gradient of the 'flat' power region. Where other analyses in this project will search for a tallest peak, in this case only the (smoothed) peak at 10 kHz is measured regardless of other peak heights. The spectral tests from section 3.4.1 are further modified such that only the flat region below the peak frequency is studied to find the mean and standard deviation of the flat power region. Else the presence of tall peaks will dominate both measures. The plots in figure 4.4 show first the change in flat power amplitude and mode amplitude with the multiplier (of signal standard deviation) used to generate the mode first. Then plotted are the ratio of the peak amplitude above the noise to the standard deviation of the noise below the peak (a measure of contrast.) Next is the change in fitted width of the mode peak with input multiplier. Finally, the mode multiplier in the velocity time series calculated from the spectrum peak is compared to the known input that produced it to test for loss of signal strength. The results are considered in detail below.

The results for a mode in the velocity times series only are included for completeness, though they are simply the spectra of an imposed mode and so entirely predictable (a higher amplitude mode increases the power of a spectrum peak.) What is interesting is to compare spectra with and without a velocity mode component. This is done for each of these analyses by smoothing the spectra with the lowpass Butterworth filter used for BES signals and cut-off

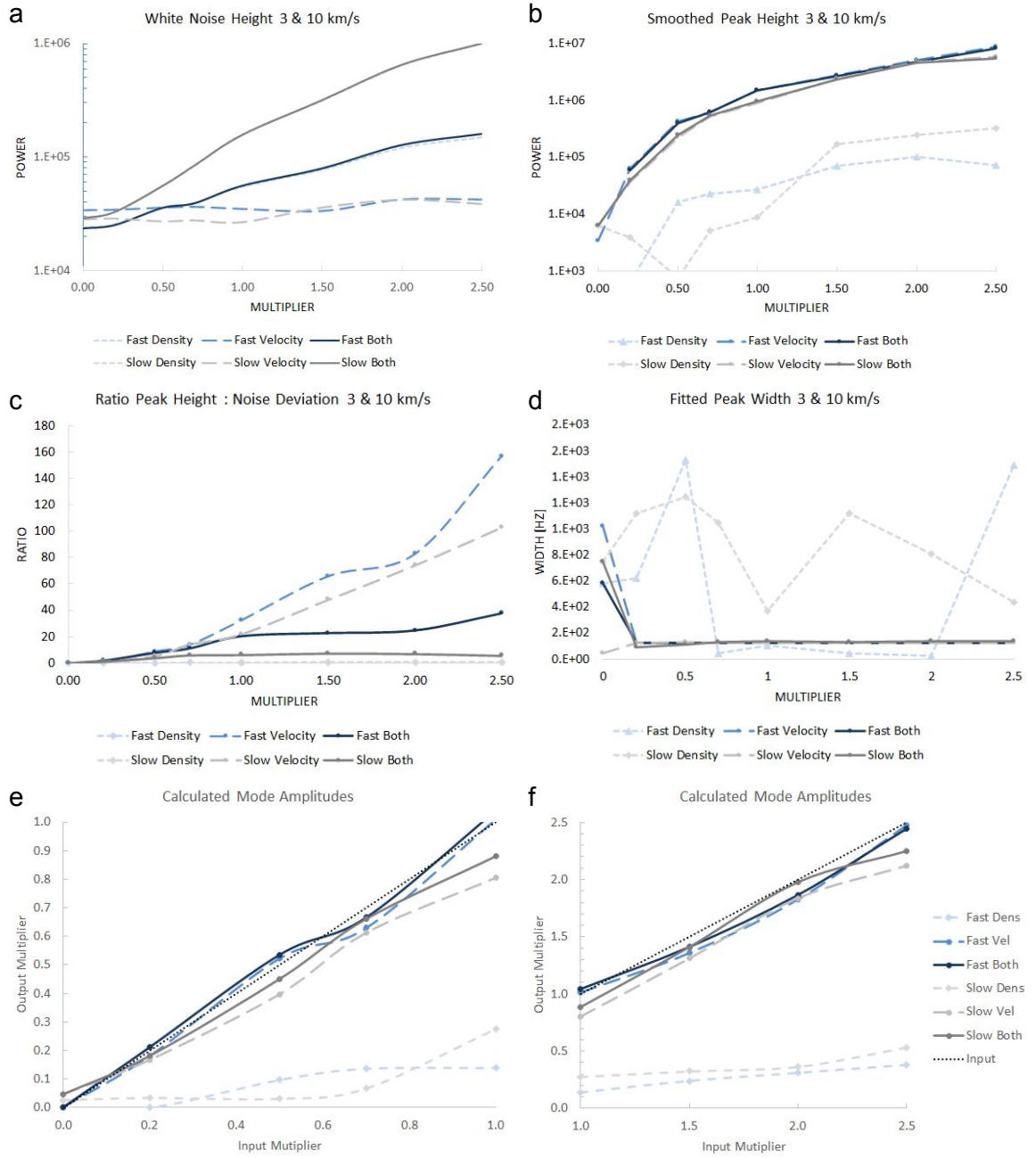


Figure 4.4: The impact of mode amplitude (measured as a multiple of the standard deviation) is shown on key spectrum and mode peak metrics. The results are the average of test data using shot 29380 channel 10,11 and 18. Each chart compares a fast (10 km/s) case in blue and a slow (3 km/s) in grey. The results for a mode in the density signal that is the input to the velocimetry are shown dotted. The dashed line shows the results for a mode in the velocity signal that is the output of the velocimetry. The solid line is for a mode imposed with the same multiplier in both signals.

frequency set at 50 kHz.

From the peak height plot it is clear that even a density time series that is primarily composed of the imposed mode produces a smaller response in the velocity spectrum than a small mode in the velocity time series. The power in the peak of a mode imposed on the velocity time series only compared to a mode in both input and velocity signals is so similar as to imply the density mode makes no additive contribution.

The height of the flat shoulder increases steadily as the input mode amplitude grows in all cases. Without additional input (density) signal to the velocimetry (ie when the mode is in the velocity time series only) the noise does not vary with mode amplitude. The noise height of the cases with a mode in both signals matches that of the signals with input mode only.

Studying the peaks next, we first compare the peak heights to the noise variance as a measure of the contrast of the peaks from an imposed mode. The ratio for input-mode-only signals is extremely low given the small peak height even at large mode amplitudes. Often below unity, the peak at 10 kHz in these spectra is indistinguishable from the variance of the noise floor. The fast and slow velocity cases then follow the same pattern but with different amplitudes as a result of the additional noise in the mixed mode cases. From the graph we can say that when the imposed mode multiplier is above 0.5 times the standard deviation of the velocity time series it is added to, the peak it creates is clearly distinct from the noise floor. The second analysis of the peaks seeks to quantify their shape. This is done using two low pass filters - a low cut-off one (50 kHz) to identify the peak positions and a higher cut-off (150 kHz) to find the troughs either side of that peak as a measure of its domain. These numbers then form the initial guesses for an optimised Gaussian curve fit to the raw spectrum. Where the filter fails, the formula for full width at half maximum is used instead. Measuring the peaks in this way we can see that the (single frequency) imposed modes that have high contrast – have a mode in the velocity time series – are extremely narrow. Note that the frequency resolution is approximately 100 Hz which is approximately the calculated width of the peaks.

Finally we attempt to quantify the transfer of the mode through the velocimetry routine. Understanding that the peaks are extremely narrow we can approximate the power as in a single frequency bin. We therefore use Parseval's theorem to find the amplitude required to create the measured peak using the equation

$$A^2 = \frac{P \cdot T}{\sum |\sin(2\pi f_m t_i)|^2} \quad (4.1)$$

Where power P is the height of the peak the sum is over each timestep of the series that was transformed, the total length T of which (in seconds) is the duration. We can expect that there should be some slight discrepancy caused by our assumption of a single frequency when some broadening of the peak is likely. Studying our signals this way shows very good

agreement between the applied and measured mode amplitudes until the mode dominates the rest of the signal (amplitude multiplier > 1) in the cases with a mode in velocity time series. Some of the mode power is unaccounted for (likely spread) above this amplitude. Again, there is similarity between the velocity-only and mixed mode cases at both speeds and all amplitudes (the faster cases are slightly nearer the line of matching input to output amplitude.) Shown in figure 4.4 f, The cases with a mode imposed in the input signal alone produce velocity spectra with peaks that correspond to around 0.2 and never more than 0.5 of the deviation of the velocity time series, even when the multiplier is as high as 2.5 of the density deviation.

Taken together these results suggest that even an imposed mode with a frequency below the nominal Nyquist that dominates the input (BES) signal to the velocimetry is insufficiently powerful or fast changing to strongly influence the velocity time series. Here, strong means sufficient to produce a high contrast peak in the velocity spectrum. This is likely because the velocity is calculated on the fluctuating components of the input (via cross-correlation); sampled at 2 MHz, well above the mode frequency.

Figure 4.5 shows the spectra for one test signal with a fast velocity (10 km/s.) The spectra of a mode only in the input signal never finds the tallest peak at 10 kHz, where the mode was imposed. By contrast with a mode in the velocity signal every amplitude above 0.2 times the standard deviation of a fast carrier case and any amplitude for a slow case has a tallest peak at 10 kHz. The same is true with mode in both signals except the amplitude must be above 0.2 for both speeds. There is potential evidence of an upshift in the frequency with a peak at 11 kHz at high amplitudes not in the input spectrogram, though this feature is not universally reproduced.

The other trends identified above are evident in these plots: the flat region power is raised in the presence of a mode in the input signal and a mode in the output velocity gives peaks that are much more prominent than with input modes alone (including at the same multiplier.) Unlike the averaged plots in figure 4.4, these clearly indicate the spectra with a mode in velocity time series only measure higher peaks. Likely because the spectra with modes in both signals suffer from increased noise variation affecting the peak base. If the combined effect of the two modes were at least additive then the result should be peaks roughly 10% higher than without any input mode. It is also evident here that the extreme sharpness of the peaks causes the filter to smooth the signal below zero.

<i>Shot</i>	<i>Freq [kHz]</i>	<i>Max</i> <i>[km²/s²/Hz]</i>	<i>Base</i> <i>[km²/s²/Hz]</i>	<i>Width [Hz]</i>	<i>Multiplier</i>	<i>Contrast</i> <i>Ratio</i>
30176	9	8 260 000	890 000	150	2.87	8.69
26885	19	4 370 000	710 000	1505	2.09	0.54

Table 4.1: Measurements of real velocity spectra peaks resulting from cases with powerful input modes.

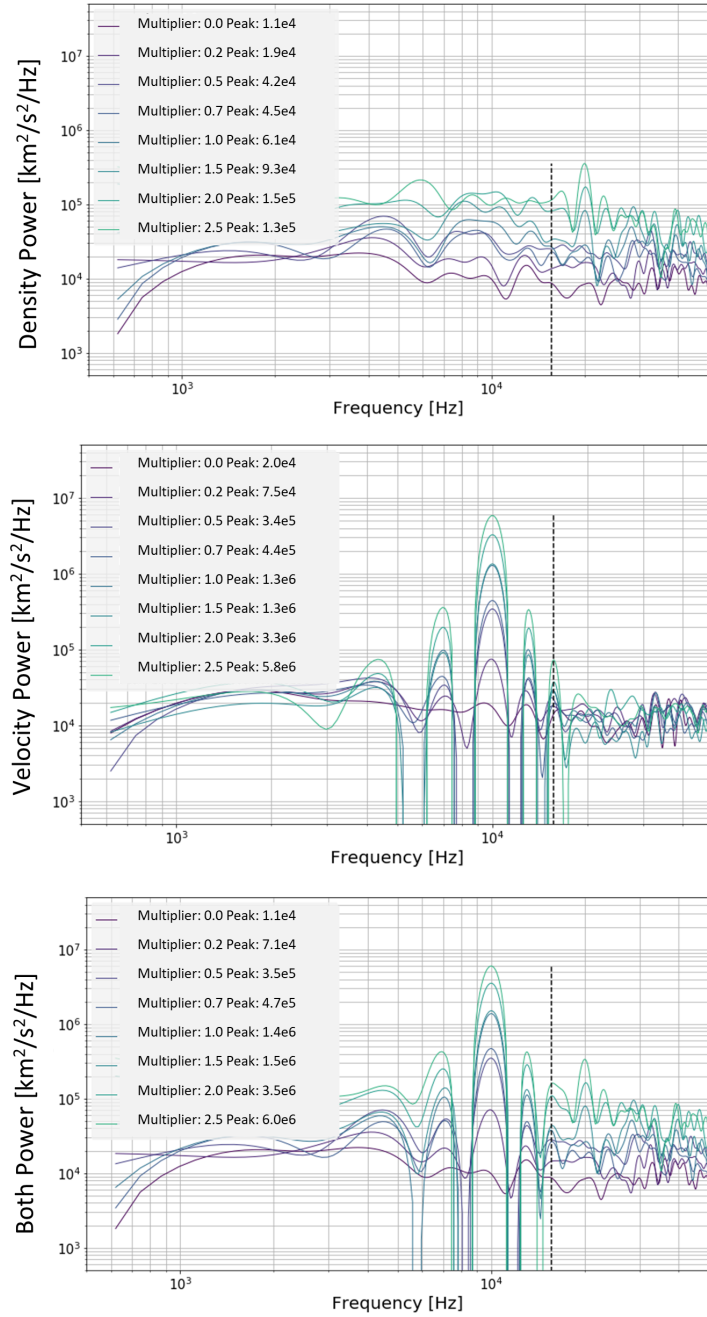


Figure 4.5: The spectra for the signals produced with an imposed mode using just the case with input data from shot 29380 channel 18 and the 10 km/s imposed velocity are shown with all tested multipliers for mode amplitude from 0 to 2.5. In turn they show the effect of a mode in the input data only, output data only and in both.

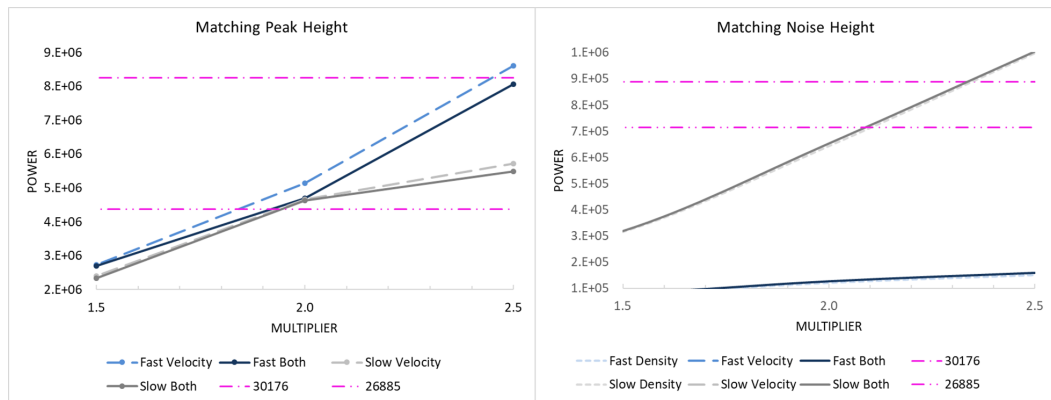


Figure 4.6: Two plots compare real detected peaks to the surrogate data with imposed modes. The real values are marked with horizontal lines. The data are compared for mode peak amplitude and average flat region power.

The last analysis of an imposed mode compares the work done in test data to real data. Two examples of shots with both a mode in the density and velocity time series were found since these produce the highest amplitude peaks. A peak from each was measured according to the method described above. Each example was treated differently because they were chosen to represent an example of a wide and narrow peak from real data. The wide peak was in shot 26885 at a higher frequency and so could use the optimised fit method, though the base was found by fitting rather than averaging the flat region since the peak frequency is above the nominal Nyquist frequency. The narrow peak was in shot 30176 at a frequency below the nominal Nyquist frequency and so conversely could use the shoulder measurement but not the optimised fit - using instead the calculated full width at half maximum. The data are presented in table 4.1.

Figure 4.6 shows the real measured data superimposed on the test data plots shown previously. It is immediately striking that the measured peaks only intersect the trial data at very high mode amplitudes (well above the standard deviation of the signals.) It is also clearly shown that the peak heights exceed those produced by the input signals alone at any amplitude. If we were to have measured both signals using a fitting routine the peaks would be even taller. There is potentially diagnostic value in the 30176 peak being uniquely comparable to the results for a fast velocity flow. Both real examples' average noise amplitudes match our data for a slow signal but our test data were selected to have the most broadband signals possible where the measured data come from real shots with more complex BES spectra.

We conclude by reviewing the questions posed at the start of this section. The effect of a mode in a density (input) signal is primarily to increase the height of the flat spectrum region. At no mode amplitude, including where the mode dominates the signal, is a peak highly contrasted above the noise floor at the imposed mode frequency. A mode in the output velocity time series produces tall peaks in the spectrum that are clearly distinct

above a mode amplitude of 0.5 times the standard deviation of the velocity time series. The familiar pattern of the velocity spectrum does not otherwise change. Taken together these imply that a mode in the input signal alone is insufficient to reproduce the peaks seen experimentally. After the velocimetry routine the power at the mode frequency in the input signal is spread with a weakly monotonic relationship to the input mode amplitude. The velocity peaks stay narrow and match the input mode across velocities and amplitudes.

4.3 High Frequency Burst Modes

The second part of this work investigated the effect of high frequency (above 30 kHz) bursts. These are common in spherical tokamaks – in particular, the ‘fishbone’ instability.¹²⁵ They have been identified routinely as an impediment to velocimetry for their ability to distort the correlation function of data they affect. A high frequency pattern obscures the true position of the peak of the correlation function. This is the reason test data and the preliminary BES work all rely on first seeking out broadband regions of data in spectrograms. In this section we seek to understand the effect of such bursts on our measurements over long time series, quantify real bursts and so assess the implications of our adapted approach to CCTDE for discovering zonal flow.

These more complicated frequency patterns are short lived, across multiple frequencies and recurring. Typically, research using BES has been done by isolating the data between such bursts. Their prevalence in spherical tokamaks, though, has meant a dearth of continuous shot data available for study. Turbulence studies can be done with snapshots of time series but velocimetry investigating flows requires larger amounts of data. Some attempts have been made to concatenate useful segments of data in the past, though these make a generous assumption about the similarity of parameters and flows during and between shots. However, the approach taken in my version of velocimetry – with an emphasis on short measurements closely spaced in time – may be able to preserve much of the broadband signal without being affected by the ‘bursting’ sections.

In order to test the response to bursts, the input to the velocimetry code is again adapted; this time to add short high frequency signals to the delayed stochastic signals. This is done simultaneously i.e. the bursts are not delayed in each channel with an imposed velocity. In this way different patterns of bursts can be studied. Each is compared to the same signals without bursting modes and, as previously, we make note of the effects on velocimetry and velocity spectra.

Count	Interval [s]	Err [s]	Duration [s]	Err [s]	Range [kHz]	Err [kHz]
9	0.0051	0.001	0.001	0.00005	56	8

Table 4.2: Measurements of real bursting modes from spectrograms of BES data from 9 shot numbers - 7 at high frequencies, two at low frequencies. Recorded are the time between bursts, length of burst and frequency range of the bursts. Errors are the standard error of the mean

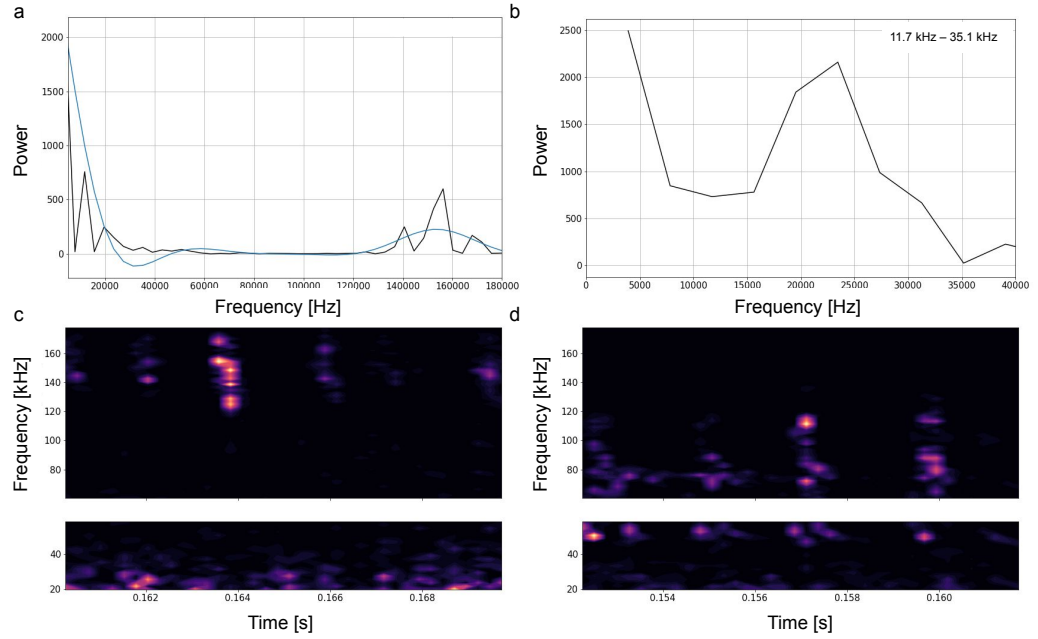


Figure 4.7: Two spectra show real bursts at high (a - shot 30449) and low (b - shot 29378) frequencies in BES data. Also shown in (a) is the smoothing method used to identify the frequency range of bursts with the high and low frequencies found in the legend. Below (c,d) are spectrograms of bursting patterns in BES signals from shots 30449 and 27283.

Frequency	Count	Range [kHz]	Err [kHz]	St Dev [V]	Amp	Multiplier	Err
High	30	21	3	0.6674	0.1078	0.2239	0.01
Low	6	25	1	0.0809	0.0275	0.4023	0.09

Table 4.3: Measurements of real bursting modes from spectra of BES data from 9 shot numbers - 7 at high frequencies, two at low frequencies - at multiple times. Spectra are found using 2^9 timesteps in every case. Recorded are the bandwidth of the bursts, standard deviation of the BES data and the multiplier calculated necessary to produce the amplitude of spectrum peak observed. Errors are the standard error of the mean.

This scenario test starts with measuring the bursts seen in real shots. There are a few qualitative types, some cascading patterns and some tall, repeating ‘fishbone’ type as in figure 4.7. These have similar characteristics to each other. There are also bursts at low frequencies. First by looking at the spectrograms of 9 shots we can establish the average duration and separation of bursts is 0.001 s and 0.005 s respectively. When the spectra of the bursts produced with signals cropped to the same length as the average burst duration as set out in table 4.2 are measured we use a smoothing method shown in figure 4.7 to identify the frequency range of high and low frequency bursts. By analysing these bursts - using the calculation of power and mode amplitude set out in the previous scenario work at equation 4.1 – we can estimate the multiplier of signal standard deviation needed to make these bursts as 0.4 for low and 0.2 for high frequencies as in table 4.3. We note that in reality the spreading of power implies a slightly higher multiplier.

The test data for evaluating bursts uses the characterisation of bursts and the burst

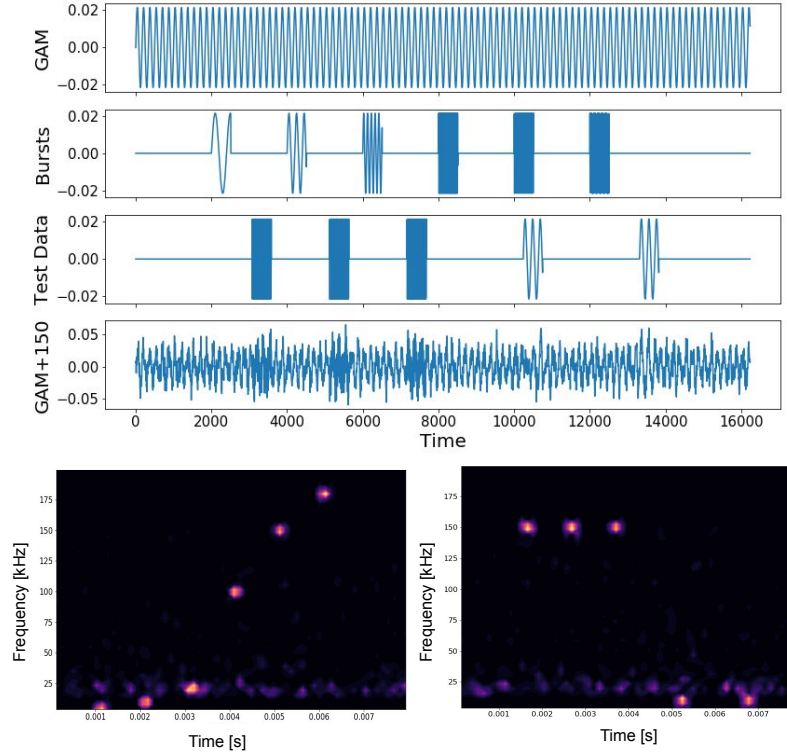


Figure 4.8: The signal patterns used to test the impact of data with high frequency bursts. Underneath are spectrograms of the stochastic data with each of ‘Bursts’ and ‘Test Data’ patterns in turn to compare to the real examples. Bursts are added to the signal from 29380 channel 10 these cases.

duration in particular. Shown in figure 4.8 are various patterns used to evaluate the impact of bursting modes at different frequencies on velocimetry and zonal flow detection. Shown first are the time series of a purely sinusoidal mode, a range of frequencies, a repeated high and low pattern and a fully developed stochastic input signal with the sinusoid and repeating pattern imposed. This last is the signal used in the testing described in this chapter. In particular we use the spectrogram in figure 4.8 with a repeating pattern of high (150 kHz) and low (10 kHz) bursts at varying amplitude superimposed on a signal with a constant sinusoidal mode at a GAM-like frequency of 20 kHz. These are always applied to the input (fluctuating density) signals to the velocimetry algorithm.

These signals - a combination of BES series with bursts and a GAM-like frequency mode added to the resulting velocity time series are again tested across four surrogate inputs, slow and fast imposed velocities and a range of mode amplitudes. In this test we are particularly interested in disruption to the velocity measurement. The velocimetry tests shown in figure 4.9 include a count of negative velocities calculated, the ratio of poor to good measurements in the time series (as defined in 3.3) and the ratio of average measured velocity to imposed velocity. All of these metrics increase monotonically with the burst mode amplitude except for the slow case measured versus imposed velocity ratio which stays constant. The percentage of bad measurements rises from 4 % to 7 % in the slow case and 12 % to 19 % in

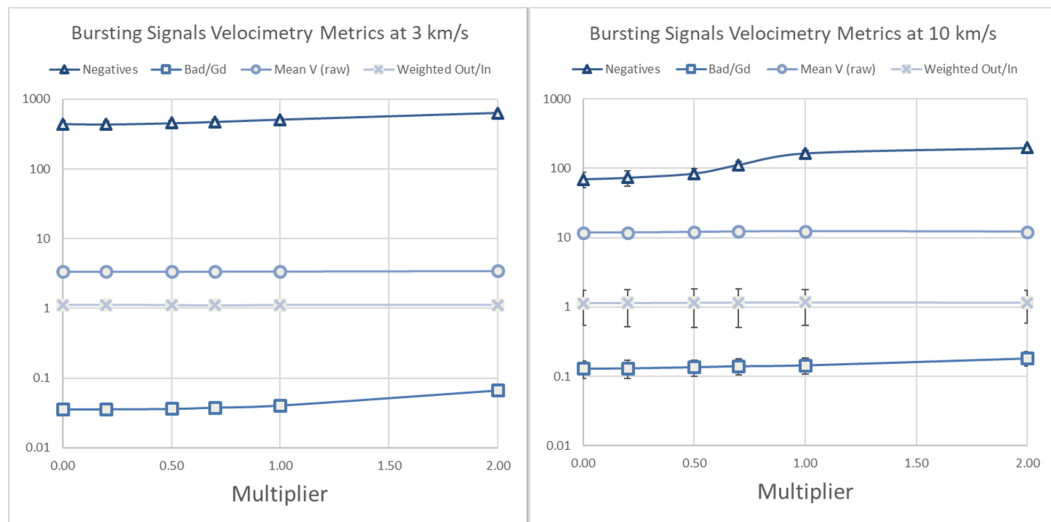


Figure 4.9: A comparison of slow and fast cases of bursting surrogate data on the velocity measurements. The data were produced using shots 30449 channel 22 and 29380 channels 10, 11 and 18. Error bars show the standard error of the mean, plotted for all cases but typically smaller than the marker.

the fast. The ratio of measured to imposed velocity increases from 1.14 to 1.17 (peaking with mode amplitude multiplier of one times the standard deviation of the input signal) in the fast case and is always 1.12 in the slow case. At extreme burst mode amplitudes the accuracy of individual measurements seems to be compromised around the bursting times (as expected) but otherwise the overall velocity measurement remains good.

To see these effects on velocimetry, figure 4.10 shows graphs at three amplitudes for one of the test signals. They show the difference between velocity measured with and without the bursts in the input signal as well as the correlation coefficient measured and amplitude of residuals to the fit. This is to show how the technique is affected in the time series, by the weighting of the velocity average and by the scatter of the plots used in the calculation respectively. It is evident that the magnitude of the velocity excursion grows with the amplitude of the modes. The high frequency bursts have a bigger excursion than low frequency at faster imposed velocities, whereas they are comparable for low frequency bursts. The most powerful bursts (more than the standard deviation of the density signal) are the only time the low frequency bursts match the high frequency in the magnitude of velocity excursion. In the presence of a slow imposed velocity, the deviation of the velocimetry is more than the fast case for higher amplitude bursts too. The affected times are always narrowly constrained to those where the bursts take place with a slightly longer period for bigger mode amplitudes (though this may be an artefact of the smoothed signal being shown.)

Looking at the data on the goodness of fits that produce these measurements we can see that bursts with the fast imposed velocity produce worse fits than slow. With small burst amplitudes there is no apparent change in the fitting parameters. Only the slow imposed velocity appears to suffer worse fitting in the presence of low frequency bursts than high. The

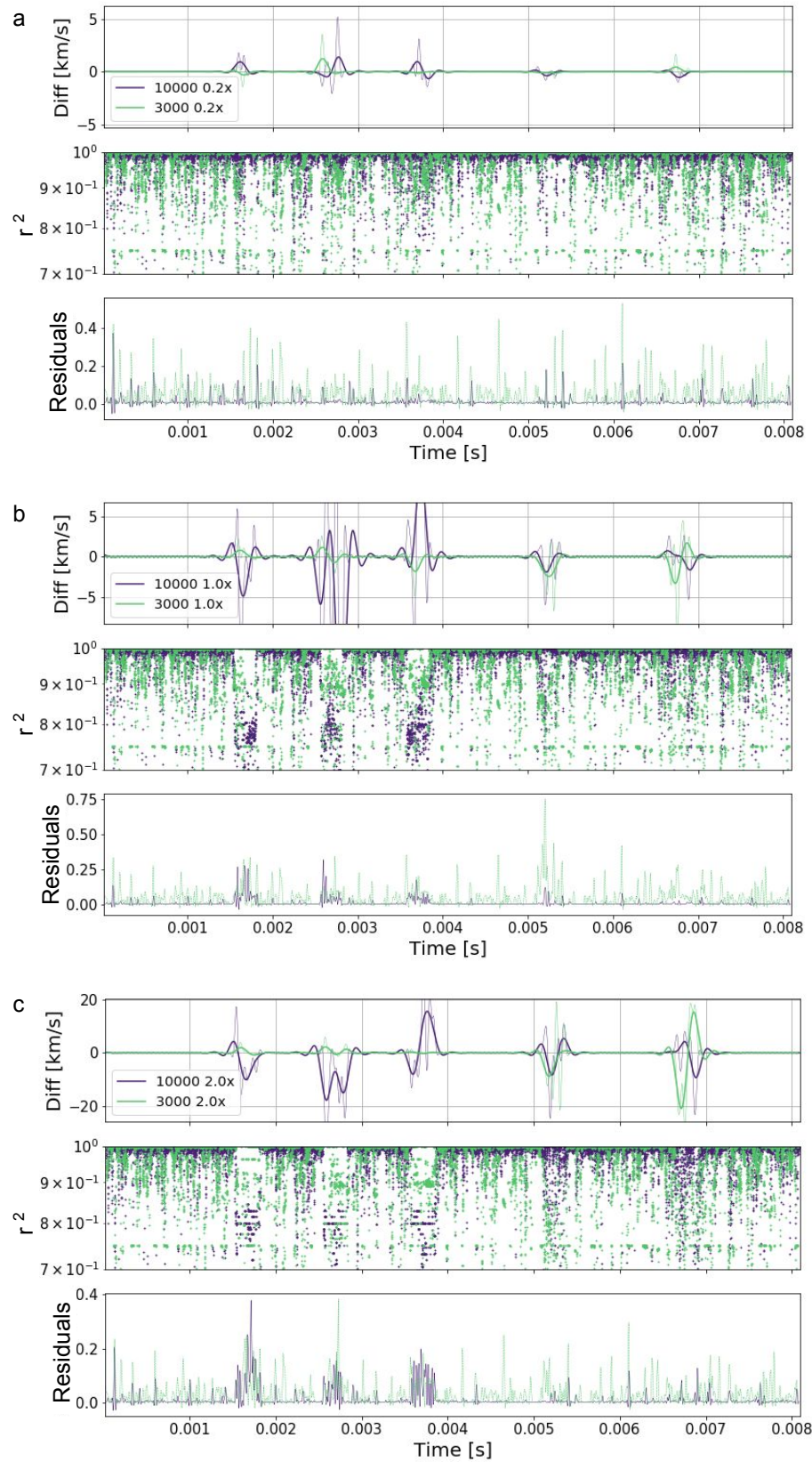


Figure 4.10: Three graphs show the effect on velocity measurements of increasing bursting mode amplitude multiplier (0.2 times the deviation in (a), 1.0 in (b) and 2.0 in (c)). The first plot in each case is the difference between the measurement using the broadband signal and the one with imposed bursts, smoothed. In each plot the slow (3 km/s) and fast (10 km/s) imposed velocity cases are compared. Also shown are the average correlation coefficients of each velocity measurements and the residuals of the fits used to calculate velocity.

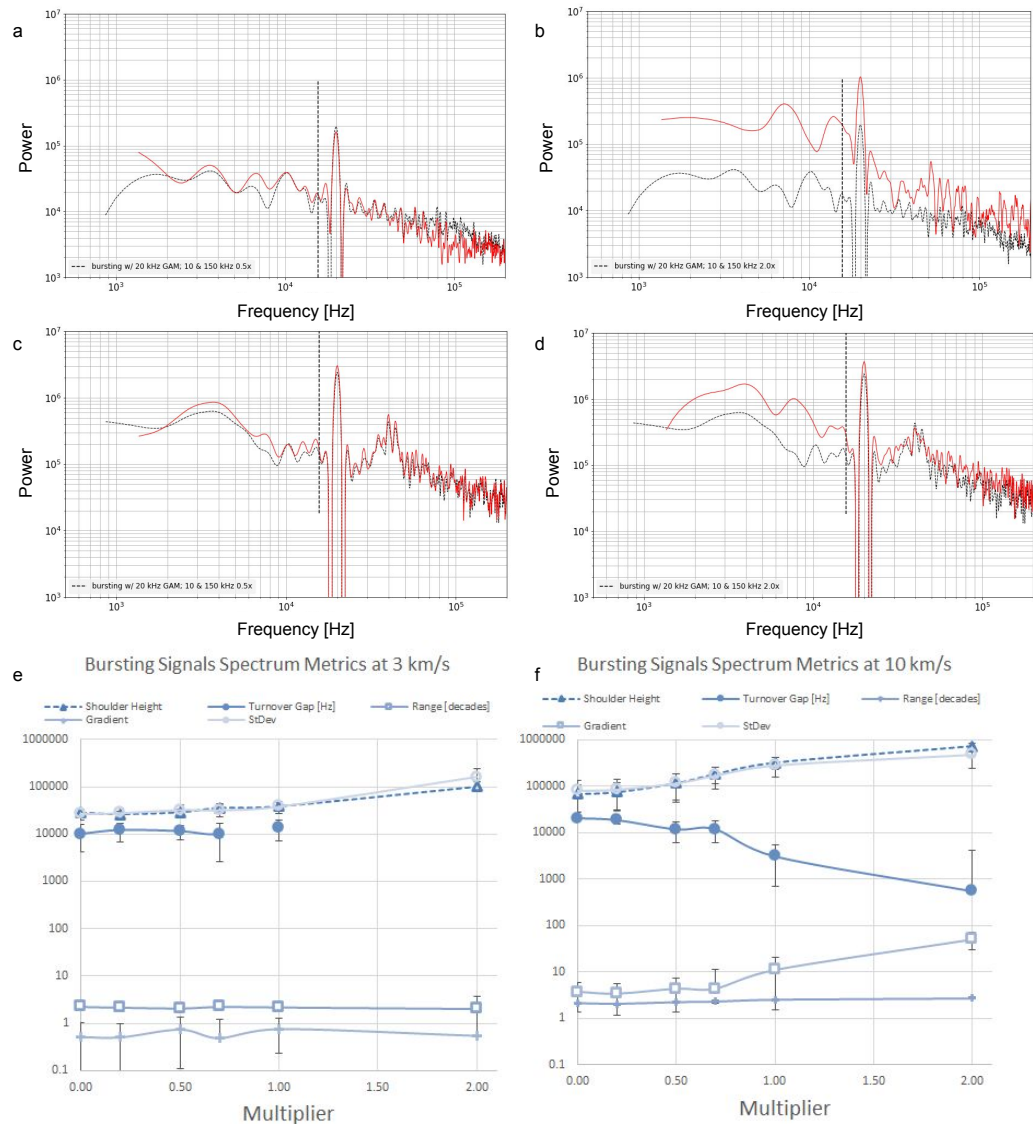


Figure 4.11: Velocity spectra are shown with a broadband case in black and the bursting signal in red, each with a 20 kHz mode added to the velocity time series. All use input data from shot 30449 channel 22. (a,b) are for a slow velocity with fast in (c,d); low mode amplitude is on the left (a,c) and high amplitude on the right in (b,d). (e,f) underneath are plots of the spectrum metrics using multiple input signals. Error bars show the standard error of the mean.

residuals are always higher for the slow velocity measurements. The residuals are increased for high velocity measurements in the presence of high frequency bursts. We therefore have a clear picture that, in the presence of the bursts, the velocity measurement is indeed disrupted and that this results in a poor fit seen either in low correlation coefficient or high residuals. That fact allows us to exclude the affected data when finding an average velocity over a time series. The velocimetry responds quickly so that the remaining data points are unaffected. It would appear that higher frequency bursts have a bigger effect on the velocimetry than low.

Turning to the impacts of these distortions on the spectra of our measurements we note

that this time the GAM-like mode on the velocity time series was imposed above the nominal Nyquist frequency and so the spectral tests in their original form can be used. The plots in figure 4.11 are examples from the same four input signals as figure 4.10 and compare a slow and fast imposed velocity. The only consistent change across cases and imposed velocities is in the flat region's power and its standard deviation. These increase monotonically with mode amplitude. The ratio between the two decreases from 1.2 to 0.7 in the fast case with amplitude and varies non-monotonically between 0.9 and 1.5 in the slow case. We note that in the fast case, though, the standard deviation of the noise measures the gradient of the shoulder associated with higher flow velocities (as measured in the ratio between standard deviation of the noise and the gradient.) This is not true of the slow case until the highest mode amplitudes, well above the signal's standard deviation.

The other metrics that the spectra are measured on – 'flat' region gradient, falling region power range and gap between transition and nominal Nyquist – all vary monotonically in the fast velocity case. They increase with mode amplitude except the turnover gap which reduces from 20 kHz towards zero. With a slow velocity, the transition gap stays roughly constant at around 10 kHz (negative at the biggest amplitude.) The gradient is constant at around 0.5, far below the 3.5 – 11.0 range of the fast velocity cases.

Again, comparing the spectra for a specific test case as in figure 4.11 shows these trends. We can also see the imposed GAM mode (multiplier always 0.5 times the velocity time series' standard deviation) is clear in the spectrum. High amplitude signals show a separation between the two spectra but otherwise the null pattern is unchanged. For low amplitude bursting signals, the disruption to the velocity measurements does not affect the pattern and contrast of velocity spectra we would use to search for zonal flow at finite frequencies.

This set of tests sought to understand the effects of bursts on our implementation of velocimetry. We have confirmed the expectation that a time-localised disruption of the ability to accurately measure flow velocity is caused by a short, high frequency mode. However, unlike other measurements, our code has enough good data around the bursts to make an accurate overall assessment of the imposed velocity. Because only a small portion of the data is affected the velocity spectrum with and without bursts looks very similar at low and medium frequencies. The noise floor is raised in the presence of powerful modes. The imposed GAM-like mode is not diminished and still has the contrast established in the previous scenario. Quantifying real spectra, we see that low frequency bursts are likely to affect slow plasmas only and are in a range that is filtered out anyway. High frequency modes are typically of low amplitude (a 0.2 multiplier) compared to the range needed to establish an effect here (above 0.7.) This implies that for most high frequency bursts we can proceed on the assumption that their impact will not impede our ability to detect zonal flow peaks.

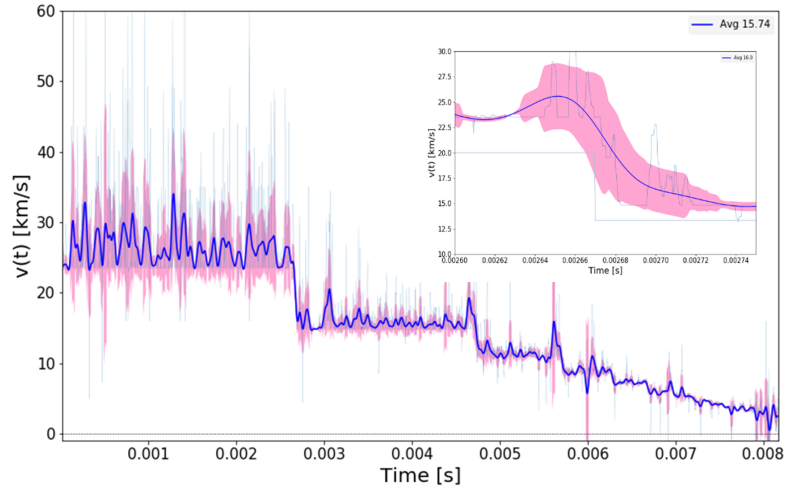


Figure 4.12: The velocity time series is plotted for an imposed velocity that varies in discrete steps over the duration of the input signal. The thick solid line is the smoothed time series, the raw measure is shown in a thin line. The velocity varies from 2 to 20 km/s for input data from shot 29380. The shaded uncertainty region is a moving standard deviation of the signal. An instantaneous change in imposed velocity is shown inset.

4.4 Time Varying Imposed Velocity

The final test of the code, and last investigation of this chapter, is to assess the accuracy of a maximally realistic application of the code. We have already as standard a detector-like configuration of the code, a turbulence-like input signal and noise that recreates the effects of channel separation. Previous tests have used a single slow or fast input velocity. Performance in those circumstances is well understood. However, since we are investigating flow physics, the code is adapted once more so that the input velocity evolves in time. As before, we will verify the effect of time-evolving velocity in the input signal on velocity and spectral outputs. Then, taking this as the most ‘complete’ case in terms of realistic desirable phenomena, we will finally quantify the accuracy of the velocimetry code across the range of measurable velocities.

To modify the delay we implement a quarter-wavelength cosine function that varies the velocity from fast to slow velocity bounds. The delay across channels is therefore monotonically increasing for the duration of the test signals to avoid overlapping data. Where the previous tests have used realistic single velocities, we now implement realistic accelerations using the theory in 3.2.1 across the full useful range of the velocimetry. That range, defined by the channel separation, time resolution and size of the correlation functions, is 1 875 m/s to 40 000 m/s. We have been using time series of 16 384 timesteps length; taking the acceleration reported previously over that time interval gives a ‘realistic’ change in velocity over the duration of test signals of up to 8 km/s/s.

Implementing this for a wider range of imposed velocities than previously tested to explore

the limitations for detection by this method reveals key issues in the code's performance. A qualitative evaluation of the velocity time series produced with the full surrogate flow physics reveals two. First, by modifying the variation of the input velocity to integer timestep delays (i.e. sharp jumps) as shown in figure 4.12, we can see the recovery of the measurement. At each step the velocity measurement is distorted. However, a close examination of the biggest step shows recovery of the measurement (measured by the variance of the raw time series) within 160 timesteps and adaptation of the smoothed signal to the new carrier speed in around 40. Given the 2 MHz resolution of the detector this is an extremely quick reaction to changes in the input signal. The full 160 timestep response time corresponds to two correlation bins of 64 steps each where one would start and the other finish at the step change. This once again shows advantages of adapting the method to every-step sampling with very short correlation functions.

Leaving the velocity transitions as a smoothly varying sinusoid allows us to see the changing response of the velocimetry to varying imposed velocity. Looking at the full time series plotted next to the input signal as in figure 4.13 shows the trend toward overestimation at higher velocities. There is also extremely good performance of the measurement up to around 10 km/s with a high degree of overlap between the smoothed line of velocity and the error associated with its variance and the changing input velocity. At high velocities, though, we can see a gap between even the error estimation and the input. This is shown explicitly at the bottom of figure 4.13 with the percentage difference of input and measure plotted for two test cases and two different velocity ranges, with and without noise decorrelating the input signals. Excitingly, these plots show that in the very fast velocity regime, in which the time delay between adjacent channels is less than one time step, our velocimetry implementation is still able to track the pattern of changing velocity. The average overestimate percentage across a full time series for multiple test cases is shown in figure 4.14. These results show that velocity far more than noise (relative signal) correlation is a determining factor for the performance of this algorithm. Even though the overestimation increases with imposed velocity, the input data is still a major determinant of the velocimetry's performance.

We quantify the velocimetry in the presence of a changing flow with the core metrics of measurements in the velocity time series that record multiple undelayed peaks and those that underestimate the velocity as in figure 4.15. This is done for a set of velocity ranges that span the full measurement range of the technique. They are shown in order of increasing lowest velocity. The addition of noise to these signals does not alter the ability to accurately track a changing velocity. The avoidance of undelayed peaks is best achieved away from the extremes of the measurement range and the rate of underestimation monotonically decreases as the velocity increases (reinforcing the expected tendency to overestimate.) The change we are imposing on these signals we know has a quarter period of 0.008 seconds. That equates to a 32 Hz mode which is both well outside of the range we are inspecting for zonal flow and

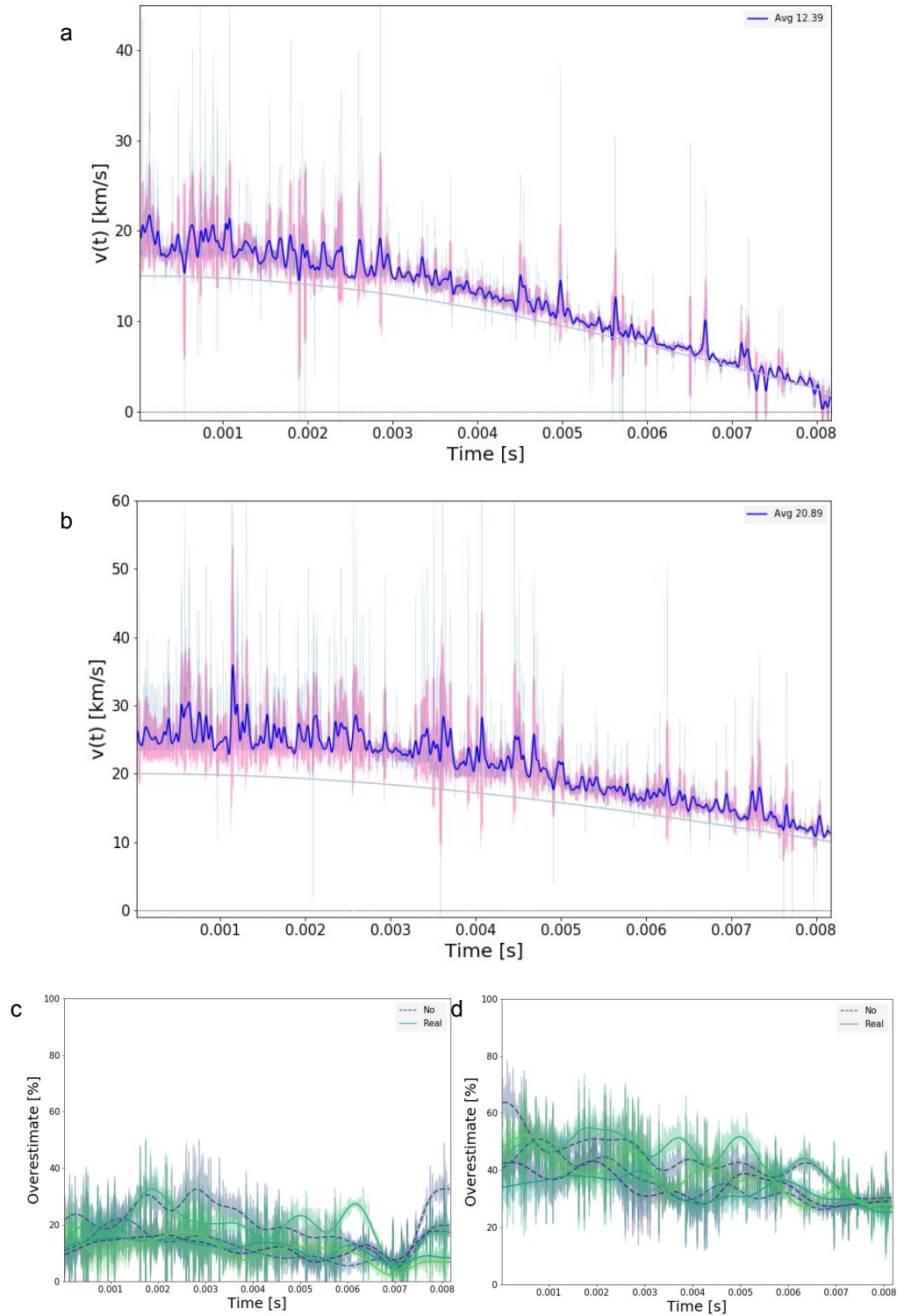


Figure 4.13: (a,b) are two plots of the velocimetry for data using shot 29380 channel 18 and a smoothly sinusoidally varying velocity for a slow and fast range. The uncertainty shown in the shaded region is the moving standard deviation of the raw velocity signal. Underneath (c,d) are two graphs for the same ranges shown above plotting the percentage overestimate of the imposed velocity measured at every time step (smoothed with a moving standard deviation shaded again.) Each graph shows two channels, each with and without the imposed additional noise.

Shot/ Channel	Velocity Range [km/s]	No Noise [%]	Real Noise [%]
29380/11	2 - 15	23.5	22.3
29380/18		16.8	19.6
30449/15		34.9	40.8
30449/22		41.4	47.7
29380/11	10 - 20	34.9	37.7
29380/18		29	28.4
30449/15		51.5	55.6
30449/22		52.5	61.3
29380/11	10 - 30	48.5	48.9
29380/18		41.5	39.8
30449/15		60.7	59.8
30449/22		64.8	62.6

Figure 4.14: Table showing the average overestimation of the velocimetry as a function of imposed velocity. Overestimation is scaled from low in blue to high in red.

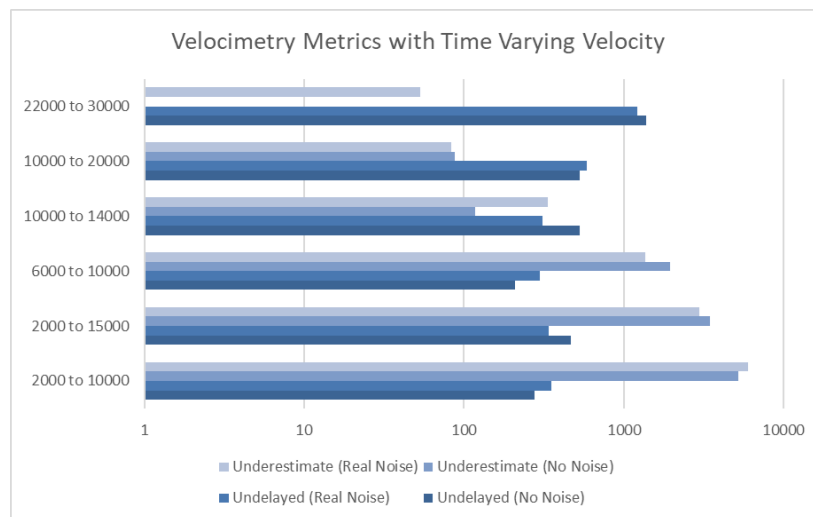


Figure 4.15: The effect of a time-varying imposed velocity on the velocimetry accuracy is compared for two key metrics. Measurements with three or more undelayed peaks and the count of underestimations of the input velocity. Each is compared with and without noise. From bottom to top the slowest imposed velocity (m/s) increases. The number of data points affected is counted.

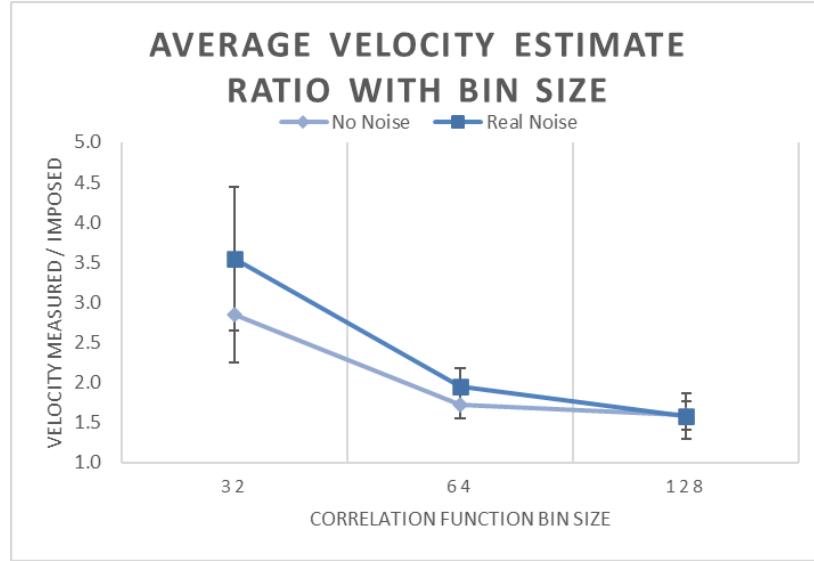


Figure 4.16: Comparison of overestimation of velocimetry with a time varying imposed velocity with different correlation function sizes. Three channels from shot 29380 are used for input data and the standard error of the mean shown by error bars. Cases with and without additional noise are compared in dark and light blue respectively.

less than the frequency resolution of the velocity spectra. We therefore expect no impact on the null spectral pattern. To complete the analysis of our technique design we compared the average overestimate of the technique under a time-varying velocity with the size of the correlation functions in figure 4.16. We know that a size of 128 has near-perfect reliability of measurements (though poor frequency resolution) but can see that our choice of 64 time steps gets close to its level of overall accuracy.

Finally, we can quantify the performance of the velocimetry technique across its measurable range. To make this calculation maximally robust we fit to data from multiple input data with and without added noise across multiple velocity ranges. For each, a weighted average of the measured overestimation at each step of each velocity range is made according to the correlation coefficient associated with that velocity measurement. From that we produce a fit to the average overestimation across the full measurable velocity range. Since each time series is 16 384 time steps long we down-sample to 1 in 16 data points and those data are plotted in figure 4.17. We have preferentially used velocity ranges in the previously identified velocity range of plasma flows. Additionally, it can be seen that below 10 km/s a very close match to imposed velocity is seen where higher velocities overestimate outside error bounds, we therefore compare a linear and quadratic fit of velocimetry overestimation.

The weighted quadratic fit to the data in figure 4.17 shows that, contrary to the previous qualitative, unweighted assumption, the quadratic contribution is extremely small (0.005 in the noisy case). We therefore proceed with a linear fit across the velocity range. The addition of noise slightly steepens the overestimation trend but lines overlap within the error range indicated by previous figures. The gradient of the fit line is 1 : 1.79 with an intercept at 0.019

%. The standard error of fit is small at 0.04 suggesting a strong relationship. This is reflected in the plot of measured gradients and error which shows good consistency across multiple velocity ranges except at the lowest starting velocity where the error remains small but the gradient of overestimation can be much lower than for ranges with higher velocities. This is therefore a usefully predictive relationship when interpreting the absolute measurement of the velocimetry technique we have designed – especially when it reports higher flow velocities. This understanding of the degree of overestimation inherent to the technique is an important correction to combine with others (for example the barber pole effect described in section 2.2) to measuring plasma flows.

Recall that the purpose of this project is to optimise time and so frequency resolution for zonal flow detection. On that basis we have shown that the spectra produced under multiple realistic scenarios have a robust pattern and have a measurable range that overlaps those frequencies at which we expect to find zonal flows. By shortening the correlation functions there is a cost in the accuracy of the velocimetry. However, the performance of that velocimetry algorithm is generally good at low velocities, predictable across its measurement range between 2 and 40 km/s and, with clean turbulent data, capable of excellent measurement of the average flow velocity.

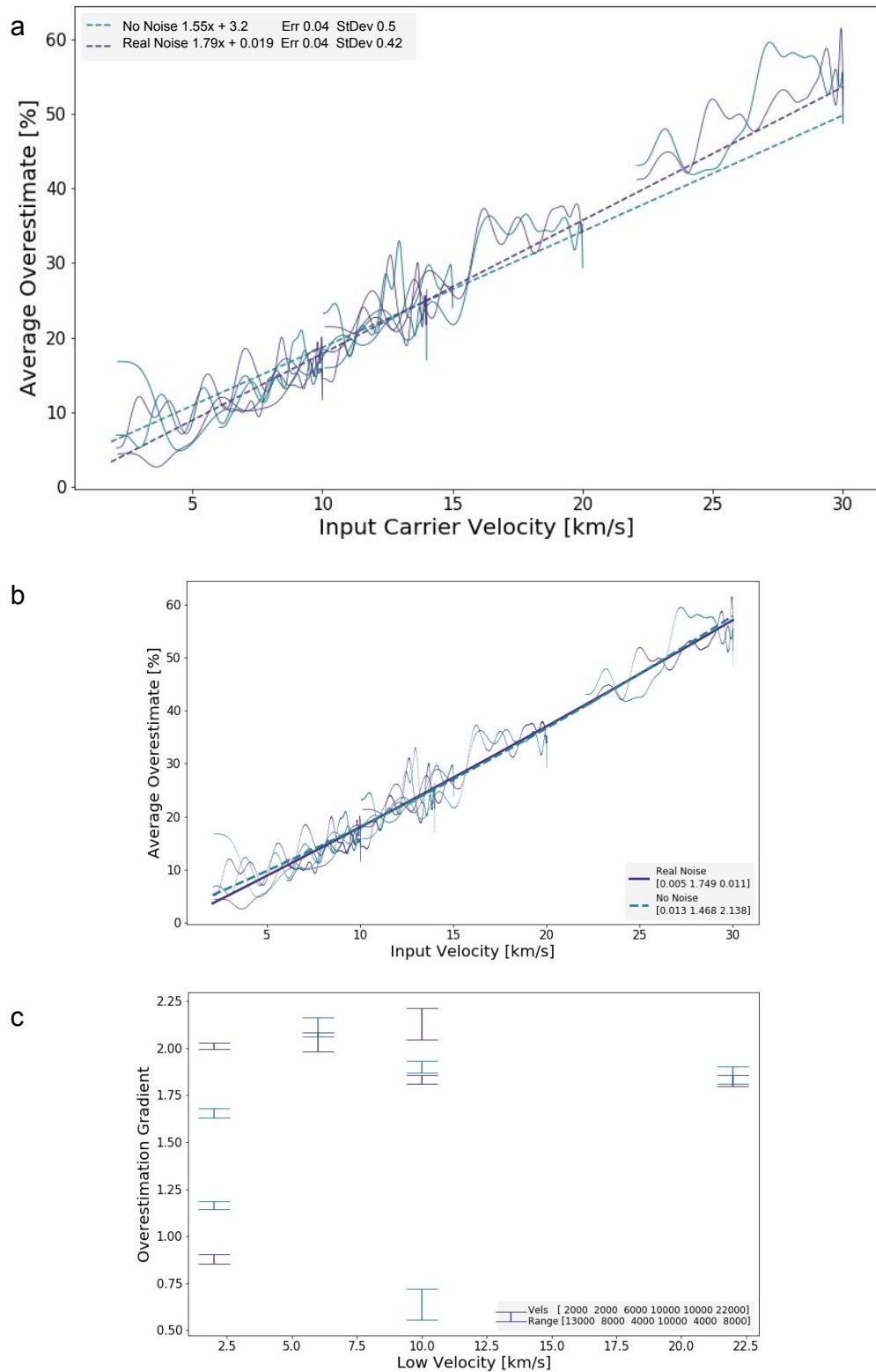


Figure 4.17: The overestimation of velocimetry for multiple ranges of varying input velocity are shown in (a), each averaged over data from inputs from shot 29380 channel 10, 11 and 18. Cases with and without noise are shown in purple and green respectively. Overlaid in a dashed line is a linear fit. The equations of the fit lines are shown along with the standard deviation of the overestimates data and standard error of the fit in the legend. (b) is a comparison to a quadratic fit with fit parameters shown. (c) shows the linear fit gradient data for each velocity range tested (low velocities and range of each test are listed.) Error bars show the average standard error of the fit.

Chapter 5

Velocity Spectra of MAST BES Data

This chapter introduces the results of applying the velocimetry code we have made to data from experiments of the MAST tokamak. This project's intention is to find experimental evidence of zonal flow in MAST data and so a basis for identifying zonal flow. First, we focus on the most reproducible part of zonal flow theory - the frequency of flow changes.

In so doing we will see a tendency for peaks in the medium frequency range (between 3 and 30 kHz) of those spectra to correspond with powerful magnetic modes. This chapter, therefore, also explores the present theoretical understanding of the relationship between zonal flow and detectable magnetic signals.

5.1 Velocity Spectra Classification

The first list of shot numbers to be analysed was sourced in order to capitalise on the advantages of the BES diagnostic for plasma turbulence research. The diagnostic logbook was searched to identify shot numbers that studied the edge region (for zonal flow) but that were part of experiments in which the diagnostic was scanning the full radial profile across adjacent shot numbers.

Time slices of 0.01 seconds from these shots were sampled, including 11 times specifically targeting the L-H transition. A total of 175 time slices from around 80 shots had spectra produced for all 8 columns of the detector. These data were inspected to find common patterns on a log-log plot. The result of that was a taxonomy of four kinds of spectra illustrated in figure 5.1. The first and second are flat and gently sloping low frequency regions respectively; representing just over half of the examples surveyed. These are familiar from the null spectrum cases found with surrogate data in chapter 3.4 as slow and fast purely turbulent flow and demonstrated in figure 5.2.

The third case is flat for some portion of the low frequency region with a marked increase

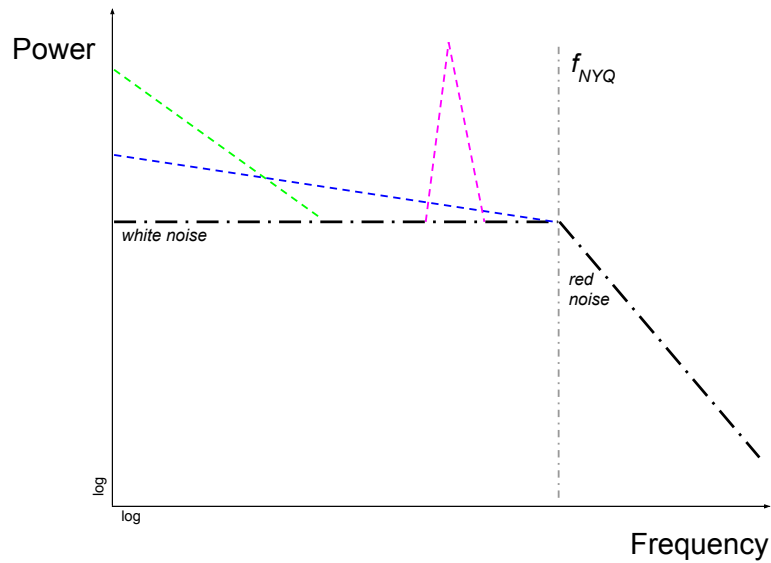


Figure 5.1: An illustration of the four types of spectra seen in velocity studies of MAST BES data. The flat region transitions to falling, but may present on a logarithmic plot as a flat line (black dot-dash), a shallow gradient (blue dash), a flat line with high power at low frequencies (green dash) and, finally, flat with a tall peak at medium frequencies (pink dash).

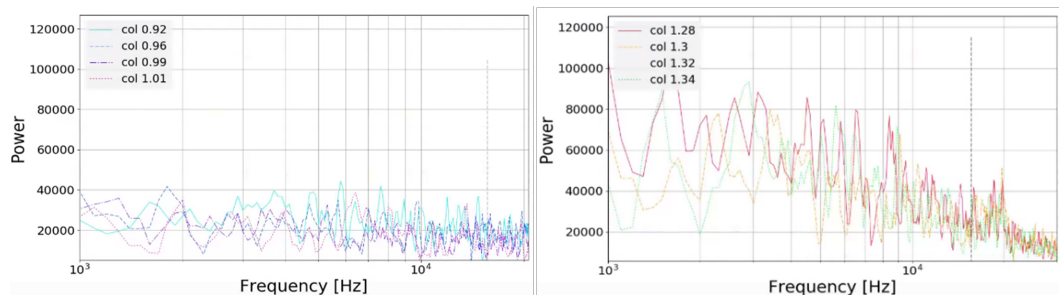


Figure 5.2: Examples of type one and two velocity spectra. From shot 26885, 0.27 to 0.28 seconds, the four outboard columns' spectra (blue/pink) show a flat pattern. From the same shot at time 0.34 to 0.35 seconds, the four inboard columns' spectra (red/green) show a shallow gradient across the 'flat' region.

in height at the lowest frequencies (below 3 kHz.) Around a third of the examples show this pattern of low frequencies with height at least twice as high as the flat noise at the nominal Nyquist frequency and a sharp transition between those noise heights. The fourth case is a generally flat low frequency region with a distinct peak at medium frequencies (between 3 and 30 kHz.) Only a small number of examples (representing 5% of the survey) showed this clear peak pattern.

With the focus on zonal flow, the null patterns are not investigated in depth. Except that, since we have examples of spectra from real data, they can be compared to those produced previously with surrogate data. Recall that the surrogate data is intended to represent cases with a turbulent density field and a common (to all measurement locations) imposed velocity. Figure 5.3 shows three example spectra for each of four scenarios. From surrogate data we

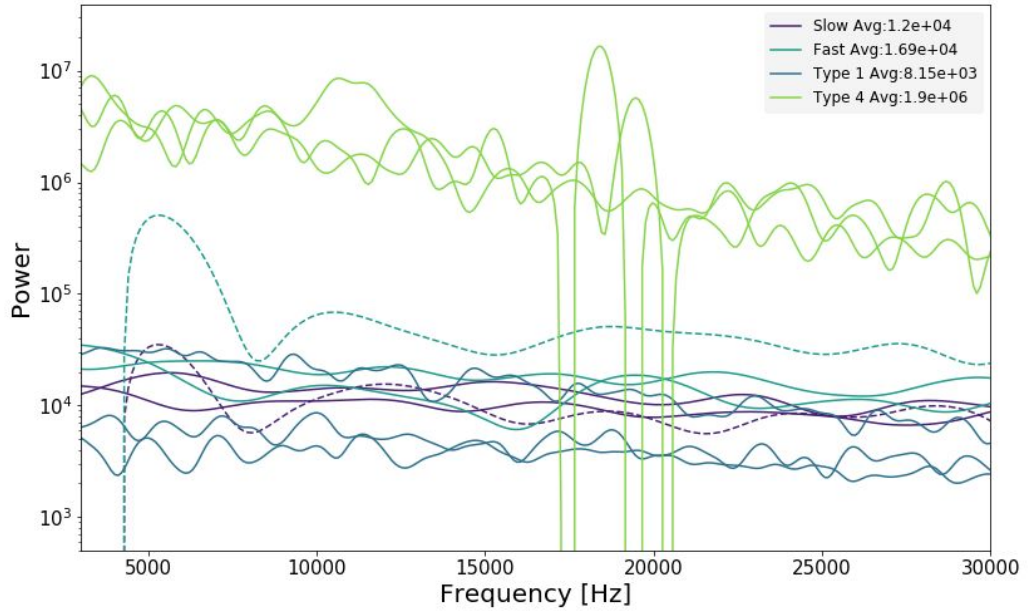


Figure 5.3: A comparison of typical spectra from surrogate and real cases. Type one (flat) spectra and type four (peaked) spectra are chosen from real data. Synthetic cases with slow and fast imposed velocities – including one time varying example in each case – are plotted next to them. Smoothing below zero in the presence of sharp peaks is seen in two of the type 4 cases and at low frequencies for the time varying surrogate examples where the plot shows steep lines.

plot examples of relatively fast and relatively slow carrier velocities – including both fixed and varying carrier velocities. From real data we have plotted examples of the first and fourth patterns of spectra we identified above. All of these spectra use signals of the same length and $0.5 \mu s$ sampling interval.

While the examples with a time evolving imposed velocity show tall peaks at the lowest frequencies, these, the surrogate and type 1 examples all have roughly the same amplitude. Type 2 were not tested. The flat, type 1 real cases are the smallest amplitude spectra - approximately a decade below the fast surrogate cases. However, the type 4 cases with clear peaks are at nearly two orders of magnitude higher amplitudes than the rest. Two have very sharp peaks (as shown by the dips in the smoothed signals), one has a broad peak at medium frequencies. Higher amplitude power spectral density implies more energy in the signal mode. This marks those examples as ones in which more complex flow physics than a simple imposed velocity is driving fluctuation patterns.

5.2 On Zero-Frequency Peaks in Velocimetry Spectra

The third type of spectrum, with pronounced amplitudes at the lowest frequencies, is suggestive of the slow changes of zero-frequency zonal flow (ZFZF). It is understood that this mode of zonal flow is harder to study because of its indiscernibility from mean flows. It is

still possible to find examples consistent with ZFZF flow physics for further study.

However, the high amplitude region spans only a narrow range of frequencies before dropping abruptly. The lowpass smoothing of spectra is such that the plot drops below zero and the spectrum height is recovered, with a first apparent peak at around 5 kHz common. This was seen as an effect with time-varying flow velocity in logarithmic figure 5.3. It has the effect of obscuring interpretation below that frequency. Those spectra with broader domains of high amplitude were replotted as spectrograms in order to understand the pattern of frequencies over time producing that spectrum shape. These showed that the low frequencies do indeed dominate the spectrogram but in irregular low frequency bursts. Plotted next to the velocity time series that produced them as in figure 5.4, these bursts clearly correspond to excursions of the velocity measurement. Not all time series with an excursion produced a type 3 spectrum if the velocity time series excursion was extremely short. That suggests a large number of adjacent velocity measurements at extreme velocities is necessary to amplify low frequencies (rather than one or two anomalous data points.) That, in turn, is consistent with a real physical event interrupting the data series. In all examples studied, those high velocities were measured with consistently low correlation coefficients, undermining our confidence in them. The scatter this implies in the measured delays seen by every channel suggests an advected, coherent feature is not being measured. While we expect the flow velocity to be increased in the presence of poloidal flows, this pattern (short and intermittent) as well as velocity approaching 100 km/s is inconsistent with the expected evolution of zonal flow.

One further low frequency pattern could be identified, albeit in very few spectra. We found very sharp peaks at frequencies typically close to 1 kHz. These features were identified in spectra of velocity near the end of MAST shots. An example is shown in figure 5.5 from the subset of shots with the peaks nearest the edge (numbers 27404, 27370, 27277 and 27274.) At present we lack the resolution to characterise these peaks and corroborating information (especially on axisymmetry) necessary to investigate them as potential ZFZF flow markers. Given the caveats to the available evidence from velocity spectra we conclude that we cannot distinguish 'zero-frequency' zonal flow in this introductory study of spectrum types.

5.3 On Medium-Frequency Peaks in Velocimetry Spectra

Having considered the spectra that make up the majority of surveyed cases, for the remainder of this work we focus on type 4 - those with peaks in the medium frequency range (3 – 30 kHz.) This range matches that of the principal finite frequency zonal flow mode, Geodesic Acoustic Modes (GAMs). The approach is consistent with other experimental investigations of zonal flow measurement that target the characteristic frequency of the flow; anticipated to result in high contrast peaks as in the works described in section 1.4.2.

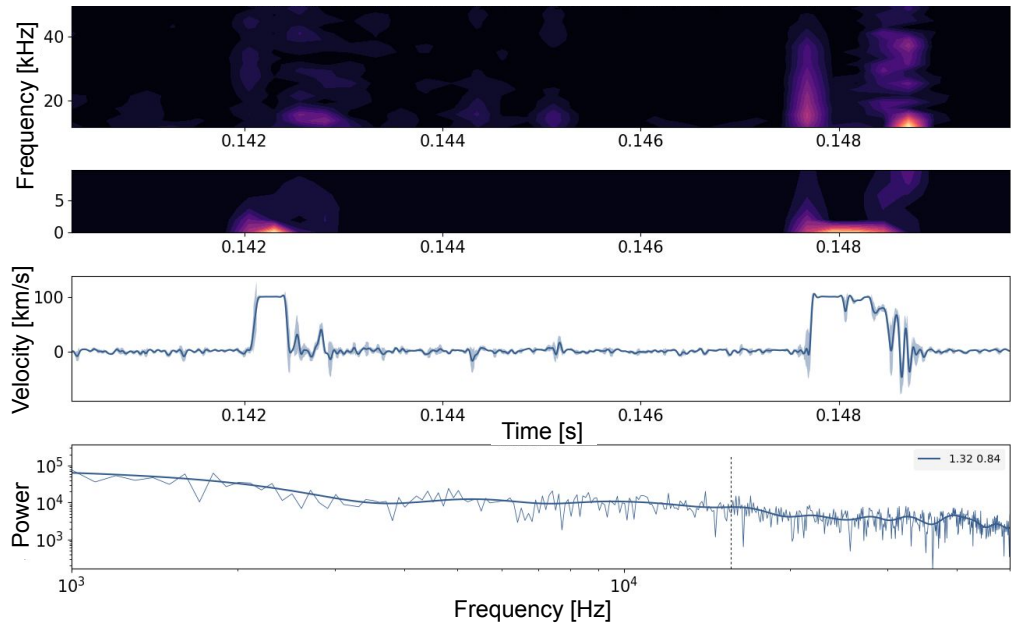


Figure 5.4: Comparison of spectra and a spectrogram for an example of type three spectra with typical velocity. Shot number 29761 times 0.14 s to 0.15 s inboard spectra are plotted. The plot domain is extended to low frequencies. Column two's spectrogram is plotted above its velocity time series. The synchronicity of velocity excursions and powerful low frequencies is clear from the spectrogram.

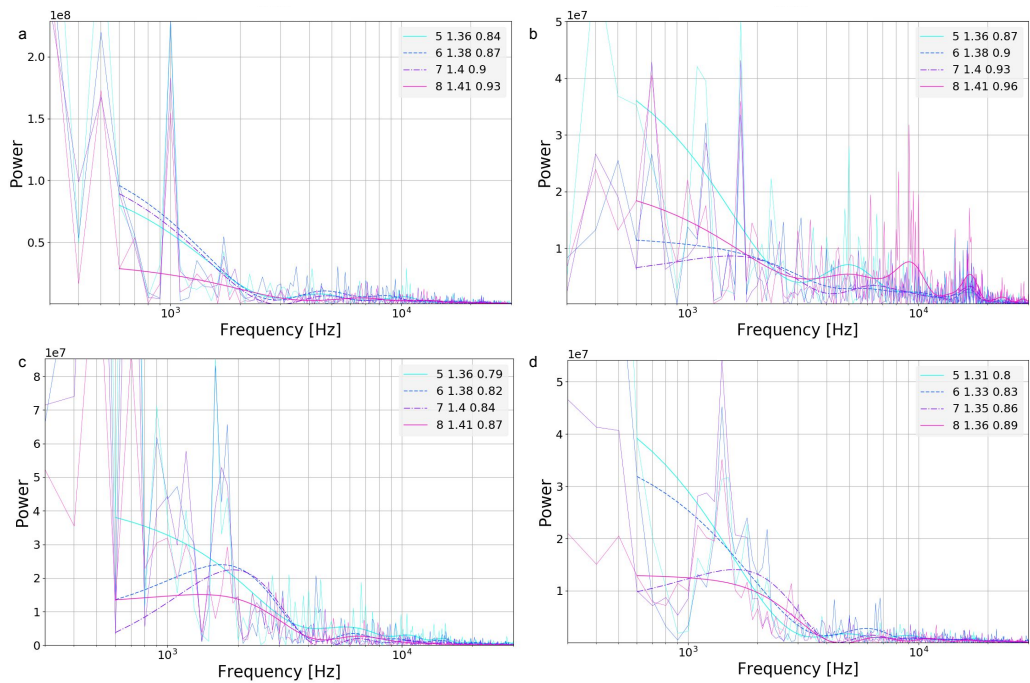


Figure 5.5: Examples of sharp spectral features at extremely low frequencies in our data. Clockwise from top-left are (a) shot numbers 27404 at 0.24165, (b) 27404 at 0.34165, (d) 27370 at 0.1766 and (c) 27277 at 0.1616. Column number, radius and normalised radius are in the legend.

The initial survey of shots revealed a few examples of these kinds of peaks based on a visual inspection from which first observations can be made. To be marked as in the fourth type a spectrum would have to show either a tall peak, peaks in multiple columns' spectra at one frequency or both in the low and medium frequency range. Peaks are found by smoothing the power spectral density with a lowpass filter with cutoff at 50 kHz so that only the highest amplitude or widest low peaks, i.e. the clearest cases, are visible.

In all, 22 time slices studied had such peaks, of which 6 had peaks in all of the columns' spectra implying changes over a very wide radius. None of the 22 were found at the times chosen to target the L-H transition. The intention was to measure the values of plasma performance parameters as well as those associated with GAM theory with and without the presence of these peaks. A crucial diagnostic contributing to the study is the set of Mirnov coils situated around the tokamak.¹²⁶ The signals of Mirnov coils fluctuate with the amplitude of fast magnetic activity of the plasma. Spectrograms of the Mirnov signal from coil 210 - situated at the outboard midplane - were produced for each of these studied times. We expected these to show any potentially disruptive high frequency magnetic activity as investigated in section 4.3. Instead it was clear that those cases we had found on the basis of peaks well above the spectrum noise floor ('high contrast') were almost always accompanied by a corresponding peak in the Mirnov spectrum. All but two of the 22 cases first examined had this feature. Those without were times in shots 26317 and 30449. The former was subsequently discounted as a time too early in that shot for the plasma shape to have been established.

Given the predominance of the magnetic signal at time that produce velocimetry spectra with clear peaks and the strength of evidence afforded by a flow velocity measurement, we persist with this data set. The research question now, without prejudice to whether or not these particular cases are GAMs, becomes 'what is the correct interpretation of the presence of the magnetic mode?' By extension we will advance an understanding of how to report observing GAM-like frequency peaks in velocimetry at the same times as a magnetic signal. This connection is pervasive in our observations but unseen in literature. In particular, it is critical to establish if there is reason to expect a magnetic signal alongside zonal flow. The remainder of this chapter explores the relationship between these cases, zonal flow theory and the small experimental database to answer these.

5.3.1 Mirnov Coil Signals

First, we characterise the magnetic mode that is observed in each case.¹²⁷ This is done by reviewing the spectrogram of the magnetic signal for the whole shot in the cases identified. These graphs show that the magnetic mode tends to persist for several tenths of a second. Its onset appears to be preceded by an intermittent cascading pattern of high frequency magnetics. The mode comes on part way through shots and lasts for some or all of the

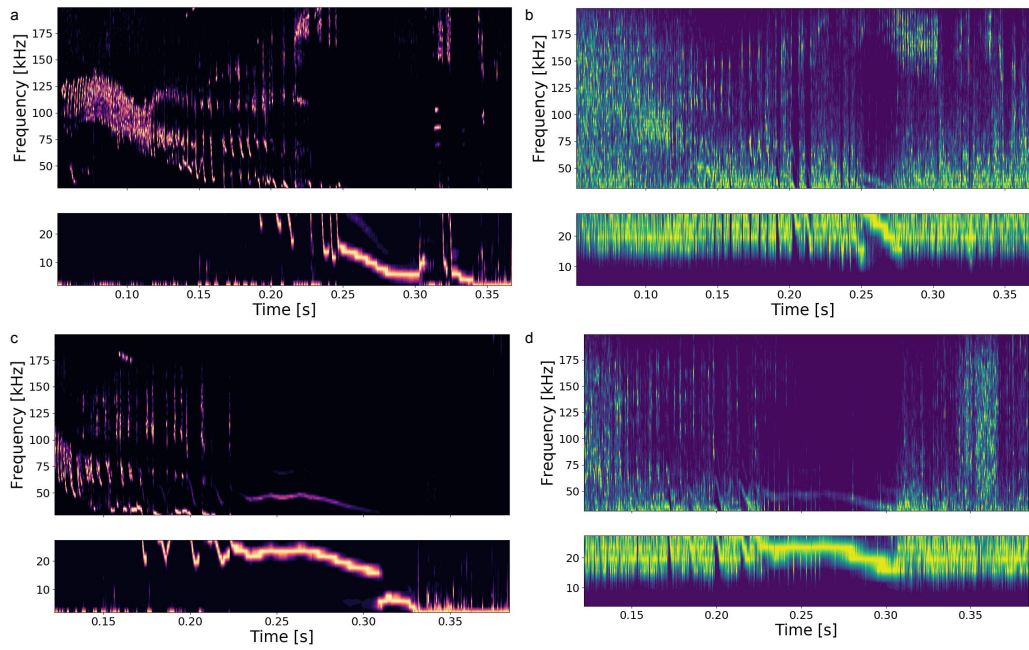


Figure 5.6: Spectrograms of the full time and frequency range studied with BES show two patterns of continuous magnetic mode. (a,b) above is the descending frequency type from shot 29761 and (c,d) below is the constant frequency with strong harmonic mode from shot 30166. (a) and (c) are spectrograms of the Mirnov signal and (b) and (d) are of the BES signal from channel 20.

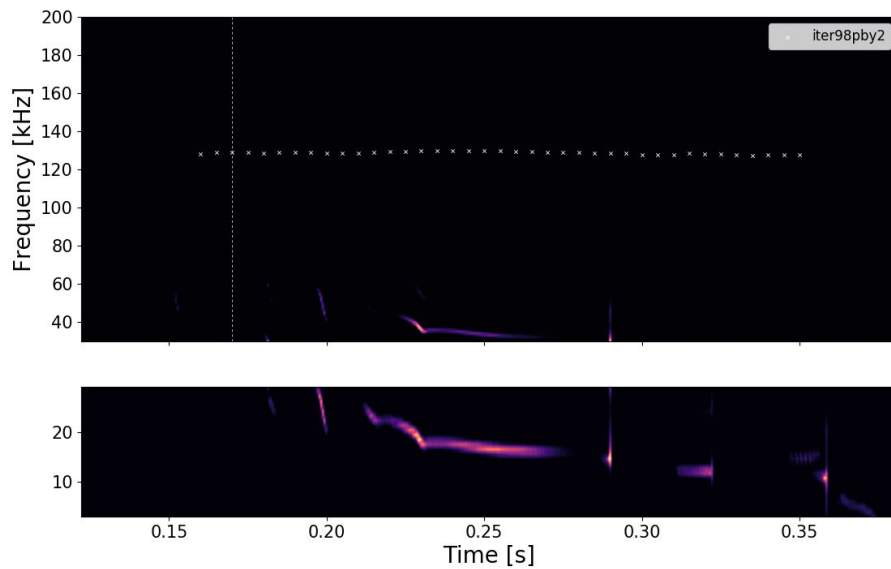


Figure 5.7: Mirnov signal spectrogram from shot number 30170. The time at which the H factor is calculated to be higher than unity are marked with crosses. The third time in a sequence of at least five is marked with a dashed line.

remaining shot time. The mode persists from approximately the same time as the shots' 'H factor' measure reaches values above unity. The factor is a comparison to the empirically found scaling of confinement time in the baseline ITER98y2 plasma scenario¹²⁸ and implies an association of the observed mode with high confinement plasmas. For these few examples the post-transition plasma state was verified in the notes of the shot logs where L-H transition times are recorded.

There are apparently two trends of the mode as it persists. First, examples can be seen in which the frequency of the magnetic mode is relatively constant and has harmonics visible at frequencies above that of the velocity spectra peak. Alternatively, the frequency of the mode slows over time in which cases the harmonics tend to appear diminished. It is likely that these are just different manifestations of the same generic mode behaviour. Here at least there are too few examples to conclude two different modes are being seen. There is no clear correlation of constant or reducing frequency types with production of velocity peaks (both result in velocity peaks at the same frequency as the magnetic mode at a given time.) Extending the survey to 27 time slices with magnetic modes shows that 70% of 15 'falling frequency' cases produce velocity peaks compared to 50% of 12 'constant harmonic' cases.

Since we know that the frequency of GAMs is a function of several plasma parameters, the magnetic frequency trends found were compared to other shot data. These signals were marked alongside the spectrogram pattern as in figure 5.8. We pay particular attention to the plasma temperature at the radius of the centre of the BES field of view (higher temperature increases GAM frequency). Also shown was plasma elongation (tends to decrease GAM frequency) which is expected to have a stronger effect in spherical over conventional tokamaks. Neither consistently showed a correlation with the changing frequency of the magnetic mode (though elongation tended to vary over a very small range.) If we accept the theoretically predicted dependencies on these parameters in the MAST context, this might suggest the magnetic modes are leading the velocity spectra peaks of the same frequency.

5.3.2 Theory in Support of Magnetic Mode and GAM Co-existence

The second evidence we consider is whether there are theoretical grounds to expect a magnetic signal as part of the experimental signature of a GAM. The flow effects a local movement of the plasma, so some electromagnetic field perturbation is expected. Very recently, work done by Wahlberg and Graves described this effect.^{82 88} Their work, using the geometry of a conventional tokamak and plasma, largely considered the theory of mode structure of the magnetic signal but offers an order of magnitude estimate for the amplitude of the magnetic fluctuation. Here ε is the inverse aspect ratio of the plasma, β the plasma beta metric and B_0 the on-axis magnetic field strength.

$$\mathcal{O}(\delta B_{\theta,r}) \simeq \varepsilon \beta B_0 \quad (5.1)$$

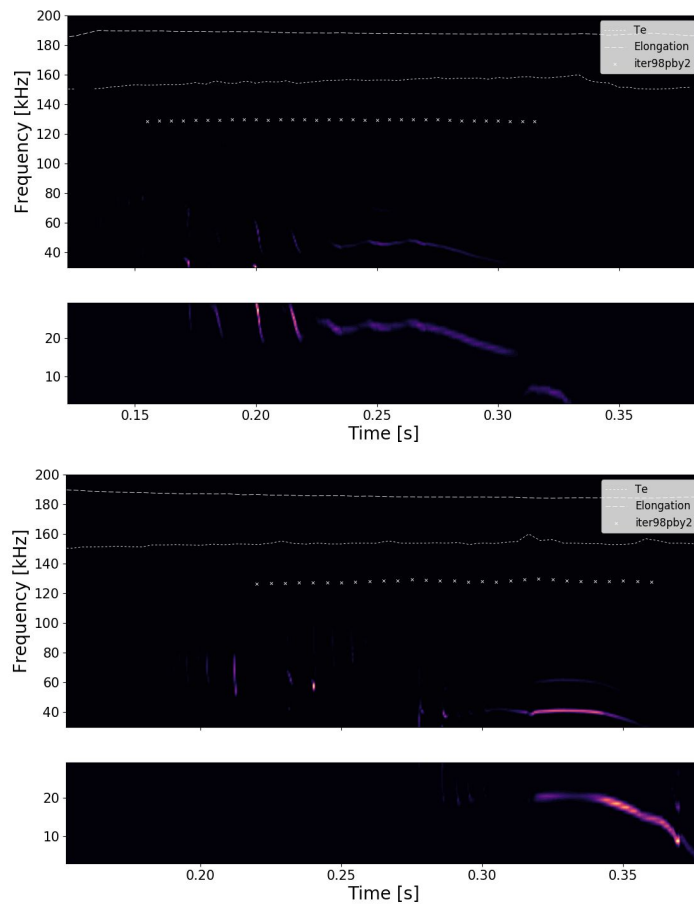


Figure 5.8: Key GAM frequency parameters are plotted along with the high H factor times for Mirnov spectrograms from shot numbers 30166 and 26885 respectively. The dashed line plots plasma temperature and the dotted shows elongation. Neither correlates with the changing frequency of the continuous magnetic mode.

Evaluating the equation for typical MAST parameters, we can readily discover if this prediction matches the Mirnov signals or not. The typical magnetic field strength of MAST is 0.4 T with inverse aspect ratio around 0.75 and a plasma beta of around 1%. Put together these give an estimated magnetic fluctuation of order 0.003 T. Comparing this to the magnetic modes in the shots we have seen requires converting the Mirnov signal in Volts to Tesla. The calibration done for one coil at their installation on MAST is reported at 27 T/s/V¹²⁹ This is unlikely to be exactly true for all coils, for all time, but we take it to be approximately accurate. We then calculate the root-mean-square (RMS) Mirnov signal fluctuation amplitude measured in coil 210 at the outboard midplane for the times studied. The relevant data are those that produce velocity spectrum peaks so equation 5.2 is calculated using the average root-mean-square value from those times that correspond to velocity spectrum peaks only. Finally, we use an indicative mode frequency of 10 kHz (typical of GAMs reported in 1.4.2) for the calibrated units conversion.

$$\varepsilon\beta B_0 \simeq RMS[V] \cdot \frac{27[T/s/V]}{10000[Hz]} \quad (5.2)$$

These give an estimate of the order of magnitude of the fluctuation as 0.001 T. Evidently there is good agreement between these values for an order of magnitude theoretical estimate and the measured Mirnov response. The consistency of measurements to GAM theory supports the hypothesis of a relationship between velocity and magnetic spectra in the zonal flow physics we are looking for. In the most recent literature reporting experimental observations of GAMs there is a precedent being established for this association. Multiple papers now report especially the magnetic mode structure but also the magnetic fluctuation amplitude that accompanies the observed GAM signal. None investigate the relationship in detail. The amplitudes are reproduced in table 5.1.

<i>Paper</i>	<i>Machine</i>	<i>Diagnostic</i>	δB [T]
Bulanin 2015 ⁸⁵	Globus-M	DBS and Mirnov	1×10^{-5} to 2×10^{-4}
Xu 2018 ⁸⁶	EAST	Mirnov	1×10^{-5}
Wang 2018 ⁸⁷	EAST	DBS and Mirnov	1×10^{-6}
Wang 2013 ⁶²	DIII-D	DBS, BES and Mirnov	5×10^{-7} and 1×10^{-5}

Table 5.1: Reported values of magnetic fluctuation amplitude in tokamak experiments.

The third aspect of the relationship between GAM flows and magnetics to consider, like the parameter dependence result above, reverses the direction of causation assumed thus far. We know that zonal flow derives its energy from turbulence. In the typical picture of the onset of zonal flow it is also turbulence that provides the perturbation required for the flow mode to grow (NB this was the conventional scenario explored in simulations of turbulence and associated with studies of the L-H trigger mechanism.) However, magnetic modes can also be plasma density perturbing. This means that, assuming conditions in the plasma support zonal flow, the magnetic modes may be driven by other physics and

then stimulate zonal flow. The original theory paper proposing the mechanism sustaining GAMs²⁵ linked their excitation and magnetic surface geometry in an electrostatic model. Since then a few authors, by taking account of the magnetic response to GAMs \tilde{B} have shown a connection with an MHD pattern around the GAM¹³⁰ and the reverse current associated with the characteristic $m = 1$ density perturbation.^{131 88} These may provide routes to MHD perturbation of the plasma that stimulates flow via Reynolds Stress. If this is the correct interpretation it would also explain why not all magnetic modes in this range also have high contrast peaks in velocity spectra. Allowing for this possibility means two mechanisms by which a GAM signal as revealed in the velocity spectrum can come with a medium frequency peak in the magnetic spectrum - the magnetic frequencies as driver or driven modes. It also then provokes a question of what turbulence driven flows are doing at these shot times and whether they may co-exist.

It would be beneficial to our investigation of this phenomenon to compare these results to other GAM papers' examples. On MAST there are suggestions of GAM detection using Langmuir probe and Doppler Back-Scattering (DBS) data.¹⁰⁹ If the density oscillations they found could be compared with our velocity spectra it would be an excellent test of the method and the expectations of the circumstances in which zonal flow can be detected. Unfortunately, no BES data exist for any of the shot numbers used in either paper (including the reference experiments those shots' parameters were replicating.) We can take note of the following from the DBS detection paper. First, they specifically show a blank magnetic spectrum at the times they identify a GAM-theory-consistent density mode as part of their argument. Second, not only is there no BES data but there is no NBI power heating the shots in question. That implies an L mode throughout. Their paper is also focused on the idea that coupling to magnetic physics is affecting the signal they identify as GAMs. They propose the $n = 3$ resonant magnetic perturbation magnetics used to stabilise edge localised modes.

5.3.3 Study of high contrast velocity spectrum peaks

We compare the data from the 12 shots (27 times) study of the magnetic modes described previously to investigate the relationship between density, velocity and magnetic signals. In many, though not all, cases the Mirnov and BES spectra look similar as in figure 5.9. The velocity spectrum there has a peak at the same fundamental frequency (though not at harmonic frequencies.) Note that these shots are chosen on a random sampling basis from our set of shot numbers with type 4 spectra for the presence of the magnetic mode rather than for velocity spectrum peaks. To study velocity data without the magnetic perturbation, we introduce a higher lower cutoff frequency to the bandpass filter of BES data. We test the direct introduction of the perturbation frequency (present in magnetic and density data) to the velocity signal by filtering the density data above the frequency of the magnetic peak. Note that this test is complementary to the work undertaken in section 4.2 in which it was

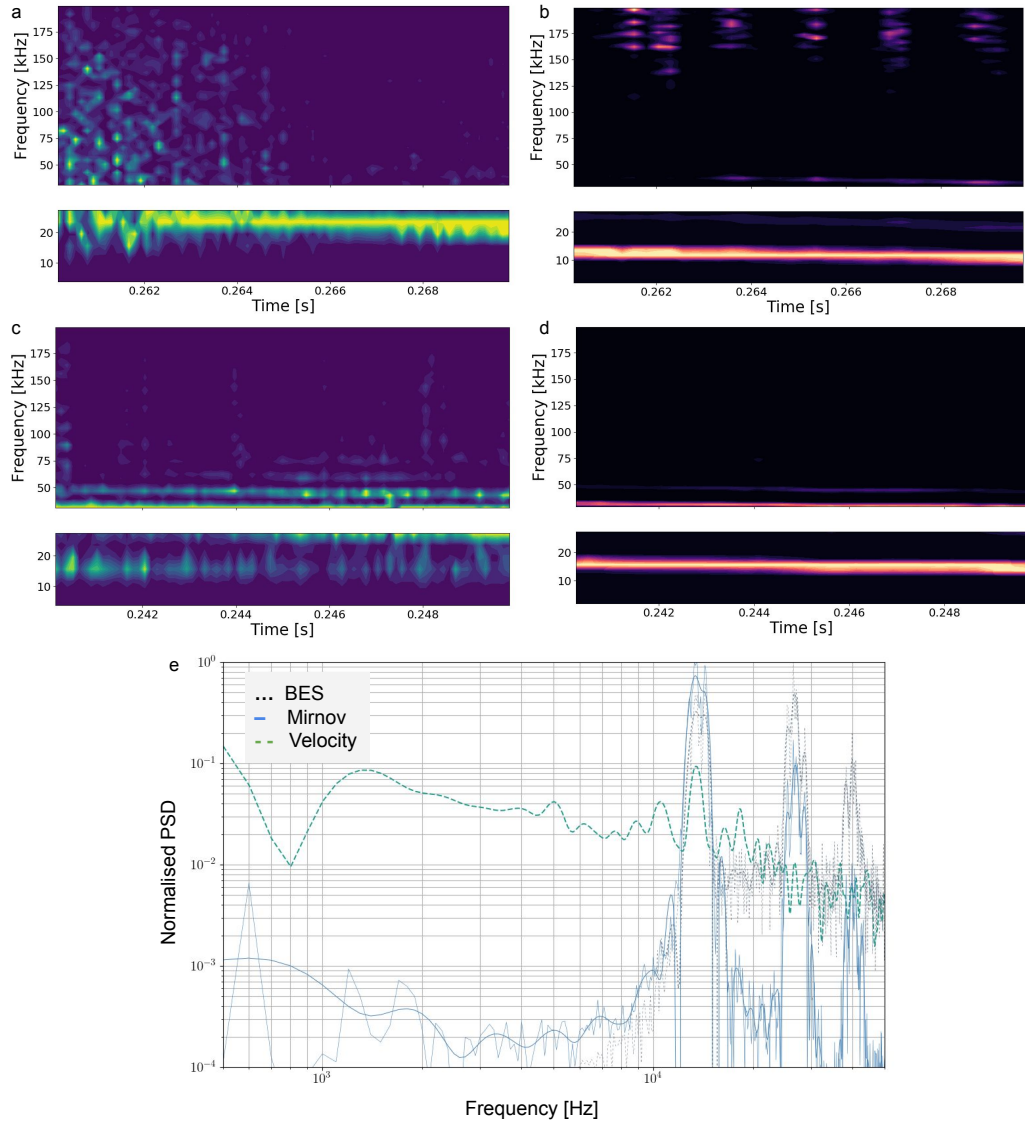


Figure 5.9: Comparison of BES and Mirnov normalised spectrograms for times containing the continuous mode. (a,b) are shot number 29764 from times 0.26 s to 0.27 s and (c,d) 30258 from 0.24 s to 0.25 s. BES channel 20 (with a high pass filter at 15.625 kHz) is plotted in (a,c) and Mirnov is on the right in (b,d). (e) shows the spectra of these signals for the same pattern in shot 29761 at 0.25 s with velocity spectrum from column 6 included.

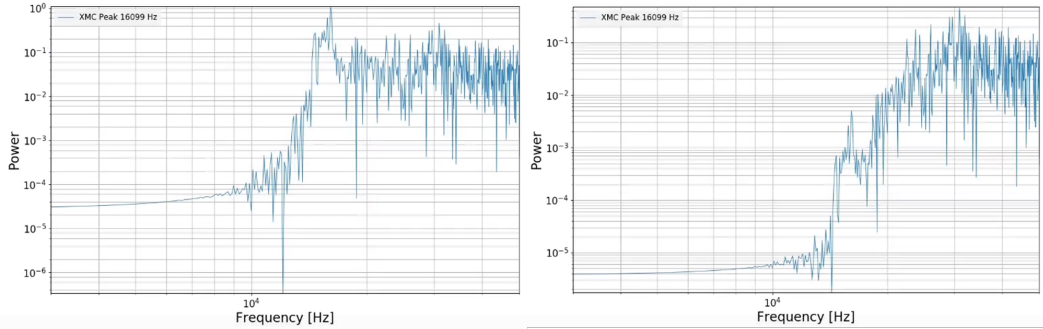


Figure 5.10: The effect of raising the lower cutoff frequency of the BES bandpass filter is shown for channel 20 of shot number 30178 from 0.23 s to 0.24 s. The left spectrum has the nominal Nyquist frequency as its cutoff, the right has the cutoff set at 5 kHz above the fundamental magnetic mode. The Mirnov (code ‘XMC’) peak frequency is labelled.

clearly established that a density mode alone is insufficient to produce a high contrast peak of matching frequency in velocimetry spectral data. That result is relevant when we consider this data set as it is the high amplitude, narrow peaks in velocity spectra that we see with the magnetic modes present. If these were purely a result of a magnetic perturbation then we would expect them to be removed by this test.

The filter cutoff frequencies are found using a lowpass filter of the magnetic signal at 50 kHz (the filter is designed for BES and still assumes a Nyquist frequency of 1 MHz.) The tallest magnetic peak’s argument is taken as the mode frequency. The bandpass filter applied to fluctuating BES data is then adjusted to be whichever is greater of the nominal Nyquist frequency (at 15.625 kHz) or the mode frequency plus 5 kHz. If the latter was above 30 kHz then the nominal Nyquist frequency was used as usual.

The velocity spectra found using BES data with and without the magnetic mode frequency filtered out as the input data for our velocimetry algorithm were compared. Smoothing the velocity time series again by lowpass filtering at 50 kHz we get a set of peak frequencies for each spectrum. The list of frequencies for each filter cutoff are compared. For the 27 time slices studied (5 without a magnetic mode in the detectable range) only 7 did not have a peak at the magnetic frequency after filtering it out in the BES data. This is as true of both types of Mirnov spectrogram patterns (harmonic and falling) identified before. With both types it remains the case that 60% of all time slices show tall velocity peaks with magnetic modes.

The density input mode may be the result of the magnetic activity perturbing plasma density. Since in all of these cases the input mode is diminished going into the velocimetry, the persistence of the velocity mode strongly suggests an independence of the velocity and density modes. This is additional evidence to that found in 4.2 that density modes cannot cause the high amplitude peaks seen in our velocity spectra. It follows that the magnetic and velocity modes would have to be directly related rather than mediated by density. In that case we can rely on the power of velocimetry as a diagnostic method for zonal flow in

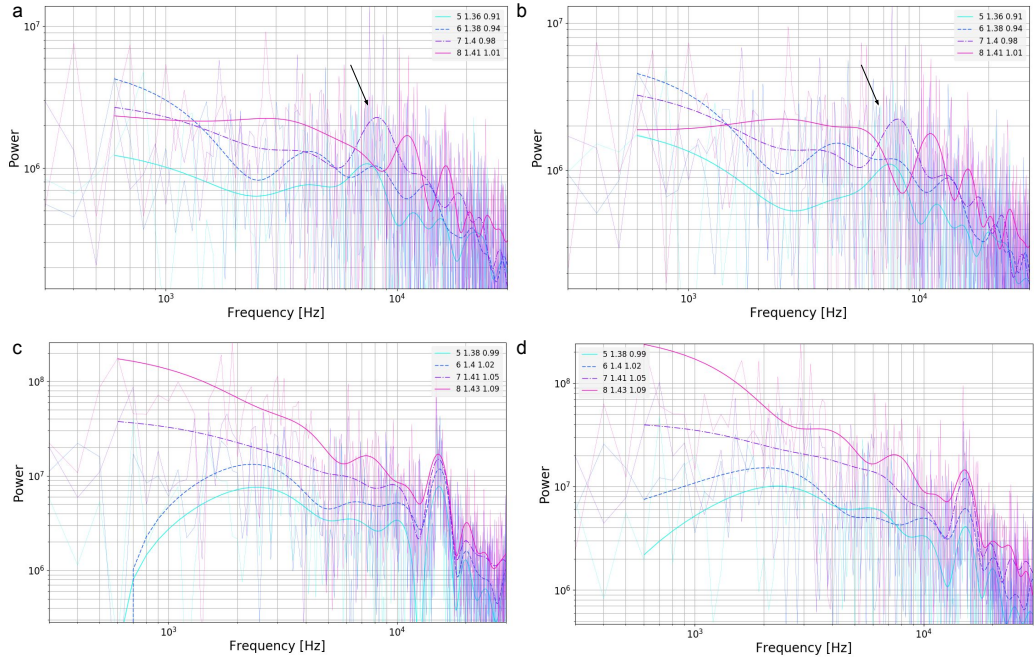


Figure 5.11: Comparison of type four velocity spectra before (a,c) and after (b,d) the bandpass cutoff frequency is raised in which peaks in the velocity spectra are preserved. (a,b) above are shot number 30175 at 0.24 to 0.25 seconds, (c,d) below show 30258 from 0.24 to 0.25 seconds. The spectra are from the outboard side of the detector with the nominal Nyquist frequency cutoff in (a,c). (b,d) on the right have adjusted BES filter cutoff frequency, set to 18.199 kHz and 19.899 kHz respectively. The major radius and normalised radius of columns are labelled.

these cases still.

5.4 Summary

We have begun the application of our velocimetry technique to real BES data from MAST. Experiments were selected from the diagnostic logbook for study. The observation of zonal flow is an important target for this work so measurements focus on the analysis of spectra of the velocity time series. From an initial broad sweep of 80 shots, four patterns of spectra were defined. The first two correspond to the broadband turbulent data with a slow and fast imposed velocity that were observed in the testing of the technique. A third had high power associated with low frequency which was consistent with zero-frequency zonal flow theory. However, there is evidence that the low frequency is associated with long sections of the time series at extreme velocities and so further investigation of these was ruled out in favour of GAM detection. The fourth spectrum type was a peak in an otherwise flat region. This is the most promising as it is consistent with the theory and experimental observations elsewhere of GAMs, the primary finite frequency and most detectable zonal flow mode.

Inspection of the spectra in this category showed a number of velocity spectra with very tall peaks. Corroboration of the results by looking at magnetics data from Mirnov

coils showed that these velocity spectra peaks are concurrent with pronounced modes in the spectra of Mirnov time series also. This is not like the plasma scenarios reported by other diagnostics claiming to detect zonal flow that often explicitly show broadband magnetic signal spectra. Those diagnostics typically study only the density perturbation, though, and do not have the strength of evidence afforded by velocity measurements. We initially check the consistency of a magnetic mode with the presence of zonal flow in literature. Two mechanisms were identified. The first, proposed by Wahlberg and Graves, shows that the perturbation of a zonal flow on the plasma should produce its own magnetic signature. They provide an order of magnitude estimate for the amplitude of the magnetic fluctuation. A sample of 12 shots with magnetic modes was used to identify an order of magnitude match in the signals we observe to their theorised amplitude. The second mechanism is that of the original proposal of the existence of finite frequency zonal flow i.e. GAMs in which medium frequency magnetic instabilities provide the perturbation necessary to stimulate the zonal flow.

Having established that the magnetic signal is a potential feature of GAM detection we reviewed 27 times from the 12 shot numbers. The BES signal has the same frequency mode as the magnetic data. By filtering the BES signal at a frequency 5 kHz above that of the magnetic mode and comparing the frequencies of velocity spectrum peaks before and after filtering, we establish that the observed velocity peaks are independent of the BES mode in the majority of cases. Considering the benchmarking of the effect of density modes in the previous chapter reinforces this argument. We therefore conclude the velocity peaks, a key tool for GAM detection, are not just an artefact of the magnetic peak.

Chapter 6

A Systematic Search for Signatures of GAMs

With the principle that co-incident magnetic and velocity spectral peaks may be a feature of Geodesic Acoustic Mode (GAM) signals established, we proceed to interrogate MAST data to identify evidence of GAMs. Initially using the examples already discussed and a visual inspection of spectrum peaks, but then an increasingly automated search of many more shot numbers. The end result is an automatic, systematic approach to interrogating data for GAM behaviour. This chapter will list the best candidates for GAM signals detected with our velocimetry method, and how they were decided upon.

First, we introduce a set of criteria in the form of automated weighted tests against which the potential for a spectrum to be of a GAM signal will be scored. These criteria are informed by typically identified markers of zonal flow in the literature and may be adapted as future expectations change. The results of searching MAST data with this approach are then listed according to several categories of interest to capture all data that may be usefully compared. The data from a scan of shots to produce velocity data are shown in totality first to better understand the approach taken. Specific categories for GAM detection are then the highest scoring categories with and without a long magnetic mode. These are compared to the data from low scoring cases. We also specifically examine low confinement mode cases as the regime in which we expect zonal flow to be strongest.

6.1 Study of Cases with a Magnetic Mode: Developing Systematic Tests of MAST Data

6.1.1 Literature Sources for Zonal Flow Characteristics

A number of well-established features of experiments reporting zonal flow provide the physics tests. ^{87 86 62 65 132} They identify zonal flow according to observation of an axisymmetric po-

tential mode, a poloidal mode number of $m = 2$ in the magnetic signals and velocity mode frequency dependencies on plasma parameters that correspond to GAM theories. The first two are tested directly, the latter in the relationship of frequency peaks to GAM theories. This in addition to a criterion continuing to test the signal fluctuation amplitude against the theoretical work of Wahlberg and Graves as in section 1.4.2. Some of these papers also report the energy exchange between high and low frequencies shown in bispectral analyses. Our project defers this last analysis pending a good candidate case of zonal flow in turbulent L mode MAST data.

Much work has gone into predictions of the frequency of GAM oscillations. This work builds on the basic prediction for oscillation time of GAMs, expanded in equation 6.1.

$$w_{GAM} = \frac{c_s}{R} = \frac{1}{R} \cdot \sqrt{\frac{T_e}{m_i}} \quad (6.1)$$

in which c_s is the sound speed, R the major radius, T_e the electron temperature and m_i the ion mass.

Various studies have since sought to add terms to account for other tokamak parameters (though few explicitly examine spherical tokamak behaviour.) For this work we reduce these to two models – with terms for plasma shaping in 6.2¹³³ and for plasma rotation in 6.3¹³⁴.

$$\omega_{shaped} = \omega_{GAM} \cdot \sqrt{\frac{7}{4} \frac{2}{\kappa^2 + 1}} \cdot \left(1 - \frac{\kappa - 1}{\kappa} \cdot \frac{\kappa^2}{4\kappa^2 + 4} - \varepsilon^2 \frac{9\kappa^2 + 3}{8\kappa^2 + 8} \right) \quad (6.2)$$

$$\omega_{rotation}^2 = \frac{\omega_{GAM}^2}{2} \left(2 + \frac{1}{q^2} + 4M^2 + \sqrt{\left(2 + \frac{1}{q^2} + 4M^2 \right)^2 + \frac{2M^4}{q^2}} \right) \quad (6.3)$$

with ε for inverse aspect ratio, κ for plasma elongation, q is safety factor and M toroidal flow Mach number.

When seeking to match the observed velocity spectrum frequencies to GAM theory we will assess the data against the predicted oscillation frequencies using terms from each of the naïve, shaped and rotating theories and then both approaches together. Note that the tendency of shaping terms is to slow the predicted frequency and rotation terms to quicken it. This is an integrated approach to assessing the frequency response of our cases to those parameters GAMs are expected to depend upon. Following the predicted change of frequency with these parameters is therefore evidence of the presence of GAMs (albeit with the caveat that we also investigate the possibility of an eigenmode pattern.)

Unique to this project will be a set of additional tests of the magnetic modes we have observed. Their properties and relationship to the other signals as well as theoretical predictions for GAMs are of interest too now. We will measure the presence of a magnetic mode and its correspondence to modes in the other signals.

6.1.2 Tests

To develop the metrics we start by measuring the density, velocity and magnetic signals and spectra that were used in the 27 times study of the magnetic mode in section 5.3.3. Then the code used to report on the signals is adapted to automatically score the metrics and report data. The patterns of interest, the relation to expected GAM behaviour and automation written into the code are described below for each test. The questions are presented in groups of similar methodology. Tests 1 - 8 measure the magnetic mode relationship with density and velocity signals; tests 9 - 14 measure expected GAM physics concurrent with the spectra; 15 & 16 measure the spectral peaks; 17 marks the confinement mode and 18 records the overall score assigned to the time in question. The code makes no decision on which tests to measure at each time of interest, running all every time, though some tests will be assigned a zero score with null returns in the absence of data.

- 1 - Was a magnetic mode identified?
- 2 - Is an identified magnetic mode the dominant peak in the averaged BES spectrum?
- 3 - Is an identified magnetic peak in the averaged BES spectrum at all?

The first question is intended to filter those cases that match the pattern found so far in tall velocity peak examples from other cases that may be seen by testing for the presence of the magnetic mode that lasts for tenths of a second. A lowpass filter approach is taken to identify a magnetic mode and a positive result recorded if a peak is found within a range of interest between 3 and 30 kHz. The mode is identified by smoothing each signal with a lowpass filter at 50 kHz and finding the argument of the maximum value. Where multiple peaks are found only those with amplitude at least one third of the tallest will be considered.

The next question is of the density-magnetic mode interaction and repeats the testing of section 4.2. We seek to measure whether the velocity modes persist in the absence of a density (BES) mode. We therefore investigate whether or not there is a peak in the density signal (now always with the low cut-off of the bandpass filter set at the nominal Nyquist frequency) at the same frequency as that of the most powerful (tallest) magnetic peak. If there is and it is the tallest in the average filtered BES signal the test is successful. If the magnetic mode is related to a GAM we expect it to be present in the density perturbation. The pattern of data so far suggests that, where a velocity mode exists at the same frequency, the tallest peak of the other density signal will be at the magnetic mode frequency.

The dominant modes are again identified by smoothing each signal with a lowpass filter at 50 kHz and finding the argument of the maximum value. If the two frequencies are within 1500 Hz of one another they are counted as matching. This margin was identified by measuring the difference between tallest peaks in all cases where a mode is identified in both. The average gap size is 590 Hz, median average 0 Hz and average absolute difference

is 1770 Hz. 1500 Hz above and below the comparator mode was chosen to preserve a strict matching criterion for signals where multiple peaks are possible. This approach guarantees only close matches get high scores. The 1500 Hz standard will be consistently applied across frequency-matching tests.

A corollary question tests whether the peaks found with this method and in this range are peaks in the density spectrum regardless of being the dominant peaks. This identifies rare cases where the spectral peak is identified in density signals at a frequency that coincides with the peak in the power spectrum of the Mirnov coil signal but is not the fundamental mode there. For example, where the magnetic fundamental is below the bandpass filter and a strong harmonic also effects a density perturbation. It also tests the role of magnetic oscillations that affect the density perturbation in producing velocity peaks.

We assume throughout that if the GAM signal is causing or caused by the magnetic signal then it will be the fundamental frequency that is responsible.

- 4 - Is an identified magnetic mode a peak in any column's velocity spectrum?
- 5 - Is an identified magnetic peak in multiple columns' velocity spectra?
- 6 - Is the same mode in all of BES, velocity and Mirnov signals?

Each column's velocity spectrum is lowpass filtered with the same 50 kHz cut-off described above to smooth it and the tall peaks in the range of 3 to 30 kHz again are listed. Each listed peak in each velocity spectrum is compared to those in the magnetic signal. If any is within 1500 Hz a successful score is recorded. If the magnetic mode and GAM are co-incident we expect the frequency to appear in the velocity signal.

It is the intention of this project to characterise the zonal flow detected. So, we additionally consider whether the magnetic mode is common to multiple columns' velocity spectra. For the purposes of identifying a common mode across multiple radii, a stricter test is introduced so that we can be confident the spectra have the same form. The peak in question must be well-defined which we here assign the meaning of having a width of at least 400 Hz. Full details of how the width is calculated are included with tests 15 and 16. In principle the radial extent of modes is of interest in all likely GAM cases, however, this is reserved as a test of cases with a measured magnetic mode. Others may be studied as they are identified. The width of eigenmode structure GAM modes is an open research question and so no outcome is *a priori* preferable to any other. This is a zero weighted question.

Another zero-weighted test confirms whether a mode is common to all of the density, magnetic and (at least one of the) velocity signals studied. This is typical of the examples with a continuous magnetic mode thus far observed.

- 7 - Does the identified magnetic mode match GAM theoretic predictions?

The evidence for zonal flow emphasised by velocimetry techniques is that of the velocity spectrum. This question uses the magnetic spectrum as an alternate theory comparator. This test identifies magnetic mode peaks in the usual range and compares them to the calculated GAM theory frequencies instead. Since this is so closely associated with tall velocity peaks in our observations a successful match may count as evidence of the effect of GAMs, many matches would be evidence of the eigenmode hypothesis. The theory matched to is recorded.

- 8 - Does the power in the Mirnov spectrum peak dominate the Mirnov RMS amplitude?

The assumption that the magnetic diagnostic's fluctuation is dominated by the fundamental mode is tested in the next, zero-weighted question. We use the mode amplitude calculation set out in equation 4.1 to estimate the signal amplitude contribution of the power in the spectral peak. The ratio of this number to the measured amplitude (n.b. without converting to Tesla) is recorded. If the ratio is found to be higher than 0.3 of the measured RMS fluctuation amplitude a successful result is recorded. In principle this could be used to modify the order of magnitude estimate in question 12.

- 9 - Is there an axisymmetric magnetic mode?
- 10 - Is an identified axisymmetric mode at the same frequency as an identified magnetic peak?

Next, we measure the theoretically understood behaviour of GAMs. The zonal flow (zero & finite frequency) is an axisymmetric flow. If the magnetic mode is a result of the zonal flow, it should be similarly axisymmetric. MAST has Mirnov coils positioned around the midplane as well as around a poloidal cross section which means this property can be checked. The toroidally separated Mirnov coils numbered 110, 210 and 310 and the poloidally separated coils 202, 210 and 218 are compared. Their smoothed spectra are compared to identify a common toroidal and poloidal peak. If these peaks match frequency to within 1500 Hz a positive result is recorded.

Since the zonal flow could in principle generate its own peak in the magnetic spectrum, a further test seeks to match the mode identified as axisymmetric with the fundamental magnetic mode. If they do match, then we have good evidence that the magnetic mode is associated with flow physics and not magnetohydrodynamic (MHD) instability alone.

- 11 - Is there an axisymmetric mode with poloidal mode number 2?

Another important feature of GAM magnetic signals described in theoretical and corroborated in experimental works is a poloidal mode number of two. Since MAST has good coverage with Mirnov coils places around a poloidal cross section we can test for this pattern. A set of coils are chosen where there is a symmetrically arranged pair above and below the

Signal	Radius [m]	Height [m]	Tor. Angle	Pol. Angle
XMC_OMV/202	1.44	1.25	270	65
XMC_OMV/205	1.59	0.65	270	41
XMC_OMV/206	1.85	0.3	270	17
XMC_OMV/208	1.85	0.15	270	9
XMC_OMV/210	1.85	0	270	0
XMC_OMV/212	1.85	-0.15	270	-9
XMC_OMV/214	1.85	-0.3	270	-17
XMC_OMV/216	1.59	-0.725	270	-44
XMC_OMV/218	1.44	-1.25	270	-65
XMC_OMV/110	1.85	0	330	0
XMC_OMV/310	1.85	0	150	0

Table 6.1: The locations of Mirnov coils on MAST used to measure mode axisymmetry and poloidal mode number.

midplane per the layout described in 6.1. This creates a quasi-regularised real-space distribution. Fourier transforming their signals over angular rather than distance separation gives a two-dimensional mode number – frequency spectrum. We can then look for the argument of the maximum of this spectrum at the magnetic mode’s frequency as the measured mode number. Given the need for oversampling to achieve a useful resolution in mode numbers, a result of the limited number of measurement locations, a generous boundary is set for this test. A successful result is recorded if the peak is found at any sampled mode number between 1 and 3.

- 12 - Does the Wahlberg & Graves order of magnitude estimate match the measured fluctuation in the Mirnov signal using the Wang correction?

We next formalise a test of the new theory around zonal flow described in section 1.4.2. The equation for the order of magnitude estimate of magnetic fluctuation produced by GAMs is given in formula 5.1. The estimate is calculated using the data from MAST signals ‘efm_bvac_val’ for magnetic field on axis and ‘efm_betan’ for plasma beta at the first time of each time slice being studied. Once again, we approximate the power driving the fluctuations as being in the dominant magnetic mode. Instead of an indicative frequency we now calculate our expectation using the actual mode frequency.

The measured amplitude is still the RMS fluctuating amplitude of the Mirnov signal using the calibration value for conversion to Tesla. The Wahlberg and Graves theory is for inside the plasma and so we apply a multiplier to the value measure at the outboard midplane coil. The factor is based on the equation used by Wang for neoclassical tearing modes with a value of 1.4 for the nominal BES viewing radius.⁶²

$$0.5 \cdot \left(\frac{R_{diagnostic}}{R_{GAM}} \right)^{m+1} \simeq 1.4 \quad (6.4)$$

Wang's correction factor is applied assuming a mode number of 2, radius for the Mirnov coil $R_{diagnostic}$ of 1.85 m and of the GAM R_{GAM} based on the recorded BES centre position. If the ratio of the two numbers is within an order of magnitude, defined as the range 0.1 to 10, we score the test.

- 13 - Does any peak of any column's velocity spectrum match the prediction of GAM theory?
- 14 - Which BES columns have spectrum peaks that match GAM theoretic values?

The four equations for theoretical frequency predictions that we are comparing velocity spectrum peaks to have been set out in equations 6.1, 6.2 and 6.3. Any peak of any columns' spectrum matching a theoretically predicted value is taken to be enough for a successful outcome of this test. Given the detector's spatial resolution it is possible (in our present understanding of zonal flow) for the flow to appear in only one column of the BES field of view. As section 1.4.2 indicates, there is also the potential for the flow to exist over a wide radius.

Peak frequencies are identified with the lowpass filter method already described but with the cut-off set to 150 kHz. Only peaks at frequencies between 3 and 30 kHz are considered. For each case (shot and time) studied the GAM frequency predictions for each equation at the radii of detector columns are calculated. Each identified peak is compared to the calculated values first by establishing which prediction of all theories it most closely matches. If the measured peak frequency is in a range defined by the calculated frequencies of the columns on either side of that which produced the peak, it is counted as a match. For edge columns the range is for the two columns next to that edge column since those columns in the tokamak scrape off layer often have undefined predicted GAM frequencies. Calculated frequencies are capped between 0 and 30 kHz. For this question, when any match is made, a positive score is recorded and the theory it matched, as well as the measured and calculated frequencies, are recorded.

A separate question uses the same process to find matches but instead of recording the frequencies, this question scores if multiple (three or more) columns contain a matching velocity peak. This is a zero-weighted question. The recorded data are the number of columns with matches, velocity peak frequency, details of the velocity peak (height, width and base) and normalised radii of matches.

- 15 - What are the BES mode peak's measurements?
- 16 - What are the magnetic mode's measurements?

The last tests record the details of the modes observed in density and magnetic data (in addition to those of velocity peaks recorded in question 14) to evaluate correlations with

other metrics. The height of the peaks is of particular interest, but we save data on their noise floor and width too. Measuring the peak's properties first requires a peak frequency which is found by lowpass filtering the signals at the usual 50 kHz cut-off.

Peak properties are found as follows, assuming an approximate peak frequency is provided. The spectrum is lowpass filtered at 150 kHz and the minima either side of the given frequency identified as the bases of the peak. Their average value is taken as the noise floor of the peak. An attempt is then made to fit a Gaussian curve to the subset of spectrum data between these points with the floor subtracted to find the true width of the peak. The maximum of these data smoothed with a lowpass filter at 50 kHz is given as the peak height and height guess, the frequency of the maximum value is the guessed centre and the standard deviation given as 2.355 times the full width at half maximum of the smooth data. If a Gaussian curve can be fit, the peak's width is given as the difference in frequency between the arguments of the curve where its value is $1/e$ times the fitted maximum. If no curve could be fit, or the width is otherwise found to be 0 Hz, the width is given according to the standard formula

$$Width = 2 \cdot \sqrt{2 \cdot \log(2)} \cdot \sigma \quad (6.5)$$

in which σ is the standard deviation of the curve described above.

- 17 - What are the measured L-H transition times?

Finally, as a way of understanding how our examples compare to the expectation that zonal flow should be strongest in turbulent pre-transition plasmas, we record the L-H confinement mode transition time. Though a critical feature of fusion plasmas, and often recorded in written notes accompanying shots, the time of the transition is not routinely measured. The metric that comes closest is the multi-dimensional 'H factor' measure of the plasma's performance relative to an ITER H-mode baseline.¹³⁵ The non-linear improvement in confinement reduces plasma losses and turbulence which can also be seen in diagnostic signals often used to mark the transition. Our automated measure of the transition time uses two of these. The first is the H factor as previously described. Where that signal is above one (i.e. the plasma scenario compares favourably to an H mode plasma) for five or more consecutive times, the middle (third) point is taken to be the time of transition. As figure 6.1 shows, however, this metric often fails to match the transition in plasma properties associated with confinement.

We therefore develop an alternative measure based on the emissions recorded in the D-alpha light signal. At the transition there is a step reduction in the value of this signal. This can be discovered by differentiating the signal. MHD instabilities can cause eruptions of plasma that leave spikes in the light signal which interfere with the ability to identify the transition in the turning points of the differentiated signal. To smooth these out we

Filter [kHz]	50	100	150	200	250	300	400
Count /11	3	4	6	3	4	3	3

Table 6.2: Count of accurately marked L-H transition times with varying smoothing of D_α lowpass filter cutoff frequency. 11 shots were studied.

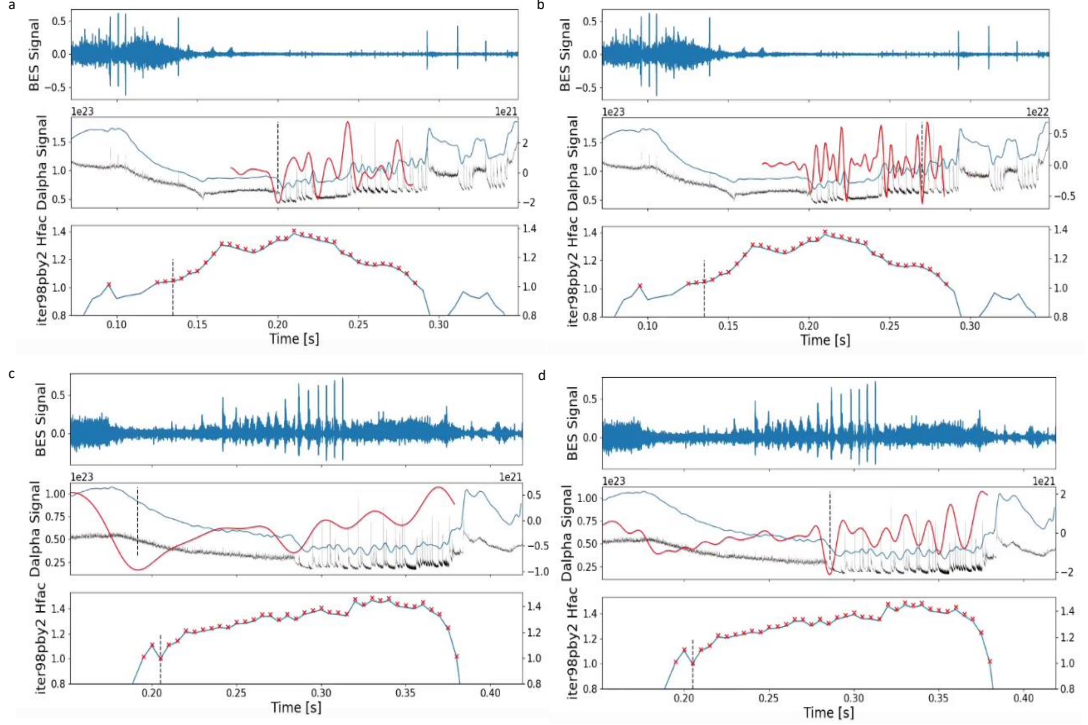


Figure 6.1: The D_α signal transition time method with different cutoff frequencies. The BES, D_α (black), integrated D_α and differentiated integrated D_α (red) and H factor (when above unity) signals are plotted. Above for shot number 27294 with the cutoff set at 150 kHz (a) and 250 kHz (b.) Below for shot number 27404 with cutoff set at 50 kHz (c) and 150 kHz (d). In each case the transition time found by the automated methods are marked with a dashed line in each of the D-alpha and H factor signals.

both use the integrated signal and smooth it with a lowpass filter. Table 6.2 shows the results of adjusting the cut-off frequency of this step on accurately finding the small, sudden step change. This signal-based approach is still vulnerable to mis-identifying the small step-change we can see visually if very large excursions occur or lots of light is recorded at the start of the shot. As figure 6.2 illustrates the two approaches typically identify different transition times. The H factor rises early in the shot and clearly does not match the time at which the D-alpha signal first drops and then shows ELM behaviour indicative of the H mode much later at 0.23 seconds.

We close noting that the BES signal could also be used to find the transition in the turbulence reduction (e.g. a Hilbert function of the fluctuations.) Since we are looking for corroboration of BES data, we use these other signals. Multiple signals are used because

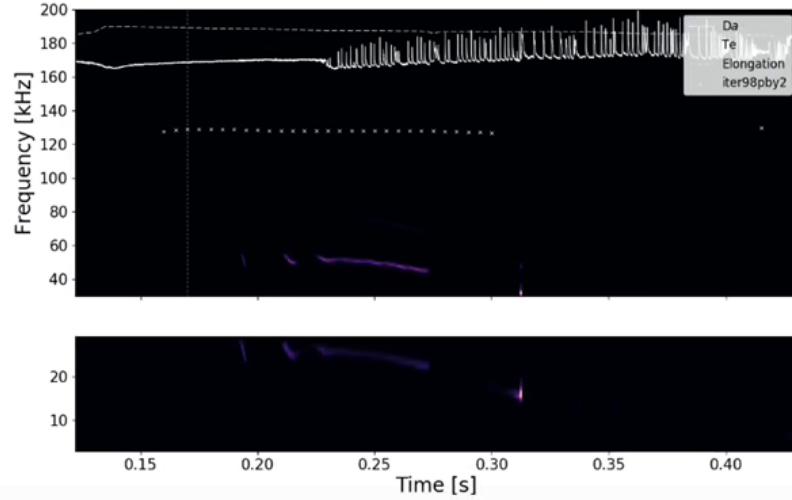


Figure 6.2: Spectrogram of the Mirnov signal for shot number 30169 with D-alpha plotted. Also shown is the H factor signal with its L-H transition prediction plotted at 0.16 seconds.

these measures do not always agree on the transition time. This test records the times measured by each approach and a label based on whether the time slice being studied begins before both, one or other or neither.

6.1.3 Weighting the Scores Assigned to Tests

The systematic approach is further developed by weighting the question set. Initially developed as a binary pass/fail score, with one mark for a GAM-like ‘yes’ answer to each, we instead prioritise the most reproduced data across reported GAM experiments. A positive result on these tests is weighted with a higher score than the magnetic mode relation questions. The most important of these we take to be the GAM frequency parametric models. Where the most persuasive metric (velocity modes) matches theory, we assign the highest scores. It is also possible to give zero weighting to some questions that add important detail without necessarily revealing more GAM-like behaviour. For example, finding modes at multiple radii, which is important for characterising zonal flow though not *a priori* a better marker of GAMs. Within this system we can also automate reporting of data by introducing zero-weighted questions.

Note that with multiple questions about the magnetic mode included, the highest scores can only be achieved with such a mode. We therefore weight the frequency matches without a magnetic mode higher in order to distinguish them from low scoring cases. Figure 6.3 summarises the list of tests, scores, criteria for success and data reported by our code. The tests use a strict frequency matching criterion to restrict the number of overlapping peaks. However, there are relaxed matching criteria for ratios and mode numbers to give the best possible chance of high scores.

No.	Questions	Criteria	Score	Reported Detail
1	Was a magnetic mode identified at all?	At 50 000/ 1 000 000 lowpass filtering, is any peak in the range 3 - 30 kHz	1	None
2	Is an identified magnetic mode the dominant peak in the averaged bandpass filtered BES spectrum?	Each spectrum lowpass filtered to 50 000 / 1 000 000 and tallest peak frequencies match to within +/- 1500 Hz	1	The BES peak frequency
3	Is an identified magnetic peak in the averaged BES spectrum at all?	Each spectrum lowpass filtered to 50 000 / 1 000 000 and peak frequencies match to within +/- 1500 Hz in range 3 - 30 kHz	1	The frequency of the tallest matching peak
4	Is an identified magnetic mode a peak in any column's velocity spectrum?	Each spectrum lowpass filtered to 50 000 / 1 000 000 and peak frequencies match to within +/- 1500 Hz in range 3 - 30 kHz	3	The number of frequencies that match; the frequencies and column number of matches.
5	Is an identified magnetic peak in multiple columns' velocity spectra?	Is there a peak in 3 or more column's smoothed velocity spectra that matches the magnetic mode to +/- 1500 Hz & that has a measurable width of > 400 Hz.	0	The number of frequencies that match; the frequencies and column number of matches.
6	Is the same mode in all of BES, velocity and Mirnov signals?	A match of the magnetic and BES mode frequencies to any column's peaks	3	None
7	Does the identified magnetic mode match GAM theoretic predictions?	Identified magnetic mode compared to calculated GAM theoretic predicted values. Score when mode frequency matches the range described by the predicted values of each column's (radius) prediction adjacent for closest matching theory.	3	The theory matched
8	Does the power in the Mirnov spectrum peak dominate the Mirnov RMS amplitude?	The ratio of calculated mode amplitude using peak height to the measured RMS fluctuation > 0.3	0	ratio
9	Is there an axisymmetric magnetic mode?	A mode frequency in vertical and toroidally aligned Mirnov coils that is common to +/- 1500 Hz, higher score if in 3 - 30 kHz range	1 / 3	The common mode frequency
10	Is an identified axisymmetric mode at the same frequency as an identified magnetic peak?	Mode frequency in question 6 match the magnetic mode to +/- 1500 Hz	1	None
11	Is there an axisymmetric poloidal mode with mode number 2?	Mode number at frequency of magnetic mode in vertically aligned Mirnov coils between 1 - 3	3	The poloidal mode number
12	Does the Wahlberg, Graves order of magnitude estimate match the measured fluctuation in the Mirnov signal using the Wang correction?	The ratio of measured (corrected) to predicted in the range 0.1 to 10	3	The ratio, measured and predicted fluctuation amplitudes, the Wang correction factor.

13	Does any peak of any column's velocity spectrum match the prediction of GAM theory?	Each column's spectrum is lowpass filtered at 150 000 / 1 000 000 and peak frequencies in the range 3 – 30 kHz compared to calculated GAM theoretic predicted values at corresponding radius. Score when any measured peak frequency matches the range described by the predicted values of each adjacent column (radius) for closest matching theory. High score if no magnetic mode was found in question 2.	5 / 10	The matching peak frequency, the theory matched, the predicted frequency, if calculated, the velocity signal RMS amplitude.
14	Which BES columns have spectrum peaks that match GAM theoretic values?	Each column's spectrum is lowpass filtered at 150 000 / 1 000 000 and peak frequencies in the range 3 – 30 kHz compared to calculated GAM theoretic predicted values at corresponding radius. Score each measured peak frequency matches the range described by the predicted values of each adjacent column (radius) for closest matching theory.	0	The number of matching frequencies; for each match: the measured frequency, the matching theory, the normalised column radius, the predicted frequency & the velocity peak's height, base and width
15	What are the BES mode peak's measurements?	Peak parameters found by fitting function	0	The BES peak's height, base, width and signal's RMS amplitude
16	What are the magnetic mode's measurements?	Peak parameters found by fitting function	0	The Mirnov peak's height, base, width and signal's RMS amplitude
17	What are the measured L-H transition times?	Where the H factor is greater than one at five consecutive times, the third is taken as the transition time. Where the integrated D alpha signal is available the time at the minimum of the time derivative of the signal lowpass filtered at 150 000 / 1 000 000 is taken as the transition time.	0	H factor and D alpha measured transition time, SS NBI on and off times and an L or H label.
18	<i>The sum of scores for each case. Highest score is 24 with and 19 without a magnetic mode.</i>		Sum	None

Figure 6.3: A full list of tests, success criteria, scores and saved data. Highlighted cells mark tests that can be scored without a magnetic mode.

6.2 Overall Test Results From Study of BES Turbulence Shots

With a programme of automated tests implemented, we can significantly expand the list of shot numbers used to investigate zonal flow. A new list was informed by previous investigations of plasma turbulence on MAST. The shots are divided into time slices of length 0.01 s as determined previously. The times measured start from the development of the plasma shape, defined by the normalised radii covered by the detector becoming a positive value between 0.5 and 1.5. The measured times end when the south neutral beam injection system turns off or the plasma current crashes, whichever is sooner.

Each time slice is run through the velocimetry algorithm to produce velocity spectra for each column. Sets of four columns inboard and outboard are visually inspected, at every time, on both logarithmic and linear plots for peaks in the frequency range 3 to 30 kHz. Those times with spectra that have either tall peaks or multiple peaks coincident at the same frequency were selected to have their scores assessed. On this basis 220 times were identified from 63 shots to study for evidence of zonal flow in MAST data. In this section we consider the results from the overall data set to evaluate the use of velocity spectra as a signature of zonal flow.

6.2.1 Distribution of Results

We first report the distribution of scores across turbulent shots, displayed in figure 6.4. Recall that the highest score available is 24 for cases where a magnetic mode is identified for study and 19 without. The overall distribution of scores shows a normal spread centred around a score of 13. This is a low centre score compared to the highest marks available, with no shots studied scoring more than 75% of the available points. Since 10 is the minimum achievable score with a velocity spectral peak that matches one of the GAM theories, all scores lower than this have been grouped together. The lowest recorded score is 7. The symmetry of the histogram implies a tendency against extreme scores. Since the data were selected for spectral properties relevant to GAM physics, this is expected when considering lower scores. However, if velocity spectra were sufficient data for identifying physics consistent with zonal flow, we would expect that the scores have a higher average and skew.

Further, we can limit the data to only the categories that match literature expectations of GAM detection i.e. have no concurrent magnetic mode and/or are pre- L-H transition. Figure 6.4 shows that the former cases return on average the same score but with a tail into the highest scores. The latter low confinement ‘L’ mode cases have an even distribution at lower scores than the overall distribution. Higher scores without a magnetic mode would match the expectation, though the number of high scoring cases is too low for significant conclusions to be drawn. That only the lowest scores (even accounting for the lower maximum achievable score) are found in the L mode is contrary to the expectation of shot times to

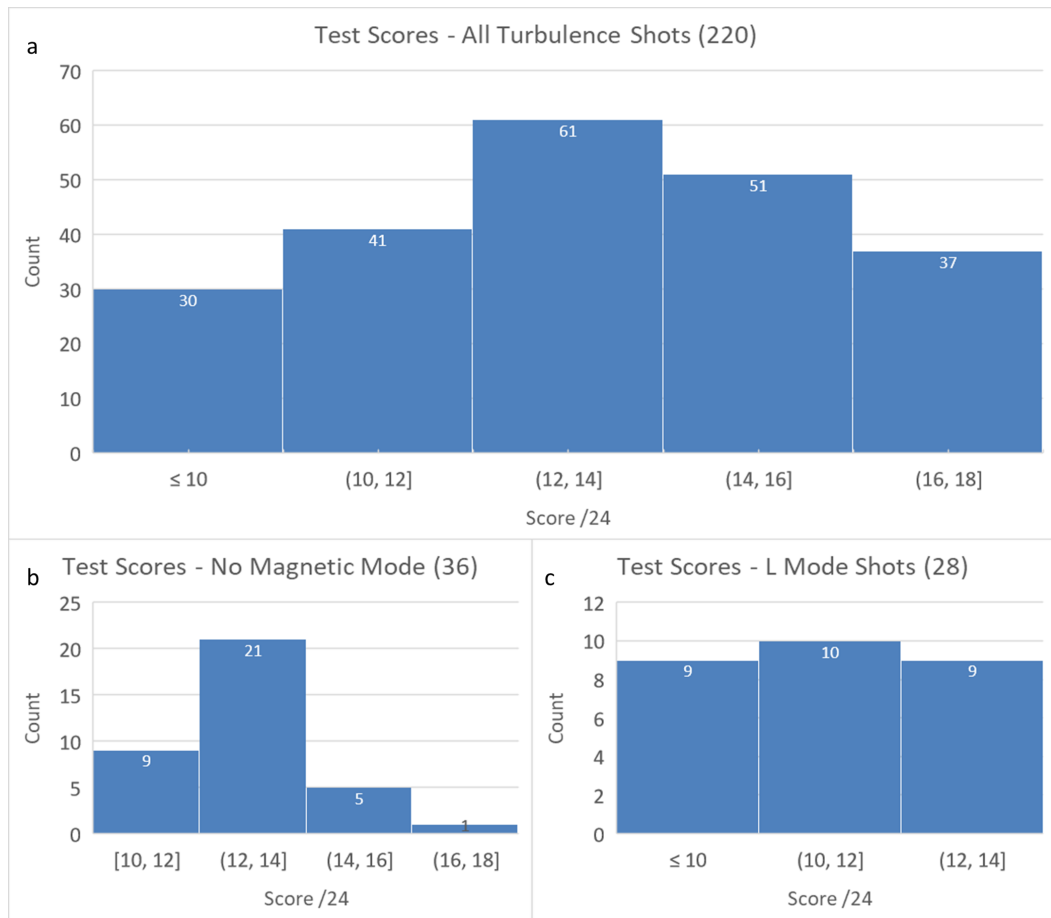


Figure 6.4: Histograms of the distribution of scores assigned to cases in the shot survey. All cases in (a) then (b) for those shots with no detected magnetic mode. (c) for cases before the transition in both metrics.

study for zonal flow. We know H mode suppresses turbulence and the L-H mode transition involves strong zonal flow.

The highest score with no magnetic mode is 17 out of 19 available points. Contrast that with cases where a magnetic mode is identifiable in which the highest score is 18 of 24. This might be evidence of mutual exclusion whereby positive scores in one group of tests is correlated with negative results elsewhere in the table. In particular it would be important to identify if scoring highly in the magnetic mode tests precludes positive scores in the zonal flow physics tests.

To investigate this, we compare the percentage of positive results in each scoring test for each of the categories of interest – overall distribution, high scoring cases and cases without a magnetic mode - as in table 6.3. The distribution of positive test results with overall score per test number is displayed in figure 6.5. The graph weights each data point by the number of cases for which a positive result produces a given total score.

Analysing these numbers, it is clear that the highest scoring cases beat the overall average in tests 1 and 4, where the average is already high, and, more significantly, in question 2

Category	Q2	Q1	Q4	Q3	Q9	Q10	Q12	Q13	Q11	Q7	Q6
<i>Overall [%]</i>	44	84	81	59	72	46	49	100	11	52	59
<i>High Scores [%]</i>	73	97	97	97	100	95	97	100	5	51	97
<i>No Mode [%]</i>	-	-	-	-	89	-	56	100	11	-	-

Table 6.3: Success rate of each test metric in the categories of all cases, highest scoring cases (score 17 and above) and cases with no detected magnetic mode.

where the average is low. These are all tests of the magnetic signal. Tests 3, 6, 10 and 12 are the markers of high scoring cases - those cases score in all of these tests. While 3 and 6 again test the impact of magnetic signals on the density fluctuation, 10 and 12 are key tests of received zonal flow theory. All cases in the study have a theory matching peak in at least one velocity spectrum per question 13. There is an even distribution of cases where the fundamental magnetic mode also matches a GAM theory frequency across our categories of interest. The only question in which exclusion is evident is 11 in which high scoring questions score lower than the average. Although only a five point difference, this is fractionally a large discrepancy. 11 is the test of poloidal mode number and it is more common for our cases to find no mode or m between 3 and 4. All but one of the highest scoring cases are in that range instead of being around $m = 2$ as found in other experiments reporting GAMs.

Looking at the distribution of these results with total score, it is at first only evident that test 12 (Wahlberg's estimate of the magnetic fluctuation amplitude associated with zonal flow) tends not to produce the lowest scores of our distribution. If there were clear exclusivity or tests that better predict high scores then strong asymmetry of results would be expected, in fact the physics tests show a broadly even distribution. Similarly, if the physics tests were themselves a compelling signature of zonal flow we would expect a strong correspondence with high scoring cases. Tests 10 and 12 have the strongest left-to-right asymmetry. Tests 11 and 7 can be seen from this graph to have the lowest success rate among the high scoring cases which otherwise gain points from all the tests evenly. The data from those two tests mark the magnetic mode in our high scoring cases as unlike one predicted by other investigations of zonal flow. Specifically, an unexpected magnetic frequency and poloidal mode number.

6.2.2 GAM Theory Representation

We also consider how our spectra compare to the most commonly found parameters of zonal flows. Those are the frequency and radius of zonal flow modes, which we measure for velocity and magnetic spectra. It is then possible to evaluate whether our data repeat these patterns in a spherical tokamak and if those patterns support the idea that our candidate spectra show GAMs.

First, we compare the fundamental frequency of magnetic modes in the range 3 to 30 kHz to the predicted values of our four models for GAM frequency. Recall that these are calculated for the radii of columns of the BES detector. With this approach it is clear from

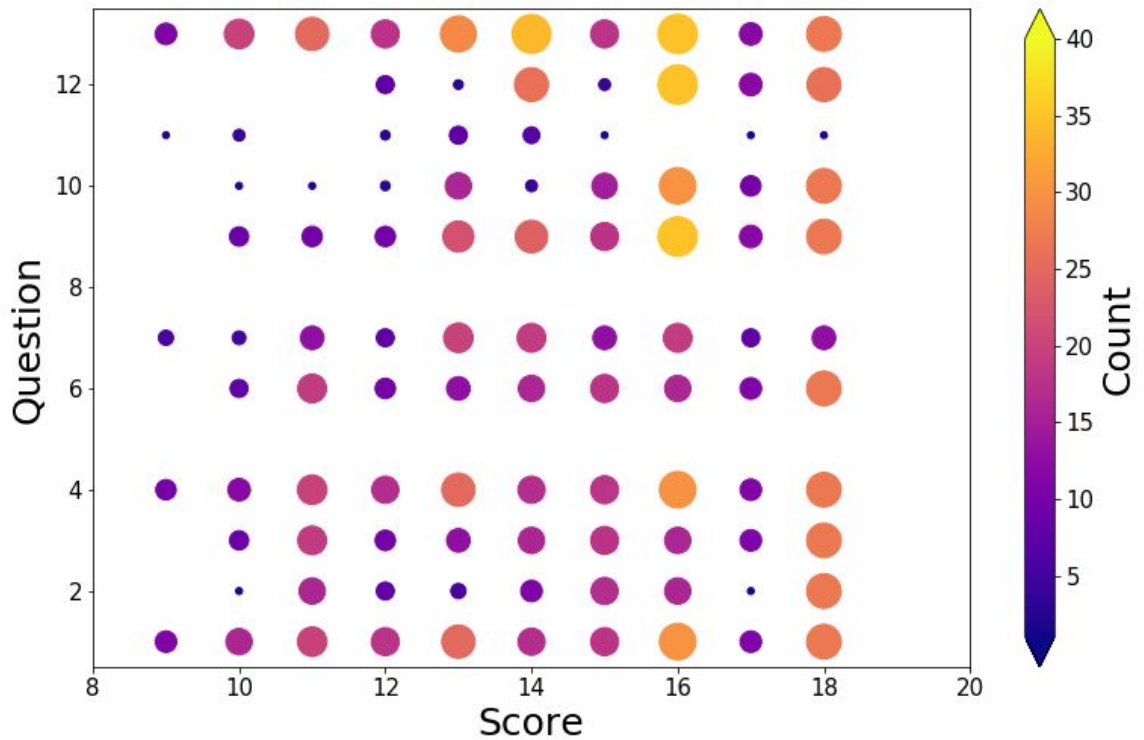


Figure 6.5: The distribution of scores per test for all cases. The scores are weighted by the number of cases that are assigned the score.

figure 6.6 that the theories with shaping terms predict the magnetic mode frequency far less than others. Fundamental magnetic modes are found to match the plasma rotation theory more often than any other model. Including the combination of rotation and shaping effects. This is especially true of the cases with the highest overall scores shown in the darkest colours. If these modes are associated with GAMS then this implies that shaping effects, significant in the design of spherical tokamaks, are a weak dependence of GAM frequency. At least as it affects the possible magnetic signature of our GAM candidates.

Next, we compare our target data – the peaks of velocity spectra – to the predicted GAM frequencies. The first data for this come from the supporting data in test 13, i.e. *any* spectrum with a frequency that matches a prediction, and therefore is based on one velocity peak per time slice. With these numbers we evaluate how closely our peaks match the theoretical values. For each case a matching peak is selected and its frequency compared to the predicted value of the relevant GAM frequency model. Nearly all of the examples in the study (with four exceptions) find that the measured peak frequency is above the theoretical value. The data are reported in table 6.4. The gap is on average 2.5 kHz though the standard deviation of the data is about the same. Figure 6.7 shows the distribution to have a severe skew so that most differences are below the reported average. The data are clearly skewed with a few very large mismatches that raise the average. The bottom of the distribution is a

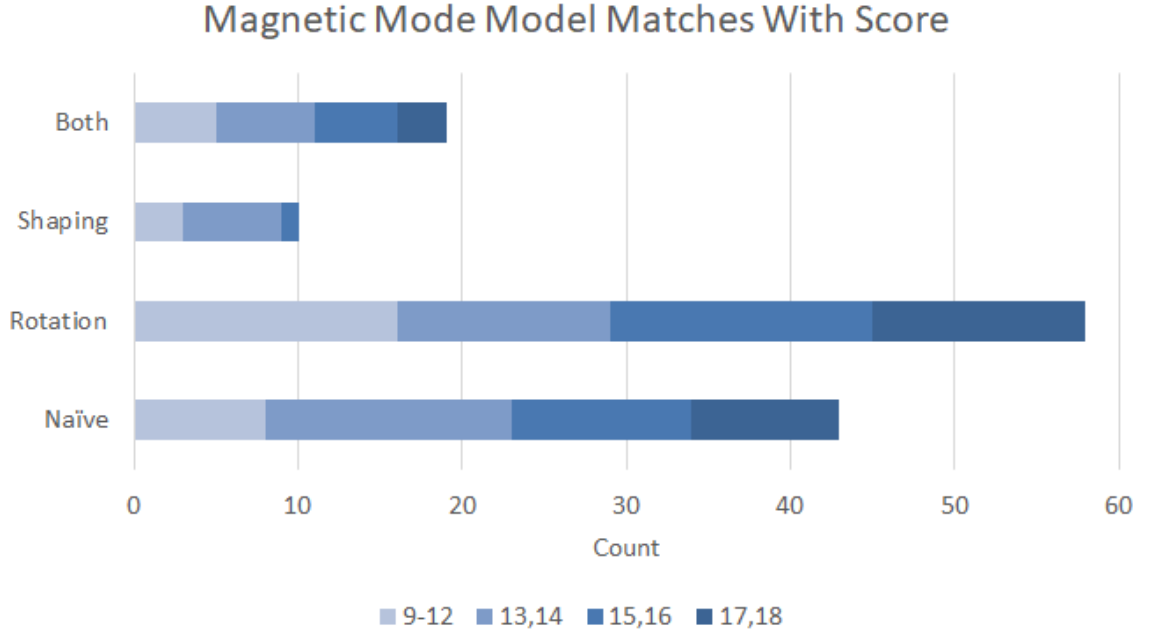


Figure 6.6: The number of just GAM candidate cases with a magnetic mode that match each GAM frequency prediction model. The scores of the cases are shown in blocks in ascending order.

Average Difference [kHz]	2.53
Including Underestimates [kHz]	2.43
Standard Deviation Difference [kHz]	2.24
Standard Deviation Difference [%]	89

Table 6.4: Statistics of the frequency difference between predicted and measured peaks, one for each case in the study. Only four were below the prediction. In all other cases velocity peaks are greater than the predicted values.

similar range to the 1.5 kHz assigned as a strict matching criterion in our testing. Therefore we conclude most of our velocity peak matches are well-matched to theory.

Expanding the data set by including *all* the velocity spectra peaks that match in every case, we can again assess the success rate of each GAM frequency model. This is done in figure 6.8. Since velocity peaks were deemed to be the most important diagnostic measure of GAM activity we do not group the results by total score this time. Instead we take it that each match is equally useful evidence. On that basis a pattern that favours rotation terms, similar to the one shown in figure 6.6 for magnetic modes, can be seen in the theories matched by velocity spectra.

A consistently reproduced experimental finding is that GAMs are found in edge plasma. Here we evaluate how the peaks observed in our set of velocity spectra compare to those observations. The normalised radius of the column used to produce each velocity spectrum is recorded. For every peak that matches a GAM frequency model we have plotted the corresponding column radius per model in figure 6.9. A box and whisker plot summarises

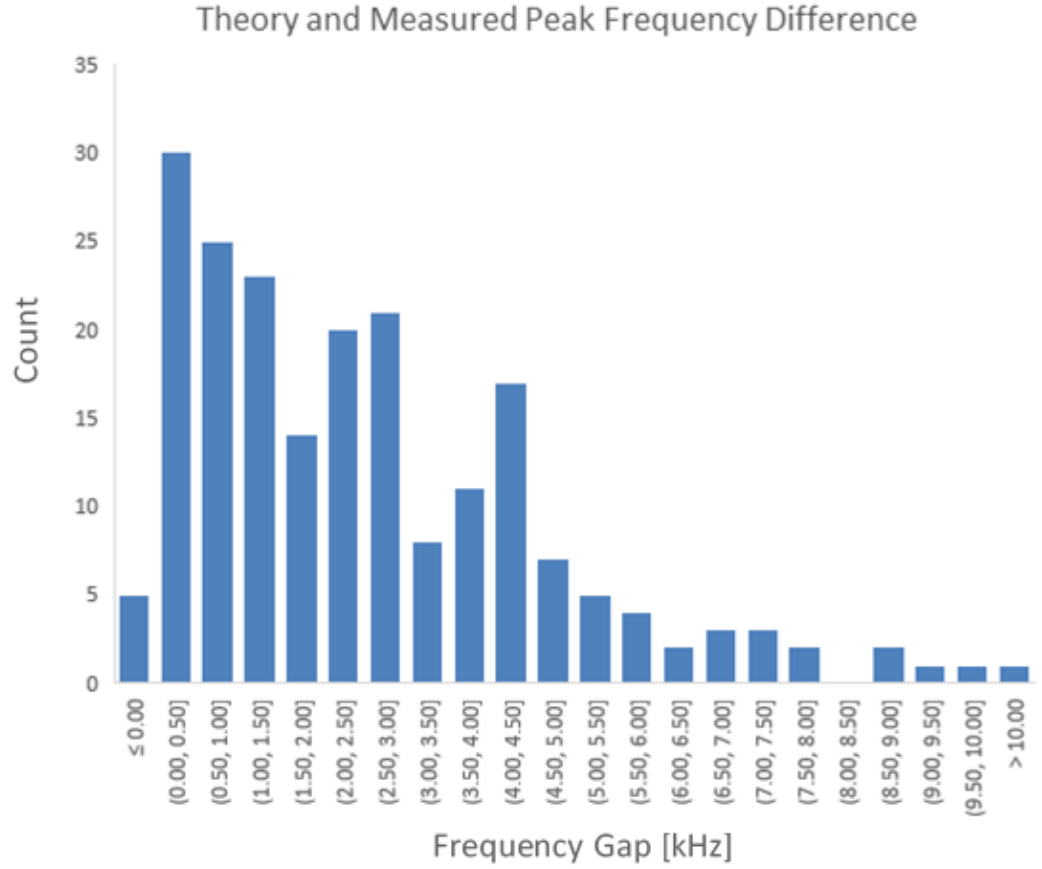


Figure 6.7: Histogram of the differences between measured and predicted frequencies of velocity spectrum peaks.

the distribution with averages, quartiles and range (with outliers highlighted) shown for the same categories. It is immediately apparent that we can find peaks in the spectrum of velocity measurements that match the predicted frequency of GAM oscillations across the range of normalised radius for each model. It is also striking that for none of the models do these matches cluster in the near-edge region of $\rho > 0.95$ that we associate with the pedestal. Instead we observe, with mean and median closely co-located, an average at $\rho = 0.8$. The exception is the rotation model found nearer 0.85 and at normalised radii not less than 0.6. The matches are centralised in the range 0.7 to 0.9 (0.8 to 0.92 for the rotation model.) These findings are especially interesting in light of the BES diagnostics ability to measure density fluctuations in core plasma. While the BES diagnostic is capable of investigating velocity fluctuations at this plasma depth where others cannot, in the absence of good reason to believe the peaks are of zonal flow, the wide range of radii is better interpreted as evidence of the insufficiency of velocity peaks for finding zonal flow.

Another of the key assumptions made by investigations of GAM physics is that the likely frequency of these modes is around 10 kHz, with a wide range of reported observations. We therefore assess at which frequencies we find peaks that match GAM models. This

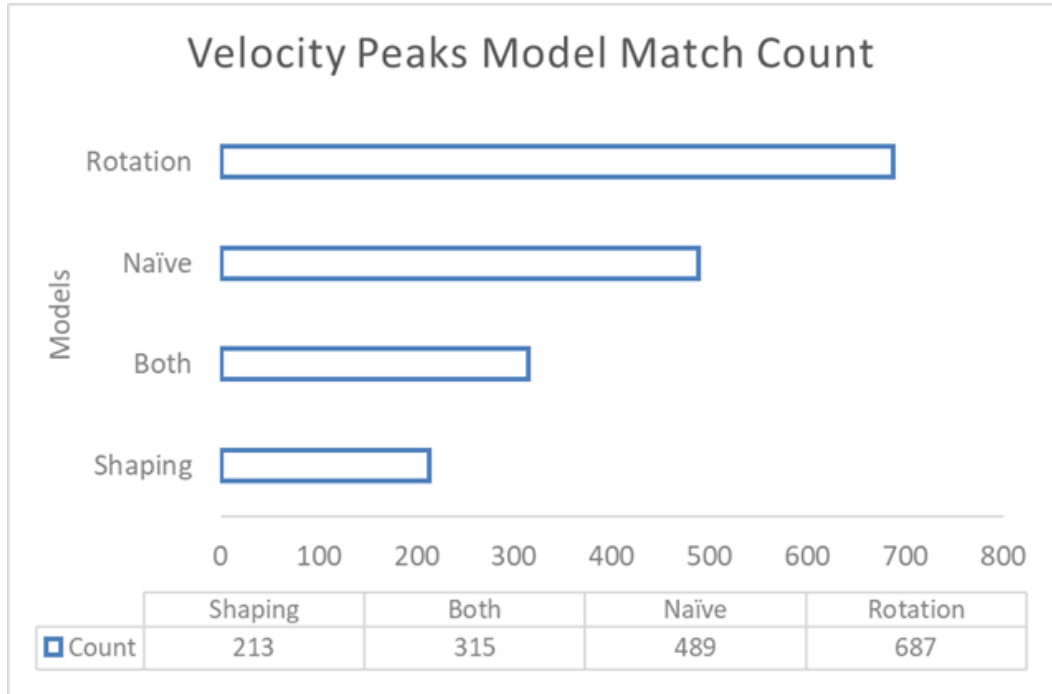


Figure 6.8: The number of velocity peaks in all spectra for all cases matching any model of GAM frequency.

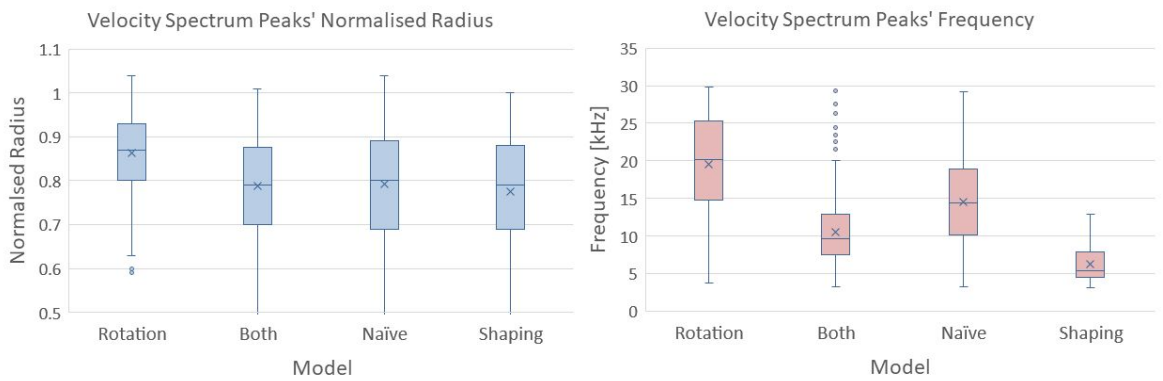


Figure 6.9: The distribution of normalised radius of columns with spectra containing peaks that match GAM models and of the frequencies of those peaks. Both are shown for each model as a box and whisker plot.

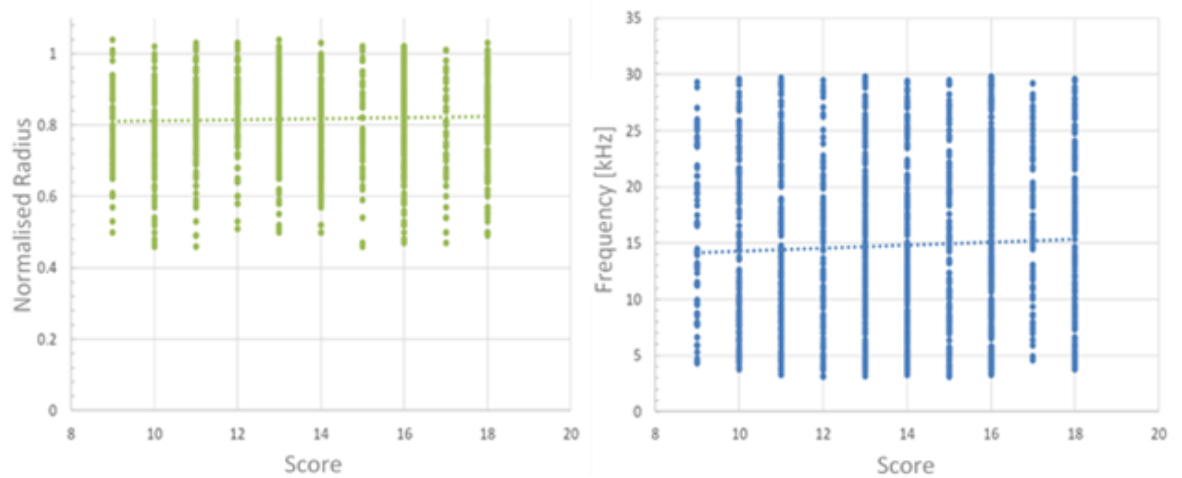


Figure 6.10: The radius and frequency results for each matching peak plotted as a function on the total score in each case. Overlaid fit lines show almost no trend with score for either physical parameter.

investigation is subject to two caveats. First, that matches are restricted to the range 3 to 30 kHz. Second, that the specialised models with shaping and rotation tend to reduce and increase the predicted GAM frequency respectively. The second is clear in the low range of the purely shaped frequency model. Note, though, that the combined effect of the smoothing of the spectrum and the high power of the lowest few frequencies tends to produce sharp effects below 5 kHz that obscure detection. The rest show matches across the full range of frequencies investigated, with a tendency to see velocity modes at higher frequencies. The standard deviations of those models without shaping terms covers the range 10 to 25 kHz in line with the reported order of magnitude of zonal flow physics.

6.2.3 Tests That Predict High Scores

As well as the spectral data we have saved data associated with each of the tests. It is therefore possible to investigate the trends of density, velocity and magnetic signal parameters with the overall score given to each case.

The first data to compare with the GAM physics scores are those just studied - the radius and frequencies identified by our inspection of spectra. Using every model matching peak we produce the plots in figure 6.10 of those values plotted against the score of the case they were spectra of. It is clear from these plots that little trend if any exists in the relationship between measured radius or velocity peak frequency and total score. This inhibits our ability to scan velocity spectra for a characteristic shape of mode peak.

Using the peak measurement tool described in section 6.1, data on the spectrum peaks themselves were recorded. This allows for a quantification of the hitherto visual interpretation of the spectra. In 6.11 we focus in particular on the height and width of spectral peaks. There is a very weak positive correlation between the height of peaks and the score

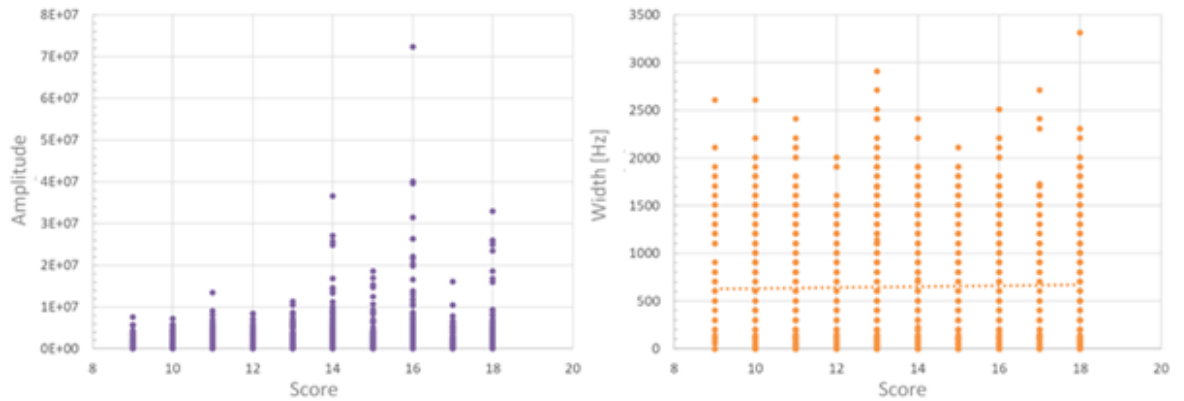


Figure 6.11: Measured parameters of the peaks for matching cases plotted as a function of score. The peak height is plotted left and peak width is right. Trend is a dashed line.

in our tests. More significantly, it can be seen that higher scores are associated with the tallest peaks. On this logarithmic plot peak amplitudes above 10^7 consistently occur only with scores above 14 where the highest score was 18. When the noise floor height is analysed it mimics the pattern shown in the plot for heights of a slight positive trend. That implies that the higher scoring spectra are those with more energy in the fluctuating signal which we know will be the case where a turbulent system has a carrier velocity. Despite this, the width of these peaks also has no trend with score. Most of the peaks measured have a width similar to the frequency resolution of the spectrum (of order 100 Hz.) Broad peaks are seen in cases across the range of scores, though.

As well as individual peaks of the velocity spectra, we analysed the spectra together. In particular, the peak data were aggregated as a count of the number of velocity spectra per case in which a peak was found that matched a GAM model. The results are shown in figure 6.12. The first plot shows, unweighted, the radial extent in number of columns (up to all 8) that matched any GAM theory with overall score. Note that the theories of GAM frequency are not considered separately here so this plot does not say whether the same theory is consistently matched across columns. When all peaks are considered there is again an even distribution of number of columns with score. We therefore have no aggregated information on radial localisation of zonal flow.

If, however, the data are restricted so that only the velocity spectrum peak with a frequency that matches the fundamental (most powerful) magnetic mode are counted, a stronger trend emerges. This is the frequency we expect to be associated with a zonal flow oscillation. Under this condition, as the second plot in figure 6.12 shows, a positive correlation is clear between the number of columns that match the magnetic mode frequency and the overall score in each case. The trend still has high residuals. A near identical trend with lower intercept is found if we further restrict the data to only broad peaks (those with width greater than 400 Hz.) This is a high-level test of the theory of zonal flow that suggests an eigenmode

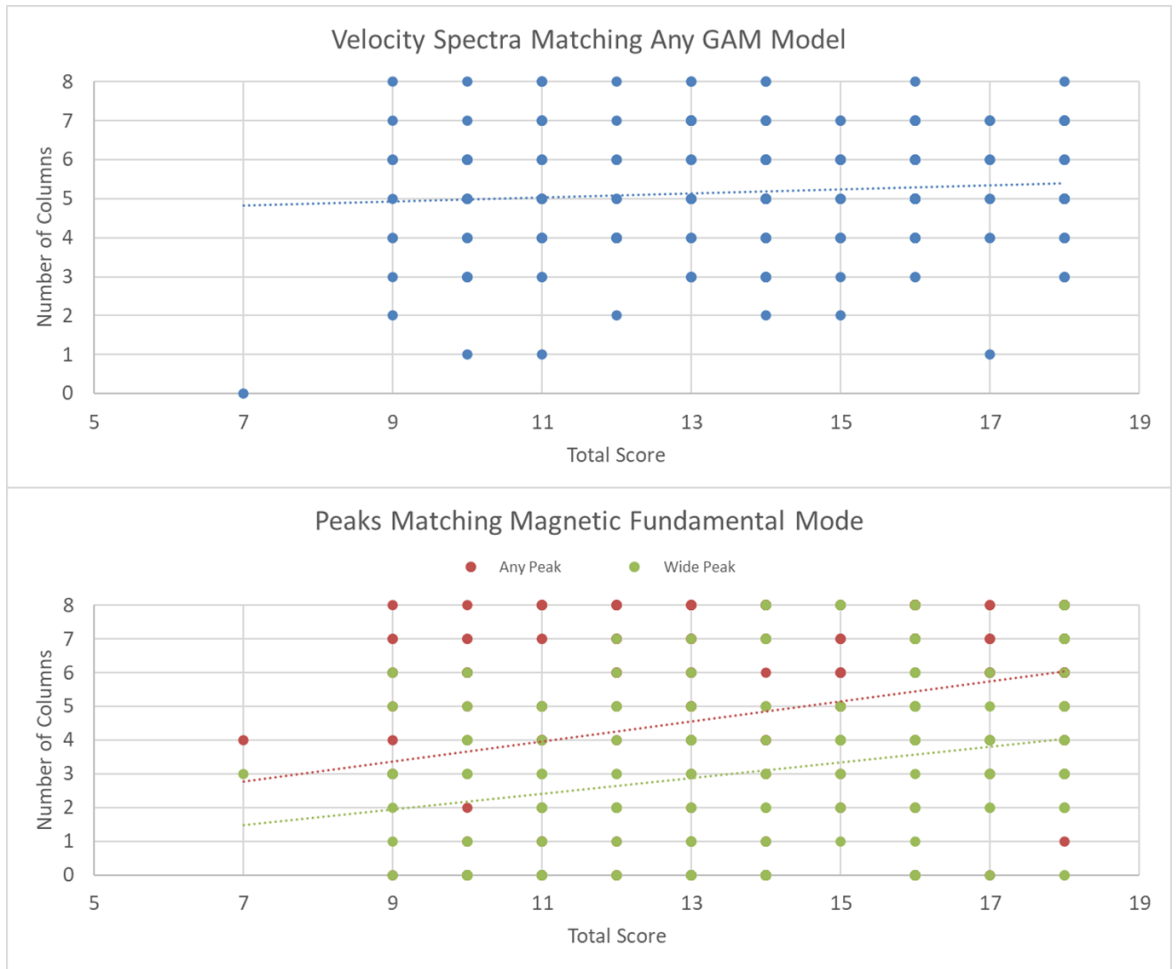


Figure 6.12: The number of columns containing velocity spectrum peaks that match GAM models is plotted with total score for each case. Above, the number of columns of the BES detector producing velocity spectra with peaks that match any GAM model prediction for frequency is plotted against total score. Below, the number of columns with a velocity spectrum peak frequency matching the fundamental long magnetic mode frequency is plotted - first for all peaks and then those of finite width (400 Hz or more). The trend is plotted as a dashed line.

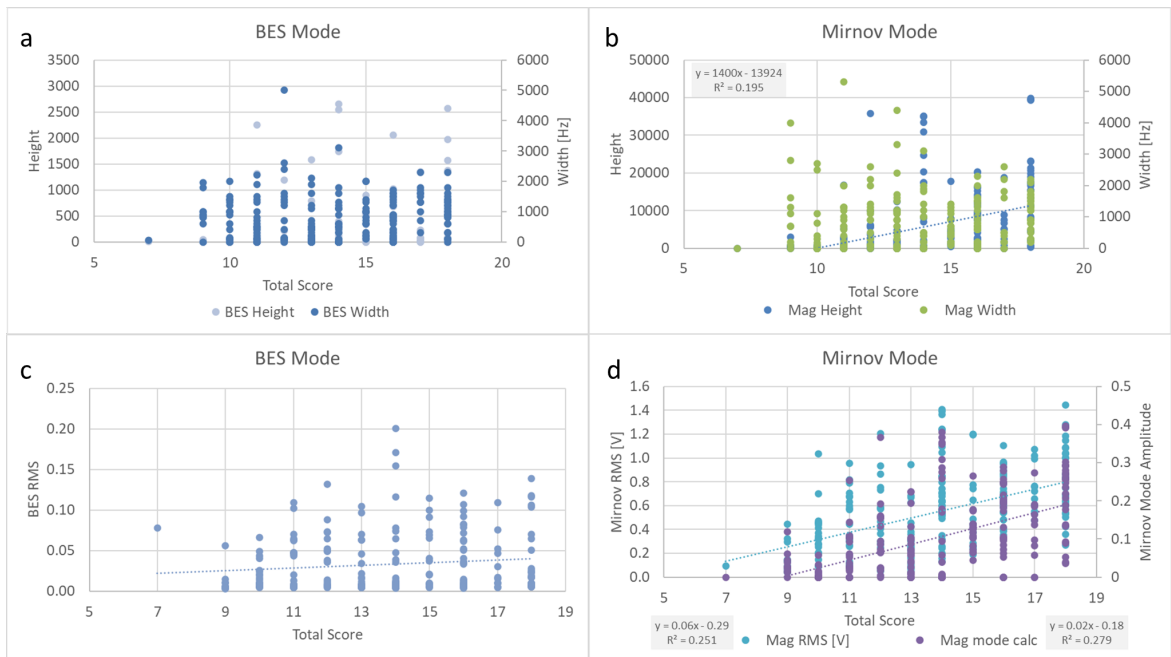


Figure 6.13: Density and magnetic signal and spectrum parameters are plotted against total score for each case. In (a,b) spectrum peak heights and widths are plotted. (c,d) the time series RMS amplitude is plotted against score. The BES signal averaged over channels 10, 14, 20 and 24 is shown in a and c, magnetic signal in b and d.

of oscillation across plasma radii. In that circumstance the same oscillation frequency should be found across many columns rather than the GAM models that predict frequency will vary as a function of radius. In our data it is the cases with a common oscillation frequency across columns that score higher overall in the tests of zonal flow physics. If the eigenmode pattern is present then we should expect a violation of the continuous variation with radius.

To understand the relationship between signals in our high and low scoring cases we can study similar data for the tallest density and magnetic signal's spectrum peaks. Height and width of those peaks are again plotted in figure 6.13. Consistent with our previous results that density modes are weakly related to velocity modes, neither height nor width in the density data show a correlation with score. Again, though, the highest scoring cases are the only ones to show multiple tall peaks. The measured width of magnetic modes also shows no trend with overall score. The tallest peaks we observed were very narrow across multiple columns of the detector. The height of magnetic modes shows a clear correlation with case score. The magnetic peak height, as well as total RMS and that calculated for the fundamental mode contribution all trend strongly positive with score with moderate residuals. Very tall, sharp peaks associated with the powerful, continuous mode are producing the highest scoring examples of velocity spectra. This reinforces the argument that they are influential in producing GAM candidate signals.

Comparing these spectrum trends to time series data, we see that the density fluctuation amplitudes are also uncorrelated with score in figure 6.13(c). The magnetic signal clearly

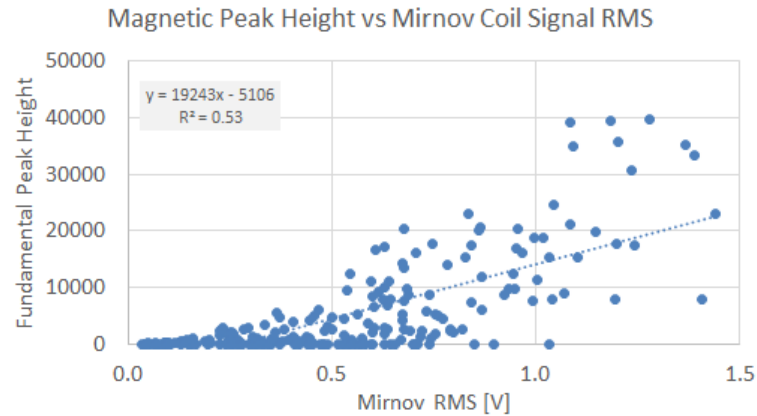


Figure 6.14: Magnetic spectrum fundamental peak height compared to total magnetic signal RMS.

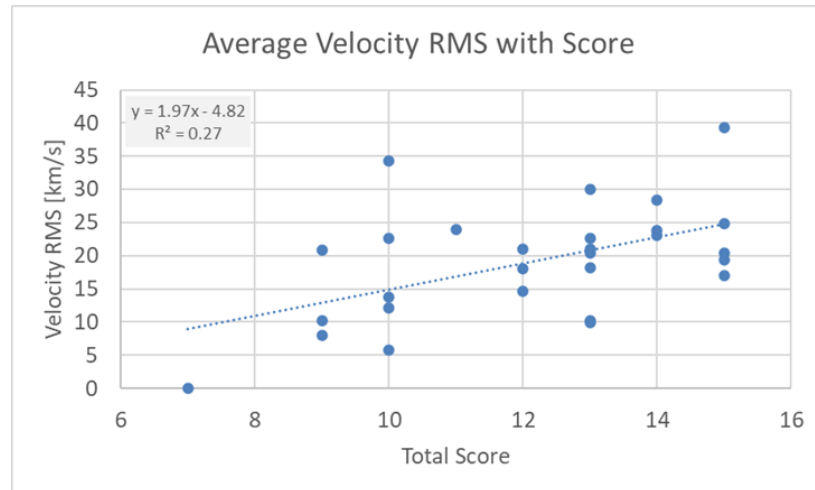


Figure 6.15: Velocity time series total RMS amplitude plotted against total score for each of a few cases in which the velocimetry was re-calculated. A positive trend is clearly shown.

has increasing RMS amplitude with score. That is expected since more powerful modes exist in the signal in cases that score highly. Also plotted is the estimated amplitude contribution from the fundamental magnetic mode (a function of mode height and frequency.) This plots an increasing contribution to the fluctuation caused by the fundamental magnetic mode; correlated with high score in exactly the same way. The relationship between magnetic peak height and the total signal RMS amplitude is plotted in figure 6.14. While there is a strong coefficient of correlation here – just under 0.55 – the extent to which RMS amplitude does not predict the fundamental peak height is a measure of the distribution of power across the spectrum. The magnitude of residuals to a linear fit implies power elsewhere in the spectrum; showing that the potential GAM-related mode does not necessarily dominate the Mirnov time series fluctuation in the cases studied, complicating the comparison to theoretical predictions of amplitude.

Finally here, we looked at the velocity time series. Fewer cases are used in figure 6.15 since there is only data for those passing visual inspection, for which velocimetry was performed

again. For those that do, the RMS amplitude of each column's time series were averaged to produce an overall value for the fluctuation in each case. From these data it is clear that a positive correlation exists between velocity time series fluctuation and overall score. This implies that the higher scoring cases are those in which the velocity varies more. That would be consistent with a picture of varying flow speed as poloidal flows grow.

6.3 Cases From the Study of BES Turbulence Shots

For the remainder of this chapter we present examples of the best data found using our methodology. We begin to characterise these examples according to zonal flow physics categories of interest. These are the highest scoring cases overall, in turbulent low confinement mode, the highest scoring cases where no magnetic mode was identified and a list of lowest scoring cases. GAM studies typically involve only a few shot numbers, so, where appropriate, we limit the data presented to a sample of five highest scoring cases for each comparator category. Ten are chosen from the highest scoring cases on a stratified sampling basis to cover multiple shots as well as examples of shots with multiple high scoring times. This avoids cherry picking results of our approach on the basis of corroborating data that comes from other methods. Where those data score, the overall score is higher anyway. In general, this sample number is most or all of the cases in question. For these best cases we have also repeated some of the previous analyses to show the distribution of experimental parameters for the GAM candidate cases. These examples are used to evaluate the evidence of GAMs in MAST archive data and the implications of that evidence for key hypotheses of zonal flow research.

6.3.1 Highest Scoring Cases

The first scenario reviewed is overall high scoring cases listed in table 6.5. A sample of shot numbers and the time that starts the BES data studied (duration 0.01 seconds) is listed along with their scores. A marker of the time's position relative to the transition times is included where lower case indicates the test signal (D-alpha or H factor) and upper case whether the time is before (L mode) or after (H mode) each automatically marked transition time. Those that are not clearly 'L' or 'H' are nearly all 'dLhH' i.e. before the marked d-alpha transition time but after the H factor transition time. Key data from the tests are also shown: whether a magnetic mode was identified; the frequency of an identified axisymmetric mode; the ratio of measured to predicted magnetic fluctuation amplitudes; the poloidal mode number of an identified magnetic mode and whether an identified magnetic mode frequency matches a GAM model's prediction. For these sample cases we also include the Mirnov fluctuation amplitude to compare to table 5.1. We also inspect the Mirnov spectrograms to corroborate the assignment of an L-H transition time and magnetic mode presence, the results of visual

26 times from 13 shots score 18									
Shot	Time	Score	L-H Marker	Mode?	Q9 [Hz]	Q12	Q11	Q7	$\delta B[T]$
27293	0.25155	18	dLhH [H]	Y [Y]	18600	0.13	-3.33	N	2.65E-4
27294	0.17155	18	dLhH [L]	Y [N]	22600	0.10	-3.33	Y	1.16E-4
27294	0.24655	18	dLhH [H]	Y [Y]	18000	0.13	-3.33	Y	3.19E-4
27297	0.19660	18	dLhH [L]	Y [Y]	17200	0.14	-3.33	N	2.13E-4
27396	0.30155	18	dLhH [H]	Y [N]	17000	0.06	2.12	N	8.20E-5
27397	0.37660	18	H [H]	Y [Y]	14300	0.14	-3.33	Y	5.49E-4
28152	0.22165	18	dLhH [H]	Y [N]	28000	0.13	-3.33	N	1.16E-4
28156	0.24165	18	dLhH [?]	Y [N]	23000	0.11	-3.33	N	4.26E-5
29470	0.39650	18	H [H]	Y [Y]	19100	0.22	-3.33	N	5.73E-4
29982	0.36645	18	dLhH [H]	Y [Y]	18100	0.24	-3.33	Y	6.11E-4

Table 6.5: A sample of cases from the high scoring category. Their score, confinement mode and magnetic mode detection are shown, confirmed by inspection in square brackets. Text in bold has been changed on inspection, not for scoring questions. The frequency of an axisymmetric mode (Q6), the ratio of magnetic RMS to the Wahlberg and Graves prediction (Q8), the poloidal mode number (Q12) and whether the magnetic mode matches GAM theory predictions (Q14) are recorded. Also shown is the calculated magnetic fluctuation due to the fundamental magnetic mode (note without Wang correction for detector outside the plasma.)

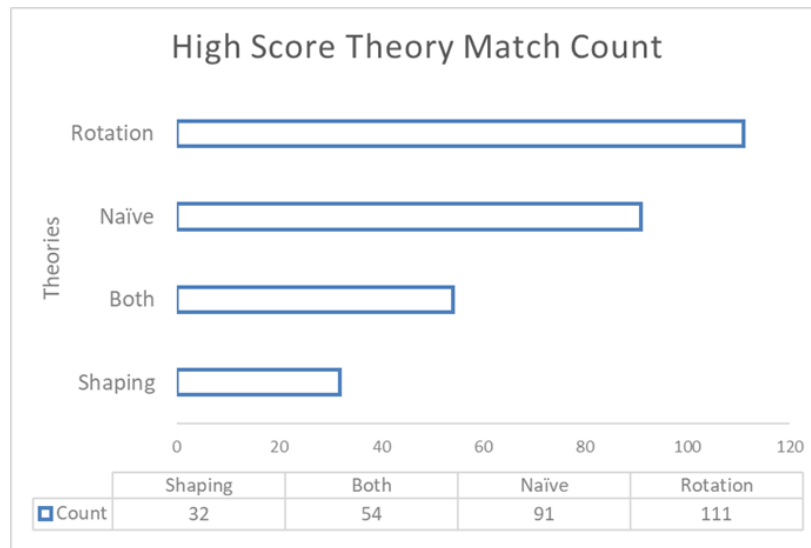


Figure 6.16: The models of GAM theory matched by peaks of the velocity spectra of cases in the high scoring category.

checks are shown in square brackets.

The first investigation of the highest scoring cases is of the GAM frequency models. For this all cases, not just the sample listed above, are used since our visual inspection selected for distinct velocity spectrum peaks in every case. In figure 6.16 the velocity peaks of all spectra of high scoring cases are compared to the GAM models with matches counted in the way described previously. Once again, shaped predictions match less often than not. The distribution of matches for the high scoring subset is the same as the pattern over all cases. Repeating the same test on the fundamental magnetic modes in each case returns

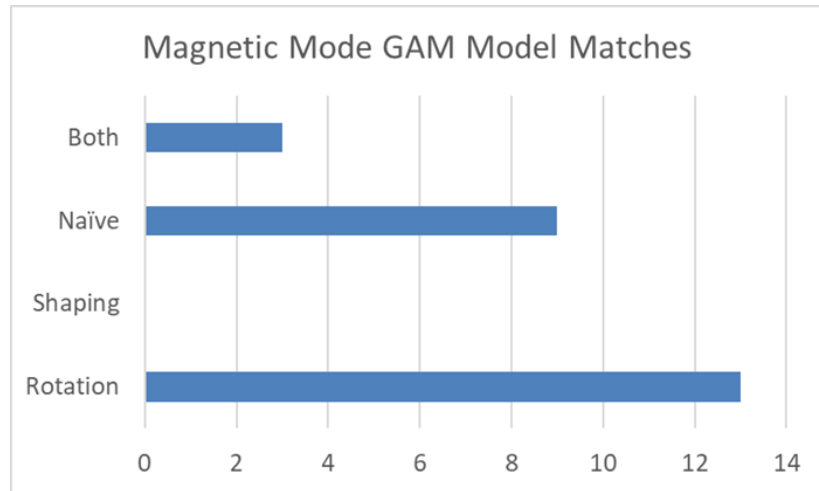


Figure 6.17: The GAM models matched by the frequency of the fundamental magnetic mode in high scoring cases with a continuous magnetic band in their spectrogram.

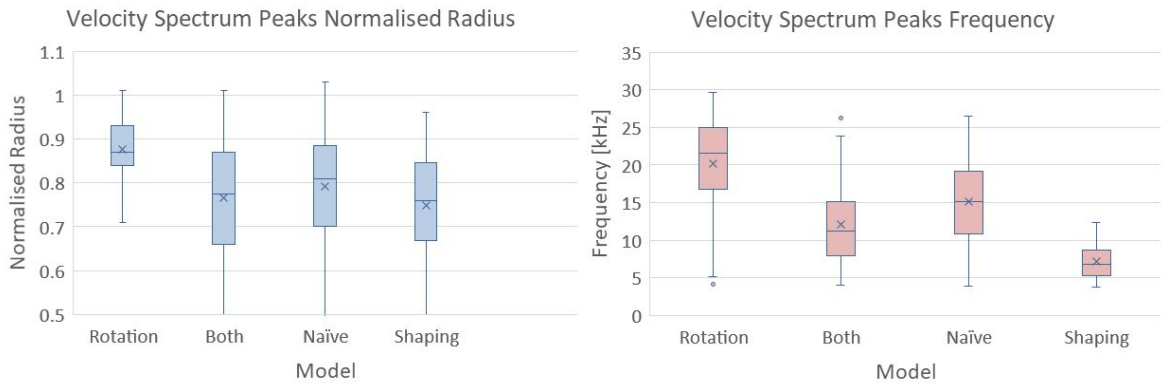


Figure 6.18: The distribution of physical parameters radius (a,b) and frequency (c,d) for peaks of the velocity spectra that match GAM frequency models for cases in the high scoring category. The plots (a,c) show an ordered bar chart of the results, (b,d) are box and whisker plots.

the same pattern again. The predominance of peaks at frequencies with rotational terms for GAM theory is shown in figure 6.17. Note this matches the distribution for peak frequencies of velocity spectra. Of all of the sampled high scoring cases only half have a fundamental magnetic mode with finite width (defined as clearly wider than frequency resolution of the spectrum or greater than 400 Hz) that matches any GAM model.

Turning to the experimental parameters of the matching peaks, we again observe matches across the full range of radii and frequencies of cases studied for figure 6.16. The distribution of frequencies resembles the overall pattern exactly, remaining strongly a function of the tendency of the models to increase or decrease the predicted GAM frequency. The normalised radial locations of matches have a similar distribution, again focused in the range of 0.7 to 0.9. However, in high scoring cases the rotational model is found farther out with quartiles closer to normalised radius of $\rho = 0.86$.

Importantly, with long lasting magnetic modes in the spectrograms of the Mirnov signals

CASE	ρ	1	2	3	4	5	6	7	8	COL'S	PEAK
27293	0.66-0.90	0.41	1.0	0.27	0.23	0.10	0.07	0.12	0.11	4	✓
27294	0.65-0.89	0.09	0.06	0.10	0.19	0.18	1.0	0.31	0.20	3	✓
27294	0.66-0.91	0.42	0.41	1.0	0.30	0.16	0.13	0.20	0.12	4	✓
27297	0.64-0.87	0.09	0.23	0.21	0.17	0.24	1.0	0.33	0.30	4	✓
27396	0.79-1.03	0.21	0.12	0.23	0.16	0.30	0.30	0.48	1.0	4	✓
27397	0.77-1.0	0.77	0.84	0.59	0.73	1.0	0.72	0.55	0.45	8	✓
28152	0.46-0.69	0.20	0.15	0.24	0.16	0.32	0.26	0.54	1.0	4	✓
28156	0.46-0.68	0.14	0.08	1.0	0.21	0.32	0.13	0.07	0.16	3	✓
29470	0.78-1.01	0.61	0.74	0.76	0.79	1.0	0.85	0.77	0.60	8	✓
29982	0.65-0.89	0.74	0.66	1.0	0.67	0.53	0.27	0.06	0.24	6	✓

Table 6.6: The coherence of columns for each high scoring sample case around a reference column chosen as that with the highest coherence in columns either side. Normalised radius spanned by the detector is shown. Contiguous positions with coherence above 0.18 are marked in bold. If those sequences are visible in the spectra is also marked.

from most of our sample, we investigate the relationship of high scoring time slices to each other. The question to answer here is whether or not the high scoring physics persists. Of the ten sampled highest scoring times, only one is not part of a chain of successive times marked as having interesting velocity spectra in this study. Note two are from the same shot number. The duration of successive times averages 0.07 seconds with two longer than 0.1 seconds long. Comparing the scores of each time in these sequences it is clear that the total score fluctuates as the mode persists with no pattern of increasing or decreasing scores repeated in any of the sampled shots. The highest scores (18) of the sample are evenly distributed at the start, middle and end of these sequences. The average length of high scoring sequences of spectra (taken as successive scores of 14 or higher) is 0.06 seconds. Higher shot numbers that are typically longer shots have the longest sequences of highest scoring spectra (18) with both 29470 and 29982 having 0.03 seconds of spectra scoring highest in all tests.

The remainder of this section will characterise the samples listed. The patterns in the spectra that produce high scoring time slices are categorised and examples shown. The magnetic signal has been the focus of our measurements and four patterns are seen in the ten samples. These are shown in the spectrograms in figure 6.19 and described as a solid band (5 of 10), one frequency varying band and two each of long and short intermittent magnetic modes.

In each of these circumstances the velocity spectra were inspected and categorised according to whether velocity spectral peaks were tall or low and if they are present in many or few columns' spectra. Four samples produce tall peaks, all of them cases with a continuous magnetic band in the Mirnov spectrogram. Three of those cases cover the full radius of the detector. Lower amplitude peaks are always associated with fewer columns.

A quantitative analysis of the overlap of velocity spectral peaks is performed by studying the coherence of each columns' signals. The velocity time series are windowed to blocks

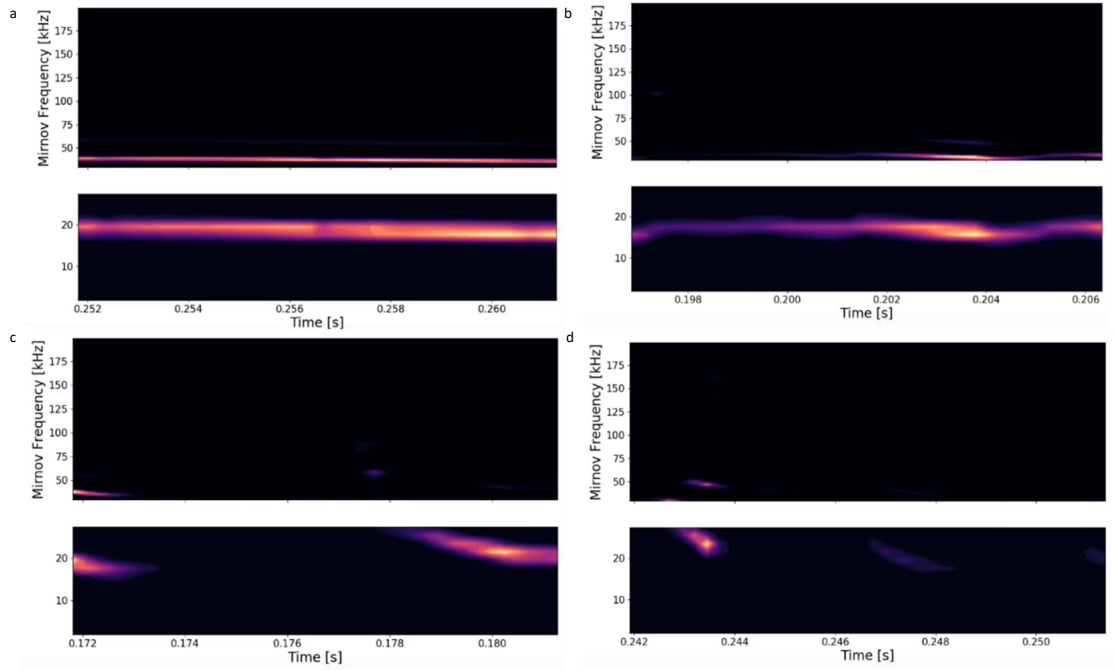


Figure 6.19: Spectrograms of Mirnov signals for cases in the high scoring sample set. These show the four types of magnetic mode observed in the sample set. They are clockwise (a) a continuous band from shot 27293, (b) a varying band from shot 27297, (d) short intermittent bursts from shot 28156 and (c) long intermittent bursts from shot 27294.

of 1024 time steps for the coherence calculation so that spectral features that last most of the 0.01 s will be compared. Every column is compared to all others for each sample. The results for the reference column with the highest coherence to adjacent columns are listed in table 6.6. The width (in number of columns) of spectral features is also recorded; defined as adjacent columns with significant coherence as defined in equation 6.6. A threshold for significance is found using the approximation in Thomson.¹³⁶

$$c_{sig} = 1 - \alpha \frac{1}{\frac{DOF_c}{2} - 1} \quad (6.6)$$

$$DOF_c = 2 \frac{N}{NFFT} \quad (6.7)$$

Taking α to again be 0.05 and using windows of length 1024 this gives a threshold coherence of 0.18. In the final column we compare the frequency of high coherence values to the peaks of plotted spectra to confirm correspondence between the quantitative and qualitative approaches. All do match. The sample from shot 27396 has multiple peaks coherent across columns. The low absolute scores are partly the result of frequency resolution over so

small a range of the available detector nominal Nyquist frequency relative to the sharpness of peaks. Nonetheless, the long time series used for the coherence and other measurements means that the threshold for significant coherence is very low. Radial coherence is a key part of the characterisation of the extent of zonal flows. Access to poloidal and toroidal signals to corroborate with the current BES would be a useful means of further diagnosing the axisymmetric flow.

The high values for coherence, 0.7 to 0.9, are clearly associated with those velocity spectra with a frequency mode that covers the widest possible radial extent. In turn that implies the continuously present magnetic mode. The same ‘type’ of spectrum (continuous band, common peak in all columns) is also apparent with the lowest coherence, though. The next highest scores of 0.4 are for cases with wide and narrow intermittent signals.

Taking all of these data together we classify three types of GAM candidate case in our sample set. First, tall peaks over a large number of columns. Second, low peaks in a few columns’ spectra. Finally, an empty magnetic signal (no identified mode). Key plots of magnetic signal, velocity spectra and spectrogram and coherence are compared for each class in figure 6.20. The velocity correction shown as a dashed line with the velocity time series is due to shaping of turbulence and depends on the pitch angle across the plane of the detector.¹³⁷ It marks the apparent velocity from non-orthogonal transport across the detector field of view.

Spectrograms of the velocity time series calculated for each sample’s reference column per table 6.6 are shown together in figure 6.21. Not included are those graphs already shown in figure 6.20 and shot number 28152 which was not part of a sequence of spectra. To balance temporal and spectral resolution these have frequency resolution of 1.9 kHz. Bands of persistent velocity oscillation are clearly visible in most cases. Some also show harmonic bands. Where significant disruption to the velocity signal occurs, the spectrum is dominated by the low frequency oscillations. To counter this, normalised spectrograms were used to assess the persistence of velocity modes. In table 6.7 the visually determined duration of modes (neglecting intermittency), based on appearance of peaks in velocity spectra, is compared to consecutive spectrograms. Velocity modes are evident for shorter durations in these plots than of the spectrum alone. Again, only the reference channels were measured. While the modes persist, they do so as continuous bands. In the Lotka-Volterra model of zonal flow physics we would expect periodic intermittency over hundreds of microseconds.

The parameter dependence of these modes can be assessed in an integrated way in the comparison to GAM frequency models. In figure 6.23 the velocity peaks of each column are marked with a cross and identified matches with a plus sign. Starting from the reference columns – i.e. those with a distinct peak observed in the spectrum – it is found that the sampled cases with short radial extent tend not to consistently match any particular model in the few columns they cover. Two of the wide extent cases show agreement to a theory

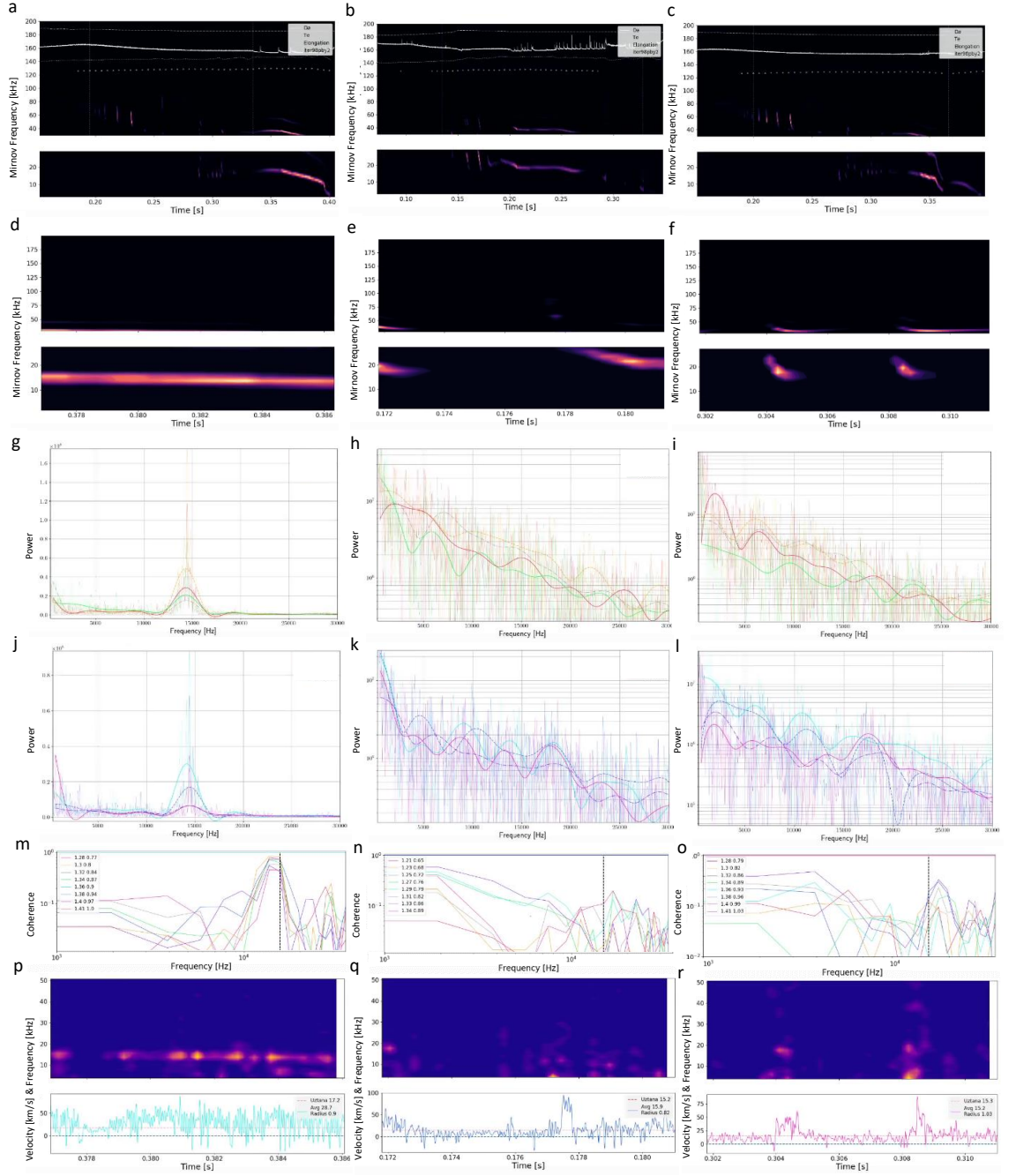


Figure 6.20: The data from a case in each of three high-scoring types found is plotted for comparison. From left to right: (a) cases that are coherent over a wide radial extent (27397), (b) a short extent (27294) and cases with a near broadband magnetic spectrum (c) (27396). From top to bottom are (a-c, d-f) magnetic spectrograms for the whole shot and for the time of interest, (g-i) inboard and (j-l) outboard columns' velocity spectra, (m-o) the coherence as listed in table 6.6 and the (p-r) velocity spectrogram and time series of the reference column (colour per column) therein. The velocity measured and that due to shaping, measured as $U_z \tan(\alpha)$ are reported.

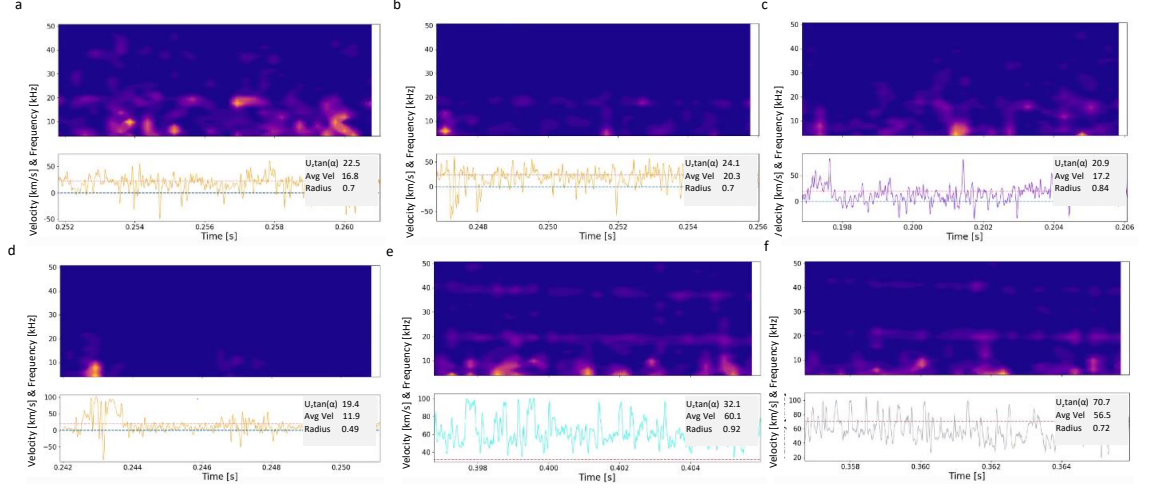


Figure 6.21: Spectrograms of velocity time series for the high scoring cases not already shown in figure 6.20 are plotted for the reference channels in table 6.6. Shot 29982 which was investigated for a peak in one column only is not shown. The velocity measured and that due to shaping, measured as $U_z \tan(\alpha)$ are reported.

across their full radius – the rotational model in both cases per figure 6.23. This is the most commonly matched theory with 5 more of the 10 in the sample showing three adjacent columns that match the rotation model’s predicted frequencies. 1 case matches the combined model. No high scoring sample case matches the predictions of the shaping model in multiple columns. These cases support a continuum theory of GAM frequency.

However, the spectra with tall peaks are consistently those where peaks in multiple columns of the detector occur at the same frequency. No cascade of tall peak frequency with radius, as GAM theories predict, is observed. Again, we underline that it is not better evidence of GAMs to match in many columns than one until their character in MAST is well known. Though we note that the number of columns involved would imply a very wide radial extent for zonal flow.

Evaluating evidence for the eigenmode frequency pattern, the same plots show that in 8 of our cases there is evidence of velocity peaks at a common frequency (of the fundamental magnetic mode) across the detector. In 3 cases these peaks are only those columns in the core plasma (radius less than 0.9), in 1 case at the edge only and the remainder across a range of radii. It is these that the coherence study identifies. Only one case studied shows

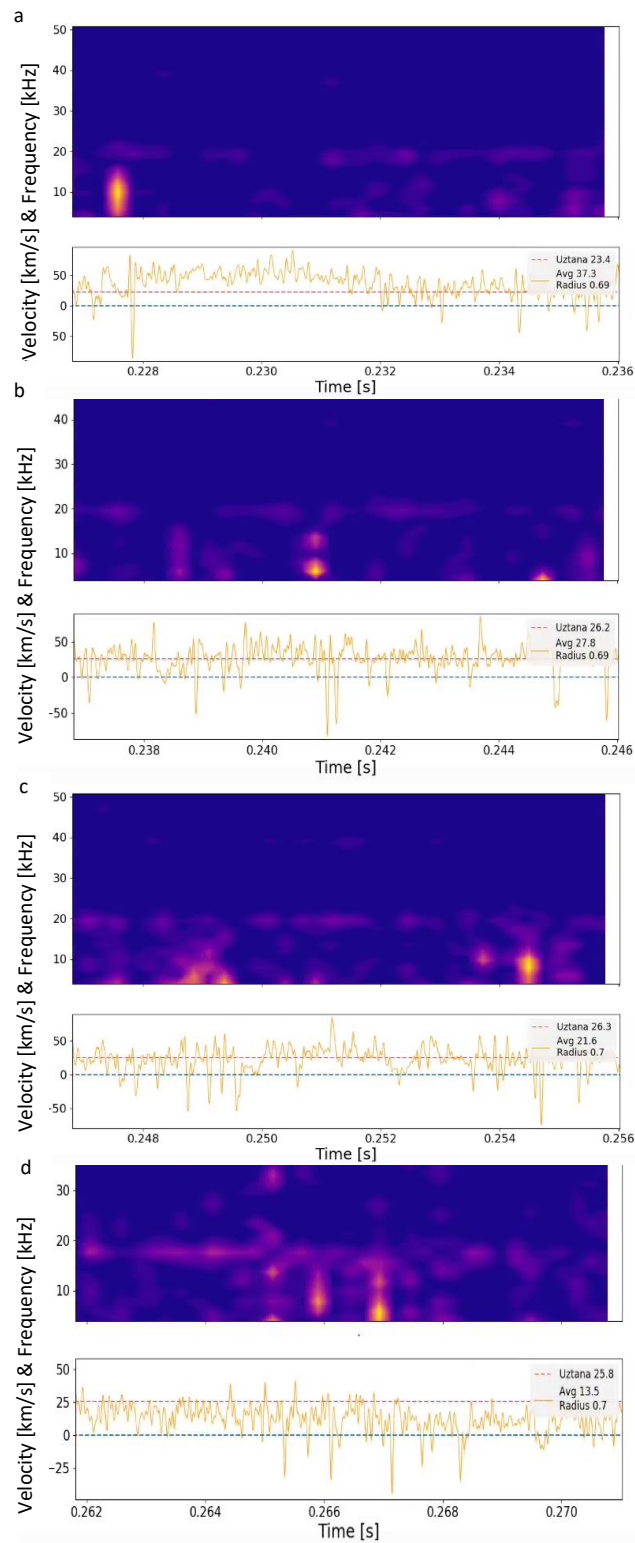


Figure 6.22: Spectrograms of velocity in consecutive time series for shot number 27293 from column 2 (normalised radius 0.7).

Shot	Time [s]	Mirnov [s]	Spectrum [s]	Length [s]	Spec'gram [s]	Length [s]	Diff [s]
27293	0.25155	0.19 - 0.27	0.22155 - 0.26155	0.045	0.22655 - 0.26155	0.035	0.010
27294	0.17155	0.19 - 0.26	0.17155 - 0.26155	0.090	0.17155 - 0.26155	0.090	0.000
27294	0.24655	0.19 - 0.26	0.17155 - 0.26155	0.090	0.22155 - 0.26155	0.040	0.050
27297	0.19660	0.20-0.28	0.17660 - 0.23660	0.110	0.19160 - 0.21160	0.020	0.090
27396	0.30155	0.32 - 0.36	0.30155 - 0.35655	0.055	-	-	0.055
27397	0.37660	0.34 - 0.40	0.35660 - 0.38660	0.040	0.37160 - 0.38660	0.015	0.025
28152	0.22165	-	0.37660	-	-	-	0.000
28156	0.24165	0.25 - 0.26	0.22665 - 0.26665	0.045	-	-	0.045
29470	0.39650	0.34 - 0.41	0.37150 - 0.41150	0.040	0.39150 - 0.41150	0.020	0.020
29982	0.36645	0.30 - 0.40	0.33645 - 0.36645	0.030	0.33645 - 0.36145	0.025	0.005

Table 6.7: Duration of the velocity peaks identified with the reference column in table 6.6. The continuous band length in the Mirnov spectrogram is recorded and compared to the persistence of peaks in velocity spectra and spectrograms for 0.01 second time slices with 50% overlap.

5 times from 5 shots marked L score 14, 15 times from 8 shots marked dLhH score 18									
Shot	Time	Score	L-H Marker	Mode?	Q9 [Hz]	Q12	Q11	Q7	$\delta B [T]$
27283	0.15160	14	L [L]	N [N]	-	0.03	-1.51	N	-
27284	0.16165	14	L [L]	Y [N]	-	0.04	-2.72	N	3.71E-6
27403	0.17160	14	L [L]	Y [N]	-	0.03	-1.51	N	7.71E-6
28152	0.11665	14	L [L]	N [N]	-	0.04	-2.72	N	-
28154	0.17160	14	L [L]	Y [N]	-	0.11	-3.33	N	7.89E-6

Table 6.8: Sample cases that were at times before the transition found using both H factor and D-alpha methods. Data shown are as for table 6.5.

peaks that match neither model nor magnetic mode. Examples are also shown in figure 6.23.

6.3.2 Low Confinement Mode Cases

Since the expectation of zonal flow is that it is strong in turbulent plasma, we consider separately the highest scoring low confinement mode times studied. These, listed in table 6.9, show a mix of times where modes in the spectrum of Mirnov data can be found and not. The spectrograms of these signals and examples of the relevant velocity spectra are shown in figure 6.24. There we can see a lack of magnetic modes. Spectra show some peaks that share frequency but the overall shape is flatter. No tall peaks are seen in these velocity spectra. This sample has the best results in the GAM physics questions with high ratios of

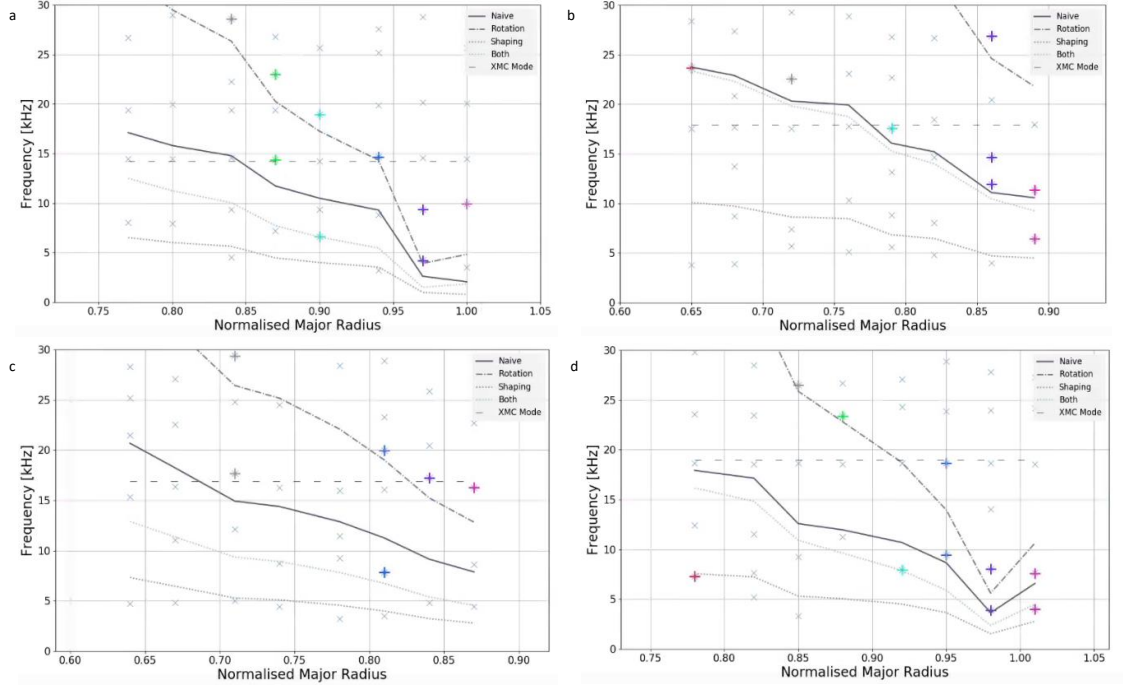


Figure 6.23: Plotting velocity spectra peak frequencies against the predictions of 4 GAM models. Peaks are shown with a cross, those found to match a model are indicated with a plus, colour per column number. The samples that match theory over a wide radial extent (a 27397 and b 29982) and a narrow extent (c 27297 and d 29470). In each case the frequency of the fundamental magnetic mode is also marked with a horizontal dashed line.

CASE	ρ	1	2	3	4	5	6	7	8	SPECTRUM
27283	0.80	0.17	0.15	0.11	0.14	1.0	0.33	0.11	0.15	10 kHz \times
27284	0.69	0.24	1.0	0.14	0.18	0.19	0.32	0.10	0.08	18 kHz \times
27403	0.99	0.14	0.13	0.26	0.17	0.14	0.36	1.0	0.27	12 kHz \times
28152	0.77	0.13	0.18	0.13	0.14	0.27	0.14	0.29	1.0	10 kHz \times
28154	0.70	0.36	0.28	0.19	0.45	0.22	0.28	1.0	0.21	12 kHz \checkmark

Table 6.9: Coherence across radial positions for cases in the L mode sample set. The reference column is that containing the peak in the spectra to be investigated, with normalised radius shown. Also marked is whether coherence plots peak at the frequency of peaks seen in the spectra.

5 times from 5 shots score 16, 1 scores 17									
Shot	Time	Score	L-H Marker	Mode?	Q9 [Hz]	Q12	Q11	Q7	$\delta B[T]$
27294	0.26155	16	dLhH	N	16600	0.11	-3.33	N	-
27398	0.37160	16	H	N	24700	0.13	-3.33	Y	-
27399	0.31160	17	H	N	-	0.19	-2.72	Y	-
29455	0.29650	16	H	N	20300	0.13	-3.33	Y	-
29983	0.32645	16	H	N	23700	0.18	-3.33	N	-

Table 6.10: A sample of cases in which no magnetic mode was identified. Data reported are as in table 6.5.

predicted to measured magnetic fluctuation and poloidal mode numbers closest to 2. This despite an absence of clear peaks in any velocity spectrum. Given the evidence of individual peaks we don't expect coherence across radii. Studying the plots of GAM frequency models versus velocity spectrum peaks shows no match in three case's target columns. The other two match either the naïve or rotational models.

The quantitative study of these spectra using coherence show consistently lower and narrower values across spectra. Note the L mode times do not have a continuous magnetic mode shared across radii. As the final column of table 6.9 indicates by the absence of common medium frequency peaks, the reported values are only high where spectra look the same across all low and medium frequencies. Note that this time the reference channel is chosen to match the target peak, not highest coherence. That is to say that the high values are not associated with a particular peak frequency that would have marked the spectra as of candidate times. These peaks show no persistence across times.

It should be noted (and is shown in figure 6.24) that these L mode cases have extremely slow measured flow velocity compared to the high scoring cases for similar normalised radii (average $\rho = 0.75$.) No velocity, after accounting for the pitch angle effect, is above 5 km/s and two are measured as slightly negative. The measurement is a weighted average of the velocity time series. The velocity spectrum does not have long modes. At times when the spectrum has frequencies of interest we also measure speed up in the flow.

6.3.3 Cases Without Magnetic Mode

Cases without magnetic modes that score highly are shown in table 6.10. All of these times in these shots we know to correspond to the middle of long sequences of spectra with tall peaks. Potentially because the peaks are too sharp, weakly present or at too high a frequency (more than 30 kHz) they do not get recorded as finding a mode. Irrespective of cause, an inspection of their spectra as in figure 6.26 shows velocity peaks at the magnetic mode frequencies in these cases which implies that in fact these cases should be treated in the same way as our overall high scoring cases. We conclude no case is properly high scoring in the current weighting without a magnetic mode and, further, from a plasma that will have been sampled already as a high scoring case.

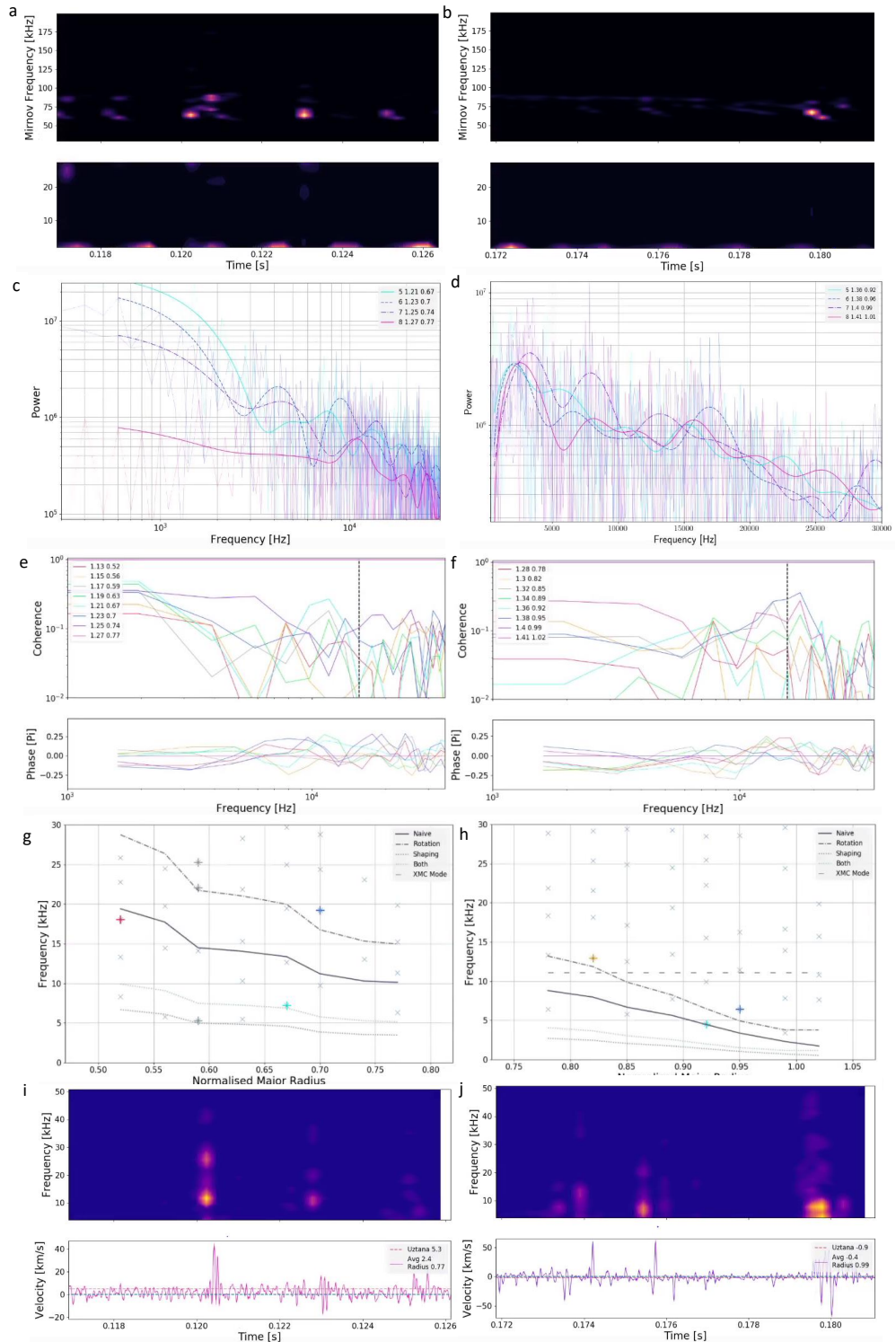


Figure 6.24: The data from two L mode cases are presented. Left is shot 28152 without an identified magnetic mode and right is shot 27403 where one was found. From top to bottom the data shown are (a,b) the magnetic spectrogram at time of interest, (c,d) the spectra with peaks, (e,f) coherence of the column with the peak, (g,h) the comparison of peak frequencies to GAM models and (i,j) the spectrogram of the velocity time series from the column with the peak.

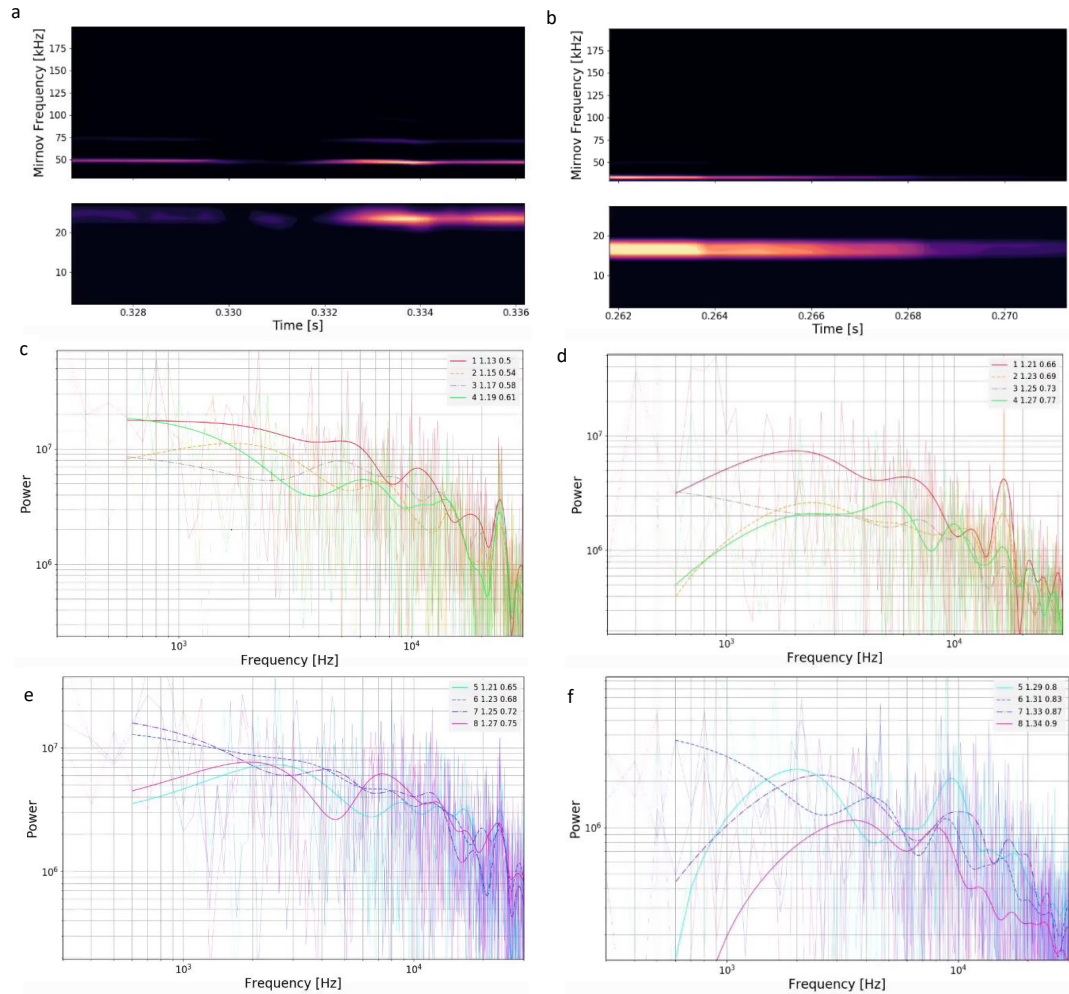


Figure 6.25: The magnetic spectrogram and velocity spectra are shown for two samples (29983 and 27294) from the category where no magnetic mode was detected. Continuous magnetic bands can be seen beginning or ending in the spectrograms a and b followed by inboard (c,d) and outboard (e,f) channels' spectra.

Shot	Time	Score	L-H Marker	Mode?	Q9 [Hz]	Q12	Q11	Q7	$\delta B [T]$
27282	0.29665	9	L	Y	-	0.01	-3.33	N	1.73E-5
27370	0.21660	9	dLhH	Y	-	0.00	-4.54	N	-
29876	0.24150	10	dLhH	N	-	0.07	-3.33	Y	-
29982	0.31645	10	dLhH	N	-	0.06	-3.93	Y	-
30175	0.22645	10	dLhH	Y	-	0.05	-3.93	N	5.40E-5

Table 6.11: A sample of lowest scoring cases. Data reported are as in table 6.5.

6.3.4 Lowest Scoring Cases

To complete the data set a selection of the lowest scoring times is included in table 6.11. Again, many are part of a sequence with a distinct magnetic mode. They score poorly because of the absence of any match of velocity peaks to GAM frequency models at any radius of the detector. Nonetheless, the evidence of the velocity spectra alone would have included these as compelling candidate times. The spectra of both density and velocity are shown in figure 6.26. These underline the need for a rigorous approach to zonal flow detection. Searching with spectra alone suggests examples like these as signatures of zonal flow, though they may meet no other experimental expectation, or even match the range of predicted frequencies.

6.4 Fully Automated Study of Confinement Transition Times

The final experiment of this project takes the automated, systematic approach devised above and runs it on a large list of shot numbers without checking velocity spectra. The pattern of spectral behaviour is already established in the wide shot search performed in section 6.3 – tall peaks across a wide radius correspond to a magnetic mode and peaks in single or few columns of the detector tend to be low contrast. Since we have designed tests of the L-H transition and know that this is expected to be a time of maximum zonal flow amplitude, this experiment targets those times exclusively. A list of all shot numbers was produced for which BES data can be found and a transition identified. This was cropped to include only those shot numbers where an L mode of at least 0.1 seconds exists after the NBI is switched on so that critical turbulence can develop and the list is made tractable for study with MAST data. This gives 209 shot numbers to study. The initial times for velocimetry are selected as 0.005 s before the marked transition time and 0.01 and 0.02 s before that. With two transition markers we therefore study 6 times in each shot. The expectation is that only one of the D alpha or H factor markers will accurately find the transition time and each has a roughly 50% accuracy rate such that no more than 25% of the data in this survey will properly be of the pre-transition times for peak zonal flow. Once again, we will reduce the data set by sampling the highest scoring cases with and without a detected magnetic mode.

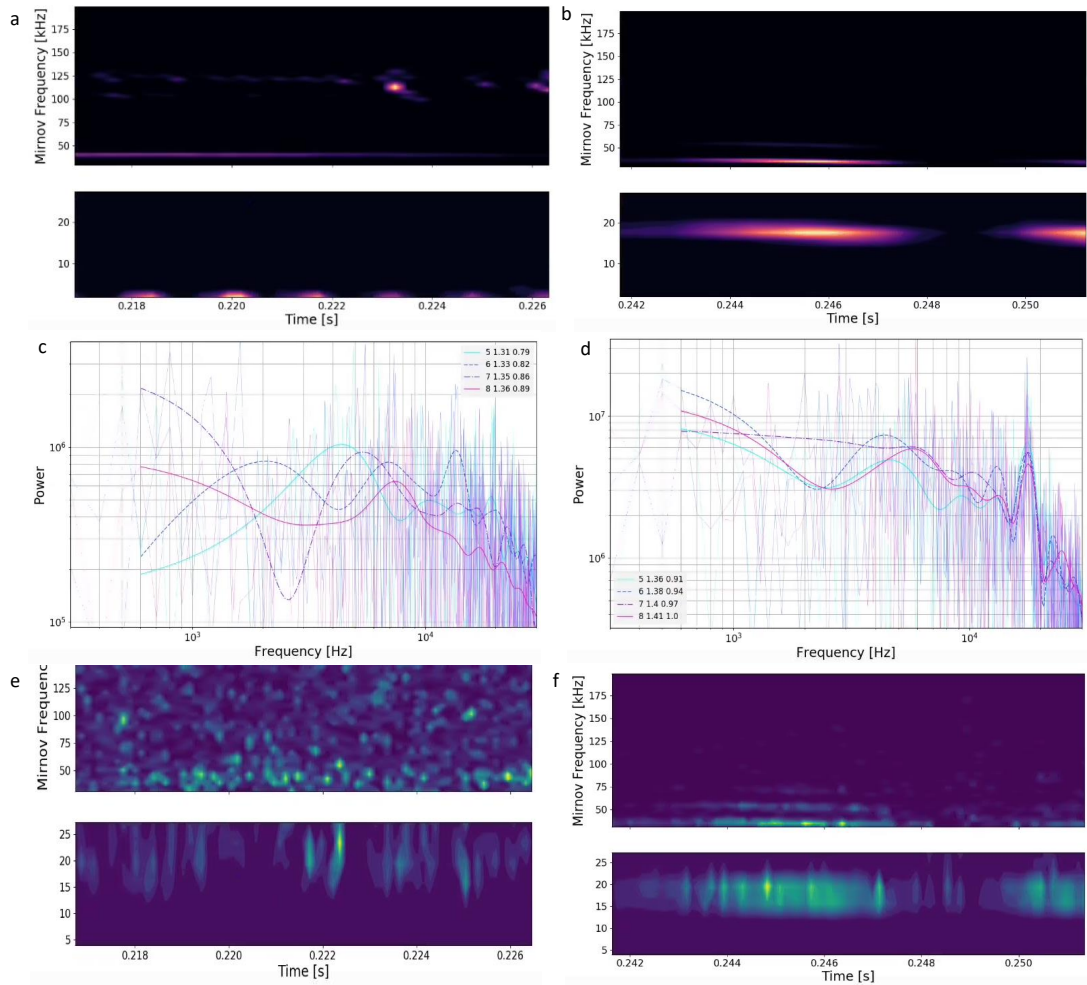


Figure 6.26: Magnetic spectrograms (a,b), outboard velocity spectra(c,d) and BES channel 20 spectrograms for shots 27370 (a,c,e) and 29876 (b,d,f) from the sample of lowest scoring shots. The velocity spectra clearly show peaks at medium frequencies, with and without density modes.

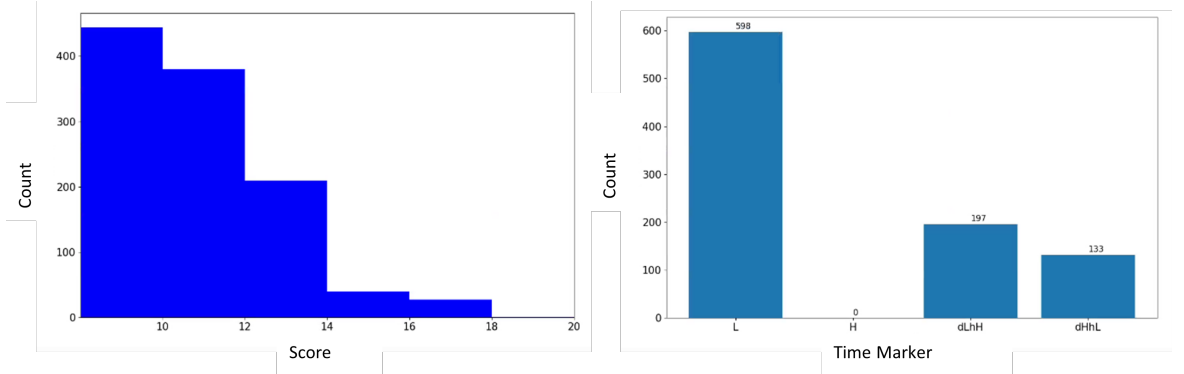


Figure 6.27: Review of the survey method data. The full scores are shown in a histogram left, showing almost all score very low. They must score at least 14 to be considered (without a magnetic mode.) Right is a chart of the time markers involved showing that more than half the results are from times before both transition markers. dLhH denotes before the d-alpha marker and after the h factor marker, vice versa for dHhL.

Results of the full survey are shown in figure 6.27 for completeness but given the low L-H prediction accuracy we are only concerned with the highest scores in this study (whereas before the spectra had all been pre-approved as ‘of interest’ and so the full data set was valuable.) Evidently the vast majority of pre-transition times still score lowly even accounting for the low success rate of the transition markers. That implies a lack of zonal flow physics in these measurements too. More times are successfully measured at ‘L’ times i.e. in advance of both transition markers than one or other.

When the physical tests of the data set are considered we see that a large number fit in the ranges of interest at middling scores in figure 6.28. Axisymmetric magnetic modes continue to be found at the upper end of our predictions for GAM frequency. Low scores show results for the ratio of predicted and measured magnetic fluctuation that are extremely low – the measured value is much lower than predicted. The ratio matches within an order of magnitude in the pre-transition times far more often than in previous shots studied and is in general a much higher ratio. Studying the prevalence of magnetic modes as in figure 6.29, we see that it is still very common at all scores for a majority of cases to measure a wide peak in the Mirnov spectrum at GAM frequencies, though no limit is set on the width or height of these peaks so they may not be sharp with high contrast. The same figure shows the distribution of GAM theoretic poloidal mode numbers (of axisymmetric magnetic modes) in which it is clear that most are measured below the range of interest still but several cases at high scores do have an approximately $m = 2$ pattern. Detailed results from the highest scoring cases with and without a magnetic mode from L-H transition times are presented in tables 6.12 and 6.13 respectively.

The cases without a magnetic mode detected, those definitely in a turbulent L mode plasma, still do not show a consistent match with the expected GAM physics. By contrast, the highest overall scoring transition cases show examples in which the transition is correctly

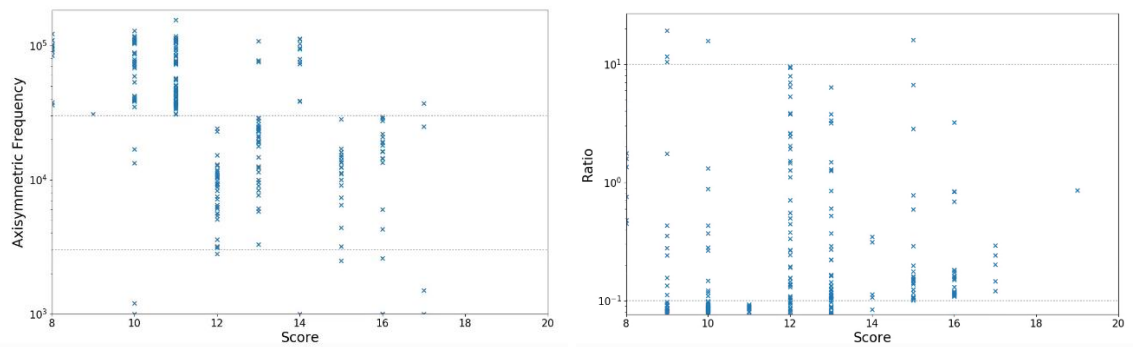


Figure 6.28: Plots of the magnetics data from the L-H transition sweep. On the left the frequency of modes found to be axisymmetric with Mirnov coils is shown as a function of test score. The range of interest – between 3 and 30 kHz – is marked. On the right, the ratio of measured to predicted magnetic fluctuation is shown as a function of score. The order of magnitude boundaries are marked.

Shot	Time	Score	L-H Marker	Mag. Mode?	Q6	Q8	Q12	Q14
30325	0.34734	19	H	Y	600	0.856	1.5	N
27579	0.19523	17	-	Y	25000	0.292	-3.3	N
29769	0.26500	17	-	N	1000	0.146	12.3	N
27399	0.31353	17	Da	Y	37000	0.203	-2.7	N
27579	0.20523	17	-	N	700	0.121	-3.3	N
29803	0.18500	17	H, Da	Y	1500	0.241	20.1	N
28091	0.29950	16	H	Y	0	3.228	2.7	N

Table 6.12: Data from the highest scoring cases in the L-H transition time sweep. Column headings are as in table 6.5 except L-H marker which shows which if any of the transition markers accurately finds the transition according to an inspection of the Mirnov spectrogram and D-alpha signal.

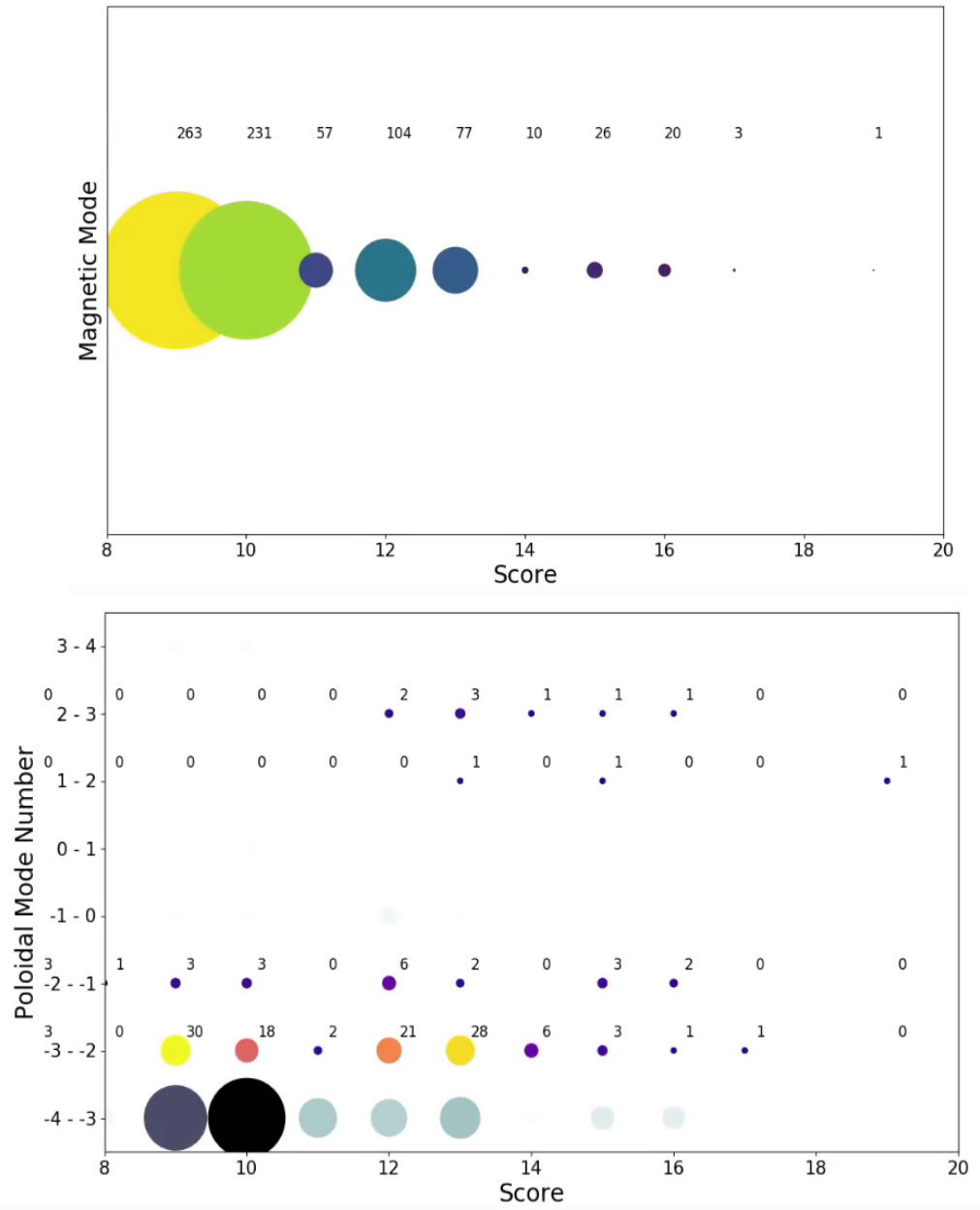


Figure 6.29: Distribution of cases with result and score weighted by number of cases for GAM physics results. Above for whether or not a magnetic mode was identified at the time being studied. Below for the poloidal mode number of axisymmetric magnetic modes. In this plot those cases with the expected mode number range $\pm 1 - 3$ are marked in colour and counted. The majority of cases at every score have mode number below -3.

Shot	Time	Score	L-H Marker	Mag. Mode?	Q6	Q8	Q12	Q14
27865	0.28493	16	L	N	14400	0.113	-3.3	N
26582	0.24000	16	L	N	2600	0.837	-3.3	N
29782	0.30593	14	L	N	1000	0.084	20.1	N
27597	0.21523	14	L	N	600	0.058	-3.3	N
27398	0.20000	14	L	N	79200	0.024	-2.1	N

Table 6.13: The highest scoring cases from the L-H transition sweep without a magnetic mode identified. Their score, confinement mode and magnetic mode detection are reported. The frequency of an axisymmetric mode (Q6), the ratio of magnetic coil RMS amplitude to the Wahlberg and Graves prediction (Q8), the poloidal mode number (Q12) and whether the magnetic mode matches GAM theory predictions (Q14) are recorded.

CASE	ρ	1	2	3	4	5	6	7	8
30325	0.86 – 1.12	0.14	0.16	0.23	0.10	0.46	0.41	0.76	1.0
27579	0.88 – 1.12	0.24	0.18	0.12	0.20	0.21	0.41	1.0	0.45
29769	0.80 – 1.04	0.10	0.36	0.49	0.44	1.0	0.54	0.32	0.08
27399	0.78 – 1.02	0.21	1.0	0.41	0.26	0.28	0.4	0.35	0.15
27579	0.90 – 1.15	0.12	0.21	0.21	0.09	0.52	1.0	0.18	0.09
29803	0.86 – 1.12	0.05	0.07	0.23	0.41	0.37	1.0	0.14	0.16
28091	0.54 – 0.80	0.33	0.27	0.37	1.0	0.37	0.30	0.13	0.52

Table 6.14: Coherence across radial positions for highest scoring transition time cases. The reference column is chosen on the basis of highest coherence with neighbouring columns.

marked, the magnetic fluctuations have correct order of magnitude and the expected poloidal mode number can be evidenced. A further two show axisymmetric modes near zero frequency, potentially motivating ZFZF rather than GAM physics studies. Examining the velocity spectra of these most compelling cases' peaks and comparing to models of GAM frequency we see evidence in figure 6.30 in support of the rotational model once again, on the assumption of a continuum frequency pattern.

For comparison, we once again present an analysis of coherence between spectra of high scoring cases in table 6.14, though this time without seeing the spectra in advance. The reference columns indicate those spectra that have the highest coherence in our measurable frequency range. These scores are generally lower than for the cases chosen on the basis of high contrast spectra. Once again we see a significant radial extent to the coherence, based on values of a common frequency. However, velocity spectrograms of the reference columns' velocity time series in each of these cases show no indication of a constant mode, though often dominated by powerful extreme low frequency events. This suggests that GAMs are not strongly present in these data despite the commonality of powerful frequencies.

6.5 Summary

In response to the unexpected strength of magnetic signals in the initial survey of MAST shot numbers that were strongly turbulent, a rigorous system testing density, velocity and

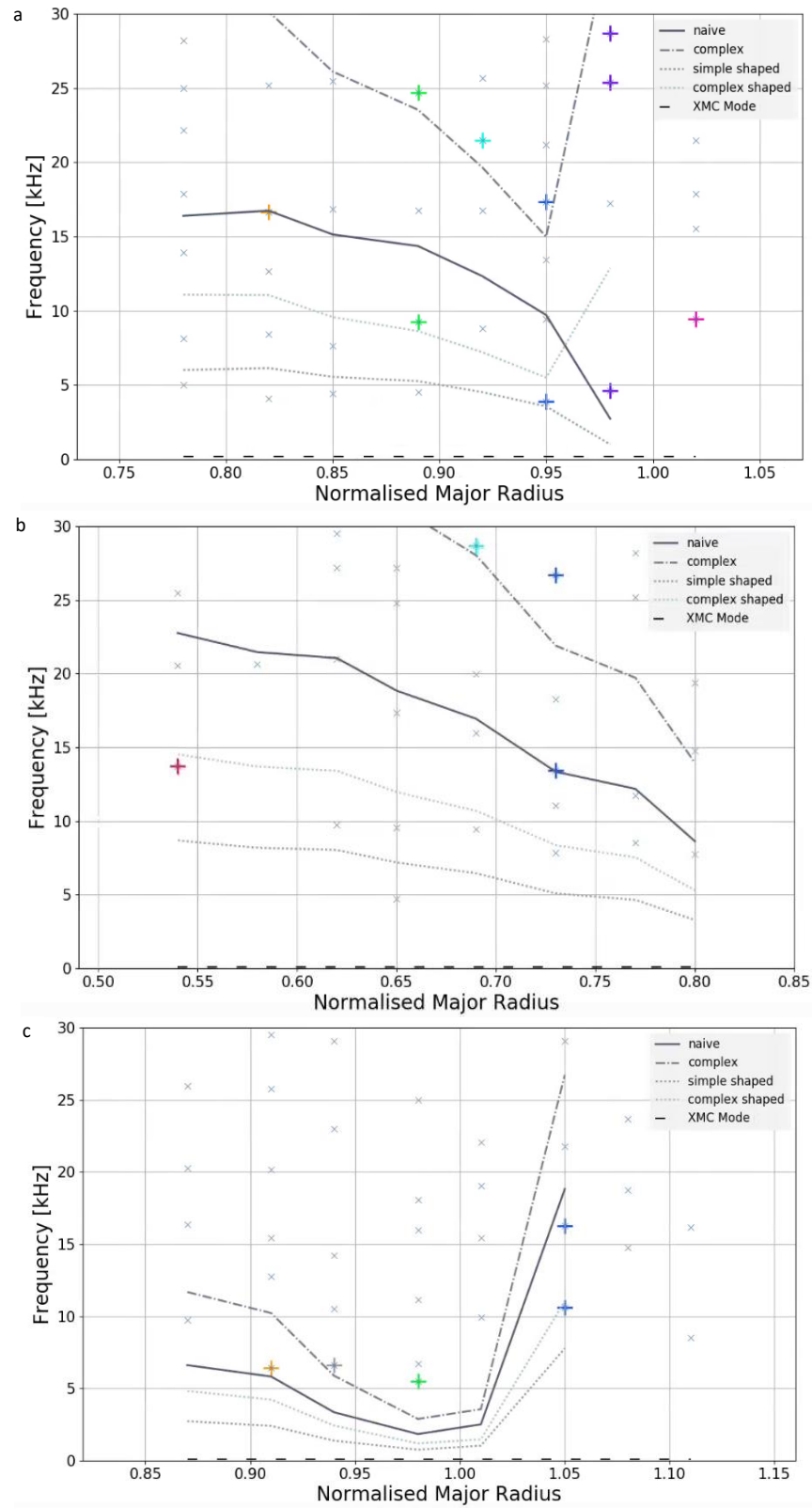


Figure 6.30: Comparison of theories of GAM frequency and velocity spectrum peaks for the three cases that match GAM physics in table 6.13. From top to bottom, shot numbers (a) 27399, (b) 28091 and (c) 30325. The 'complex' model is the rotational model in equation 6.3.

magnetic signals was devised. In each case studied the first data used is the pattern of the velocity spectra. These should indicate substantial peaks (or common peaks) in line with the basic expectation of GAM signatures in velocimetry data.

The first investigation uses the typical approach of research into zonal flow in studying only a few shot numbers. 12 that had the magnetic phenomenon in question were identified in section 5.3.3. These were compared according to a series of tests designed first to establish the relationship between the density, velocity and magnetic signals and second to identify known physical behaviour of plasmas with GAMs. The responses in those shots were recorded and used to determine what criteria would count as passing each test so that those tests could be automated. The systematising of our investigation into GAM detection was taken further by introducing weighting of the tests, not just pass/fail measurement. A full breakdown of the tests, their success criteria and weighting is given in figure 6.3.

The automation enabled a greatly expanded investigation. A long shot list was created, pooled from previous investigations, turbulence experiments and the diagnostic logbook to select for shot numbers with the best chance of revealing GAMs. The full duration of each of these shots was run through the velocimetry algorithm in time slices of length 0.01 seconds. The resulting velocity spectra were inspected to identify 220 cases of interest. For each case (shot and time) the weighted score was recorded. This enables an evaluation of both cases for evidence of GAMs and the method for their detection using BES and velocimetry.

The pattern of scores across all 220 velocity signal spectra of interest showed none that scored more than 75% of points. This was true of both cases with and without a strong magnetic signal which could score 24 and 19 marks respectively. Note that investigating the highest scoring cases without such a mode indicated a failure of detection rather than truly broadband magnetic signals and so the category was discounted from the list of candidate times.

We can therefore identify a key result: best candidate cases of GAMs in two physical categories – those times with the highest scores overall in table 6.5 and those with highest scores in L mode plasmas in table 6.8. Bispectral analysis is required to rule in or out these examples. All shots that score highly must have velocity peaks that match a model of GAM frequency. Our cases therefore represent shots with the best evidence of zonal flow behaviour in the signature of velocimetry. The overall highest scores tend to come from shots where strong magnetic modes can be measured but that tend not to match expected GAM behaviour.

The five best cases in L mode shots match some expected GAM behaviours but do not have the same magnetic behaviour and tend to score lower. While a magnetic mode can sometimes be detected in the GAM target range of 3 kHz to 30 kHz and with $m = 2$, none in our sample is measured as axisymmetric and their spectrograms are not dominated by continuous bands. The L mode cases have much more diminished peaks in their velocity

spectra relative to their noise - counter to our expectation of a significant impact of zonal flow on velocity. In the L mode sample the BES signals peak in the GAM frequency range and the magnetic mode is neither at the same frequency nor matches the velocity spectra.

On inspection, two of the ten overall highest scoring cases turn out to be in the L mode and 4 do not have the continuous magnetic mode. One such case (27297 at 0.0.1966 seconds) is immediately before the L-H transition. Investigating these cases shows that the peaks that match models of GAM frequency can be found across a broad range of radial positions and frequencies. The most commonly matched models are those that neglect shaping terms. The model with terms for plasma rotation has the highest number of matches. For these cases the spectrum peaks are produced mainly over a normalised plasma radius from 0.84 to 0.92 at a mean average frequency of 20 kHz. An analysis of the coherence of spectra across the BES detector shows a modal average extent of four columns with substantial peaks at the same frequency and three cases that cover substantially all of the detector's width. Plotting all of the velocity spectra peaks shows that in 5 of the 10 cases sampled the frequency of the fundamental magnetic mode is present in all spectra. By contrast, only two cases show matches to a GAM theory across the same range. If GAMs present over a wide radius, in line with evidence of velocimetry, then we have evidence of the eigenmode hypothesis of GAM frequency in larger spherical tokamaks. We have investigated the Wahlberg and Graves amplitude hypothesis in our H mode cases and find a mismatch of amplitude. When spectrograms are produced to evaluate the persistence of the velocity modes (recall that the magnetic modes exist over long time scales in each shot) we find that those cases without a concurrent magnetic mode do not persist beyond one time slice. Those that do, can be seen for an average of 0.036 seconds and the longest lasts 0.09 seconds.

These cases that start from the velocity spectra are supplemented by a sweep of 209 shot numbers at L-H confinement mode transition times. This was performed on a fully automated basis and the scores analysed again for highest scoring cases with and without a magnetic mode. Three of the highest scoring cases show evidence consistent with GAM physics, the Wahlberg and Graves fluctuation amplitude estimation and a rotational continuum model of GAM frequency. However, they have broadband velocity spectrograms i.e. weak modes. Axisymmetric modes at extremely low frequencies may suggest zonal flow nonetheless.

Chapter 7

Discussion and Conclusions

7.1 Discussion

In this final chapter the results found from the investigation of each preceding chapter's research questions are summarised in turn. These are the basis of our answer to the overarching question of this project – can we identify experimental signatures of zonal flow in spherical tokamak data? The argument advanced in this thesis, and discussed below, is that the only strong evidence consistent with our expectation so far detected is of the influence of magnetohydrodynamic (MHD) modes as a perturbation driving geodesic acoustic modes (GAMs). This is starkly at odds with the expectation based on literature that zonal flows should be ubiquitous and easy to detect. Our discussion considers this and focuses on why it has proved difficult to make unambiguous identification of zonal flow. We close with a summary of the evidence that is our contribution to answering this question, suggestions for adaptations to the extensive framework developed over the course of this project and experiments on MAST-U to narrow the gap between expectation and observation.

7.1.1 Part 1: Adapted Cross Correlation Time Delay Velocity Estimation

7.1.1.1 Code

The principal question of chapter 3 was to design and implement a Cross Correlation Time Delay Estimation (CCTDE) code using Beam Emission Spectroscopy (BES) data. This technique had been applied in other machines and with other diagnostics but not yet with success when studying zonal flow on MAST. With significant changes to the usual design of the techniques – continuous measurements, averaging of multiple positions, correlation tests, velocity limits and corrections and much shortened data series for each velocity measurement – we were able to implement a velocimetry technique with sufficient frequency resolution (time resolution of velocity measurements) to be used for zonal flow study.

The next question was what constituted appropriate test data for the MAST BES system.

Using the correlation principles already established in the velocimetry design and a random phase technique for signal production we produced stochastic data series that replicated a time series without flow as seen by each channel of the BES system.

Using those data allowed us to interrogate the failure modes of CCTDE using MAST BES data. Reversing the time-delay principle, a velocity could be imposed on the surrogate data. Running the velocimetry routine with various real input signals and imposed velocities led to the addition of series of tests within the routine that improve its accuracy and reliability. These are unique to this implementation of CCTDE. The result was up to 98% validity of measurements and only 5% overestimation of velocity (by weighted average of the time series) for tests with the most ideal – broadband – input data.

The final research question answered here was the characterisation of an expectation for a spectrum of velocity data produced by this technique. Deviations from this would reveal the presence of additional physics. The test case used is of turbulent surrogate data with an imposed velocity. Its generic pattern is of flat power at low frequencies transitioning to falling power close to the nominal Nyquist frequency of the velocity measurement.

7.1.1.2 Benchmarking

The second piece of work tested the performance of the velocimetry routine and presentation of the spectrum in response to a series of realistic scenarios anticipating spherical tokamak conditions. This included first measuring and devising a means of imposing the turnover time of tokamak turbulence. This allows for generation of data on velocity using four channels' signals as real BES measurements do.

The first test asks what the impact of powerful modes in both the input and output data of the velocimetry does to the spectrum pattern. It was found that modes in the input signal (BES data) increases the flat region power but does not cause a peak in the velocity spectrum even when the mode dominates the density time series fluctuation. Modes in the velocity time series produce tall peaks without affecting the noise level. The peaks show high contrast as long as 0.5 or more of the velocity time series RMS fluctuation amplitude is because of the imposed mode. Tall modes like this were found to be typical of those found in real data, with factors greater than 1.0.

The second test probed the effects of high frequency, intermittent features in the input data - to replicate the magnetic instabilities of spherical tokamaks. Our data showed that they disrupt the velocity measurement locally in time. However, our velocimetry routine has a sufficiently robust design that the velocity excursions can be excluded from the average measured velocity by considering goodness of fit. The times affected are localised to only those of the imposed feature. As a result, neither average velocity nor the spectrum measured are affected by these bursts. Again, these signals raise the flat region power. The spectra are otherwise unaffected by these features with real bursts at high and low frequency measured

as having an amplitude well below that needed to seriously affect our measurements.

The final test of our code looked at the effect of an evolving flow. The imposed velocity was modified to vary with time. The velocimetry tracked changes in the imposed velocity closely and so we have confidence that we can resolve flow evolution. The result was a clear prediction of the anticipated overestimation of our CCTDE technique as a linear function of the imposed velocity with equation $1.79x + 0.019$. The relationship is strongly linear with significant variation depending on the input data. The full measurable range between 2 and 40 km/s was investigated.

7.1.2 Part 2: Studies of BES data from MAST experiments

The second section shows the results of searching for spectral features consistent with zonal flow in MAST data. Few MAST experiments show distinct peaks at any frequency, those that do fall into two categories. First, broad, low amplitude peaks from the signal at a single radius measured by the detector often in the low confinement (L) mode. Second, narrow, tall amplitude peaks, sometimes at multiple radii, in the high confinement (H) mode of the plasma. The latter are typically found at the same time as a long-lasting, continuous magnetic mode of the same frequency.

7.1.2.1 Turbulence Shot Sweep

The first study of real data with our technique looked at times across 80 shot numbers and categorised the observed spectra. Four types were found including the generic turbulent flow pattern seen in testing and peaks at the bottom and middle of our spectra. Initial study of the low frequency peaks proved inconclusive. The medium frequency peaks – present at very few of the times surveyed - were looked at further, including beginning to corroborate in other diagnostic signals. It was found that nearly all such peaks were accompanied by a magnetic mode in the Mirnov coil signal. The magnetic mode is the dominant peak in the Mirnov spectrum, a continuous mode and associated with high H factor. It tends to develop during an ELM-ing H mode time of a MAST shot.

The second question of the real data survey was to understand what relationship, if any, might exist between a magnetic mode and GAMs i.e. whether or not to discount these spectra from GAM analyses. Most studies of GAMs evaluate density or potential at a single location and so were largely incomparable to the velocity spectra information. Within the literature two precedents for association of GAMs with magnetic data could be found. One from recent theoretical work that predicts the electromagnetic fluctuations GAM oscillations in plasma flow might cause, the other from the first theoretical work to propose GAMs in which the magnetic perturbation is a driver of zonal flow formation. Testing each theory found that both were viable routes in the preliminary data. A further association was made in a previous study of GAM evidence on MAST and magnetic signal data are routinely

reported in papers since the theoretical result.

We therefore investigated the dependencies of these signals: density, magnetic and velocity time series. Our test of this relationship filtered the effect of the magnetic mode out of the BES data used for the velocimetry. It was found that in most cases the velocity and density modes are independent, with velocity peaks persisting despite the higher cutoff of the filter on BES data.

7.1.2.2 Systematic Search of Candidate Velocity Spectra

27 examples of spectra in the presence of a magnetic mode were inspected and measured to design a series of tests of the relationship between density, velocity and magnetic signals; of the magnetic mode per GAM literature and of expected experimental parameters in the presence of a GAM (based on other reported GAM studies.) In all, 18 tests to gather data on each example were written. The examples already found were tested manually and their results used as the basis for automated passing criteria. As such we have designed and implemented a systematic approach to testing any velocity time series. Weighted test scores allow for rapid identification of promising candidate velocity spectra for time slices of MAST shots. These can then be characterised in future zonal flow studies.

The new GAM test system was applied across a wide range of shot numbers. This time the shots were chosen from the logbook information, turbulence experiments and previous work to maximise the likelihood of successful GAM identification. Every time with NBI heating in the shots was analysed using the velocimetry code and the test system. Consequently 220 spectra with features of potential interest for GAM discovery were found by inspection, and their score and data compared. A number of trends were evident in the data for GAM-like spectra. It was evident that no cases score highly against both magnetic and physics criteria. Velocity spectrum peaks that correspond to predictions of GAM frequency are found more often with terms for plasma rotation than shaping and in the normalised radius range 0.7 to 0.9, inside the edge plasma.

The results were analysed by category of interest. The two categories with most interesting results were highest scoring overall and the highest scoring turbulent L mode cases. A sample of cases from each of these were the subject of a series of characterisation investigations. Velocity spectrum peaks in each are still found across a wide range of radii and frequencies. In the highest scoring cases the spectrum peaks match predictions of frequency with rotation terms most often - two quartiles in the radial range 0.84 to 0.92 and at an average of 20 kHz. Complicating this picture is the prevalence of cases (half of the sample) in which a velocity peak is found at the magnetic mode frequency across a wide radius of the BES detector. Coherence analysis showed there is a strong relationship at the mode frequency across half the detector in half of cases, the full width in three further cases and isolated in one column in one case. Spectrograms were used to study the temporal extent

of these modes which showed they persist continuously for an average 0.035 seconds during the magnetic mode. By contrast the L mode cases have peaks in single columns with no apparent radial or temporal extent.

Given its importance in literature, the evidence of spectra in L-H transition times was expanded by a sweep of 209 shot numbers at L-H confinement mode transition times was performed on a fully automated basis (including designing an automatic transition time measure.) The scores were used again to determine the highest scoring cases with and without a magnetic mode. Three of the highest scoring cases show evidence consistent with GAM physics and a rotational continuum theory of GAM frequency but blank velocity spectrograms. Axisymmetric modes at extremely low frequencies may nevertheless suggest zonal flow and attention of future work should include the zero frequency zonal flow branch.

7.1.3 Tension: Expected Identification versus Incomplete Evidence

Discussion of these results is focussed on resolving an apparent tension between the expectation of zonal flow detection as in experimental literature; the capability of the tool developed using BES data for CCTDE and the results of a systematic search of available experimental data. The expectation of the project was that zonal flow should be a common phenomenon emergent from turbulent plasmas. The evidence of other studies is that peaks at characteristic frequencies can be clearly discerned from spectra of experimental data. Given that, we would expect that characterisation, not identification, would be the principal research goal. This is at odds with our data in which the strongly GAM-like signals come exclusively from plasmas where consideration must be given to convoluted magnetic and density signals. Moreover, these signals tend not to show other characteristics of plasma that are expected in the presence of zonal flows.

Unambiguous detection of just a few cases is the usual target of experimental work in this domain. That would allow for clear characterisation and validation of simulation work, as well as a basis for finding other examples. This was the intent behind doing this analysis with BES data. Given the strength of velocimetry evidence in identifying zonal flow physics, the remaining discussion asks what is the strongest claim these data support about the absence of clear detection in MAST data? The credibility of three positions will be compared. That either (a) the advanced CCTDE method is incapable of measuring zonal flow in MAST data, (b) it does work and that truly no zonal flow is present at any of the times in any of the shot numbers surveyed or that (c) the incomplete evidence of the best sample cases nonetheless supports them as good candidates for zonal flow detection.

7.1.3.1 Method is flawed

In principle, even a rudimentary two-point version of the CCTDE technique should be capable of a flow velocity measurement and as such produce a spectrum that revealed GAMs.

The version we use has a number of adaptations and features that should make it even more robust in the spherical tokamak context. When considering flaws in the methodology, it seems unlikely that the implementation of CCTDE would be failing to adequately capture changes. Reflecting on further possible changes to the technique we have implemented it is hard to imagine methods that have not already been tried (e.g. longer correlation bins, measurements farther apart) without success. It may be possible to make adjustments to the functions used in our method such as modifying to a conditional cross-correlation definition. However, we judge the potential for improvements from such changes to be marginal.

We note that the chosen length of signal (0.01 s) and the frequency resolution it gives, combined with our decision to smooth spectra with a filter cut-off at 50 kHz creates a limit of detection of spectral peak width. If the affected frequencies are across a very narrow range they tend not to change the smoothed signal unless powerful. GAM flows are not expected to be weakly confined to so sharp a peak, though.

Instead, it is useful to consider whether the design of the CCTDE method may be introducing noise to the spectra. On top of a high low and medium frequency power, the relative height of any spectral features may be being obscured in the variance (we certainly have seen few high contrast cases.) One approach to resolving this used elsewhere is to concatenate broadband data so that only flow is being measured. However, to do so requires knowing in advance which data contain flow, otherwise only additional turbulence is studied and the noise floor raised. The problem of contrast is also contradicted by our testing in surrogate data. There it was shown that tall peaks come from even a modest contribution to RMS amplitude of signal fluctuations from the flows. Determining the strength of signal needed in real data to overcome noise and smoothing would be a useful future exercise.

The last limitation of our velocimetry method that deserves serious consideration is the spatial resolution of the BES detector. A number of issues may arise. First, the columns are separated by 2 cm (increasing as the major radius of the field of view reduces) which we have seen may be a difference in normalised radius of 0.3 across the BES detector. If flow is weakly present in a narrow region of plasma the remaining gathered signal may be noisy (though this is not what other experiments observe in conventional aspect ratio tokamaks.) Similar convolution of the signal may occur if field line curvature is strong at the outboard midplane. In those cases, the identification of each column with a single normalised radius (and so flow velocity) is no longer appropriate. This has been observed in shot numbers with high triangularity and where the plasma is below the midplane. This tends to accompany early shot times – that we avoided with our choice of NBI heating times – and otherwise is rare in high MAST shot numbers (longer shots) and shot numbers as part of experimental campaigns (ie full-vessel plasmas not part of a commissioning process.) Both of these were prioritised, though not exclusively, in our survey. Nonetheless, comparing each individual channel's spectra (or average velocity) to their column's may indicate such an error in future.

Finally, we may consider the study of CCTDE methods by Sierchio¹¹⁹ that implies strong orthogonal flow confounds flow measurements. This is not a concern for us since we study the dominant flow direction of the detector orientation.

Our test results are reported according to categories of interest to capture data in as many viable circumstances as possible. However, the structure of the tests is, by design, a significant area of interpretation. Additional testing has been discussed already in section 7.1.2.2. It would also be possible to revise the assignment of scores in weighting each test and the focus of tests as the expectation of GAM physics in the large spherical tokamak context changes. In this study a high contrast spectral peak was prioritised as an important precursor to unambiguous detection. It would also be possible to report results according to a ‘physics filter’ instead of categories i.e. to investigate only those cases with the correct mode number or axisymmetry.

This discussion of the method addresses the reasonable concerns that could be identified in light of the results. Though some small improvements and tests can be suggested, it is not clear that any undermines the ability to measure GAMs in velocity spectra and their accompanying data. As long as the oscillation occurs in flow velocities in the range we can accurately measure (roughly 2 to 30 km/s) we expect our implementation of CCTDE should be able to detect the change to plasma flow velocity GAMs cause. The only other methodological consideration may be the shots and times chosen for our survey. Our survey systematically reviewed many shots according to multiple criteria so if zonal flow were typically present in turbulent plasmas we expect to have observed it. Most shots with long L modes pre-transition were surveyed as a proxy to guarantee fully developed turbulence, though we did not consider the effects of back transition (H to L confinement mode) in those shots with transitions. Again, we would not expect this to prejudice our ability to measure zonal flow at expected times earlier than a back-transition in each shot.

7.1.3.2 Zonal Flow Cannot Be Detected

A radical alternative conclusion might argue that if we naively assume a correct implementation of the method; use of a reliable technique and that the zonal flow physics would have been observed if present, that there is no zonal flow in large spherical tokamaks. If we wish to reject such a strong negative conclusion then we must account for the lack of evidence of strong flow modes. Even rejecting the last assumption, claiming instead that zonal flow is not strong enough to be detected in any of the shot numbers studied, would be an unexpected negative result.

To assess the extent to which these conclusions might be supported by our data we focus on the results found in L mode plasmas in table 6.8. The understanding of zonal flow in published literature promotes an expectation that L mode plasmas are the most likely origin of zonal flow in tokamak plasmas. Among these cases we did not find the highest amplitude

velocity spectrum peaks, nor was there evidence of radially extended flow physics. The best examples found magnetic modes at the expected $m = 2$ pattern but these were not associated with axisymmetric modes at GAM theoretic frequencies. A magnetic peak could be found in the expected frequency range of 3 to 30 kHz but it was not also the tallest peak of the BES signal (though it was also a peak in that signal for some cases.) The magnetic fluctuation amplitudes are consistently below that predicted by Wahlberg and Graves. These peaks appear in a single column of the detector at a single time. The spectrograms that show velocity modes do not suggest intermittency consistent with a Lotka-Volterra model. Almost none of these results are consistent with our expectation of turbulence driven zonal flow. One high scoring case was found at a transition time, though with similarly inconsistent peak frequencies in velocity and magnetics data. Across a wide survey of shots for which detailed analysis was done we did not find a consistent pattern of radius or frequency of peaks in velocity spectra of L mode plasmas.

There are reasons to resist an affirmative conclusion that no L mode zonal flow is detected given the lack of dedicated turbulence experiments in the campaigns studied. MAST shots often target an L-H transition at early times. Since BES passively uses NBI beams (which are used to induce the transition) there is also a bias towards studying shots with the transition. While the transition is expected to be a time with strong zonal flow, MAST shots (currently much shorter than the conventional tokamak shots we are comparing to) have very short L mode times to develop and measure turbulent physics. The strong magnetic and diamagnetic flow shear stabilisation of spherical tokamaks may suppress the growth of turbulence driven zonal flow, the turbulent field in powerful spherical tokamaks may rarely be sufficiently far from a critical turbulence threshold for strong zonal flow drive to establish itself. The limit of detection may be underestimated given the tendency of simulations in simplified slab geometry to exaggerate zonal flow growth rates. Longer lead times in dedicated shots may change that. A more thorough understanding of our limit of detection, ideally validating our technique against proven examples, would give the level of proof demanded for a negative finding.

Since other experiments have claimed to positively identify GAMs in MAST data we can compare these assumptions to their investigations (though cannot corroborate results without BES data.) In particular, the Robinson experiment that found GAM-like modes¹⁰⁹ was done without NBI heating and therefore in an entirely L mode plasma with no transition and (low energy) turbulence. They were able to find supporting experimental data consistent with GAM physics. Recreating their experimental conditions as far as possible with NBI on would improve understanding in the L mode. This is consistent with the example from small spherical tokamak Globus-M that also found evidence from an L mode plasma.⁸⁵ The Robinson experiment was also based on coupling of the GAM and magnetic modes in the plasma edge which further motivates our interpretation of H mode plasmas.

It is significant in the context of zonal flow and CCTDE literature that no turbulence-emergent flow modes could be seen in our spectra. There is some velocimetry evidence for GAMs in H mode but a lack of data supporting their presence in L mode plasmas. Since this contradicts findings of zonal flow in conventional tokamaks and on MAST a focussed investigation of the phenomenon is needed to have confidence in the pattern. Most especially, a dedicated experiment is needed. Experiments with long L mode, late transition and minimising magnetic instabilities would be ideal. They should also be able to account for RMP activity, safety factor profile and the direction of the NBI beam. As MAST-U proceeds to longer (5 second) shot times there is a good opportunity for such an experiment in a large spherical tokamak. BES has excellent data and now a method and rigorous framework for detection but a multi-diagnostic approach to validate the interpretation of results, for now, remains necessary.

7.1.3.3 MHD Activity Mediates GAMs on MAST

The evidence we do have of zonal flow detection is from the high scoring cases where spectra and spectrograms show velocity modes at GAM frequencies. As with the L mode cases, the consistency of the supporting data is poor. It is understood that evidence presented for zonal flow is often circumstantial. We therefore consider how best to interpret the evidence found.

If the cases with strong, continuous magnetic signals (typical of the high scoring cases) strongly matched experimental expectations of GAMs we might say that the magnetics were a consequence of GAMs. Since they do not, we do not have evidence for that direction of causation. There is still a mechanism for these magnetic oscillations to be a driver of GAM flows in which case we would need to better understand whether we expect the same magnetic signature ($m=2$, axisymmetric, Wahlberg and Graves magnitude) from GAMs driven by MHD instability. The presence of harmonics of the magnetic signal in the velocity spectrograms too may also be indicative of the direction of causation. Though, sidebands are not unknown with GAM generated magnetics and were suggested as a feature of signals produced at the MAST midplane by Robinson. The magnetic mode associated with GAMs was assumed to be the fundamental magnetic frequency, which may not be the case if the GAM is driving magnetics. There is good evidence of matches to the rotational model of GAM frequency proposed in equation 6.3 - including accounting for safety factor - by the fundamental mode in these high scoring cases. If those are GAMs, as indicated by the partial correspondence of those global magnetic modes to the velocity spectral modes, we can say the coherence data is an initial characterisation of them.

If we accept the medium frequency magnetic mode as a GAM driver, a new set of questions arise in characterisation. For example does a magnetic mode have to be at the GAM theoretical frequency to drive them? If not, how different can their frequencies be? What is the poloidal variation of the drive mechanism and so flow velocity? Crucially we

would have to investigate a turbulence state in the H mode with insufficient amplitude for Reynolds Stress to drive GAMs but with high enough amplitude to sustain the mode.

Our interpretation would be improved by a fuller understanding of the dependencies of the peaks we have observed. To do that we would need to interrogate the contiguous radial extent of matches to each GAM frequency model in each case. Currently any match in any column is counted. Counters for each theory in each of the magnetic and velocity spectral data could also better characterise the typical radial extent of cases. The cases with a continuous magnetic mode produce clear patterns at a single frequency in the velocity data that are consistent with GAM theory. Additional data reinforce theories of mode number and amplitude of GAM magnetic signatures at L-H confinement transition times.

7.1.4 Future Routes to Verification

Further evidence to include or exclude the proposed cases of zonal flows found so far, as well as to characterise the most likely examples, can now be suggested for the signals already in use.

Using the velocity time series data, it would be possible to begin approximating velocity shear (and measure its change with time) as a first approximation for energy exchange. The kinetic energy terms for Reynolds Stress could be evaluated. A model specific count of velocity peak matches to GAM frequency predictions using the spectral data could be compared to score to better characterise the patterns observed. This can be supplemented by a detailed study of the phase relationships between adjacent columns with common velocity peaks. Ultimately a bicoherence test of energy exchange will be a key determinant of the turbulence – zonal flow relationship. The magnetic behaviour expected of GAMs includes a poloidal fluctuation amplitude dependence on $\sin(2\theta)$ that could be tested.

The principal route to good data on zonal flow is to control the parameters of a turbulent experiment. We have suggested a priority for a MAST-U campaign should be the stimulation and study of zonal flow. The motivation for this study is the lack of knowledge of how best to do that in a spherical tokamak but the results we have found imply a need to look in longer L mode cases as well as H modes with a magnetic mode. The precise character of zonal flow is uncertain in the spherical tokamak context still – including some disqualifying criteria in our framework will be important to classifying future velocity spectra as examples of zonal flow.

7.2 Conclusions

It was expected that zonal flow driven by turbulence would be a common feature of tokamak plasmas. A velocity measurement with high time resolution should be able to see the distinct flow pattern. The occurrence of multiple instabilities that affect density in spherical tokamaks

means that experimental zonal flow research demands an involved approach. The starkest characteristic behaviour of GAMs is their finite frequency plasma flow oscillation. The focus of this research is therefore the spectra of velocity measurements of BES data from MAST.

This project first developed a bespoke cross correlation time delay estimation velocimetry method. The code was designed to use data from the advanced BES system on spherical tokamak MAST but is compatible with any input time series. The design is optimised for temporal resolution of velocity spectra. As part of commissioning work for the upgraded BES diagnostic for MAST-U, a function reporting the accurate field of view at each radial viewing position was produced to give the accurate spatial separations of channels for velocity measurements. Correlation functions of 64 data points length give the time delay used to measure velocity at every time of BES data, sampled at 2 MHz. A single radial velocity measurement is returned by weighted average of the channels in a detector column. We further developed surrogate data to test the velocimetry. The result was the inclusion of many unique tests and limits that enhanced reliability and accuracy of the velocity measurements and time series average. For the best input data (broadband turbulent density signals) the routine made for this project has 98% valid measurements and 5% velocity overestimation. A result of the substantial development of a CCTDE technique for MAST BES data is a user-friendly version of the velocimetry code available and in use for researchers using BES. Some functions for turbulence analysis and early commissioning of the diagnostic also formed part of this work.

In three benchmarking studies we tested the effect of anticipated spherical tokamak physics on the velocimetry outputs – time series and spectra. The spectrum pattern we expect from a purely turbulent signal with constant velocity is of flat power transitioning to falling power at approximately the nominal Nyquist frequency of the velocimetry technique. In each study a typical GAM frequency mode was imposed on the velocity time series. In the study of powerful modes in the input and output data it was shown that density modes do not produce tall peaks in velocity spectra. Modes in the velocity time series always produced a peak in the spectrum. A high contrast peak in velocimetry was seen for modes in the velocity time series that contributed above 0.2 of the RMS fluctuation. Real peak heights were found to match the most powerful tested mode amplitudes, well above this threshold. A second study considered the high frequency bursts often seen in magnetic and density data from MAST. These were found to disrupt the velocity measurement at amplitudes comparable to the standard deviation of the velocity time series. They did not affect the spectrum or time series weighted average. Real bursts were found to have amplitudes corresponding to the lowest tested amplitudes. The final study imposed a time varying velocity on the turbulent signals. Again the spectrum pattern was not changed, though a slight gradient was found to be introduced for higher velocities. A comparison of time series data showed a strongly linear relationship between input velocity and the percentage overestimation of the

velocimetry technique, with equation $1.79x+0.03$. A significant variation of the gradient was seen depending on the input data. In no study was the GAM mode obscured in the spectrum. This series of studies demonstrate a robust method of detection despite perturbations to the density (input) signal, contrary to other implementations of the CCTDE technique.

Applying our new detection method to MAST data at 175 times from 80 shots showed that most spectra resemble the turbulent flow pattern. 5% of the surveyed times showed distinct peaks in the 'flat' region consistent with the expectation for GAM detection. Investigation of these peaks showed that tall velocimetry peaks in the MAST context were very often associated with a powerful magnetic mode at the same frequency. Two precedents were found for this in literature – one each with GAM as the cause and consequence of the mode. A study of 27 times from 12 shots modifying the input signals showed that the velocity peaks persist in the absence of the magnetic signal's effect on the density fluctuations. These cases, with the tallest peaks in velocity spectra, were therefore included as candidates for times with GAMs.

With two routes to GAM formation possible in our data, a new framework for characterising candidate times was developed. This consisted of codifying GAM physics reported from across experiments in conventional tokamaks into a single set of testable metrics. In addition, tests of the possible magnetic mode were introduced. Unlike other investigations of GAMs, these clear criteria were then automated and given weighted scores to enable testing of a large set of MAST BES data; characterising all times of many shot numbers. With this new systematic framework 220 times from 67 shots were identified on the basis of GAM-like velocity spectra and characterised in this way.

While several of the spectra of interest scored highly in our test of GAM and magnetic physics, no example could be found of a time with (a) visible velocity peaks, (b) no magnetic mode and (c) corroborating GAM physics (encompassing plasma parameter dependences and magnetic patterns.) The best examples of velocity spectra are associated with H mode physics. It is surprising and significant that clear cases could not be seen in the turbulent L mode times studied, including near the L-H transition, as expected in zonal flow investigations. The L mode cases found had short-lived, small amplitude peaks at GAM frequencies typically in the spectrum of a single column of the detector. They had axisymmetric modes at the right poloidal mode number $m = 2$ but not at GAM frequencies. The H mode cases, nearly all with a magnetic mode, had an average coherent radial extent of 4 adjacent columns of the detector (typically 2 cm separation) matching a GAM frequency model. This was wider, at 4 or 8 columns, if peaks at the magnetic mode frequency were considered. These had axisymmetric modes at the magnetic mode frequency, matching GAM theory, but with a higher mode number $m = 3$ than expected. This number matches the RMP magnets used to control H mode plasmas. These velocity modes were found to persist for an average of 0.035 seconds and up to 0.09 seconds. Their radial location spanned the full plasma but

was mostly between normalised radii 0.84 and 0.92, inside the edge plasma. Without further examination we note that the L mode cases in particular show velocity modes but often no fast (more than 1 km/s) flow velocity after correcting for pitch angle. The GAM frequency prediction that performed best included terms for plasma rotation and safety factor but not shaping (elongation.) Adapting our focus in light of the L mode results, an automated sweep of L-H confinement mode transition cases found evidence of very low frequency axisymmetric modes. Further investigation of these may reveal the presence of zero-frequency zonal flows.

The intended characterisation of zonal flow in a large spherical tokamak assumed the discovery of a few, obvious examples. Their absence, given the substantial data set surveyed, is itself an unexpected result. The candidate cases we have identified in a first rigorous search of MAST data reveal initial findings of the frequency and location of velocity spectra peaks in MAST. These results motivate further study of the question of how strong a zonal flow mode has to be before being detectable by BES velocimetry.

There is evidence in the data we have collected on the best cases to support ideas from recent theoretical work done on GAMs. An eigenmode frequency structure is implied in the common peak frequency of the tallest velocity peaks we measure. We have an order of magnitude match to the predicted fluctuation amplitude of the magnetic perturbation due to GAMs too, albeit typically far lower than the theoretical value. There is evidence of a complex poloidal structure to magnetic fluctuations associated with GAMs. The framework for testing these hypotheses we have devised is transferable to new suggested times to study, as well as future experiments. Most interestingly there is a similarity to the previous experiment on MAST interrogating GAMs in proposing a coupling to the tokamak magnetics. We extend this by proposing a perturbing magnetic instability as potentially a driver of GAMs. ZFZF frequencies and axisymmetry are found at a very few confinement transition times but additional testing of energy transfer is needed to evaluate those cases.

The best-case scenario would have allowed us to proceed with BES data alone in pursuit of examples of GAMs, having robustly identified their experimental signature. Instead it has been demonstrated that peaks in velocity spectra, as with density signals previously, are necessary but insufficient evidence of zonal flow. On this basis it is clear that a multi-diagnostic approach to corroborating GAM detection will still be necessary in future experiments.

Future work should prioritise an understanding of the amplitude limits of detection of zonal flows in spherical tokamaks with velocimetry. The critical independent variables of a dedicated experimental shot series are highlighted so that zonal flow formation is highly likely for investigation of the results observed in the first exploration of MAST data undertaken in this thesis. In particular, this will enable verification of the finding that turbulent L mode plasmas are poor targets for GAM identification by velocimetry in spherical tokamaks. This is an unorthodox claim and needs to be carefully understood in the context of a lack of expected GAM plasma behaviour. On the merit of the evidence of velocity modes at GAM

theoretic frequencies we propose investigations of GAMs consider H mode zonal flows pending a comprehensive explanation of these phenomena. It may be that the magnetic instability of powerful large spherical tokamaks promotes their turbulent stability.

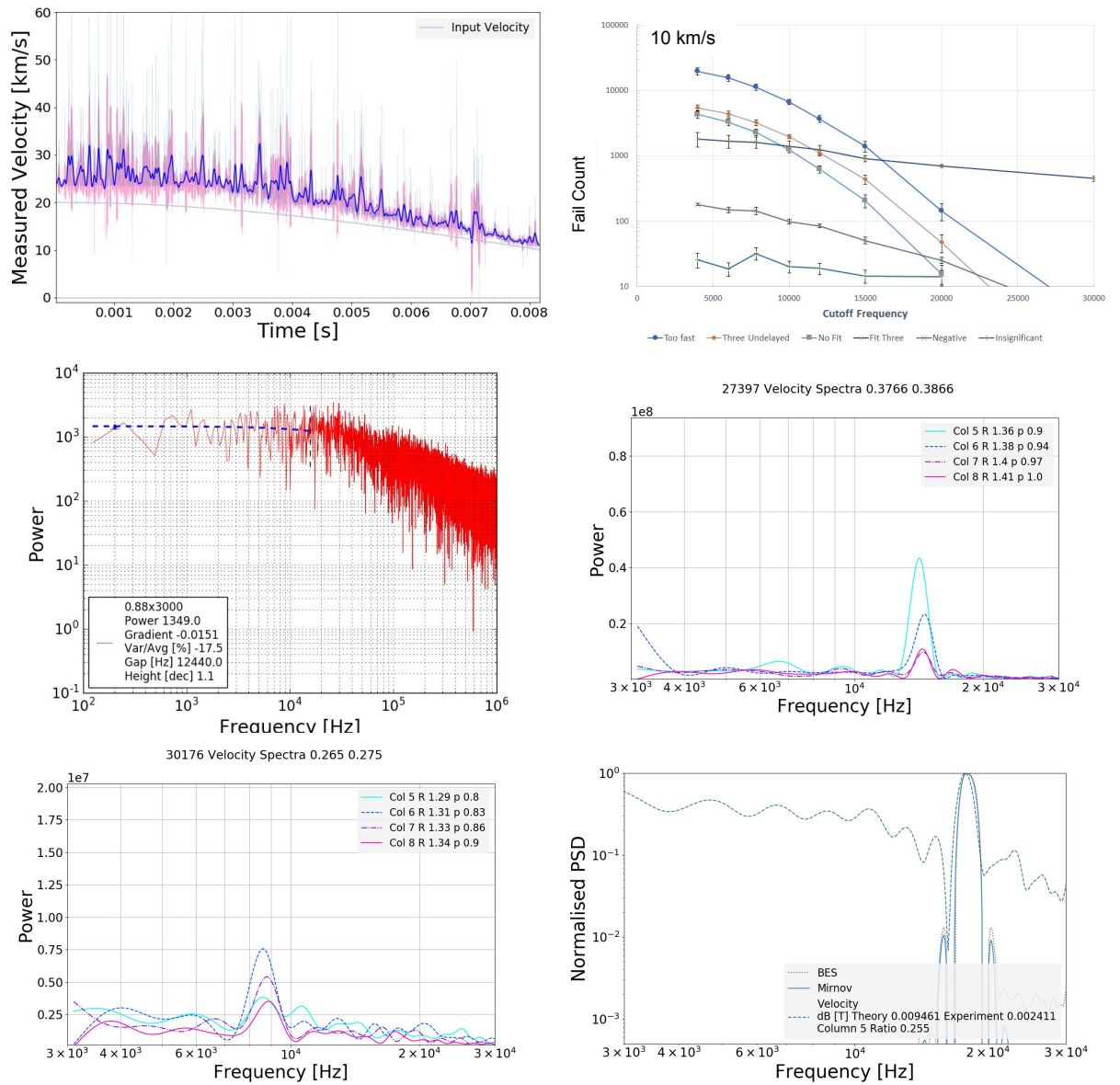
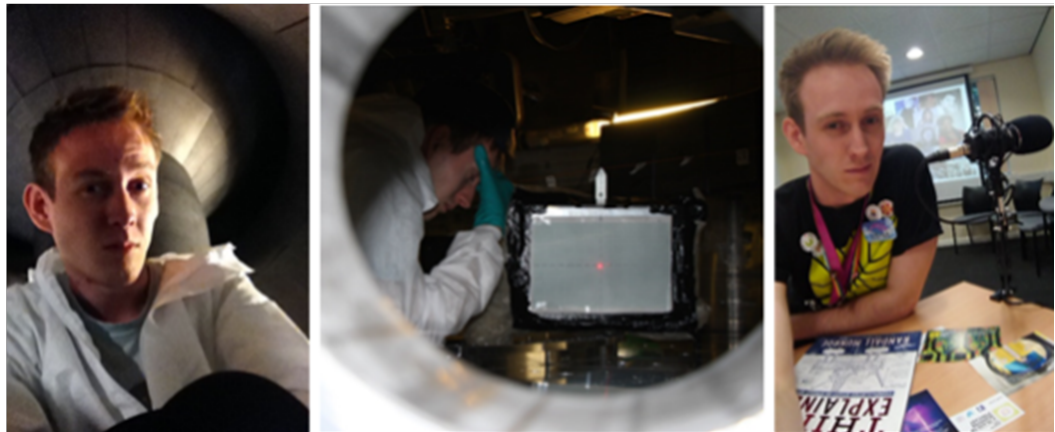


Figure 7.1: Key results are re-displayed featuring the high degree of accuracy of the velocimetry even with a changing input; the high success rate of our implementation after filtering and other post-processing; our null hypothesis for spectrum pattern based on a slow input velocity; two examples of distinct velocity modes from different shot numbers and the overlaid, normalised spectra of density, velocity and magnetic signals for these distinct peak cases.



List of References

- [1] Andrew Malcolm-Neale. Using the wider science curriculum to investigate fusion energy. *Physics Education*, 54(4):044001, 2019.
- [2] PW Terry. Stable modes in saturation of instability-driven plasma turbulence. In *APS Division of Plasma Physics Meeting Abstracts*, volume 2016, pages UT2–001, 2016.
- [3] Lord Rayleigh. On the instability of jets. *Proceedings of the London mathematical society*, 1(1):4–13, 1878.
- [4] François Charru. *Hydrodynamic instabilities*, volume 37. Cambridge University Press, 2011.
- [5] P. W. Terry. Suppression of turbulence and transport by sheared flow. *Rev. Mod. Phys.*, 72:109–165, Jan 2000. doi:[10.1103/RevModPhys.72.109](https://doi.org/10.1103/RevModPhys.72.109). URL <https://link.aps.org/doi/10.1103/RevModPhys.72.109>.
- [6] Patrick H Diamond, SI Itoh, K Itoh, and TS Hahm. Zonal flows in plasma—a review. *Plasma Physics and Controlled Fusion*, 47(5):R35, 2005.
- [7] J Seidl and L Krlin. Interchange driven turbulence and bellan instability in tokamak scrape-off layer. *WDS09 Proceedings of Contributed Papers: Part III-Physics (eds. J. Safrankova and J. Pavlu)*, Prague, Matfyzpress, 2009.
- [8] OE Garcia, V Naulin, AH Nielsen, and J Juul Rasmussen. Turbulence and intermittent transport at the boundary of magnetized plasmas. *Physics of plasmas*, 12(6):062309, 2005.
- [9] PN Guzdar, Liu Chen, WM Tang, and PH Rutherford. Ion-temperature-gradient instability in toroidal plasmas. *The Physics of Fluids*, 26(3):673–677, 1983.
- [10] Bruce Scott. Low frequency fluid drift turbulence in magnetised plasmas. Technical report, Max-Planck-Institut für Plasmaphysik, 2001.
- [11] N.T. Howard, C. Holland, A.E. White, M. Greenwald, and J. Candy. Multi-scale gyrokinetic simulation of tokamak plasmas: enhanced heat loss due to cross-scale coupling of plasma turbulence. *Nuclear Fusion*, 56(1):014004, dec 2015. doi:[10.1088/0029-5515/56/1/014004](https://doi.org/10.1088/0029-5515/56/1/014004). URL <https://doi.org/10.1088/0029-5515/56/1/014004>.
- [12] PA Davidson. *Turbulence. an introduction for scientists and engineers* oxford university press, 2004.
- [13] GW Hammett. Physical mechanisms driving gyrokinetic turbulence. In *Vienna Gyrokinetic Workshop*, pages 15–19. Citeseer, 2008.

- [14] DR Mikkelsen, H Maassberg, MC Zarnstorff, CD Beidler, WA Houlberg, W Kernbichler, H Mynick, DA Spong, Pär Strand, and V Tribaldos. Assessment of transport in ncsx. *Fusion science and technology*, 51(2):166–180, 2007.
- [15] John D Lawson. Some criteria for a power producing thermonuclear reactor. *Proceedings of the physical society. Section B*, 70(1):6, 1957.
- [16] Stephen B Pope. *Turbulent flows*. IOP Publishing, 2001.
- [17] PH Diamond and Y-B Kim. Theory of mean poloidal flow generation by turbulence. *Physics of Fluids B: Plasma Physics*, 3(7):1626–1633, 1991.
- [18] W Horton. Drift waves and transport. *Reviews of Modern Physics*, 71(3):735, 1999.
- [19] P Li, YD Li, JG Li, GJ Wu, T Lan, B Zhang, JS Geng, YK Zhang, LQ Xu, HL Wang, et al. Study of turbulence modulation and core density peaking with co2 laser collective scattering diagnostics in the east tokamak. *Nuclear Fusion*, 60(6):066001, 2020.
- [20] Pijush K Kundu, IM Cohen, and HH Hu. *Fluid mechanics. 2004*. 2008.
- [21] Akihide Fujisawa. A review of zonal flow experiments. *Nuclear Fusion*, 49(1):013001, 2008.
- [22] RJ Hajjar, PH Diamond, and GR Tynan. The ecology of flows and drift wave turbulence in csdx: A model. *Physics of Plasmas*, 25(2):022301, 2018.
- [23] C Holland, PH Diamond, S Champeaux, E Kim, O Gurcan, MN Rosenbluth, GR Tynan, N Crocker, W Nevins, and J Candy. Investigations of the role of nonlinear couplings in structure formation and transport regulation: experiment, simulation, and theory. *Nuclear fusion*, 43(8):761, 2003.
- [24] Zhe Gao, Ping Wang, and H Sanuki. Plasma shaping effects on the geodesic acoustic mode in toroidally axisymmetric plasmas. *Physics of Plasmas*, 15(7):074502, 2008.
- [25] Niels Winsor, John L Johnson, and John M Dawson. Geodesic acoustic waves in hydromagnetic systems. *The Physics of Fluids*, 11(11):2448–2450, 1968.
- [26] VI Ilgisonis, VP Lakhin, AI Smolyakov, and EA Sorokina. Geodesic acoustic modes and zonal flows in rotating large-aspect-ratio tokamak plasmas. *Plasma Physics and Controlled Fusion*, 53(6):065008, 2011.
- [27]
- [28] Young-chul Ghim. Characteristics of plasma turbulence in the mega amp spherical tokamak. *arXiv preprint arXiv:1302.6171*, 2013.
- [29] K Miki and PH Diamond. Role of the geodesic acoustic mode shearing feedback loop in transport bifurcations and turbulence spreading. *Physics of Plasmas*, 17(3):032309, 2010.
- [30] Katsumi Ida. Experimental studies of the physical mechanism determining the radial electric field and its radial structure in a toroidal plasma. *Plasma Physics and Controlled Fusion*, 40(8):1429, 1998.
- [31] PW Terry, DE Newman, and AS Ware. Suppression of transport cross phase by strongly sheared flow. *Physical Review Letters*, 87(18):185001, 2001.

- [32] K Miki and PH Diamond. Novel states of pre-transition edge turbulence emerging from shearing mode competition. *Nuclear Fusion*, 51(10):103003, 2011.
- [33] MG Shats and WM Solomon. Experimental evidence of self-regulation of fluctuations by time-varying flows. *Physical review letters*, 88(4):045001, 2002.
- [34] GD Conway, B Scott, J Schirmer, M Reich, A Kendl, et al. Direct measurement of zonal flows and geodesic acoustic mode oscillations in asdex upgrade using doppler reflectometry. *Plasma physics and controlled fusion*, 47(8):1165, 2005.
- [35] GS Xu, BN Wan, HQ Wang, HY Guo, HL Zhao, AD Liu, Volker Naulin, PH Diamond, GR Tynan, M Xu, et al. First evidence of the role of zonal flows for the l- h transition at marginal input power in the east tokamak. *Physical review letters*, 107(12):125001, 2011.
- [36] V Sokolov, X Wei, AK Sen, and K Avinash. Observation and identification of zonal flows in a basic physics experiment. *Plasma physics and controlled fusion*, 48(4):S111, 2006.
- [37] Giovanni Manfredi, CM Roach, and RO Dendy. Zonal flow and streamer generation in drift turbulence. *Plasma physics and controlled fusion*, 43(6):825, 2001.
- [38] JA Alonso, JL Velasco, J Arévalo, C Hidalgo, MA Pedrosa, B Ph Van Milligen, D Carralero, and C Silva. Dynamics of zonal-flow-like structures in the edge of the tj-ii stellarator. *Plasma Physics and Controlled Fusion*, 55(1):014001, 2012.
- [39] GR Tynan, C Holland, JH Yu, A James, D Nishijima, M Shimada, and N Taheri. Observation of turbulent-driven shear flow in a cylindrical laboratory plasma device. *Plasma physics and controlled fusion*, 48(4):S51, 2006.
- [40] S Gallagher, B Hnat, C Connaughton, S Nazarenko, and G Rowlands. The modulational instability in the extended hasegawa-mima equation with a finite larmor radius. *Physics of Plasmas*, 19(12):122115, 2012.
- [41] BN Rogers, William Dorland, and M Kotschenreuther. Generation and stability of zonal flows in ion-temperature-gradient mode turbulence. *Physical review letters*, 85(25):5336, 2000.
- [42] JC Hillesheim, E Delabie, H Meyer, CF Maggi, L Meneses, E Poli, JET Contributors, EUROfusion Consortium, et al. Stationary zonal flows during the formation of the edge transport barrier in the jet tokamak. *Physical review letters*, 116(6):065002, 2016.
- [43] S Coda, Miklos Porkolab, and Keith H Burrell. Signature of turbulent zonal flows observed in the diii-d tokamak. *Physical review letters*, 86(21):4835, 2001.
- [44] M Jakubowski, RJ Fonck, and GR McKee. Observation of coherent sheared turbulence flows in the diii-d tokamak. *Physical review letters*, 89(26):265003, 2002.
- [45] George R McKee, Raymond J Fonck, Marcin Jakubowski, Keith H Burrell, Klaus Hallatschek, Rick A Moyer, Dmitry L Rudakov, W Nevins, Gary D Porter, Paul Schoch, et al. Experimental characterization of coherent, radially-sheared zonal flows in the diii-d tokamak. *Physics of Plasmas*, 10(5):1712–1719, 2003.
- [46] DK Gupta, RJ Fonck, GR McKee, DJ Schlossberg, and MW Shafer. Detection of zero-mean-frequency zonal flows in the core of a high-temperature tokamak plasma. *Physical review letters*, 97(12):125002, 2006.

- [47] GR McKee, DK Gupta, RJ Fonck, DJ Schlossberg, MW Shafer, and P Gohil. Structure and scaling properties of the geodesic acoustic mode. *Plasma physics and controlled fusion*, 48(4):S123, 2006.
- [48] T Ido, Y Miura, K Kamiya, Y Hamada, K Hoshino, A Fujisawa, K Itoh, SI Itoh, A Nishizawa, H Ogawa, et al. Geodesic-acoustic-mode in jft-2m tokamak plasmas. *Plasma physics and controlled fusion*, 48(4):S41, 2006.
- [49] AV Melnikov, LG Eliseev, AV Gudozhnik, SE Lysenko, VA Mavrin, SV Perfilov, LG Zimeleva, MV Ufimtsev, LI Krupnik, and PM Schoch. Investigation of the plasma potential oscillations in the range of geodesic acoustic mode frequencies by heavy ion beam probing in tokamaks. *Czechoslovak Journal of Physics*, 55(3):349–360, 2005.
- [50] AV Melnikov, VA Vershkov, LG Eliseev, SA Grashin, AV Gudozhnik, LI Krupnik, SE Lysenko, VA Mavrin, SV Perfilov, DA Shelukhin, et al. Investigation of geodesic acoustic mode oscillations in the t-10 tokamak. *Plasma physics and controlled fusion*, 48(4):S87, 2006.
- [51] MG Shats, Hua Xia, and M Yokoyama. Mean $e \times b$ flows and gam-like oscillations in the h-1 heliac. *Plasma physics and controlled fusion*, 48(4):S17, 2006.
- [52] Y Nagashima, K Itoh, SI Itoh, A Fujisawa, K Hoshino, Y Takase, M Yagi, A Ejiri, K Ida, K Shinohara, et al. Bispectral analysis applied to coherent floating potential fluctuations obtained in the edge plasmas on jft-2m. *Plasma physics and controlled fusion*, 48(4):S1, 2006.
- [53] Y Xu, I Shesterikov, M Van Schoor, M Vergote, RR Weynants, A Krämer-Flecken, S Zoletnik, S Soldatov, D Reiser, K Hallatschek, et al. Observation of geodesic acoustic modes (gams) and their radial propagation at the edge of the textor tokamak. *Plasma physics and controlled fusion*, 53(9):095015, 2011.
- [54] C Silva, G Arnoux, M Groth, C Hidalgo, S Marsen, JET-EFDA Contributors, et al. Observation of geodesic acoustic modes in the jet edge plasma. *Plasma Physics and Controlled Fusion*, 55(2):025001, 2012.
- [55] Laure Vermare, Pascale Hennequin, Özgür D Gürçan, et al. Detection of geodesic acoustic mode oscillations, using multiple signal classification analysis of doppler backscattering signal on tore supra. *Nuclear Fusion*, 52(6):063008, 2012.
- [56] A Fujisawa, T Ido, A Shimizu, S Okamura, K Matsuoka, H Iguchi, Y Hamada, H Nakano, S Ohshima, K Itoh, et al. Experimental progress on zonal flow physics in toroidal plasmas. *Nuclear fusion*, 47(10):S718, 2007.
- [57] Guido Van Oost, M Gryaznevich, E Del Bosco, A Malaquias, G Mank, M Berta, J Brotankova, R Dejarnac, E Dufkova, I Duran, et al. Joint experiments on the tokamaks castor and t-10. In *AIP Conference Proceedings*, volume 996, pages 24–33. American Institute of Physics, 2008.
- [58] AD Liu, T Lan, CX Yu, W Zhang, HL Zhao, DF Kong, JF Chang, and BN Wan. Spectral characteristics of zonal flows in the edge plasmas of the ht-7 tokamak. *Plasma Physics and Controlled Fusion*, 52(8):085004, 2010.
- [59] CA De Meijere, S Coda, Z Huang, Laure Vermare, T Vernay, V Vuille, S Brunner, J Dominski, Pascale Hennequin, A Krämer-Flecken, et al. Complete multi-field characterization of the geodesic acoustic mode in the tcv tokamak. *Plasma Physics and Controlled Fusion*, 56(7):072001, 2014.

- [60] F Palermo, E Poli, and A Bottino. Complex eikonal methods applied to geodesic acoustic mode dynamics. *Physics of Plasmas*, 27(3):032507, 2020.
- [61] Zhe Gao, K Itoh, H Sanuki, and JQ Dong. Eigenmode analysis of geodesic acoustic modes. *Physics of Plasmas*, 15(7):072511, 2008.
- [62] G Wang, WA Peebles, TL Rhodes, ME Austin, Z Yan, GR McKee, RJ La Haye, KH Burrell, EJ Doyle, JC Hillesheim, et al. Multi-field characteristics and eigenmode spatial structure of geodesic acoustic modes in diii-d l-mode plasmas. *Physics of Plasmas*, 20(9):092501, 2013.
- [63] I Cziegler, PH Diamond, N Fedorczak, P Manz, GR Tynan, M Xu, RM Churchill, AE Hubbard, B Lipschultz, JM Sierchio, et al. Fluctuating zonal flows in the i-mode regime in alcator c-mod. *Physics of Plasmas*, 20(5):055904, 2013.
- [64] Guilhem Dif-Pradalier, G Hornung, X Garbet, Ph Ghendrih, V Grandgirard, G Latu, and Y Sarazin. The $e \times b$ staircase of magnetised plasmas. *Nuclear Fusion*, 57(6):066026, 2017.
- [65] AV Melnikov, LG Eliseev, SV Perfilov, SE Lysenko, RV Shurygin, VN Zenin, SA Grashin, LI Krupnik, AS Kozachek, R Yu Solomatin, et al. The features of the global gam in oh and ecrh plasmas in the t-10 tokamak. *Nuclear Fusion*, 55(6):063001, 2015.
- [66] AV Melnikov, LG Eliseev, SE Lysenko, SV Perfilov, DA Shelukhin, VA Vershkov, VN Zenin, LI Krupnik, NK Kharchev, et al. Correlation properties of geodesic acoustic modes in the t-10 tokamak. In *Journal of Physics: Conference Series*, volume 591, page 012003. IOP Publishing, 2015.
- [67] AV Melnikov, LG Eliseev, SE Lysenko, SV Perfilov, RV Shurygin, LI Krupnik, AS Kozachek, and AI Smolyakov. Radial homogeneity of geodesic acoustic modes in ohmic discharges with low b in the t-10 tokamak. *JETP letters*, 100(9):555–560, 2015.
- [68] Haijun Ren and Jintao Cao. Landau damping of geodesic acoustic mode in toroidally rotating tokamaks. *Physics of Plasmas*, 22(6):062501, 2015.
- [69] Haijun Ren. Finite-orbit-width effects on the geodesic acoustic mode in the toroidally rotating tokamak plasma. *Physics of Plasmas*, 24(5):054504, 2017.
- [70] T Kobayashi, M Sasaki, T Ido, K Kamiya, Y Miura, Y Nagashima, K Ida, S Inagaki, A Fujisawa, S-I Itoh, et al. Quantification of turbulent driving forces for the geodesic acoustic mode in the jft-2m tokamak. *Physical review letters*, 120(4):045002, 2018.
- [71] M Cavedon, T Pütterich, E Viezzer, G Birkenmeier, T Happel, FM Laggner, P Manz, F Ryter, U Stroth, et al. Interplay between turbulence, neoclassical and zonal flows during the transition from low to high confinement mode at asdex upgrade. *Nuclear Fusion*, 57(1):014002, 2016.
- [72] Ahmed Diallo, S Banerjee, SJ Zweben, and T Stoltzfus-Dueck. Energy exchange dynamics across l-h transitions in nstx. *Nuclear Fusion*, 57(6):066050, 2017.
- [73] I Cziegler, GR Tynan, PH Diamond, AE Hubbard, JW Hughes, J Irby, and JL Terry. Nonlinear transfer in heated l-modes approaching the l-h transition threshold in alcator c-mod. *Nuclear Fusion*, 55(8):083007, 2015.
- [74] Scott E Parker, JJ Kohut, Y Chen, Z Lin, FL Hinton, and WW Lee. Fine-scale zonal flow suppression of electron temperature gradient turbulence. In *AIP Conference Proceedings*, volume 871, pages 193–203. American Institute of Physics, 2006.

- [75] S Maeyama, Y Idomura, T-H Watanabe, M Nakata, M Yagi, N Miyato, A Ishizawa, and M Nunami. Cross-scale interactions between electron and ion scale turbulence in a tokamak plasma. *Physical review letters*, 114(25):255002, 2015.
- [76] A Biancalani, F Palermo, C Angioni, A Bottino, and F Zonca. Decay of geodesic acoustic modes due to the combined action of phase mixing and landau damping. *Physics of Plasmas*, 23(11):112115, 2016.
- [77] GQ Wang, J Ma, and J Weiland. Zonal flows near marginal stability in drift wave transport. *Physica Scripta*, 90(6):065604, 2015.
- [78] C Ehlacher, Xavier Garbet, V Grandgirard, Y Sarazin, P Donnel, E Caschera, P Ghendrih, and David Zarzoso. Contribution of kinetic electrons to gam damping. In *Journal of Physics: Conference Series*, volume 1125, page 012010. IOP Publishing, 2018.
- [79] C Holland, GR Tynan, RJ Fonck, GR McKee, J Candy, and RE Waltz. Zonal-flow-driven nonlinear energy transfer in experiment and simulation. *Physics of plasmas*, 14(5):056112, 2007.
- [80] ASDEX Upgrade Team, GD Conway, C Angioni, F Ryter, P Sauter, and J Vicente. Mean and oscillating plasma flows and turbulence interactions across the l- h confinement transition. *Physical review letters*, 106(6):065001, 2011.
- [81] I Cziegler, AE Hubbard, JW Hughes, JL Terry, and GR Tynan. Turbulence nonlinearities shed light on geometric asymmetry in tokamak confinement transitions. *Physical review letters*, 118(10):105003, 2017.
- [82] C Wahlberg. Low-frequency magnetohydrodynamics and geodesic acoustic modes in toroidally rotating tokamak plasmas. *Plasma Physics and Controlled Fusion*, 51(8):085006, 2009.
- [83] W Chen, XT Ding, LM Yu, XQ Ji, ZB Shi, YP Zhang, WL Zhong, GL Yuan, JQ Dong, QW Yang, et al. Observation of energetic-particle-induced gam and nonlinear interactions between egam, baes and tearing modes on the hl-2a tokamak. *Nuclear Fusion*, 53(11):113010, 2013.
- [84] W Chen, XT Ding, LM Yu, XQ Ji, JQ Dong, QW Yang, Yi Liu, LW Yan, Y Zhou, W Li, et al. Egam induced by energetic electrons and nonlinear interactions among egam, baes and tearing modes in a toroidal plasma. *Physics Letters A*, 377(5):387–390, 2013.
- [85] VV Bulanin, VK Gusev, AD Iblyaminova, NA Khromov, GS Kurskiev, VB Minaev, MI Patrov, AV Petrov, Yu V Petrov, NV Sakharov, et al. Geodesic acoustic mode investigation in the spherical globus-m tokamak using multi-diagnostic approach. *Nuclear Fusion*, 56(1):016017, 2015.
- [86] Ming Xu, Jizong Zhang, Tianchun Zhou, Yanmin Duan, Liqun Hu, Yingying Li, Liqing Xu, Tonghui Shi, Yong Liu, Songtao Mao, et al. Observation of electromagnetic gams excited by nbi in east. *Nuclear Fusion*, 58(9):096004, 2018.
- [87] MY Wang, C Zhou, AD Liu, J Zhang, ZY Liu, X Feng, JX Ji, H Li, T Lan, JL Xie, et al. Investigation of electromagnetic geodesic acoustic mode in east rf-heating plasma. *Physics of Plasmas*, 25(10):102508, 2018.
- [88] Christer Wahlberg and JP Graves. Magnetohydrodynamic theory of the global structure and magnetic components of the geodesic acoustic continuum modes in tokamaks. *Plasma Physics and Controlled Fusion*, 58(7):075014, 2016.

- [89] J Seidl, J Krbec, M Hron, J Adamek, C Hidalgo, T Markovic, AV Melnikov, J Stockel, V Weinzettl, M Aftanas, et al. Electromagnetic characteristics of geodesic acoustic mode in the compass tokamak. *Nuclear Fusion*, 57(12):126048, 2017.
- [90] M Leconte and R Singh. Enhancement of zonal flow damping due to resonant magnetic perturbations in the background of an equilibrium $e \times b$ sheared flow. *Physics of Plasmas*, 25(8):082311, 2018.
- [91] Mikhail Gryaznevich, J Stöckel, G Van Oost, E Del Bosco, V Svoboda, A Melnikov, R Kamendje, A Malaquias, G Mank, R Miklaszewski, et al. Contribution of joint experiments on small tokamaks in the framework of iaea coordinated research projects to mainstream fusion research. *Plasma Science and Technology*, 22(5):055102, 2020.
- [92] T Estrada, C Hidalgo, T Happel, and PH Diamond. Spatiotemporal structure of the interaction between turbulence and flows at the lh transition in a toroidal plasma. *Physical review letters*, 107(24):245004, 2011.
- [93] I Cziegler, GR Tynan, PH Diamond, AE Hubbard, JW Hughes, J Irby, and JL Terry. Zonal flow production in the l-h transition in alcator c-mod. *Plasma Physics and Controlled Fusion*, 56(7):075013, 2014.
- [94] L Schmitz, L Zeng, TL Rhodes, JC Hillesheim, EJ Doyle, RJ Groebner, WA Peebles, KH Burrell, and G Wang. Role of zonal flow predator-prey oscillations in triggering the transition to h-mode confinement. *Physical review letters*, 108(15):155002, 2012.
- [95] GR Tynan, I Cziegler, PH Diamond, M Malkov, A Hubbard, JW Hughes, JL Terry, and JH Irby. Recent progress towards a physics-based understanding of the h-mode transition. *Plasma Physics and Controlled Fusion*, 58(4):044003, 2016.
- [96] F Van Wyk, EG Highcock, AR Field, CM Roach, AA Schekochihin, FI Parra, and W Dorland. Ion-scale turbulence in mast: anomalous transport, subcritical transitions, and comparison to bes measurements. *Plasma Physics and Controlled Fusion*, 59(11):114003, 2017.
- [97] Felix I Parra and Michael Barnes. Intrinsic rotation in tokamaks: theory. *Plasma Physics and Controlled Fusion*, 57(4):045002, 2015.
- [98] P. C. De Vries. Mhd-mode stabilization by plasma rotation in textor. *Plasma Physics and Controlled Fusion*, 38(4):467, 1996.
- [99] M Barnes, FI Parra, EG Highcock, AA Schekochihin, SC Cowley, and CM Roach. Turbulent transport in tokamak plasmas with rotational shear. *Physical Review Letters*, 106(17):175004, 2011.
- [100] EG Highcock, M Barnes, AA Schekochihin, FI Parra, CM Roach, and SC Cowley. Transport bifurcation in a rotating tokamak plasma. *Physical Review Letters*, 105(21):215003, 2010.
- [101] FI Parra, M Barnes, EG Highcock, AA Schekochihin, and SC Cowley. Momentum injection in tokamak plasmas and transitions to reduced transport. *Physical review letters*, 106(11):115004, 2011.
- [102] A Yu Yashin, VV Bulanin, VK Gusev, NA Khromov, GS Kurskiev, VB Minaev, MI Patrov, AV Petrov, Yu V Petrov, DV Prisyazhnyuk, et al. Geodesic acoustic mode observations in the globus-m spherical tokamak. *Nuclear Fusion*, 54(11):114015, 2014.

- [103] DR Smith, H Feder, R Feder, RJ Fonck, G Labik, GR McKee, N Schoenbeck, BC Stratton, I Uzun-Kaymak, and G Winz. Overview of the beam emission spectroscopy diagnostic system on the national spherical torus experiment. *Review of Scientific Instruments*, 81(10):10D717, 2010.
- [104] Y Sechrest, T Munsat, DA D'Ippolito, RJ Maqueda, JR Myra, D Russell, and SJ Zweben. Flow and shear behavior in the edge and scrape-off layer of l-mode plasmas in national spherical torus experiment. *Physics of Plasmas*, 18(1):012502, 2011.
- [105] MFJ Fox, F van Wyk, AR Field, YC Ghim, FI Parra, AA Schekochihin, MAST Team, et al. Symmetry breaking in mast plasma turbulence due to toroidal flow shear. *Plasma Physics and Controlled Fusion*, 59(3):034002, 2017.
- [106] AR Field, D Dunai, YC Ghim, P Hill, B McMillan, CM Roach, S Saarelma, AA Schekochihin, S Zoletnik, MAST Team, et al. Comparison of bes measurements of ion-scale turbulence with direct gyrokinetic simulations of mast l-mode plasmas. *Plasma Physics and Controlled Fusion*, 56(2):025012, 2014.
- [107] JR Robinson, B Hnat, A Thyagaraja, KG McClements, PJ Knight, A Kirk, and MAST Team. Global two-fluid simulations of geodesic acoustic modes in strongly shaped tight aspect ratio tokamak plasmas. *Physics of Plasmas*, 20(5):052302, 2013.
- [108] GJ Colyer, AA Schekochihin, FI Parra, CM Roach, MA Barnes, YC Ghim, and W Dorland. Collisionality scaling of the electron heat flux in etg turbulence. *Plasma Physics and Controlled Fusion*, 59(5):055002, 2017.
- [109] JR Robinson, B Hnat, P Dura, A Kirk, P Tamain, MAST Team, et al. Interaction between a low-frequency electrostatic mode and resonant magnetic perturbations in mast. *Plasma Physics and Controlled Fusion*, 54(10):105007, 2012.
- [110] SJ Zweben, DP Stotler, JL Terry, B LaBombard, M Greenwald, M Muterspaugh, CS Pitcher, Alcator C-Mod Group, K Hallatschek, RJ Maqueda, et al. Edge turbulence imaging in the alcator c-mod tokamak. *Physics of Plasmas*, 9(5):1981–1989, 2002.
- [111] YC Ghim, AR Field, D Dunai, S Zoletnik, L Bardóczi, AA Schekochihin, MAST Team, et al. Measurement and physical interpretation of the mean motion of turbulent density patterns detected by the beam emission spectroscopy system on the mega amp spherical tokamak. *Plasma Physics and Controlled Fusion*, 54(9):095012, 2012.
- [112] M Willensdorfer, G Birkenmeier, R Fischer, FM Laggner, E Wolfrum, G Veres, F Aumayr, D Carralero, L Guimaraes, B Kurzan, et al. Characterization of the li-bes at asdex upgrade. *Plasma Physics and Controlled Fusion*, 56(2):025008, 2014.
- [113] D Dunai, S Zoletnik, J Sárközi, and AR Field. Avalanche photodiode based detector for beam emission spectroscopy. *Review of Scientific Instruments*, 81(10):103503, 2010.
- [114] AR Field, D Dunai, NJ Conway, S Zoletnik, and J Sárközi. Beam emission spectroscopy for density turbulence measurements on the mast spherical tokamak. *Review of Scientific Instruments*, 80(7):073503, 2009.
- [115] Young-chul Ghim, AR Field, S Zoletnik, and D Dunai. Calculation of spatial response of 2d beam emission spectroscopy diagnostic on mast. *Review of Scientific Instruments*, 81(10):10D713, 2010.

- [116] MFJ Fox, AR Field, F van Wyk, YC Ghim, AA Schekochihin, Mast Team, et al. Experimental determination of the correlation properties of plasma turbulence using 2d bes systems. *Plasma Physics and Controlled Fusion*, 59(4):044008, 2017.
- [117] AR Field, D Dunai, R Gaffka, Y-c Ghim, I Kiss, B Meszaros, T Krizsanoczi, S Shibaev, and S Zoletnik. Beam emission spectroscopy turbulence imaging system for the mast spherical tokamak. *Review of Scientific Instruments*, 83(1):013508, 2012.
- [118] DR Smith, SE Parker, W Wan, Y Chen, A Diallo, BD Dudson, RJ Fonck, W Guttenfelder, GR McKee, SM Kaye, et al. Measurements and simulations of low-wavenumber pedestal turbulence in the national spherical torus experiment. *Nuclear Fusion*, 53(11):113029, 2013.
- [119] JM Sierchio, I Cziegler, JL Terry, AE White, and SJ Zweben. Comparison of velocimetry techniques for turbulent structures in gas-puff imaging data. *Review of Scientific Instruments*, 87(2):023502, 2016.
- [120] Balazs Tal, Attila Bencze, Sandor Zoletnik, Gabor Veres, and Gabor Por. Cross-correlation based time delay estimation for turbulent flow velocity measurements: Statistical considerations. *Physics of Plasmas*, 18(12):122304, 2011.
- [121] L Hausammann, RM Churchill, and L Shi. Synthetic diagnostic for the beam emission spectroscopy diagnostic using a full optical integration. *Plasma Physics and Controlled Fusion*, 59(2):025017, 2017.
- [122] Wikipedia contributors. Surrogate data testing — Wikipedia, the free encyclopedia. https://en.wikipedia.org/w/index.php?title=Surrogate_data_testing&oldid=1075559288, 2022. [Online; accessed 7-March-2022].
- [123] Jong S Kim, You Huh, and Moon W Suh. A method to generate autocorrelated stochastic signals based on the random phase spectrum. *The Journal of The Textile Institute*, 101(5):471–479, 2010.
- [124] L Schmitz. The role of turbulence–flow interactions in l-to h-mode transition dynamics: recent progress. *Nuclear Fusion*, 57(2):025003, 2017.
- [125] Feng Wang, GY Fu, JA Breslau, and JY Liu. Linear stability and nonlinear dynamics of the fishbone mode in spherical tokamaks. *Physics of Plasmas*, 20(10):102506, 2013.
- [126] T Edlington, R Martin, and T Pinfeld. Mast magnetic diagnostics. *Review of Scientific Instruments*, 72(1):421–425, 2001.
- [127] MP Gryaznevich, SE Sharapov, M Lilley, SD Pinches, AR Field, D Howell, D Keeling, R Martin, H Meyer, H Smith, et al. Recent experiments on alfvén eigenmodes in mast. *Nuclear fusion*, 48(8):084003, 2008.
- [128] V Mukhovatov, M Shimada, AN Chudnovskiy, AE Costley, Y Gribov, G Federici, O Kardaun, AS Kukushkin, A Polevoi, VD Pustovitov, et al. Overview of physics basis for iter. *Plasma physics and controlled fusion*, 45(12A):A235, 2003.
- [129] N Ben. Omv diagnostic summary, 2010. URL <http://fusweb1.fusion.ccfе.ac.uk/~nben/html/OMVDiagnosticSummary.html#OMVDiagnosticSummary>.
- [130] HL Berk, CJ Boswell, D Borba, ACA Figueiredo, T Johnson, MFF Nave, SD Pinches, SE Sharapov, et al. Explanation of the jet $n=0$ chirping mode. *Nuclear fusion*, 46(10):S888, 2006.

- [131] Deng Zhou. Electromagnetic geodesic acoustic modes in tokamak plasmas. *Physics of Plasmas*, 14(10):104502, 2007.
- [132] Zhouji Huang, Stefano Coda, Gabriele Merlo, Stephan Brunner, Laurent Villard, Benoit Labit, Christian Theiler, et al. Experimental observations of modes with geodesic acoustic character from the core to the edge in the tcv tokamak. *Plasma Physics and Controlled Fusion*, 60(3):034007, 2018.
- [133] Zhe Gao. Plasma shaping effects on the geodesic acoustic mode in the large orbit drift width limit. *Physics of Plasmas*, 17(9):092503, 2010.
- [134] VP Lakhin, VI Ilgisonis, and AI Smolyakov. Geodesic acoustic modes and zonal flows in toroidally rotating tokamak plasmas. *Physics Letters A*, 374(48):4872–4875, 2010.
- [135] M Shimada, DJ Campbell, V Mukhovatov, M Fujiwara, N Kirneva, K Lackner, M Nagami, VD Pustovitov, N Uckan, J Wesley, et al. Progress in the iter physics basis-chapter 1: overview and summary. *Nuclear Fusion*, 47:S1–S17, 2007.
- [136] Rory ORY Thompson. Coherence significance levels. *J. Atmos. Sci.*, 36:2020–2021, 1979.
- [137] K Miki, PH Diamond, Özgür D Gürçan, GR Tynan, T Estrada, L Schmitz, and GS Xu. Spatio-temporal evolution of the l i h transition. *Physics of Plasmas*, 19(9):092306, 2012.

Chapter 8

Appendices

8.1 Appendix A: Copy of the Code

The python script for this code is held within the group, led by Istvan Cziegler.

```
1 import os
2 import matplotlib as mpl
3 if os.environ.get('DISPLAY','') == '':
4     print('no display found. Using non-interactive Agg backend')
5     mpl.use('Agg')
6 import pyuda
7 import matplotlib.pyplot as plt
8 from os import makedirs
9 client=pyuda.Client()
10 import Functions
11 plt.plot([1,1],[0,0])
12 plt.style('')
13 plt.clf()
14
15 from numpy import linspace,multiply, nanmean, asarray, where, delete, average, polyfit, mean, std, diff, savez,
16 \
17 sort, transpose, concatenate, round, nanmedian
18 from scipy.signal import argrelext, argrelemin
19 from scipy import zeros, arange
20
21 #####
22 ##CROSS-CORRELATION TIME DELAY ESTIMATION VELOCIMETRY ROUTINE##
23 ##developed by Andrew Malcolin-Heale##
24 ##updated 04/08/2020##
25 #####
26
27 """
28 This is the basic version (vertical velocimetry only) of a routine using CCTDE to measure plasma flows of WAST
29 BES data.
30 Key differentiating features of the design of this code include -
31 Fitting to four channels correlation not just two-point
32 Averaging velocity per column (neglecting horizontal velocity calculation)
33 Velocity calculated at every time step
34 Very short correlation functions
35 The order of calculation is as follows (numbers in parentheses in the code) -
36 (1) Calculate or load fluctuating dI/I version of BES data
37 (2) Per time slice in time range of interest slice BES data to bin size length (from that timestep forward)
38 (3) Per time slice, for every channel, calculate the cross-correlation with every other channel in its
39 column
40 (4) Per time slice, for every channel, calculate the velocity seen (subject to physics and a number of
41 tests)
42 (5) Per time slice, average the velocities over channels in a column to one velocity per column
43 (6) Clean the full time series of velocity per column data
44 (7) Calculate the spectra of time series of velocity per column (ie radial position)
45
46 Inputs: BES - dictionary of fluctuating signals, measured times and detector positions
47 barspurious - Physical limit for velocity
48 baraccn - Physical limit for acceleration
49 bar - Statistical significance cutoff
50 N - Correlation 'bin' size
51 shots - list of shot numbers to measure
52 starts - list of [lists of starts of intervals of interest for each shot number]
53 ends - list of [lists of ends of intervals of interest for each shot number]
54
55 Outputs: /velocimetry/
56 vcols - array of velocity time series for every channel
57 rawvcols - array of averaged velocity time series per column
58 vcols - array of cleaned velocity time series per column
59 vcolswerr - array of averaged r**2 values per column
60 data saved to '(0){1} (2) to (3) N(4) vcols.rpt'.format(filepath, shotno, tzero, tfinal, N)
61 data plotted as '(0){1} (2) to (3) with N(4) Velocities_stdev.rpt'.format(filepath, shotno,
62 tzero, tfinal, N, expttag)
63 /spectrum/
64 """
```

```

59      freq - list of frequencies spectra are measured at
60      velspecs - array of power spectral densities of velocity time series per column
61      data saved as '{0}(1) {2} to {3} spectra\data_{0}.format(filepath, shotno, tzero, tfinal)
62      data plotted as '{0}(1) {2} to {3} Velocity Spectra (4).png'.format(filepath, shotno, tzero, tfinal)
63      expttag
64      ...
65
66      #####
67      #CONSTANTS
68      #colomemps that will be used
69      cmap = [plt.cm.viridis(c) for c in linspace(0, 1, 8)]
70      cmap = [plt.cm.gist_rainbow(c) for c in linspace(0, 1, 8)]
71      # switch palette for Dark grey
72      cmap[2] = plt.cm.binary(c)
73      cmap = [plt.cm.viridis(c) for c in linspace(0, 1, 12)]
74
75      # cutoffs for physical results - velocity and change of velocity
76      # km/s
77      barspurious = 120.
78      # km/s^2
79      baraccn = 1e5
80      # statistical significance cutoff of correlation functions of different sizes
81      xcorrNs = asarray([32, 64, 128, 256])
82      xcorrSigs = [0.3494, 0.2461, 0.1736, 0.1226]
83      bar = xcorrSigs[nearposn(xcorrNs, N)]
84
85      # Correlation Bin Size
86      N = 64
87
88      # Some other useful constants
89      dt = 5e-7
90      tres = N * dt
91      fvyq = 1 / (2 * tres)
92
93
94      #####
95      #In general the shots we are considering are from sets of turbulence experiments as listed here
96      #Below are the groupings used for keeping similar shots together
97      #Any shot not in a group will be associated with the closest by shot number so should be listed here separately
98      allshots = [[27525, 27527, 27526, 27528], #<- done
99                [29376, 29379, 29380],
100               [29505, 29527, 30435, 30440], #<- 30449
101               [26310, 26313, 26314, 26317],
102               [26364, 26365, 26366, 26367, 26368, 26369, 26371, 26372, 26373, 26374, 26375, 26376, 26377, 26378], #<- 26371
103               [26585, 26586, 26587],
104               [26861, 26862, 26863, 26864, 26865, 26866], #<- done
105               [26884, 26885, 26886, 26887, 26888, 26889, 26891],
106               [26934, 26935, 26936, 26937, 26941, 26942], #<- done
107               [26968, 26969, 26970, 26972, 26973],
108               [26975, 26976, 26977, 26978, 26979, 26980], #<- done
109               [27267, 27268, 27269, 27270, 27272, 27273, 27274, 27278],
110               [29113, 29114, 29115, 29113, 29125, 29126, 29128, 29129], #<- 29125
111               [29139, 29142, 29143, 29144, 29149, 29151, 29153, 29156, 29158, 29159, 29160],
112               [29762, 29764], #<- done
113               [30175, 30176, 30177, 30178, 30179],
114               [30162, 30163, 30164, 30165, 30165, 30167, 30168, 30169, 30170, 30171, 30172],
115               #<- for
116               [27271, 27275, 27276, 27277, 27279, 27280],
117               [27281, 27282, 27283, 27284, 27285],
118               [27292, 27293, 27294, 27296, 27297, 27298],
119               [27308],
120               [27369, 27370, 27396, 27397, 27398, 27399, 27403, 27404, 27407, 27408, 27409],

```

```

121               [28151, 28152, 28153, 28154, 28155, 28156],
122               [29050, 29053],
123               [29447],
124               [29455],
125               [29470],
126               [29761],
127               [21856],
128               [29853, 29854, 29855],
129               [29876, 29877, 29878],
130               [29888, 29890, 29891],
131               [29982, 29983],
132               [30114, 30115, 30117],
133               [30175, 30176, 30177, 30178, 30179]
134      #Assign results an experiment number that is the first shot in the experiment 'set'
135      expts = [shotrun[0] for shotrun in allshots]
136
137      #Tag analyses (attached to saved data and plots)
138      #Can loop over multiple analyses
139      tags = ['Long']
140      for expttag in tags:
141          #Testing outcomes of long shot times of interest
142          if expttag == 'Long':
143              shots = [29762, 30449, 30258, 29378, 29505, 29761, 26317, 26885, 30170, 30171, 30166, 30167, 30169,
144                    30176, 30175, 30178, 30179]
145              startts = [[0.12], [0.18], [0.18], [0.35], [0.49], [0.38], [0.14], [0.18], [0.24], [0.23], [0.16], [0.19],
146                       [0.19], [0.19], [0.39], [0.18], [0.42], [0.31]
147                       [0.22], [0.42], [0.21], [0.45], [0.34]]
148              endts = [[0.2], [0.22], [0.38], [0.52], [0.39], [0.17], [0.13], [0.27], [0.26], [0.19], [0.22], [0.22],
149                      [0.22], [0.42], [0.21], [0.45], [0.34]]
150              assert len(shots) == len(startts)
151
152          #####
153          # Assign labels for this analysis
154          print(expttag)
155          for q, shotno in enumerate(shots):
156              nrshot = asarray(expts) - shotno
157              nrzero = max([s for s in nrshot if s <= 0])
158              exptno = expts[nearposn(nrshot, nrzero)]
159              print('{0}'.format(exptno))
160
161          # Where to save data (subfolder per shot in an experiment)
162          # filepath = '/common/scratch/malcolm/{0}_{1}'.format(exptno, shotno)
163          filepath = '/home/malcolm/Documents/NEHDATA/{0}_{1}'.format(exptno, shotno)
164          makedirs(filepath, exist_ok=True)
165
166          #####(1)#####
167          # Hence or otherwise get fluctuating BES data for the shot being studied
168          try:
169              data = load('/home/malcolm/Documents/NEHDATA/{0}_{2}/BES{1}.npz'.format(exptno, shotno, shotno))
170              BES = dict()
171              for ch in arange(1, 33, 1):
172                  BES['{0}channel{1:02d}'.format(shotno, ch)] = data['channel{0:02d}'.format(ch)]
173                  BES['{0}times'.format(shotno)] = data['times']
174                  BES['{0}pixels'.format(shotno)] = data['apdospsn']
175                  BES['{0}view'.format(shotno)] = data['view']
176                  BES['{0}coords'.format(shotno)] = data['coords']
177                  rowposns = BES['{0}pixels'.format(shotno)].reshape(4, 8, 2)
178          except:
179              # check NBI data exist before using readBESuda without specified times
180              # if no NBI will read BES with times specified inside later loop

```

```

181     try:
182         NBIdat = retrieve('anb_tot_sum_power', shotno)[0]
183     except:
184         NBIdat = None
185
186     if NBIdat is None:
187         pass
188     ## Save BES data if not already in folder
189     else:
190         BES = readBESuda([shotno], cutoff=[fvnyq, 200000], order=5)
191         rowposns = BES['{0}pixels'.format(shotno)].reshape(4, 8, 2)
192         savename = '{0}BES{1}.npz'.format(filepath, shotno)
193         savez(savename, times=BES['{0}times'.format(shotno)], apdposns=BES['{0}pixels'.format(shotno)],
194             view=BES['{0}viewr'.format(shotno)], coords=BES['{0}coords'.format(shotno)],
195             channel01=BES['{0}channel01'.format(shotno)], channel02=BES['{0}
channel02'.format(shotno)],
196             channel03=BES['{0}channel03'.format(shotno)], channel04=BES['{0}
channel04'.format(shotno)],
197             channel05=BES['{0}channel05'.format(shotno)], channel06=BES['{0}
channel06'.format(shotno)],
198             channel07=BES['{0}channel07'.format(shotno)], channel08=BES['{0}
channel08'.format(shotno)],
199             channel09=BES['{0}channel09'.format(shotno)], channel10=BES['{0}
channel10'.format(shotno)],
200             channel11=BES['{0}channel11'.format(shotno)], channel12=BES['{0}
channel12'.format(shotno)],
201             channel13=BES['{0}channel13'.format(shotno)], channel14=BES['{0}
channel14'.format(shotno)],
202             channel15=BES['{0}channel15'.format(shotno)], channel16=BES['{0}
channel16'.format(shotno)],
203             channel17=BES['{0}channel17'.format(shotno)], channel18=BES['{0}
channel18'.format(shotno)],
204             channel19=BES['{0}channel19'.format(shotno)], channel20=BES['{0}
channel20'.format(shotno)],
205             channel21=BES['{0}channel21'.format(shotno)], channel22=BES['{0}
channel22'.format(shotno)],
206             channel23=BES['{0}channel23'.format(shotno)], channel24=BES['{0}
channel24'.format(shotno)],
207             channel25=BES['{0}channel25'.format(shotno)], channel26=BES['{0}
channel26'.format(shotno)],
208             channel27=BES['{0}channel27'.format(shotno)], channel28=BES['{0}
channel28'.format(shotno)],
209             channel29=BES['{0}channel29'.format(shotno)], channel30=BES['{0}
channel30'.format(shotno)],
210             channel31=BES['{0}channel31'.format(shotno)], channel32=BES['{0}
channel32'.format(shotno)])
211
212
213     #####
214     ## Record velocities for whole experiment (will save per shot)
215     ## Record per channel and per column of the detector
216     vchs = dict()
217     rawvcols = dict()
218     vcols = dict()
219     # vcolsterr = dict()
220     ## r^2 is useful weighting measure of error (1 is good)
221     vcolswerr = dict()
222
223     ## loop over each set of times identified per shot
224     for tzero, tfinal in zip(startts[q], endts[q]):
225         tzero = round(tzero, 5)
226         tfinal = round(tfinal, 5)
227

```

```

228     ## if no BES data yet, retrieve now with specified (short) times
229     if NBIdat is None:
230         BES = readBESuda([shotno], tinit=[tzero], tend=[tfinal], cutoff=[fvnyq, 200000], order = 5)
231
232     ## get radii and normalised radii of BES viewing locations for plasma at this time
233     det_rs = BESr[shotno][1]
234     det_rhos = []
235     tol = tzero + (tfinal-tzero)/2
236     for R in det_rs:
237         det_rhos.append(round(rhomaker(R, shotno, tol), 2))
238
239     print(tzero)
240
241     ## mark the times of interest
242     t_up, t_down = [tzero, tfinal]
243     izero = nearposn(BES['{0}times'.format(shotno)], tzero)
244     ifinal = nearposn(BES['{0}times'.format(shotno)], tfinal)
245     vtimes=BES['{0}times'.format(shotno)][izero:ifinal]
246     ##start time of each measurement
247     starts = arange(tzero, tfinal - tres, dt)
248     stepno = len(starts)
249
250     ## setup arrays to record data for each shot & time of interest (together = one 'run' of the
velocimetry)
251     vchs['{0}_{1}'.format(shotno, tzero)] = []
252     rawvcols['{0}_{1}'.format(shotno, tzero)] = []
253     vcols['{0}_{1}'.format(shotno, tzero)] = []
254     # vcolsterr['{0}_{1}'.format(shotno, tzero)] = []
255     vcolswerr['{0}_{1}'.format(shotno, tzero)] = []
256
257
258     #####(2)#####
259     ##build velocity time series - measures every channel at every time step
260     ##if stepping multiple time steps NB dt changes
261     for tinit in starts:
262         ## find end time of time slice to be included in correlation calculation (bin size)
263         tend = tinit + tres
264         ## index time slice to be measured
265         opoint = nearposn(BES['{0}times'.format(shotno)], tinit)
266         clint = nearposn(BES['{0}times'.format(shotno)], tend)
267         trange = clint - opoint
268         length = tend - tinit
269         tinit = round(tinit, 0)
270
271     ## dictionary of fluctuating BES data for this time slice
272     d = dict()
273     for chi in arange(1, 33, 1):
274         d['channel{0}'.format(chi)] = BES['{0}channel{1:02d}'.format(shotno, chi)][opint:clint]
275
276     ## calculate cross correlation of refig and each datasig
277     ## long list below tracks of all the things we want to measure
278     ## use dictionaries to save data per test case for later
279     ## raw correlation data
280     colpeaks = dict()
281     coltroughs = dict()
282     colstdevs = dict()
283     coldelay = dict()
284     xcorcol = dict()
285     xcolind = dict()
286     cc = dict()
287
288     ## manipulated data
289     fitdata = dict()

```

```

290 tdata = dict()
291 vdata = dict()
292 varray = dict()
293
294 ## track pairs to reduce calculation number (xcorr is the slow part of the code)
295 ident = dict()
296 pairxcorr = dict()
297
298 ## velocity as fitted, weighted gradient & fitting errors
299 wcolgrads = []
300 cr22 = []
301 fiterr = []
302 gdfits = []
303 sdfits = []
304
305 ## track completed channels
306 polrefs = []
307
308 #####(3)#####
309 ##per time slice, make correlation measurements (row/column) using every channel as reference by
310 turn
311 for refch in arange(1, 33, 1):
312     ##reference channel data is the reference signal for correlation
313     refsig = d["channel{0}".format(refch)]
314
315     ## cross-correlate with other channels in each column
316     colpeaks["colpeaks{0}".format(refch)] = []
317     coltroughs["coltroughs{0}".format(refch)] = []
318     colstdevs["colstdevs{0}".format(refch)] = []
319     coldelay["coldelay{0}".format(refch)] = []
320     xccorcol["xccorcol{0}".format(refch)] = []
321     xccolind["xccolind{0}".format(refch)] = []
322
323     ## if the data signal is in the same column [row] as refsig then record the correlation
324     function...
325     for datasig in arange(1, 33, 1):
326         datasig = d["channel{0}".format(datasig)]
327
328         ## for a pair of channels the crosscorrelation is time-reversed (i.e.*-1) if signals are
329         swapped
330         a, b = sort([refsig, datasig])
331         tag = '{0}/{1}'.format(a, b)
332
333         ## [row and] column identifier grid...
334         if (refch > 8) and (refch < 9):
335             if (datasig == refch) or (datasig == refch + 8) or (datasig == refch + 16) or (
336                 datasig == refch + 24):
337                 if tag in ident:
338                     xccorcol["xccorcol{0}".format(refch)].append(asarray(pairxcorr[tag][0][::-1]))
339                     xccolind["xccolind{0}".format(refch)].append(datasig)
340                     colpeaks["colpeaks{0}".format(refch)].append(pairxcorr[tag][2][0])
341                     coldelay["coldelay{0}".format(refch)].append(-pairxcorr[tag][2][1])
342                 else:
343                     ident[tag] = []
344                     xcorr = xcorrrelate(refsig, datasig)
345                     pairxcorr[tag] = xcorr
346                     xccorcol["xccorcol{0}".format(refch)].append(asarray(xcorr[0]))
347                     xccolind["xccolind{0}".format(refch)].append(datasig)
348                     colpeaks["colpeaks{0}".format(refch)].append(xcorr[2][0])
349                     coldelay["coldelay{0}".format(refch)].append(xcorr[2][1])

```

```

350         if (refch > 8) and (refch < 17):
351             if (datasig == refch) or (datasig == refch - 8) or (datasig == refch + 8) or (
352                 datasig == refch + 16):
353                 if tag in ident:
354                     xccorcol["xccorcol{0}".format(refch)].append(asarray(pairxcorr[tag][0][::-1]))
355                     xccolind["xccolind{0}".format(refch)].append(datasig)
356                     colpeaks["colpeaks{0}".format(refch)].append(pairxcorr[tag][2][0])
357                     coldelay["coldelay{0}".format(refch)].append(-pairxcorr[tag][2][1])
358                 else:
359                     ident[tag] = []
360                     xcorr = xcorrrelate(refsig, datasig)
361                     pairxcorr[tag] = xcorr
362                     xccorcol["xccorcol{0}".format(refch)].append(asarray(xcorr[0]))
363                     xccolind["xccolind{0}".format(refch)].append(datasig)
364                     colpeaks["colpeaks{0}".format(refch)].append(xcorr[2][0])
365                     coldelay["coldelay{0}".format(refch)].append(xcorr[2][1])
366
367         if (refch > 16) and (refch < 25):
368             if (datasig == refch) or (datasig == refch - 8) or (datasig == refch + 8) or (
369                 datasig == refch - 16):
370                 if tag in ident:
371                     xccorcol["xccorcol{0}".format(refch)].append(asarray(pairxcorr[tag][0][::-1]))
372                     xccolind["xccolind{0}".format(refch)].append(datasig)
373                     colpeaks["colpeaks{0}".format(refch)].append(pairxcorr[tag][2][0])
374                     coldelay["coldelay{0}".format(refch)].append(-pairxcorr[tag][2][1])
375                 else:
376                     ident[tag] = []
377                     xcorr = xcorrrelate(refsig, datasig)
378                     pairxcorr[tag] = xcorr
379                     xccorcol["xccorcol{0}".format(refch)].append(asarray(xcorr[0]))
380                     xccolind["xccolind{0}".format(refch)].append(datasig)
381                     colpeaks["colpeaks{0}".format(refch)].append(xcorr[2][0])
382                     coldelay["coldelay{0}".format(refch)].append(xcorr[2][1])
383
384         if (refch > 24) and (refch < 33):
385             if (datasig == refch) or (datasig == refch - 8) or (datasig == refch - 16) or (
386                 datasig == refch - 24):
387                 if tag in ident:
388                     xccorcol["xccorcol{0}".format(refch)].append(asarray(pairxcorr[tag][0][::-1]))
389                     xccolind["xccolind{0}".format(refch)].append(datasig)
390                     colpeaks["colpeaks{0}".format(refch)].append(pairxcorr[tag][2][0])
391                     coldelay["coldelay{0}".format(refch)].append(-pairxcorr[tag][2][1])
392                 else:
393                     ident[tag] = []
394                     xcorr = xcorrrelate(refsig, datasig)
395                     pairxcorr[tag] = xcorr
396                     xccorcol["xccorcol{0}".format(refch)].append(asarray(xcorr[0]))
397                     xccolind["xccolind{0}".format(refch)].append(datasig)
398                     colpeaks["colpeaks{0}".format(refch)].append(xcorr[2][0])
399                     coldelay["coldelay{0}".format(refch)].append(xcorr[2][1])
400
401     #####(4)#####
402     ## Now for the refch we have arrays of correlation data for each other channel in its column
403     ## test the data against some known cases that will break the measurement (if fail, discard
404     to Nall)
405     ## three undelayed peaks or more indicates a broken correlation function
406     if len(where(asarray(coldelay["coldelay{0}".format(refch)]) == 0)[0]) > 2:
407         determination = 0
408         cr22.append(determination)
409         velocity = float('NaN')
410         wcolgrads.append(velocity)
411

```

```

412 positions      ## Do velocity measure (by fitting) checking whether better fit achieved with only three
413               else:
414               ## v calculation = dx/dt by gradient [ie dy/dx]: [m/ms] == [km/s]
415               ## get x axis separation values for every data channel -- in metres
416               coldx = rowposns[:,(refch-1)%8][:,1]
417               # coldx = (xccolind["xccolind(0)".format(refch)] - refch) * 0.02 / 8
418               ## get y axis delay-to-max-xcorr values for every data channel -- put in ms
419               coldt = multiply(coldelay["coldelay(0)".format(refch)], 1000 * dt)
420               ## weighting array for fit
421               wc = colpeaks["colpeaks(0)".format(refch)]
422
423               ## ignore statistically insignificant correlation peaks
424               for i, coll in enumerate(wc):
425                 if coll < bar:
426                   wc[i] = 0.
427
428               ## Cant fit a line if all the non-refch data are insignificant
429               if len(where(asarray(wc) == 0)[0])==3:
430                 determination = 0.
431                 cr22.append(determination)
432                 velocity = float('nan')
433                 wcolgrads.append(velocity)
434
435               else:
436                 ## compare cases with a turning point for fit using four or three data points
437                 ## test for peak in the fitting data and whether the r2 is better using only three
438
439               points
440               # eg:
441               # dt
442               # |
443               # |      x
444               # |     x
445               # |    x
446               # |   (x) <- refch = s1
447               # |          dx
448
449               testfourthone = argrelnax(asarray(coldt))[0]
450               testfourthtwo = argrelnmin(asarray(coldt))[0]
451               testfourth = len(testfourthone) + len(testfourthtwo)
452
453               newwmc = []
454               newcoldx = []
455               newcoldt = []
456               if testfourth == 1:
457                 ## calculate with four
458                 wcoeffs = polyfit(coldx, coldt, 1, w=wc)
459                 velocity4 = 1. / wcoeffs[0]
460
461               ## calculate the r value fitting all four points
462               r4 = determinate(coldx, coldt, len(coldx))
463
464               ## check if a peak or a trough
465               if len(testfourthone) == 1:
466                 testthefourth = testfourthone
467               elif len(testfourthtwo) == 1:
468                 testthefourth = testfourthtwo
469
470               ## force three point fit to include reference channel
471               if testthefourth[0] == 1:
472                 if 0 in coldx[1:]:
473                   newwmc = wc[1:]

```

```

474                   newcoldx = coldx[1:]
475                   newcoldt = coldt[1:]
476               if testthefourth[0] == 2:
477                 if 0 in coldx[3:]:
478                   newwmc = wc[3:]
479                   newcoldx = coldx[3:]
480                   newcoldt = coldt[3:]
481
482               ## do weighted (by xcorr peak) linear fit for three points
483               try:
484                 newwcoeffs = polyfit(newcoldx, newcoldt, 1, w=newwmc)
485                 velocity3 = 1. / newwcoeffs[0]
486
487                 r3 = determinate(newcoldx, newcoldt, len(newcoldx))
488
489                 ## compare determination coefficient for three and four point calculation
490                 ## keep the higher r option
491                 if r2 * r2 > r4 * r4:
492                   testmark = 1
493                   determination = r3 * r3
494                   cr22.append(determination)
495                   velocity = velocity3
496                   wcolgrads.append(velocity)
497               else:
498                 determination = r4 * r4
499                 cr22.append(determination)
500                 velocity = velocity4
501                 wcolgrads.append(velocity)
502
503               except:
504                 determination = r4 * r4
505                 cr22.append(determination)
506                 velocity = velocity4
507                 wcolgrads.append(velocity)
508
509               ## if no turning points then weighted linear fit with four
510               else:
511                 wcoeffs = polyfit(coldx, coldt, 1, w=wc)
512                 velocity4 = 1. / wcoeffs[0]
513
514               r4 = determinate(coldx, coldt, len(coldx))
515
516               determination = r4 * r4
517               cr22.append(determination)
518               velocity = velocity4
519               wcolgrads.append(velocity4)
520
521               ## track reference positions that have been measured
522               polrefs.append(refch)
523
524
525               #####(5)#####
526               ## How for this timeslice we have the velocity measurements fit error per channel
527               ## Array of 32 velocities (gradients)
528               wcolgrads = asarray(wcolgrads)
529               ## Array of 32 r squared coefficients of fit
530               cr22 = asarray(cr22)
531               ## Array of 32 standard error of fit
532               # fiterr = asarray(fiterr)
533
534               ## exclude velocities deemed unphysical
535               for spurious in wcolgrads[wcolgrads > barspurious] | (wcolgrads < -barspurious)]:

```

```

536         wcolgrads[where(wcolgrads == spurious)] = float('nan')
537
538     ## convert list to 2D array of 4x8 velocities and weights
539     blank = zeros([4, 8])
540     indices = [[1, 2, 3, 4, 5, 6, 7, 8], [9, 10, 11, 12, 13, 14, 15, 16], [17, 18, 19, 20, 21, 22,
23, 24],
541              [25, 26, 27, 28, 29, 30, 31, 32]]
542     for i, j in enumerate(polrefs):
543         blank[where(indices == j)] = wcolgrads[i]
544     wcolgrads = blank
545     blank = zeros([4, 8])
546     for i, j in enumerate(polrefs):
547         blank[where(indices == j)] = cr22[i]
548     cr22 = blank
549
550     ## store data for this timestep for all channels (2D)
551     vchs['{0}_{1}'.format(shotno, tzero)].append(wcolgrads)
552
553     ## Take weighted by r squared mean over the 4 available measurements per column (ie per radius)
554     ## arrays length ncols (8) for this timestep
555     vp = []
556     # vpserror = []
557     vpwerror = []
558     for column in range(8):
559         weevs = []
560         r2 = []
561         ## (if non NaN values) create array of velocities and errors to be averaged for every time
562     slice
563         for w, v in enumerate(wcolgrads[:,column]):
564             if v == vs:
565                 weevs.append(v)
566                 rcheck = cr22[:,column][w]
567                 if rcheck > bar:
568                     r2.append(cr22[:,column][w])
569                 else:
570                     r2.append(0)
571         ## record averaged measurement for this radius, timestep
572         try:
573             vp.append(average(weevs, weights=r2))
574         except:
575             vp.append(float('NaN'))
576             vpserror.append(0.)
577             vpwerror.append(0.)
578         else:
579             vpwerror.append(average(r2))
580
581     ## add this time slice's measurements (len = no. columns) to array of measurements per timestep
582     rawvcols['{0}_{1}'.format(shotno, tzero)].append(vp)
583     # wcolsterr['{0}_{1}'.format(shotno, tzero)].append(vpserror)
584     vcolswerr['{0}_{1}'.format(shotno, tzero)].append(vpwerror)
585
586     ## velocimetry calculations end
587
588     #####(6)#####
589
590     ## now have all timestep measurements per channel & per radius
591     ## will clean the signal
592     ## create array of measured times (middle time of each time slice)
593     vptimes = stants + (N / 2) * dt
594     if len(vptimes) != len(rawvcols['{0}_{1}'.format(shotno, tzero)]):
595         vptimes = vtimes[-(N+1)] + (N / 2) * dt
596     assert len(vptimes) == len(rawvcols['{0}_{1}'.format(shotno, tzero)])

```

```

597
598     ## have raw data of velocities per timestep, transpose to time series per column
599     rawvcols['{0}_{1}'.format(shotno, tzero)] = transpose(rawvcols['{0}_{1}'.format(shotno, tzero)])
600     # vcolsterr['{0}_{1}'.format(shotno, tzero)] = transpose(vcolsterr['{0}_{1}'.format(shotno,
601     tzero)])
602     vcolswerr['{0}_{1}'.format(shotno, tzero)] = transpose(vcolswerr['{0}_{1}'.format(shotno, tzero)])
603
604     ## report finishing calculation of raw velocities
605     print('{0}_{1} Vel's'.format(shotno, tzero))
606
607     ## Two signal corrections
608     for col in range(8):
609         vpsraw = rawvcols['{0}_{1}'.format(shotno, tzero)][col]
610         vpsfitter = vcolswerr['{0}_{1}'.format(shotno, tzero)][col]
611
612         ## Note raw mean measured velocity
613         vbar = round(nanmean(vpsraw), 4)
614         vps = vpsraw
615         ## count negative velocities (assume positive flow upwards), real and NaN (ie failed)
616     measurements
617         neg1 = where(0 > vps)[0]
618         negcount = len(neg1)
619         baddies = where(vps != vps)[0]
620
621         ## First FFT to get spectra needs regular data set so replace NaNs
622         ## rather than skewing to adjacent positions and poor measurements replace with an average
623         for posn, velocity in enumerate(vps):
624             if velocity != velocity:
625                 ## calculate average inside loop to bring toward vs
626                 consider = vps[posn - int(N / 2):posn + int(N / 2)]
627                 if len(consider) == 0:
628                     vps[posn] = nanmedian(vps)
629                 elif len(consider != 0):
630                     vps[posn] = nanmedian(consider)
631                 else:
632                     vps[posn] = nanmedian(vps[posn - int(N / 2):posn + int(N / 2)])
633
634         ## Second eliminate too-rapid changes in velocity as unphysical
635         dvpsdt = diff(vps)
636         mn = mean(dvpsdt)
637         sd = std(dvpsdt)
638         ## set boundary for physical acceleration as multiple of standard deviation of dv/dt
639         xstdev = (baraccn * dt - mn) / sd
640         accn = round((mn + xstdev * sd) / dt, 0)
641         ##smooth unphysical accelerations
642         eliminate = noiseelim(vps, xstdev)
643         vpscorr = eliminate[0]
644
645         ## have complete velocity time series with corrections for this column
646         ## final output: velocity time series 'vpscorr' in vcols()
647     <-----
648     vcols['{0}_{1}'.format(shotno, tzero)].append(vpscorr)
649
650     ## Velocimetry signal quality reporting metrics:
651     ## Ratio of good to bad measurements
652     stfd = eliminate[1]
653     badcount = len(reds)
654     badrat = round(badcount / len(vps), 3)
655     ## delete bad data from good array
656     gdvs = delete(vpsraw, reds)
657     gdfitter = delete(vpsfitter, reds)
658     bdtimes = []

```

```

657     ## build up array with bad data
658     for nanna in rcds:
659         badtimes.append(vptimes[int(nanna)])
660         ## weighted average of good measurements
661         gdvbar = round(average(gdvs, weights=gdfilter), 2)
662         ## weighted average of full time series including replated data (NaNs and acceleration)
663         corrvar = round(average(vpscorr, weights=vpsfilter), 2)
664
665     ## Can print all metrics of the measured time series
666     # print(col)
667     # print('loutcut {0}'.format(fvnyq))
668     # print('siglength {0}'.format(len(vtimes)))
669     ## negcount includes rapid accelerations i.e. measured before noiseelim applied
670     # print('negatives {0}'.format(negcount))
671     ## # eliminations will be sum of too fast velocities, accelerations and too low significance
672     # print('eliminations {0}'.format(badcount))
673     # print('badgdratio {0}'.format(badrat))
674     ## mean of raw velocity signal
675     # print('rawvbar {0}'.format(vbar))
676     ## mean of only good velocities in raw signal
677     # print('gdvelavg {0}'.format(gdvbar))
678     ## mean including NaN treatment
679     # print('fullcorrrelavg {0}'.format(mean(vps)))
680     ## mean including all corrections
681     # print('corrrelavg {0}'.format(corrvar))
682
683
684
685     #####
686     ## Save velocimetry data
687     savename = '{0}{1} {2} to {3} N_{4} vpol.snpz'.format(filepath, shotno, tzero, tfinal, N)
688     savez(savename, shot=shotno, t0=tzero, N=N,
689          times=vtimes,
690          rawcolVs=rawcolvs['{0}_{1}'.format(shotno, tzero)], colVs=vcols['{0}_{1}'.format(shotno,
691          tzero)], rawallVs=vcols['{0}_{1}'.format(shotno, tzero)],
692          colVserr=vcolserr['{0}_{1}'.format(shotno, tzero)])
693
694     #####
695     ## Plot Velocity Time Series v(t)
696     cmap = [plt.cm.viridis(c) for c in linspace(0, 1, 12)]
697
698     ## NB Barber pole effect of toroidal advection of tilted (along B field) turbulence eddies can be
699     ## calculated
700     try:
701         corrvs = UzCorrection(shotno, vptimes[int(len(vtimes)/2)], det_rs)
702         det_rhos = rhomaker(samarray(det_rs), shotno, vptimes[int(len(vtimes)/2)])
703         lim = nearposn(det_rhos, ..)
704         if lim == 0:
705             uzvel = 0
706         else:
707             uzvel = mean(corrvs[-lim])
708     except:
709         uzvel = 0
710         print('No Uz_tana')
711
712     for col in range(0):
713         ## plot filtered (smoothed) time series
714         velstoplot = butter_lp(vcols['{0}_{1}'.format(shotno, tzero)][col], 3, fvnyq)[int(N / 2):-int(N
715         / 2)]
716         ## add error to lowpass from sliding stdev of unfiltered velocity time series
717         velploterr = []
718         for bin in arange(int(N / 2), len(velstoplot) + int(N / 2), 1):
719             sigma = std(vcols['{0}_{1}'.format(shotno, tzero)][col][bin - int(N / 2): bin + int(N / 2)])
720             velploterr.append(sigma)
721
722     # plt.plot(vtimes, vcols['{0}_{1}'.format(shotno, tzero)][col], linewidth=1)
723     plt.plot(vtimes[int(N / 2):-int(N / 2)], velstoplot, c=cmap[col], label='col {0} Avg
724     {1}'.format(col, round(mean(velstoplot), 2)))
725     plt.fill_between(vtimes[int(N / 2):-int(N / 2)], velstoplot + velploterr, velstoplot -
726     velploterr,
727     facecolor=cmap[col], alpha=0.4, linewidth=0.)
728
729     ## plot zero on y axis to highlight change of sign
730     plt.plot([vtimes[0], vtimes[-1]], [0, 0], c='k', ls='--', linewidth=5)
731     plt.legend()
732     ## plot barber pole effect velocity
733     if uzvel != 0:
734         plt.plot([vtimes[0], vtimes[-1]], [uzvel, uzvel], c='r', ls='--', linewidth=8, label='Uztana
735     {0}'.format(round(uzvel, 1)))
736     plt.xlim(vtimes[0], vtimes[-1])
737     # plt.ylim(namin(vpavs) - 5, nmaxx(vpavs) + 5)
738     plotstyle(leg=True)
739     plt.suptitle('{0} {1} to {2} with N_{3} Velocities_stderror {4}'.format(shotno, tzero, tfinal, N,
740     expttag))
741     plt.ylabel('v(t) [km/s]')
742     plt.xlabel('Time [s]')
743     plt.savefig('{0}{1} {2} to {3} with N_{4} Velocities_stderror {5}.png'.format(filepath, shotno,
744     tzero, tfinal, N, expttag))
745     plt.show()
746     plt.clf()
747
748     #####
749     ##produce spectra of (changes over time in) velocity
750     ## common frequency axis
751     freq = psdplot(vcols['{0}_{1}'.format(shotno, tzero)]['0'], dt[1])
752     fvnyq = nearposn(freq, fvnyq)
753
754     velspecs = []
755     smoothspecs = []
756     for i in range(0):
757         velspec = psdplot(vcols['{0}_{1}'.format(shotno, tzero)][i], dt[0])
758         velspecs.append(velspec)
759         smoothspec = butter_lp(velspec, 5, 50000)
760         smoothspecs.append(smoothspec)
761
762     ## Save power spectrum data
763     psavename = '{0}{1} {2} to {3} SpectrumData.snpz'.format(filepath, shotno, tzero, tfinal)
764     savez(psavename, freqs=freq, spectrum=velspecs)
765
766     ##Plotting all frequencies of all spectra
767     cmap = [plt.cm.get_cmap('rainbow', 12) for c in linspace(0, 1, 12)]
768     cmap[2] = plt.cm.binary(4)
769     for r in arange(0, 8, 1):
770         velspec = velspecs[r]
771         smoothspec = smoothspecs[r]
772
773     plt.plot(freq, smoothspec, label='{0}_{1}'.format(det_rs[r], det_rhos[r]), color=cmap[r], lws=5)
774     ## plot nominal nyquist frequency of velocimetry
775     plt.plot([fvnyq, fvnyq], [0, 1, max(velspec)], c='k', linestyle='--', linewidth = .7)
776     plt.xscale('log')
777     plt.yscale('log')
778     plt.ylabel('Amplitude')
779     plt.xlabel('Frequency [Hz]')
780     plt.grid(True, which='both', axis='both')

```

```

775 plt.subplot(10, 1, N, 2) Velocity Spectra'.format(shotno, tzero, N))
776 plt.style('log', use, post=2, sci=1.5)
777 plt.savefig('%(0)s%(2)s to %(3)s Velocity Spectra %(4)s.png'.format(filepath, shotno, tzero, tfinal,
    expttag))
778 plt.show()
779 plt.clf()
780
781
782 =====
783 plt.close('all')
784
785 print('Done')
```

8.2 Appendix B: List of Shot Numbers Targeted

8.2.1 Classification Survey [80 Shots Total, 22 Edge Shots]

[27525, 27527, 27526, 27528] [29378, 29379, 29380], [29505, 29827, 30258, 30449], [26310, 26313, 26314, 26317], [26364, 26365, 26366, 26367, 26368, 26369, 26371, 26372, 26373, 26374, 26375, 26376, 26377, 26378], [26585, 26586, 26587], [26861, 26862, 26863, 26864, 26865, 26866], [26884, 26885, 26886, 26887, 26888, 26889, 26891], [26934, 26935, 26936, 26937, 26941, 26942], [26968, 26969, 26970, 26972, 26973], [26975, 26976, 26977, 26978, 26979, 26980], [27267, 27268, 27269, 27270, 27272, 27273, 27274, 27278], [29113, 29114, 29115, 29113, 29125, 29126, 29128, 29129], [29139, 29142, 29143, 29144, 29149, 29151, 29153, 29156, 29158, 29159, 29160], [29762, 29764], [30175, 30176, 30177, 30178, 30179], [30162, 30163, 30164, 30165, 30165, 30167, 30168, 30169, 30170, 30171, 30172], [27271, 27275, 27276, 27277, 27279, 27280], [27281, 27282, 27283, 27284, 27285], [27292, 27293, 27294, 27296, 27297, 27298], [27308], [27369, 27370, 27396, 27397, 27398, 27399, 27403, 27404, 27407, 27408, 27409], [28151, 28152, 28153, 28154, 28155, 28156], [29050, 29053], [29447], [29455], [29470], [29761], [21856], [29853, 29854, 29855], [29876, 29877, 29878], [29888, 29890, 29891], [29982, 29983], [30114, 30115, 30117], [30175, 30176, 30177, 30178, 30179]]

8.2.2 12 Shot Study

26885, 29761, 29762, 29764, 30166, 30167, 30169, 30170, 30175, 30178, 30179, 30258, 30176

8.2.3 63 Shot Study

27267, 27268, 27269, 27270, 27271, 27272, 27273, 27274, 27275, 27276, 27277, 27278, 27279, 27280, 27281, 27282, 27283, 27284, 27285, 27292, 27293, 27294, 27296, 27297, 27298, 27369, 27370, 27396, 27397, 27398, 27399, 27403, 27404, 27407, 27408, 27409, 28151, 28152, 28153, 28154, 28155, 28156, 29050, 29053, 29447, 29455, 29470, 29853, 29854, 29855, 29876, 29877, 29878, 29888, 29890, 29891, 29982, 29983, 30175, 30176, 30177, 30178, 30179

8.2.4 209 Shot Study

30174, 29782, 30277, 30280, 30067, 30272, 29483, 30184, 30345, 30210, 29151, 29771, 29776, 26526, 30154, 30071, 29799, 27865, 29036, 29484, 29088, 29485, 29379, 29380, 30019, 29759, 29876, 29377, 30251, 27399, 30112, 29378, 30351, 30117, 29570, 29493, 29976, 27398, 30320,

29420, 30323, 29133, 28065, 26490, 28222, 27138, 27317, 26493, 29961, 30007, 27001, 26553, 26366, 26378, 30375, 30102, 30124, 30271, 30321, 29495, 26527, 27333, 27327, 27530, 29749, 29743, 30406, 30260, 30148, 30122, 30441, 26459, 27330, 27329, 27473, 27579, 30163, 29751, 29750, 29421, 29550, 29506, 29209, 29272, 29142, 29270, 28091, 27872, 27144, 27332, 26377, 29785, 29752, 30405, 30266, 29089, 30021, 30113, 29423, 29545, 29417, 29182, 29507, 29552, 29472, 29090, 29131, 29181, 27325, 27510, 26371, 27408, 27137, 27407, 27369, 27331, 27578, 27328, 29803, 30369, 30094, 29964, 30378, 30101, 30010, 30086, 30418, 29406, 29418, 29419, 29424, 29425, 29557, 29549, 29543, 29261, 29548, 30023, 30142, 29264, 29262, 29273, 27653, 29275, 27430, 29132, 29056, 29208, 26496, 26354, 27603, 27143, 27380, 6369, 27474, 27431, 27335, 27440, 27334, 30444, 30100, 30092, 29954, 30261, 29944, 30390, 29758, 30279, 30087, 30143, 30144, 30262, 30263, 30264, 30325, 30282, 30020, 29502, 29071, 29407, 29473, 29470, 29567, 29416, 29503, 29060, 30458, 29175, 29207, 29061, 29210, 29077, 29091, 29129, 29114, 27323, 27433, 27324, 27489, 26582, 27387, 29580, 29578, 30031, 29946, 29769, 30060, 30188, 29628